

REFERENCE ONLY



UNIVERSITY OF LONDON THESIS

Degree phd

Year 2007

Name of Author SUET PING
KEE

COPYRIGHT

This is a thesis accepted for a Higher Degree of the University of London. It is an unpublished typescript and the copyright is held by the author. All persons consulting the thesis must read and abide by the Copyright Declaration below.

COPYRIGHT DECLARATION

I recognise that the copyright of the above-described thesis rests with the author and that no quotation from it or information derived from it may be published without the prior written consent of the author.

LOAN

Theses may not be lent to individuals, but the University Library may lend a copy to approved libraries within the United Kingdom, for consultation solely on the premises of those libraries. Application should be made to: The Theses Section, University of London Library, Senate House, Malet Street, London WC1E 7HU.

REPRODUCTION

University of London theses may not be reproduced without explicit written permission from the University of London Library. Enquiries should be addressed to the Theses Section of the Library. Regulations concerning reproduction vary according to the date of acceptance of the thesis and are listed below as guidelines.

- A. Before 1962. Permission granted only upon the prior written consent of the author. (The University Library will provide addresses where possible).
- B. 1962 - 1974. In many cases the author has agreed to permit copying upon completion of a Copyright Declaration.
- C. 1975 - 1988. Most theses may be copied upon completion of a Copyright Declaration.
- D. 1989 onwards. Most theses may be copied.

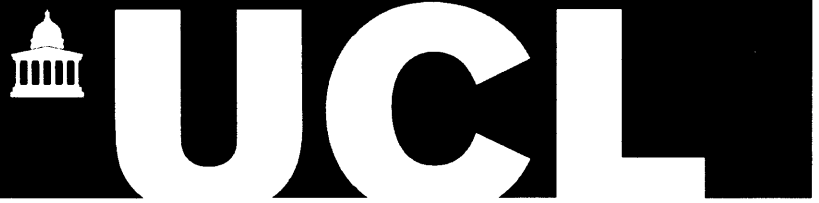
This thesis comes within category D.



This copy has been deposited in the Library of UCL



This copy has been deposited in the University of London Library, Senate House, Malet Street, London WC1E 7HU.



Microreactor Engineering Studies

for

Asymmetric Chalcone Epoxidation

Suet Ping Kee

March 2007

A thesis submitted for the degree of Doctor of Philosophy
of the University of London

UMI Number: U592075

All rights reserved

INFORMATION TO ALL USERS

The quality of this reproduction is dependent upon the quality of the copy submitted.

In the unlikely event that the author did not send a complete manuscript and there are missing pages, these will be noted. Also, if material had to be removed, a note will indicate the deletion.



UMI U592075

Published by ProQuest LLC 2013. Copyright in the Dissertation held by the Author.
Microform Edition © ProQuest LLC.

All rights reserved. This work is protected against unauthorized copying under Title 17, United States Code.



ProQuest LLC
789 East Eisenhower Parkway
P.O. Box 1346
Ann Arbor, MI 48106-1346

Declaration

'I, Suet Ping Kee, confirm that the work presented in this thesis is my own. Where information has been derived from other sources, I confirm that this has been indicated in the thesis.'

Word count (exclusive of appendices and bibliography): approximately 58000 words

Signature

Abstract

Advances in the field of microreaction technology offer the opportunity to combine the benefits of continuous processing with the flexibility and versatility desired in the pharmaceutical and fine chemicals industry. Microreactor devices, also offer their own unique advantages over traditional continuous processing, such as improved heat and mass transfer, safer handling of exothermic reactions and easy containment of explosive and toxic materials. A reaction system can be quickly scaled-up to production levels by increasing the number of units operating in parallel, allowing significant savings in time and R&D costs. Most studies of microreactor systems to date focus on the development and performance of individual microdevices. However, a top down approach is preferred, with the focus on the requirements of the process and a suitable device design derived to meet those requirements.

This work aims to demonstrate the suitability of the poly-*L*-leucine catalysed asymmetric epoxidation of chalcone reaction for continuous processing as well as the process and choices of designing and scaling a microchemical system. A suitable continuous reaction protocol was established for this reaction system, achieving a conversion of 88.4 % and enantioselectivity of 88.8 %. Mixing was found to be critical due to the low diffusivity ($\sim 10^{-11}$) of the polymeric catalyst. Design criteria were established and a microstructured reactor with a footprint of 110 mm x 85 mm and production rate of ~ 0.5 g/day was designed for the system. An external scale-out structure was selected. The staggered herringbone mixer was selected for enhancing the mixing in the microstructured reactor.

A method for characterizing the mixing performance in the staggered herringbone mixer based on stretching computations using particle tracking methods was developed, which allowed the required mixer length to be derived directly. Mixer lengths of 40 mm were provided for both deprotonation and epoxidation mixers. The effects of varying operating temperature, residence time and reactant concentrations on reaction performance in the fabricated microstructured reactor were investigated. The base case condition (13.47 g/l PLL, 0.132 mol/l H₂O₂, 0.0802 mol/l chalcone, 0.22 mol/l DBU) was found to be optimal, achieving a conversion of 86.7 % and enantioselectivity of 87.6 %. Several unexpected phenomena such as bubble clogging and increased viscosity due to the polymeric catalyst were encountered. A scaled-out system was designed and experiments carried out. Flow maldistribution, attributed to fabrication errors and bubble clogging, resulted in poor reaction performance (conversion ~ 31.4 % and enantioselectivity ~ 82.7 %) due to unequal residence times and imperfect mixing ratios of reactants. The commercial potential of the research was evaluated. Micro and macro level analysis of the market and industry were favourable and a suitable commercialisation route was suggested.

To my family

Acknowledgements

I would like thank the Overseas Research Students Awards Scheme and the DTI/EPsrc Foresight Link programme for financial support, without which this work would not have been possible. I would also like to thank the Centre for Scientific Enterprise for the excellent opportunity to expand my business knowledge at the London Business School and for providing me with a PhD scholarship to evaluate the commercial potential of my research.

I would like to express my deepest gratitude to my supervisor Prof.Gavriilidis for his guidance, advice and encouragement throughout my PhD and especially in the latter stages of the project. My sincere thanks to my subsidiary supervisor Dr.George Manos in supporting my initial application, which has enabled me to pursue my dream. I am truly grateful to Dr.Enhong Cao for his advice and for always taking the time to help me troubleshoot problems in the lab.

My warmest thanks go to all my friends at UCL and at International Hall, who have made my experience in London a memorable one. Special thanks to Sharon, Kay and Xiuyan for constantly lending a sympathetic ear. Last but most certainly not least, a very big thank you to my wonderful parents for their love, support and encouragement.

Table of Contents

List of Figures	xii
List of Tables	xviii
Nomenclature	xxi
1. Introduction	1
2. Literature Review	8
2.1. Poly- <i>L</i> -leucine Catalysed Epoxidation of Chalcone	9
2.1.1. Original Triphasic System	9
2.1.2. Non-aqueous Biphasic System	11
2.1.3. Mild System	13
2.1.4. Non-aqueous Homogeneous System	13
2.1.5. Triphasic System with Phase Transfer Catalysts	13
2.1.6. Applications and Industrial Relevance	14
2.2. Poly- <i>L</i> -leucine Catalyst	16
2.2.1. Catalyst Preparation	16
2.2.2. Catalyst Regeneration	17
2.3. Reaction Mechanism	18
2.3.1. Helicity and Catalyst Length	18
2.3.2. Influence of Terminal Groups	19
2.4. Kinetic Studies	20
2.5. Introduction to Microchemical Systems	21
2.5.1. Characteristics of Microchemical Systems	23
2.5.2. Application of Microchemical Systems	23
2.5.3. Microfabrication Methods	24
2.6. Microchemical Processing	25
2.6.1. Micromixing	26
2.6.2. T-Micromixers	27
2.6.3. Parallel Lamination Micromixers	28
2.6.4. Focussing Micromixers	32
2.6.5. Serial Lamination Micromixers	33
2.6.6. Secondary Flow Micromixers	37
2.6.7. Grooved Micromixers	43

2.6.8. Hybrid Micromixers	48
2.6.9. Miscellaneous Micromixers	51
2.6.10. Integrated Microreaction System	55
2.7. Microchemical Plant Concepts	57
2.7.1. Internal versus External Numbering-up	58
2.7.2. Microplant Structures	59
2.7.3. Instrumentation and Control	61
2.7.4. External Scale-out of Microreaction Systems	62
2.7.5. Internal Scale-out of Microreaction Systems	64
2.7.6. Commercial Microreactor Setups	66
2.7.7. Microchemical Production Units	70
2.8 Conclusion	72
3. Poly-L-leucine Catalysed Asymmetric Epoxidation of Chalcone Protocol Selection	75
3.1. Introduction	76
3.2. Evaluation of reaction systems	78
3.2.1. Cost Considerations	80
3.2.2. Safety Considerations	81
3.2.3. Environmental Hazard Considerations	82
3.2.4. Potential Scale Up Obstacles	85
3.3. Results and Discussion	85
3.3.1. Cost Evaluation	85
3.3.2. Safety and Environmental Effects	86
3.3.3. Potential Scale Up Obstacles	88
3.4. Conclusion	89
4. Batch and Continuous Small Scale Reaction System	91
4.1. Introduction	92
4.2. Experimental	95
4.2.1. Analytical Conditions	95
4.2.2. Determination of Peroxide Concentration	96
4.2.3. Batch Experimental Procedure	96
4.2.4. Continuous Experimental Procedure	97

4.3. Batch Experiments	100
4.3.1. Effect of Solvent Premixing	100
4.3.2. Effect of Deprotonation Time	101
4.3.3. Effect of Reactant Addition Sequence	103
4.3.4. Background Reaction	105
4.3.5. Effect of Higher Concentrations	106
4.4. Continuous Experiments	107
4.4.1. Background Reaction	107
4.4.2. Catalysed Reaction	108
4.5. Conclusion	112
5. Design of Continuous Microstructured Reactor for Chalcone Epoxidation	114
5.1. Introduction	115
5.2. Design Basis and Motivation	115
5.2.1. Rate Equations	119
5.2.2. Production Rate	122
5.3. Mathematical Models	124
5.3.1. Batch Reactor Model	124
5.3.2. Laminar Tubular Reactor Model	125
5.3.3. Laminar Slit Flow Reactor Model	127
5.3.4. Accuracy of Numerical Model	129
5.3.5. Comparison with Experimental Results	131
5.4. Design of Single Reaction Unit	135
5.4.1. Mixer Device Screening and Selection	135
5.4.1.1. Curved Channel Micromixer	139
5.4.1.2. Staggered Herringbone Micromixer	141
5.4.1.3. IMM Split and Recombine Micromixer	142
5.4.1.4. Conclusion	142
5.4.2. Dimensioning of Reactor Channel	144
5.4.3. Heat Management	149
5.4.4. Materials	152
5.5. Conclusion	156

6. Design and Characterisation of the Straggered Herringbone Mixer	158
6.1. Introduction	159
6.2. Numerical Methods	168
6.2.1. Velocity Field	170
6.2.2. Particle Tracking Computations	171
6.2.2.1. Particle Trajectories	171
6.2.2.2. Stretching	174
6.3. Results and Discussions	179
6.3.1. Flow Patterns	179
6.3.2. Mixing Simulation	182
6.3.3. Coefficient of Variance	187
6.3.4. Stretching	189
6.3.5. Mixer Design for Chalcone Epoxidation	198
6.3.6. Laminated Inlets	200
6.3.7. Pressure Drop	202
6.4. Conclusion	205
7. Chalcone Epoxidation Reaction in a Microstructured PEEK Reactor	207
7.1. Introduction	208
7.2. Experimental	208
7.2.1. Reactor Configuration	208
7.2.2. Setup Description	209
7.3. Results and Discussions	212
7.3.1. Base Case	212
7.3.2. Blank Runs	213
7.3.3. Effect of Temperature	213
7.3.4. Effect of Chalcone Concentration	217
7.3.5. Effect of Peroxide Concentration	221
7.3.6. Effect of DBU Concentration	225
7.3.7. Effect of Catalyst Concentration	229
7.3.8. Higher Concentrations of All Reactants	234
7.3.9. Effect of Residence Time	237
7.3.10. Effect of Mixing Sequence	239
7.4. Conclusion	241

8. Numbering-up of Chalcone Epoxidation System	244
8.1. Introduction	245
8.2. Experimental	247
8.2.1. Flow Distribution	247
8.2.2. Scaled Out Reactor Configuration	256
8.2.3. Setup	257
8.2.4. Flow Visualisation	257
8.3. Results and Discussions	258
8.3.1. Base Case Chalcone Epoxidation Reaction	258
8.3.2. Flow Visualisation	259
8.3.3. Liquid Distribution Problem	263
8.4. Conclusion	269
9. Conclusions and Future Work	271
9.1. Conclusions	272
9.2. Suggestion for Future Work	279
Bibliography	282
Appendices (CD)	
3-1 Cost Calculations for the Homogeneous System	300
3-2 Safety Score Calculation for the Homogeneous System	302
3-3 Environmental Score Calculations for the Homogeneous System	307
4-1 Estimation of Chalcone Diffusivity Values	315
5-1 gPROMS Code for Batch Reactor	320
5-2 gPROMS Code for Laminar Tubular Reactor	327
5-3 gPROMS Code for Slit Flow Reactor	333
5-4 CAD Drawings	340
6-1 Matlab Code for Particle Tracking	343
6-2 Matlab Code for Particle Tracking and Stretch Computations	362
6-3 Matlab Code using Runge-Kutta-Fehlberg Method	383
6-4 Matlab Code for Recording Particle Tracer Positions	397
6-5 Matlab Code for Velocity Vector Plots	405
6-6 Matlab Code for Calculation of COV	407

Table of Contents

6-7	Matlab Code for Recording Particle Tracer Position and Stretch Values	447
6-8	Matlab code for Particle Trajectories	459
6-9	Derivation of Equation [6-9]	467
7-1	Calculation of Equilibrium Perhydroxyl Ion Concentration	470
8-1	Calculation of Pressure Drop Across Different Flow Sections	474
9-0	Commercial Potential of Microstructured Reactors for Chiral Epoxides Synthesis	482

List of Figures

Figure 2.1	IMM Interdigital Micromixer	29
Figure 2.2	Mixing element with nozzle structures	29
Figure 2.3	Two platelet designs for the microjet mixer	30
Figure 2.4	StarLaminator from IMM	31
Figure 2.5	Schematic diagram of the 'Chessboard' mixer	31
Figure 2.6	Optimised SuperFocus micromixer	33
Figure 2.7	Splitting-reshaping-recombination (SAR) mechanism	34
Figure 2.8	PDMS Split and recombine micromixer	36
Figure 2.9	(a) Schematic of a spiral microchannel incorporating 3 spiral segments (b) Gray scale images depicting expansion of the mixed interface with increasing Re in a two-arc spiral channel incorporating expansion vortex effects.	38
Figure 2.10	Schematic diagram showing the micromixer and the mixing principle	40
Figure 2.11	Four different mixing elements tested	41
Figure 2.12	Three dimensional secondary flow microchannel mixers (from left to right, twisted microchannel, inclined micromixer, oblique micromixer and wavelike micromixer)	42
Figure 2.13	Schematic of the structure of the microfluidic device. (a) Design of one sawtooth unit. (b) Cross section of the device. The gray areas indicate the PDMS device while the white areas are the housing made of PMMA	43
Figure 2.14	(a) Slanted groove micromixer.(b) Staggered herringbone micromixer	44
Figure 2.15	Barrier embedded micromixer (a) Schematic view, (b) and (c) are cross-sectional velocity fields at two typical locations.	45
Figure 2.16	(a) Parallel grooved micromixers. (b) Phase-shift grooved micromixers	46
Figure 2.17	Staggered oriented ridges	47

Figure 2.18	Schematic diagram of a staggered overlapping crisscross (SOC) micromixer (top). Overlapping crisscross micromixer (bottom, left) and several variants of the SOC mixers (bottom, second to fourth mixers on the right)	48
Figure 2.19	Serpentine laminating mixer	49
Figure 2.20	Alternating whirl (AW) and Alternating whirl-lamination (AWL) micromixers (i) Mixing channel for counterclockwise (CCW) direction whirls (ii) Mixing channel for clockwise (CW) direction whirls (iii) Structure of both AW and AWL micromixers.	50
Figure 2.21	Micromixer with obstacle structures	51
Figure 2.22	Schematic illustration of the mixing principle (left) and the Tesla micromixer (right)	52
Figure 2.23	Schematic diagram of the passive recycle mixer	52
Figure 2.24	(a) Micromixers with intersecting devices. (b) Micromixers with helical internals	53
Figure 2.25	Micromixer based on collision of microsegments (a) The internal structure. (b) Schematic of flow in the micromixer.	54
Figure 2.26	Vertically integrated microreaction system	55
Figure 2.27	Horizontally integrated microreaction system with a nozzle-type mixing component, using microlamination and hydrodynamics focusing and a two-channel, countercurrent flow heat exchanger.	57
Figure 2.28	Four types of plant structures	60
Figure 2.29	Flow splitting unit for external scale-out	63
Figure 2.30	Vertically stacked gas-liquid microreaction layers	64
Figure 2.31	Pile-up glass microreactors	65
Figure 2.32	Modular fluidic backbone concept	67
Figure 2.33	FAMOS microreaction system	68
Figure 2.34	(a) CYTOS Lab System (b) Fluidic scheme of the CYTOS Pilot System (left) and CYTOS Production System (right)	69
Figure 2.35	External view of the DEMis reactor together with a schematic outline of the internals	71
Figure 3.1	Six reaction systems used in the case study	80
Figure 3.2	Comparison of relative cost and catalyst turnover	87

Figure 3.3	Comparison of relative safety and environmental scores	87
Figure 4.1	Assembled continuous flow reactor and mixing chips used in this work	98
Figure 4.2	Experimental setup for continuous epoxidation experiments	98
Figure 4.3	Conversion and enantioselectivity of the chalcone epoxidation as a function of deprotonation time (conditions: base case with premixed THF/ACN at 30°C)	103
Figure 4.4	Conversion and enantioselectivity of the chalcone epoxidation for various reactant addition sequences. For details see text. (Conditions: with premixed THF/ACN, 30 minutes pre-stir prior to epoxidation reaction at 30°C)	104
Figure 4.5	Conversion and enantioselectivity for chalcone epoxidation in the absence of catalyst (Conditions: premixed THF/ACN with 30 minutes deprotonation time at 30°C)	105
Figure 4.6	Flow diagram of continuous experimental setup	107
Figure 4.7	Modified flow arrangement of continuous experimental setup	111
Figure 5.1	Possible scale-out structures for chalcone epoxidation	118
Figure 5.2	Pressure driven flow between parallel plates with both plates stationary	127
Figure 5.3	Experimental and predicted values of conversion and enantioselectivity in a batch reactor.	133
Figure 5.4	Predicted and experimental conversion and enantioselectivity values in a continuous tubular reactor.	134
Figure 5.5	Curved channel mixer	140
Figure 5.6	Length for 90 % mixing versus $\ln(Pe)$	141
Figure 5.7	Change in pressure drop with channel equivalent diameter	148
Figure 5.8	Effect of Pe_r^{-1} on conversion and enantioselectivity	148
Figure 5.9	(a) Adiabatic temperature rise and (b) temperature profile at constant wall temperature, both shown here for a design temperature of 23.1°C.	150
Figure 5.10	Arrangement of scaled out reaction chips to maintain isothermal conditions in all chips	150
Figure 5.11	Temperature profile of inlet fluids	152

Figure 5.12	Microscope photograph of unbonded PEEK reactor (a) Herringbone grooves etched on SU-8 (b) Both sides of the unbonded microstructured PEEK reactor.	155
Figure 5.13	Pictures of unbonded SU-8 on PEEK microchannel before and after testing with urea-hydrogen peroxide and DBU in THF/ACN.	156
Figure 6.1	3D geometry of one of the channels with asymmetric V-shaped ridges using the Weierstrass function to generate the position of the 'V' groove on the bottom wall.	167
Figure 6.2	Staggered Herringbone Mixer	169
Figure 6.3	Computed particle trajectories at a time step of $h = 0.1$ and 0.05 , for 10 different initial locations (a) Initial location of 10 particles (b) Particle trajectories in the x -direction (c) Particle trajectories in the y -direction (d) Particle trajectories in the z -direction	172
Figure 6.4	Computed stretch values at a time step of $h = 0.1$ and 0.05 , for 10 different initial locations.	175
Figure 6.5	Cross-sectional velocity vector plots at various axial positions for $Re = 0.01$ (a) Axial position of the cross-sectional velocity vector plots (b) Velocity vector plots	180
Figure 6.6	Particle trajectories of 10 samples points at $Re = 0.01$ (a) Particle trajectories at 10 different initial locations along 8 mixing cycles for $t = 0 - 10$ s (b) X-Z plane viewed from outlet for $t = 0 - 10$ s.	182
Figure 6.7	Comparison of the evolution of particle tracer positions along the mixer length with confocal micrographs of an actual staggered herringbone mixer. Both the simulation plot and experimental confocal micrographs were obtained at $Re = 0.01$.	185
Figure 6.8	Comparison of particle distribution cross-sectional plots at the end of cycle 5, at $Re = 0.001, 0.01, 0.03, 1$ and 10 .	186
Figure 6.9	Change in coefficient of variance with number of mixing cycles at $Re = 0.001$ to 10 (All data points at different Re overlap).	188
Figure 6.10	$\ln<\lambda_{g,50}>$ vs number of mixing cycles at various Re (Data points at different Re overlap).	192
Figure 6.11	Computed and experimentally derived mixing lengths versus $\ln(Pe)$	195
Figure 6.12	Log-normal distribution of stretch values at $Re = 0.01$.	196
Figure 6.13	$\ln \lambda_{g,90}$ vs number of mixing cycles at various Re (data points at different Re overlap).	196
Figure 6.14	Cut-off point above which 90 % of computed stretch values are higher	197

Figure 6.15	$\ln \lambda_{g,50}$ and $\ln \lambda_{g,90}$ vs number of mixing cycles (data points at different Re overlap).	199
Figure 6.16	Evolution of striation patterns with mixing cycles for laminated inlet streams at $Re = 0.01$. (a) Horizontal lamination. (b) Vertical lamination.	201
Figure 6.17	Comparison of striation patterns at the end of Cycle 5. (a) Horizontal Lamination. (b) Vertical Lamination. (c) regular unlaminated inlet	202
Figure 6.18	Change in ΔP across one mixing cycle with Reynolds number	204
Figure 6.19	Change in Z-factor values with increasing Reynolds number	204
Figure 6.20	Change in friction factor with Reynolds number	205
Figure 7.1	View of the unbonded microstructured PEEK plate	208
Figure 7.2	Assembled PEEK and Acrylic microstructured reactors	209
Figure 7.3	Experimental setup with Epigem PEEK reactor	210
Figure 7.4	Effect of temperature on catalysed reaction conversion in PEEK reactor	216
Figure 7.5	Effect of temperature on catalysed reaction enantioselectivity in PEEK reactor	216
Figure 7.6	Effect of temperature on background reaction in PEEK reactor	217
Figure 7.7	Effect of chalcone concentration on conversion in PEEK reactor	219
Figure 7.8	Effect of chalcone concentration on enantioselectivity in PEEK reactor	220
Figure 7.9	Predicted effect of chalcone concentration on ratio of catalysed to background reaction rates.	220
Figure 7.10	Effect of peroxide concentration on conversion in PEEK reactor	224
Figure 7.11	Effect of peroxide concentration on enantioselectivity in PEEK reactor	225
Figure 7.12	Effect of DBU concentration on conversion in PEEK reactor.	228
Figure 7.13	Effect of DBU concentration on enantioselectivity in PEEK reactor.	228
Figure 7.14	Diffusion of high polymers	230
Figure 7.15	Effect of PLL concentration on conversion in PEEK reactor	231
Figure 7.16	Effect of PLL concentration on enantioselectivity in PEEK reactor	231
Figure 7.17	Polymer coils in solution	233
Figure 7.18	Effect of higher concentrations of all reactants on conversion	235
Figure 7.19	Effect of higher concentrations of all reactants on enantioselectivity	236
Figure 7.20	Effect of longer residence time on conversion	238
Figure 7.21	Effect of longer residence time on enantioselectivity	238

Figure 7.22	Effect of mixing sequence on conversion and enantioselectivity in PEEK reactor at 23.1 °C	240
Figure 7.23	Effect of mixing sequence on conversion and enantioselectivity in a tubular reactor at 30°C	240
Figure 8.1	Ratio R_R/R_A required for flow equipartition as a function of number of channels N and divergence from flow equipartition, FD	248
Figure 8.2	Schematic of the various flow sections (a) View of the inlet/outlet headers (b) View from the top of the reactor plate	251
Figure 8.3	Flowrates across different sections of the inlet header	253
Figure 8.4	(a) Stacked acrylic reactors using PEEK connector fittings. (b) PTFE ferrules used with the PEEK fittings provide sealing between connector fitting and PEEK reactor plate.	256
Figure 8.5	Stacked PEEK reactors	257
Figure 8.6	Flows in single reactors (5 – 8) at total flows of 0.02 ml/min at the start of the experiment (left) and at some time later (right).	260
Figure 8.7	Flows in scaled-out configurations (5, 6, 7 and 8) at a flowrate of 0.08 ml/min. Reactor 5 located at the top of the stack, followed by 6, 7 and 8.	261
Figure 8.8	Flows in scaled-out configurations (5, 6, 7 and 8) at a flowrate of 0.04 ml/min. Reactor 5 located at the top of the stack, followed by 6, 7 and 8.	262
Figure 8.9	Flows in scaled-out configurations (8, 5, 7 and 6) at a flowrate of 0.04 ml/min. Reactor 8 located at the top of the stack, followed by 5, 7 and 6.	263
Figure 8.10	'Flex reactor' from BHR group	266
Figure 8.11	Annular multilamination micro reactor	267
Figure 8.12	Vertical versus horizontal scale out of PEEK reactors.	268

List of Tables

Table 3.1	Six major reaction protocols identified for poly- <i>L</i> -leucine catalysed asymmetric epoxidation of chalcone	77
Table 3.2	Details of the six reaction systems identified as potential candidates for the case study	79
Table 3.3	Major obstacles to scale up identified for each reaction system	88
Table 4.1	Base case initial concentrations of reactants	94
Table 4.2	Channel dimensions of the mixing chips	98
Table 4.3	Initial concentrations of reactants at background base conditions	105
Table 4.4	Initial concentrations of reactants used at 6 x base case concentrations	106
Table 4.5	Calculated required mixing lengths in the first and second micromixing chips based on poly- <i>L</i> -leucine and chalcone diffusivities	109
Table 4.6	Comparison of reaction performance with different micromixers	110
Table 4.7	Calculated required mixing time for IMM Slit Interdigital Micromixer based on poly- <i>L</i> -leucine and chalcone diffusivities. Values in brackets are for characteristic dimension of 100 μm for comparison.	110
Table 5.1	Reactant concentration ranges used for kinetic studies	119
Table 5.2	Values for kinetic constants used in the rate equations for both catalysed and background chalcone epoxidation	120
Table 5.3	Conversion and enantioselectivity values at various reaction conditions.	121
Table 5.4	Estimate of cost of catalyst using different reactor volumes	123
Table 5.5	Change in component concentration due to reaction	124
Table 5.6	Solution of the gPROMS models using different number of grid points	130
Table 5.7	Reaction time constants for catalysed and background reactions at two different initial concentration values	137
Table 5.8	Calculated reaction and mixing time constants	138

Table 5.9	Calculated Dean number for a range of channel hydraulic diameters	141
Table 5.10	Details of the three mixer types evaluated.	143
Table 5.11	Details of staggered herringbone mixer design	144
Table 5.12	K values for different channel width to height ratios	146
Table 5.13	Dimensions of 0.32 ml reaction channel at different channel widths	147
Table 5.14	Reaction Channel dimensions	149
Table 5.15	Channel geometry and fluid properties used in FEMLAB simulation	151
Table 6.1	Mixer geometry and fluid properties	169
Table 6.2	Runge-Kutta-Fehlberg Method (RKF45)	178
Table 6.3	Step sizes used for all simulation cases	183
Table 6.4	Initial and minimum time step sizes for all simulation cases	191
Table 6.5	Fluid properties of chalcone epoxidation reaction	198
Table 6.6	Results of stretching computation for chalcone epoxidation conditions	199
Table 7.1	Comparison of base case chalcone epoxidation in PEEK reactor at 23.1°C and 16 minutes residence time with other similar operating conditions.	212
Table 7.2	Initial concentrations of reactants used to study the effect of [Chalcone].	217
Table 7.3	Initial concentrations of reactants used to study the effect of [H ₂ O ₂].	221
Table 7.4	Equilibrium perhydroxyl ion concentration and various reactant ratios at different peroxide concentrations	223
Table 7.5	Initial concentrations of reactants used to study the effect of [DBU]	226
Table 7.6	Equilibrium perhydroxyl ion concentrations at different DBU concentrations	226
Table 7.7	Initial concentrations of reactants in the study of the effect of [PLL	229

Table 7.8	Initial concentrations of reactants at higher reagents concentrations	234
Table 8.1	The various flow sections considered	250
Table 8.2	Pressure change on a single PEEK reaction reactor	251
Table 8.3	Inlet and outlet header dimensions	255
Table 8.4	Performance of a stack of 4 PEEK reactors at base case epoxidation compared to performance of single reactor.	258

Nomenclature

A	Interfacial surface area	m^2
C_{A0}	Initial concentration of component A	mol/l
C_{B0}	Initial concentration of component B	mol/l
C_n	Concentration of component n	mol/l
C_p	Specific heat capacity	$\text{kJ kg}^{-1} \text{K}^{-1}$
∇C	Gradient of species concentration	mol/m^4
d	Diameter	m
d_c	Characteristic dimension	m
d_h	Hydraulic diameter of mixing channel	m
D	Diffusion coefficient	m^2/s
D_o	Diffusion coefficient of solute in pure solvent	m^2/s
D_{ab}	Diffusivity of a in b	m^2/s
D_E	Equivalent diameter	m
D_n	Molecular diffusivity of component n	m^2/s
D_{PLL}	Molecular diffusivity of PLL	m^2/s
ΔP_0	Pressure drop across outlet holes	Pa
$\Delta P_{2-phase}$	Two phase flow pressure drop	Pa
$\Delta P_{Channel}$	Pressure drop in a grooveless channel	Pa
ΔP_{header}	Pressure change in the header	Pa
ΔP_L	Single liquid flow pressure drop	Pa
ΔP_P	Pressure drop over the length of the distributor	Pa
$\Delta P_{reactor}$	Pressure change across one PEEK reactor	Pa
ΔP_{SHM}	Pressure drop in a staggered herringbone mixer	Pa
Fo	Fourier number	-
FD	Flow divergence	-
$\sum F$	Sum of frictional and secondary losses	Pa
g	Gravitational acceleration	m/s^2
h	Channel height	m
h	Time step	s

H_n	Normalised helicity	-
H_{Rxn}	Heat of reaction	kJ/mol
k	Rate constant	$\text{l}^2/\text{g.mol.s}$
k_{BG}	Background reaction rate constant	l/mol.s
K	Identification number for the onset of the engulfment regime	-
K	Dean Number	-
K_c	Critical Dean Number	-
K_{Chalcone}	Equilibrium constant associated with chalcone	l/mol
$K_{\text{H}_2\text{O}_2}$	Equilibrium constant associated with hydrogen peroxide	l/mol
l	Characteristic length	m
l	Fluid filament vector tracked for stretching computations	
l_0	Initial condition for vector l	
L	Length	m
L_{cycle}	Length per mixing cycle	m
L_e	Losses in sudden contraction/enlargement in terms of equivalent pipe length	m
L_{mix}	Mixing length	m
LC_{50}	Concentration of chemical i in water which kills 50% of a test population of the most sensitive species over a 96 hour period	mg/dm^3
LD_{50}	Lethal Dose of chemical i that kills 50% of the test population of species x	mg/kg
N	Number of mixing cycles	-
N	Number of PEEK reactors	-
N_i	Number of particles in each cell	-
N_T	Total number of particles within the grid	-
N_{T0}	Initial number of tracked particles	-
\bar{N}	Average particle concentration per cell	-
p	the degree of asymmetry of herringbone grooves	-
P	Pressure	Pa
P_n	Pressure at point n	Pa
Pe_r	Radial Peclet number	-

Pe_z	Axial Peclet number	-
q	the groove wave vector	-
Q	amount of the chemical available for release, taken as the inventory of the chemical in the plant	tonne
Q	Volumetric flow	m^3/s
Q_{EQUI}	Volumetric flow under equipartition conditions	m^3/s
$Q_{R,j}$	Volumetric flow in the reaction channel j	m^3/s
r	Radial direction	-
r_n	Change in component n concentration due to reaction	$\text{mol}/(\text{l.s})$
R	Radius	m
R	Mean radius of curvature	m
R_A	Frictional resistance in the distributing header	Pa
R_g	Radius of gyration of polymer coils	m
R_n	Pressure change across section n	Pa
R_{ER}	Pressure change across epoxidation reactor only	Pa
\mathfrak{R}_n	Change in component n concentration due to reaction	$\text{mol}/(\text{l.s})$
R_R	Frictional resistance across reactor	Pa
R_T	Total pressure change across both deprotonation and epoxidation reactors	Pa
Re_d	Reynolds number based on channel diameter	-
s	Scalar s to compute optimal step size	-
s_{\min}	Minimum value of the scalar s	-
S	Enantioselectivity	-
S	Shannon entropy	bits
$s(0)$	Striation thickness at time = 0	μm
$s(N)$	Striation thickness at cycle N	μm
Sc	Schmidt number = $\frac{\mu}{\rho D_n}$	-
SE	Standard Error	-
$t_{1/2}$	Reaction time constant	minutes
t_{chalcone}	Diffusional mixing time for chalcone	s
t_{mix}	Mixing time	s
t_{PLL}	Diffusional mixing time for PLL	s

T	Temperature	K
T_{in}	Inlet temperature	K
T_{wall}	Wall temperature	K
TDI _{fx}	Daily Food intake of species x	m^3/day
TDI _{wx}	Daily Water intake of species x	m^3/day
u	Velocity	m/s
\bar{u}	Average velocity	m/s
$v(x)$	Particle velocity as a function of position	m/s
$(\nabla v)^T$	Velocity gradient tensor	s^{-1}
V_z	Axial velocity profile	m/s
w	Channel width	m
W	Width	m
W _s	Shaft work	W
W _{t_x}	Weight of species x	kg
x	Mixing cycle number	-
\bar{x}	Vector of particle position	-
X	Conversion	-
y	Mixing length	m
Y	Half of slit height	m
z	Axial direction	-
[Cata]	Catalyst loading	g/l
[Chalcone]	Chalcone concentration	mol/l
[H ₂ O ₂]	Hydrogen peroxide concentration	mol/l

Greek Letters

α	Parameter to describe the geometric shape of a polymer molecule	-
α	ratio of the groove half height to the channel height	-
α	Stretching function	-
α_{50}	Specific stretching per period (based on mean values)	-
α_L	Homogeneous liquid fraction	-
α_T	Thermal diffusivity	m^2/s
δ	Lyapunov exponent	s^{-1}

δ_x	Penetration distance	m
ζ	Dimensionless radial length	-
θ	Groove angle	°
λ	Stretching experienced by vector l	-
λ	Thermal conductivity	W/(mK)
$\lambda_{g,50}$	Geometric mean stretch over all vectors on a given cross section	-
λ_k	characteristic length denoting the scale of created vortices	m
μ	mean	-
μ	Viscosity	Pa.s
μ_0	Viscosity of the suspending medium	Pa.s
μ_{eff}	Effective viscosity	Pa.s
ν	Kinematic viscosity	m ² /s
ξ	Dimensionless axial length	-
ρ	Density	kg/m ³
σ	Standard deviation	-
σ^2	Variance (number based)	-
τ	Average residence time per period	s
τ	Residence time	s
φ	Mass fraction	-
φ	Volume fraction of polymer in solution	-
ω	vorticity	s ⁻¹

Abbreviations

ACN	Acetonitrile
CLAMPS	cross-linked aminomethyl polystyrene
COC	Cyclo olefin copolymer
COV	Coefficient of variance
DAP-PLL	1,3-diaminopropane polylysine
DBU	1,8-diazabicyclo[5.4.0]undec-7-ene
DME	1,2-dimethoxyethane
EHI	environmental hazard index
IMM	Institut für Mikrotechnik Mainz

LIGA	X-ray lithography (X-ray Lithographie), Electroplating (Galvanoformung), and Molding (Abformung))
PaaSiCats	Polyamino acid on Silica catalyst
PDMS	Polydimethylsiloxane
PEC	predicted environmental concentrations
PEEK	Polyetheretherketones
PEG-PLL	Polyethylene glycol-Poly- <i>L</i> -leucine
PET	Polyethylene terephthalate
PLL	Poly- <i>L</i> -leucine
PMMA	Poly(methyl methacrylate)
SEHI	specific environmental hazard index
STHI	specific terrestrial hazard index
SWHI	specific water hazard index
THF	Tetrahydrofuran
UV	Ultra violet

Subscripts

<i>n</i>	Component <i>n</i>
<i>mix</i>	Mixing cup average
50	Based on mean value
90	Based on cutoff point of 1.2816 σ below mean
dif	diffusional

Chapter 1

Introduction

The success of pharmaceutical companies depends largely on their ability to maintain a pipeline of new drug compounds and to optimize the production of marketable drugs. In recent years, the pharmaceutical and fine chemicals industry have been under tremendous pressure to streamline and improve its complete business; the increasing time and costs of discovering, developing and gaining regulatory approval for a new drug coupled with increased global competition from generics manufacturers all put an immense pressure on profit margins. The time to market is therefore of utmost importance, to allow for some of the costs incurred to be recovered before the patent expires.

While combinatorial chemistry and high-throughput screening have allowed rapid synthesis and identification of new lead compounds, bottlenecks occur when these need to be produced on a larger scale, due to the costs and time required to scale up to production. The need for more efficient process development and manufacturing methods as well as the general shift towards inherently safer and greener processes have led pharmaceutical companies to increasingly re-evaluate the use of continuous processing and look into using innovative new technologies as an alternative to conventional batch processes (Anderson, 2001; Stitt, 2002; Schwalbe et al, 2004). The pharmaceuticals and fine chemicals industry have traditionally relied heavily on batch reactors which are flexible towards frequent product changes and production rates and can accommodate various downstream operations. The flexibility and versatility of the equipment is required, given the relatively low volumes and short life time of the products, to limit the investment costs.

On the other hand, continuous processing is generally preferred in the commodity chemicals sector because it is operationally stable and offers better process control, consistent product quality, enhanced safety, lower operating costs and it allows more material to be made from a smaller plant with lower capital investment. However, continuous processing relies on dedicated processing plants that are inflexible and not amenable to varying production rates or product changes (Anderson, 2001).

Recent technological advances in the field of microreaction technology offer the opportunity to combine the benefits of continuous processing with the flexibility and versatility desired in the pharmaceutical and fine chemicals industry (Schwalbe et al, 2004; Roberge et al, 2005). Microreactor devices, generally defined as miniaturised reaction systems fabricated by microtechnology and precision engineering also offer their own unique advantages over traditional continuous processing. The high surface to volume ratios allow for highly efficient heat and mass transfer while small reaction volumes allow safer handling of exothermic reactions and easy containment of explosive and toxic materials. These characteristics allow precise control of reaction parameters and access to new reaction regimes that could potentially improve yield and selectivity, making the process more efficient and cost-effective. Production rates in microreactors can be increased by scaling out rather than scaling up, to supply increasing amounts of material for clinical trials as the drug progresses through the regulatory process. Scaling-out is promising as the process optimization from lab to pilot scales can be bypassed, allowing for significant savings on time and R&D costs. A reaction system can be optimised in a single microreaction unit and quickly scaled-up to production levels by increasing the number of units operating in parallel.

Advances have been made in the field of microreaction technology with numerous applications in organic synthesis involving multiphase chemical reactions, catalytic reactions as well as reactions involving reactive and potentially hazardous chemicals (Pennemann et al, 2004; Pennemann et al, 2004). Numerous micro devices have been developed, including micromixers, micro heat exchangers and various types of microreactors, many of which are now commercially available, to cater to a wide range of reactions and performance (Ehrfeld et al, 1998; Hessel et al, 2005; Hessel et al, 2005; Nguyen and Wu, 2005). Fabrication methods have been developed which allow for a wider range of materials of construction to be used, such as glass, ceramic and plastics (de Mello, 2002; Dietrich et al, 2005; Schmitt et al, 2005). More recently, there has been a growing effort to develop integrated microreaction systems complete with online analytics like UV, IR, Raman-spectroscopy or micro gas chromatography that can be used for different applications including process development as well as production of pharmaceuticals and chemicals under manufacturing conditions. Mikroglas for example offers Mikrosyn, CPC offers CYTOS, Fraunhofer offers FAMOS and IMM offers an Organic Synthesis Bench-Scale Plant (Keoschkerjan et al, 2004; Ferstl et al, 2004; Schwalbe et al, 2004; Schwalbe et al, 2005; Muller et al, 2005).

However, the application of microreactors in chemical synthesis has so far been limited and is hindered by the lack of published work on the scale-out of such systems. Production scale processes employing micro-structured devices have been reported, notably by Clariant, Degussa, Merck and Siemens Axiva (Ehrfeld et al, 2000; Kim et al, 2002; Markowz, 2003; Wille et al, 2004; Markowz et al, 2005) although detailed results are frequently not published.

The approach in most of the studies to date can be likened to a bottoms up approach where the focus is on the development and performance of individual microdevices. Applications of these new microstructured devices for various unit operations and reaction types were detailed to demonstrate the advantages of microstructured devices for chemical processing. However, in real applications, a top down approach is preferred, with the focus on the requirements of the process and a suitable device design derived to meet those requirements. Indeed, one of the main advantages of microreactors over batch reactors is the potential for designing to fulfil the process requirements rather than adapting the process to fit the available equipment. On the other hand, microreactors are also more prone to clogging/fouling compared to macro scale equipment.

This research will attempt to fill some of this gap by focussing on reaction engineering and scale out aspects, using the poly-*L*-leucine catalysed asymmetric epoxidation of chalcone as a case study. Specifically, this work aims to demonstrate the suitability of the reaction for continuous processing as well as the process and choices of designing and scaling a micro chemical system for the given reaction system. The poly-*L*-leucine catalysed asymmetric epoxidation of chalcone was selected for the case study as it allows highly enantioselective synthesis of chiral epoxides, which are useful intermediates for the synthesis of active ingredients and hence represent a commercially important synthesis for the pharmaceutical industry.

Recent efforts to scale the reaction in a batch reactor have resulted in a drastic drop in performance, providing further incentive for alternative processing methods (Gerlach and Geller, 2004). The reaction was also selected due to the substantial experience and

expertise available from research collaborators on the research project, including the group of Prof Stan Roberts, involved in developing the catalysts for the synthesis as well as Prof Donna Blackmond, who were involved in deriving the rate equations for the reaction system.

This thesis begins with a broad literature review of the developments and studies on the poly-*L*-leucine catalysed asymmetric epoxidation. Relevant concepts, developments and applications in microreaction technology are also reviewed. In Chapter 3, six reaction systems all of which are based on the poly-*L*-leucine catalyst were identified and evaluated based on economic considerations, environmental-friendliness and inherent safety. The six reaction systems were also screened for potential scale-up obstacles commonly encountered during pharmaceutical scale-up and the most suitable system was selected for the case study. Preliminary batch experimental runs were then carried out using the selected system to gain insight and experience using the experimental methods and establish critical design issues in order to establish a suitable continuous reaction protocol. These results are presented in Chapter 4.

Chapter 5 outlines the design of a microstructured continuous setup for the selected system. The design criteria and basis for scaling out the reaction system are described. The methods for screening and design of mixing devices and residence time channels, maintaining isothermal reaction conditions and choices and selection of suitable materials of construction are also described. From screening the various methods for enhanced mixing, the staggered herringbone micromixer was selected for use with the microstructured reactor.

The design and characterization of the staggered herringbone micromixer is examined in Chapter 6. The methods used to characterize the mixer and results of numerical simulations are presented. A method in which the required mixer length can be derived directly, especially useful in designing micromixers, is presented. The fabricated microstructured setup was tested experimentally and a parametric study was carried out. Chapter 7 presents the results of varying the operating temperature, residence time and reactant concentrations on reaction performance as well as comparison with performance predicted from the kinetic model. The header design for the scaled out system and experimental evaluation of the scaled out setup are described in Chapter 8. Results of flow visualization experiments were described to explain the poor experimental performance of the scaled out unit. Alternative methods for continuous large scale processing of the selected reaction system are also presented based on the results obtained.

Finally, the conclusions and suggestions for future work are presented in Chapter 9. The commercial potential of the current research, which was completed as part of the requirements for a Centre for Scientific Enterprise PhD Scholarship award is presented in Appendix 9-0.

Chapter 2

Literature Review

2.1. Poly-*L*-leucine Catalysed Epoxidation of Chalcone

Racemic and optically active epoxy ketones are among the most versatile building blocks in organic synthesis (Lauret, 2001). While there have been substantial progress in developing systems for asymmetric epoxidation of various classes of alkenes, no system for the asymmetric epoxidation of electron deficient alkenes has gained widespread popularity among synthetic organic chemists. In recent years, several systems have emerged which allow the epoxidation of a wide range of enones with high enantioselectivity, most of which are essentially asymmetric variants of the Weitz-Scheffer epoxidation using alkaline H_2O_2 . Some of these methods include diethylzinc and a chiral alcohol under an atmosphere of oxygen, a lanthanide in the presence of BINOL, metal peroxides with diethyl tartrate, chiral phase transfer catalysts, chiral dioxiranes, tert-butylhydroperoxide and bovine serum albumin and poly(amino acids), details of which are available elsewhere (Porter and Skidmore, 2000; Lauret and Roberts, 2002). Among the various methods, the polyamino acid catalyzed asymmetric epoxidation of chalcone has emerged as the most popular for acyclic E enones, with advantages over alternative procedures. A review of the developments of various reaction protocols involving this system is provided in this section.

2.1.1. Original Triphasic System

In the early 1980s, Julia and Colonna first reported using a synthetic polypeptide consisting solely of alanine residues to catalyse the epoxidation of chalcone and similar enones with a high degree of enantioselectivity. The asymmetric epoxidation of α,β -unsaturated ketones was effected via a triphasic system consisting of the substrate in a water-immiscible organic solvent such as carbon tetrachloride or toluene, aqueous sodium hydroxide containing hydrogen peroxide and the insoluble poly- (*L*)-alanine.

Over a period of about four years, Julia and Colonna systematically studied and optimised the conditions for this transformation (Julia et al, 1980; Julia et al, 1982; Colonna et al, 1983; Banfi et al, 1984). Julia and Colonna demonstrated that the asymmetric epoxidation can be similarly effected using poly-(*L*)-leucine and poly-(*L*)-isoleucine in place of poly-(*L*)-alanine, while poly-(*L*)-valine gave poorer conversion and stereoselectivity. Efforts to effect asymmetric epoxidation of other substrates other than chalcone and other substituted chalcones were less effective, leading them to conclude that the catalyst may be limited to the epoxidation of chalcone-type substrates.

Subsequent workers were able to expand the range of substrates somewhat, whereby the Julia-Colonna reaction was used for asymmetric epoxidation of various chalcone derivatives. Flisak and Lantos used the Julia-Colonna reaction to prepare a precursor of a leukotriene antagonist, demonstrating the use of the reaction up to the multi-hundred gram level (Flisak et al, 1993). Bezuidenhoudt and co-workers employed the Julia-Colonna reaction as a key step to prepare optically active flavanoids (Augustyn et al, 1990).

The gel-like catalyst remained difficult to handle, requiring long times for filtration with loss of selectivity on recycling. Subsequently, Itsuno et al (1990) synthesized polymer-supported poly (amino acid) catalyst by using cross-linked aminomethyl polystyrene as initiator for the polymerization process. The polymer supported catalysts afforded improved handling properties without any significant loss of activity on recycling and were successfully used for the Julia-Colonna epoxidation, making it the first example of an immobilised polyamino acid catalyst.

The triphasic Julia-Colonna reaction however, did not gain widespread attention largely because the optimum catalyst was not commercially available in large quantities, long reaction times and the transformation appeared to have limited substrate applicability.

2.1.2. Non-aqueous Biphasic System

Subsequently, several improvements were made to the original Julia-Colonna reaction. In a series of papers, Roberts et al reported developments which improved the physical properties of the catalyst, making it easier to handle the catalyst (Porter et al, 1999; Lauret and Roberts, 2002). The group was able to further extend the range of substrates and improve the reactivity of the system via alternative reagents.

One key improvement was to carry out the reaction under non-aqueous conditions, using THF as solvent and alternative reagents as oxidant and base. Several types of non-aqueous oxidants and organic bases were tested with the best performance achieved by using the solid complex urea-hydrogen peroxide (UHP) as oxidant and 1,8-diazabicyclo[5.4.0]undec-7-ene(DBU) as base. Several other solvents were reported with nearly identical performances. This biphasic system (the catalyst remained insoluble) enabled faster reaction times and broader range of substrates.

Under non-aqueous conditions, the insoluble catalyst is viscous and paste-like, making the procedure unsuitable for large-scale synthesis due to prohibitively long filtration times for separating the catalyst. Additionally, substantial catalyst losses and reduction in catalytic activity were reported on recycling.

Geller and Roberts (1999) presented an immobilised poly-(*L*)-leucine (pLL) catalyst to overcome some of these problems, a strategy which has been successfully employed in the field of biocatalysis. Several solid carriers were tested and the pLL catalyst supported on flash silica selected due to its outstanding performance. The pLL supported on silica (PaaSiCat) retained its granular appearance with no observable swelling of the catalyst, making it easier for separation of the catalyst as part of the work-up procedure. The PaaSiCats are robust and performed remarkably well, achieving a faster rate of reaction with much less pLL employed (23 % of pLL normally employed). While the effect of immobilising catalyst is marginal for a good substrate such as trans-chalcone, the immobilised catalyst showed improvement over non-immobilised catalyst for other less-reactive substrates. PLL was concluded to be the catalyst of choice, even though poly*neo*-pentaglucine (PLN) showed slight superiority over pLL, simply because of its ready availability and ease of immobilization (Dhanda et al, 2000).

Recently, Yi et al (2005) described a poly-(*L*)-leucine catalyst immobilised on silica gel through covalent bonding, unlike the method presented by Roberts et al, where the poly-(*L*)-leucine is supported onto silica gel via physical adsorption, for a more reliable method for modification and functionalisation of silica surface. This was achieved by treating silica with (3-amino-propyl)triethoxysilane to form the silica functionalised with primary 3-amino-propyl groups (AMPSi). The functionalised silica gel (AMPSi) was then used as initiator for polymerisation of the amino acid N-carboxyanhydride (NCA).

2.1.3. Mild System

Roberts et al also developed a ‘mild’ system, which uses sodium percarbonate as both oxidant and base, in a miscible water-1,2-dimethoxyethane solvent. This procedure allows rapid epoxidation with good enantioselectivities to be achieved at low catalyst loading and is characterised by diminished background reaction, lower cost and is environmentally more benign (Allen et al, 1999).

2.1.4. Non-aqueous Homogeneous System

A soluble version of the poly-(*L*)-leucine catalysts was prepared using an organic solvent-soluble polymer such as amino poly(ethylene glycol) (PEG-NH₂) as initiator for the amino acid N-carboxyanhydride polymerisation and successfully tested for asymmetric epoxidation of chalcone. This is significant as it allows homogeneous conditions to be used, making it easier to study the reaction as well as to run the reaction (Flood et al, 2001).

2.1.5. Triphasic System with Phase Transfer Catalysts

Geller et al reported improved reaction performance using a phase transfer catalyst (PTC) with the original Julia-Colonna procedure. Using tetrabutylammonium bromide (TBAB) as a co-catalyst, the available peroxide concentration in the organic phase is increased resulting in an accelerated reaction rate, achieving complete conversion within 1.5 hours compared to only 2 % conversion for the standard triphasic conditions. PTCs that are more hydrophilic than TBAB were found to have little influence on the reaction outcome. More hydrophobic PTCs on the other hand resulted in a faster but less selective reaction (Geller et al, 2004; Geller et al, 2006).

The group also optimised the procedure for large-scale production of poly-(*L*)-leucine, with the resulting catalyst capable of completely converting *trans*-Chalcone under PTC conditions within 10 minutes (Geller et al, 2004; Geller et al, 2006). Using PTC as co-catalyst, substantially lower catalyst loading (from 200 wt% to 5 wt%) can be used without detrimental effect to reaction performance, allowing easier work-up (Geller et al, 2004). Due to the rapid reaction rates, the amounts of oxidant and base can also be reduced substantially. The modified procedure was found to effect asymmetric epoxidation with a wider range of substrates which previously either exhibited low reactivity or were not epoxidisable at all under standard triphasic conditions.

Roberts et al recently reported using a variation of the PTC protocol, with *tetra*-butylammonium hydrogensulfate as co-catalyst in a biphasic system, by removing the aqueous phase prior to adding the chalcone substrate. This procedure enabled complete reaction after 6 hours, demonstrating that the polyleucine sequesters peroxide from aqueous solution allowing a small range of arylvinyl sulfones in addition to a wide range of α,β -unsaturated ketones to be epoxidised with good enantioselectivity (Lopez-Pedrosa et al, 2004).

2.1.6. Applications and Industrial Relevance

It is clear that the developments and various protocols developed for the poly-(*L*)-leucine catalysed asymmetric epoxidation have overcome many of the initial limitations such that the system is now ready to be explored for large scale production. The reaction times have been drastically reduced, the range of substrates expanded, catalyst handling and work-up procedures have been simplified, reliable methods for preparing the catalyst have been developed and the catalyst is now readily available commercially.

The application of the Julia-Colonna asymmetric epoxidation of chalcone for large-scale production is appropriate as epoxyketones have been proven to be useful intermediates for the syntheses of several pharmacologically active ingredients (Augustyn et al, 1990; Flisak et al, 1993; Adger et al, 1997; Cappi et al, 1998; Carde et al, 1999; Lauret, 2001). Indeed, several studies using the system for larger scale production purposes have been reported.

Tsogoeva et al from Degussa have reported using the homogeneous catalyst in a continuously operated chemzyme membrane reactor. Simple catalyst recovery is achieved in the chemzyme reactor by using a nanofiltration membrane to retain the catalyst while the epoxide and unconverted chalcone are passed through the membranes (Tsogoeva et al, 2002). More recently, Geller et al at Bayer studied the scale-up of the asymmetric Julia-Colonna epoxidation using the modified triphasic method with PTC as co-catalyst. The group was able to demonstrate scale-up of the system up to a 100-g substrate level, although the reaction time was increased with increasing scale. The reaction rate was found to be strongly dependent on stirring rate; however on increasing scale, prolonged reaction times up to 20 hours were required for complete reaction even when baffled reactors were used (Gerlach and Geller, 2004).

2.2. Poly-L-leucine Catalyst

2.2.1. Catalyst Preparation

The most common method for preparation of polyamino acids is via the polymerisation of the amino acid N-carboxyanhydride (NCA) derivatives. While other methods which allow for the synthesis of reagents of known length and purity exists, e.g. automated stepwise solid phase synthesis, these are of limited utility for large scale preparation of peptides (Ebrahim and Wills, 1997; Porter et al, 1999; Baars et al, 2003). The polymerisation method is a two-step procedure, which involves first activating the amino acid towards nucleophilic attack by formation of an NCA and subsequently, polymerisation is achieved by addition of a suitable nucleophilic initiator (Allen et al, 1998; Porter et al, 1999; Baars et al, 2003).

A number of different initiators have been reported such as water, simple primary amines, diamines, polymer-supported amines, amino poly (ethylene glycol) and aminopropyl functionalised silica. The humidity cabinet method uses water as initiator and requires highly pure, crystalline NCA derivatives. The material has to be within 2°C of the literature M.P. value for successful polymerisation (Bentley et al, 1997). While this method allows very large quantities of polymer to be prepared fairly quickly, it is not a reliable method for producing consistent, high quality catalyst (Ebrahim and Wills, 1997; Allen et al, 1998). Improved consistency in the quality of the catalyst produced is achieved using the amine-initiated polymerisation method, which allows less pure NCA to be used. Polymerisation is achieved by stirring the NCA with an appropriate amount of initiator in a suitable solvent. This method gives a range of chain lengths although the average length of the polymer product can be controlled by varying the ratio of NCA to initiator (Allen et al, 1998).

2.2.2. Catalyst Regeneration

Improvements made to the physical properties of the catalyst have allowed the recovery and recycling of the catalyst. However, repeated recycling of the polyamino acid catalysts result in increased reaction times and reduced stereoselectivity. The quality of the recycled catalyst was found to decline quickly especially when used in anhydrous conditions. The recycled catalyst can be regenerated by stirring the recycled polyamino acids in toluene with 4.0 M aqueous sodium hydroxide for 16 hours, filtered, washed and dried before use. This procedure may be repeated for optimum regeneration. Regenerated polyamino acid display catalytic activity and stereoselectivity properties that are comparable to freshly made polyamino acids (Allen et al, 1998).

Alternatively, a second regeneration procedure has also been developed, which is so effective that only one treatment is required to restore catalytic activity. This procedure is similar to the first procedure, but with addition of small amounts of aqueous hydrogen peroxide on top of the aqueous sodium hydroxide solution (Allen et al, 1998). The exact mechanism of this regeneration procedure is unclear although it is possible that the procedures above allow short chain, inactive polymer fragments which will be soluble in the aqueous medium, to be removed, thus restoring catalytic ability by enabling the polymer to reform its preferred tertiary structure. It is also possible that the aqueous regeneration procedure allows water molecules in the polymer that may have been leached out when the anhydrous biphasic process is used, to be replaced. This will also enable the polymer to reform its tertiary structure (Allen et al, 1998).

2.3. Reaction Mechanism

2.3.1. Helicity and Catalyst Length

It was established early on that several different polyamino acids were able to effect asymmetric epoxidation with varying degrees of success; for example poly-*L*-alanine, poly-*L*-leucine and poly-*L*-isoleucine gave good results while the use of poly-*L*-valine resulted in reduction of both the yield and enantioselectivity. A high degree of α -helix configuration in the polymer was believed to play a role in inducing enantioselectivity (Colonna et al, 1983). Infrared measurements of both solid and soluble peptides indicate that the degree of helical structure of the catalyst is related to both the size of the catalyst and nature of the N-terminus and thus controls the enantioselectivity, in agreement with Julia and Colonna's earlier work (Takagi et al, 2000; Takagi et al, 2000). Berkessel et al (2001) established that the minimum structural element necessary for efficient chiral induction is one helical turn, with an increase in catalytic activity observed with increasing length and proportion of α -helical content, in agreement with other similar work (Takagi et al, 2000; Takagi et al, 2000; Kelly et al, 2004).

Increasing the length of the polymer gave improved enantioselectivity with a minimum of 10 residues required for high enantioselectivity (Banfi et al, 1984). A number of studies have been reported which employed both 'free' and polymer-supported poly-*L*-leucine catalysts of specified chain lengths for mechanistic studies of the Julia-Colonna epoxidation (Bentley et al, 1998; Takagi et al, 2000; Takagi et al, 2000; Bentley et al, 2001). In agreement with earlier studies, a 10-residue polypeptide was found to effect good stereocontrol (Bentley et al, 1998) with improved yield and enantioselectivity with increasing degree of polymerization (Takagi et al, 2000; Takagi et al, 2000).

2.3.2. Influence of Terminal Groups

The enone substrate and/or peroxide reagent appear to bind to the catalyst near the N-terminus; the stereochemistry of the 5 amino acid residues and specifically, the penultimate and antepenultimate residues adjacent to the N-terminus play a dominant role in determining the stereoselectivity of the reaction (Bentley et al, 1997; Takagi et al, 2000; Bentley et al, 2001). Results from experimental work evaluating the catalytic activity of Tenta-Gel bound *L*-Leu peptides were compatible with previous reports and suggest the importance of hydrogen bonding at the N-terminus, with the three nonintrahelical H-bonded NH groups playing a crucial role in the catalytic mechanism (Berkessel et al, 2001).

However, the free NH₂ group at the N-terminal does not play a key role in the binding of peroxide and/or enone into position; substitution of the terminal amine hydrogens resulted in a drop in enantioselectivity although it does not render the catalyst completely inactive (Banfi et al, 1984; Takagi et al, 2000; Bentley et al, 2001).

The C-terminal region of the polypeptide was found to play a minimal role in chiral induction; it appears to be responsible for assembling the correct overall architecture for optimal performance of the N-terminal region. The minimum size of the C-terminal domain should be between 5 and 15 residues to allow the N-terminal region to demonstrate chiral control. The stereochemistries of the residues at the C-terminal region however are relatively unimportant (Bentley et al, 1997; Bentley et al, 1998).

2.4. Kinetic Studies

The kinetics of the homogeneous system in pure THF, determined by monitoring the disappearance of chalcone spectrophotometrically, have been reported (Carrea et al, 2004; Carrea et al, 2004). The rate of reaction, studied in the range 15 – 35 °C, was found to increase with increasing temperature. The rate of reaction at 35 °C was found to be 64 % higher than that at 15 °C and the activation energy was determined to be 17.03 kJ/mol. Water, which is believed to be a by-product of the reaction, was found to affect the rate of reaction; up to 0.8 % v/v water concentration in THF, the rate increased by 30 % but on increasing water concentration further, the rate decreased, with rate of reaction at 2.3 % water only 39 % that in pure THF.

Kinetic investigation of the Julia-Colonna epoxidation indicated that PLL behaves as an enzyme-like catalyst at relatively low concentrations of substrates and shows a steady state random bireactant mechanism with a preference for hydroperoxide to be bound before chalcone. Such systems are sequential, that is all substrates must bind to the catalyst to form a central complex (PLL:HOO⁻:Chalcone) before the formation of the hydroperoxide enolate of chalcone which eventually evolves to epoxychalcone. The lower Michaelis constant, K_M for hydroperoxide accords with the sequestration by polyleucine and there is no indication of any other kinetically significant intermediates. Hence, the peroxy-enolate is transitory and when this achieves the requisite geometry for epoxide formation, with sufficient energy, the transition is irreversibly passed (Carrea et al, 2004; Carrea et al, 2004; Kelly and Roberts, 2006).

Recent work using reaction progress kinetic analysis has allowed these mechanistic proposals to be refined. Mathew et al (2005) found an absence of kinetically meaningful concentration of bound chalcone but found kinetically meaningful concentrations of PLL catalyst and the hydroperoxide-bound species, which was around 3 times larger than the unbound PLL catalyst concentration, supporting previous results of hydroperoxide sequestration by the catalyst. The authors suggest a rapid and reversible chalcone docking to bound hydroperoxide species leading predominantly back to free chalcone and less often but with complete stereochemical specificity forward to form the epoxychalcone.

2.5. Introduction to Microchemical Systems

Microreactors refer to devices with feature sizes in the micron to hundreds of micron range fabricated at least partially using methods of microtechnology and precision engineering (Ehrfeld et al, 2000). The origins of microreaction technology can be traced back to the field of Micro-Electro-Mechanical Systems (MEMS), where mechanical elements such as sensors and actuators were combined with electronics on a common silicon substrate using compatible micromachining process. Today, MEMS devices encompass a wide range of materials and microfabrication methods and is used in automobiles, biomedical devices, inkjet printers, optical applications and a wide array of consumer products (Gavriilidis et al, 2002).

The advances in MEMS have enabled the fabrication of microchemical reaction systems. The various components in microchemical systems such as valves, pumps, flow sensors and mixers have been fabricated in various materials such as metals, ceramics and polymers (Jensen, 1999). Microchemical systems find widespread interest in fields as diverse as biology, pharmacology, analytical chemistry to chemical processing.

The major developments in microchemical systems can be broadly divided into two main groups, the first of which refer to the development of integrated micro-components on credit-card-sized chips for ‘micro-total-analysis-systems’ with applications in combinatorial chemistry, high throughput screening and portable measurement devices (Chow, 2002; Yang et al, 2002; Huikko et al, 2003; Erickson and Li, 2004; Yi et al, 2006). On the other hand, precision engineered microflow devices with three dimensional microchannel architectures can be used for lab-scale process development and on-demand chemical synthesis and potentially pilot and production scale chemical synthesis (Jensen, 1999; Haswell and Skelton, 2000; Jensen, 2001).

Due to the vast amount of literature available, this review will focus only on flow-through microchemical systems for chemical production purposes rather than miniaturized analysis systems. A brief introduction to the characteristics of microchemical systems, microfabrication techniques and potential applications is provided in this section.

2.5.1. Characteristics of Microchemical Systems

Microchemical systems display significantly improved heat and mass transport processes. The temperature and concentration gradients, which are the driving forces for heat and mass transfer, increase with a decrease in linear dimensions. A reduction in characteristic length also results in an increase in the surface to volume ratio. As a result, surface acting forces such as surface tensions play a more significant role than is usual (Stone and Kim, 2001).

2.5.2. Application of Microchemical Systems

Microchemical systems offer many technical advantages for a large number of applications related to mass screening and chemical production purposes. The high heat and mass transfer rates allow reactions to be performed under more aggressive conditions, which may not be accessible in conventional reactors for safety reasons e.g. direct fluorination of aromatic compounds (Chambers et al, 2001). The high surface to volume ratios in microchemical systems suggests further performance advantages for microfabricated multiphase systems compared to conventional systems.

The compactness of production scale microchemical systems also permit mobile distributed point-of-use chemical synthesis of chemicals with storage and shipping limitations such as highly reactive and toxic intermediates. DuPont for example has synthesized a number of potentially hazardous chemicals including isocyanates in a silicon microreactor (Jensen, 1999). This feature is also being exploited for the development of extraterrestrial chemical processing plants, which will enable production of fuel and oxygen from Martian atmosphere (Holladay et al, 2007).

The smaller hold-up and faster process control also leads to improved process safety. The ability of microchemical systems to accommodate reaction regimes and conditions not accessible using conventional equipment as well as the improved control allows for more information and precise data to be collected (Ehrfeld et al, 2000). New process chemistries and new catalysts can be screened rapidly facilitating process development. Additionally, the flow in microchemical systems is in the laminar regime making it feasible to fully characterise the heat and mass transfer and extract chemical kinetic parameters from sensor data (Jensen, 1999). The ease of scaling up to production as well as flexibility in production rates make microchemical systems particularly useful for the fine chemical and pharmaceutical industry where production rates can be as small as a few metric tons per year. Other applications of microchemical systems include high throughput screening and integrated chemical analysis systems (so called lab on a chip), where the reduced consumption of expensive reagents and fast response time are especially beneficial.

2.5.3. Microfabrication Methods

Microchemical devices are fabricated using a number of methods based on semiconductor fabrication technologies, ultra precision engineering and microerosion techniques. Some of the main methods include:

- Photolithography and etching techniques
- LIGA
- Laser Machining
- Advanced Mechanical Techniques
- Micro electro discharge machining
- Microstereolithography
- Injection Moulding

The availability of numerous fabrication methods have enabled a broader range of materials to be used including silicon, glass, polymers and more recently metals, stainless steel, special alloys as well as ceramic materials. A number of sealing methods are used to achieve fluid tightness in microreactors. Use of gaskets and a suitable housing which is tightly clamped is commonly used for systems which require assembly and disassembly. Other methods include the use of adhesives, anodic bonding and diffusion bonding which provide stronger and irreversible bonding. Selection of an appropriate fabrication technique is primarily dependent on several factors such as costs, time, accuracy, reliability, material compatibility and access. Details of the various fabrication methods are available elsewhere (Thornell and Johansson, 1998; McCready, 2000; Madou, 2002).

2.6. Microchemical Processing

Microstructured devices offer the opportunity to control precisely the contacting of different fluid streams. Contacting and mixing of different feed streams play an important role in practically every chemical process. Hence, a large number of micromixers with different performance characteristics have been developed for diverse mixing applications. A review of some of the main micromixing devices developed to date is provided. A description of the approaches used to combine these features with other unit operations to form an integrated and effective microreaction system is also provided in this section.

2.6.1. Micromixing

Micromixing devices usually operate at low Reynolds number, due to the small dimensions of the devices. Mixing in microfluidic devices relies solely on molecular diffusion, due to the laminarity of the flow in microdevices. The diffusive flux is governed by Fick's Law:

$$\text{Diffusive flux} = D \cdot A \cdot \nabla C \quad [2.1]$$

D = Diffusion Coefficient

A = Interfacial surface area

∇C = Gradient of species concentration

The mixing efficiency can be enhanced by reducing the length scale for diffusion or by increasing the interfacial area. This is achieved by various methods, which can largely be categorized as active or passive mixing. Passive mixers do not require external energy and mixing is achieved by virtue of their topology alone. The mixing process is enhanced by restructuring the flow, for example via creation of thin lamellas or by manipulating the laminar flow to promote chaotic advection.

Active mixers on the other hand achieve mixing via disturbances created by external field such as ultrasound, acoustic, bubble-induced vibrations and others. Active mixers require external power sources, making construction and integration of active mixers in continuous microfluidic systems challenging and expensive. Due to the huge interest in microchemical devices, there is an abundant volume of literature available on micromixing devices. For these reasons, the review will be limited to passive mixers for pressure driven flows, with a focus on those which are most applicable for chemical processing. Some of the more popular micromixing principles used will be described.

2.6.2. T-Micromixers

The basic design consists of a T flow structure, not unlike conventional mixing tees and has been applied for both gas and liquid mixing. A variation of this is the Y-flow mixer, where the inlet flows are oriented at an angle to the outlet flow channel. Although simple in design, they give relatively good mixing if the dimensions are sufficiently small. Gobby et al (2001) studied the mixing characteristics of two gases in a T-type micromixer using computational fluid dynamics simulations. Improved mixing performance was observed at lower flowrates and at high aspect ratios while mixing angle had a negligible effect. Incorporating an orifice immediately after the T-junction was also found to improve mixing by decreasing the diffusional distance.

Engler et al (2004) reported enhanced mixing in a T-micromixer by inducing vortex formation at the T-junction. Three flow regimes were identified; these are the stratified flow, vortex flow and engulfment flow regimes. A suitable identification number for the onset of the engulfment regime, K was introduced:

$$K = \frac{d_h}{\lambda_k} \quad [2.2]$$

d_h = hydraulic diameter of mixing channel

λ_k = characteristic length denoting the scale of created vortices

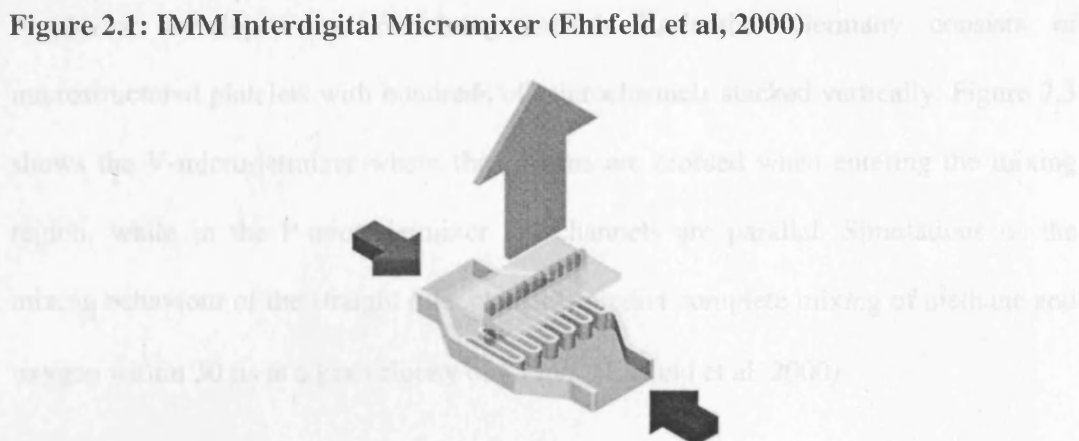
Experimental investigations were in good agreement with predicted performance and the onset of engulfment flow determined at $K \sim 40$. The onset of engulfment flow in a T-micromixer was found to be at Re of 120 - 300, beyond which two major vortices are established which relaminarise downstream in the mixing channel.

Wong et al (2004) also investigated the mixing performance of the T-micromixer using a higher range of applied Reynolds number. Rapid mixing was achieved due to the generation of secondary flow, swirling flow and vortices at the micromixer junction at high Re .

2.6.3. Parallel Lamination Micromixers

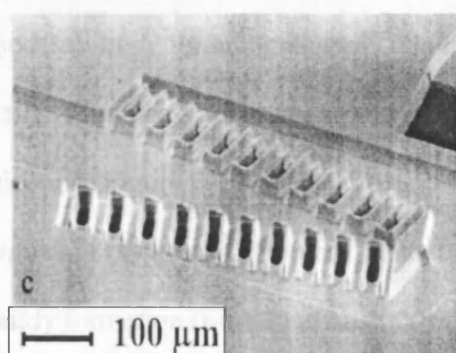
Mixing performance can also be improved by increasing the contact surface area via multi-lamination of the flows. This can be achieved via different feed arrangements. Bessoth et al (1999) reported the use of a device with bifurcation-type feeds, where the feed stream is passed through an inverse bifurcation structure into a folded delay loop channel where mixing takes place, with 95 % mixing within 15 ms. Yamaguchi et al (2004) investigated a conceptually similar device with larger dimensions using both CFD simulations and experimentally. Relatively fast mixing was achieved even at these larger dimensions.

Another widely used feed concept is based on parallel flow interdigital feed arrangements. In one micromixing device developed by the Institut fur Mikrotechnik Mainz (IMM), both the inlet streams are introduced into the mixing element as two counter-flows which stream into an interdigital channel configuration with typical channel widths of 25 or 40 μm and corrugated walls, which serve to increase the contact surface of the laminated streams, as shown in Figure 2.1. The laminated flow leaves the device perpendicular to the direction of the feed flows where fast diffusional mixing then takes place (Ehrfeld et al, 2000).



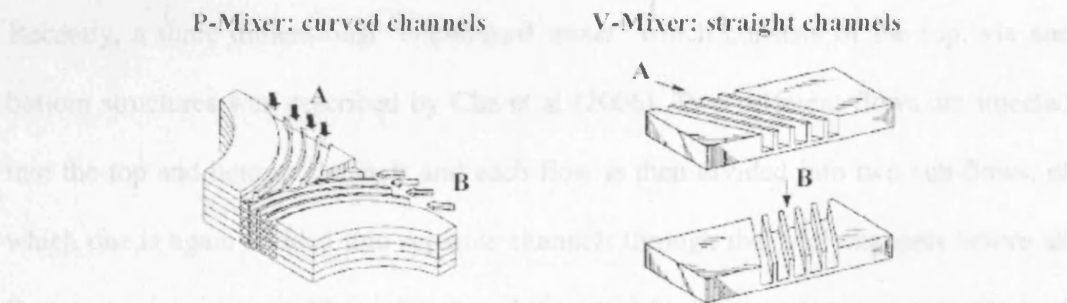
A mixing device developed by Mikroelektronik Centret in Copenhagen consists of a minichannel with a larger chamber in the middle section where two rows of U-shaped microstructures are embedded (Figure 2.2). The two rows are tilted relative to the middle axis of the minichannel, forming a V-shaped array similar to a filter structure with regular pores. One fluid enters the mini channel and is split into many substreams by passing through the interstices formed by the rows of microstructures. The other fluid is fed through the holes within the U-shaped microstructures from a reservoir below the base plate of the chamber. Clogging phenomena is minimized using the design, making it suitable for applications in enzymology and biochemical analyses (Branebjerg et al, 1996).

Figure 2.2: Mixing element with nozzle structures (Ehrfeld et al, 2000)



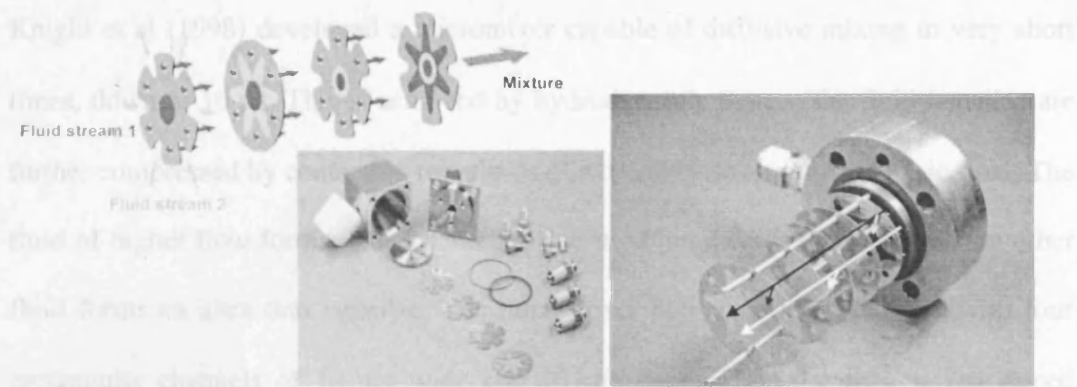
A device developed by Forschungszentrum Karlsruhe, Germany consists of microstructured platelets with hundreds of microchannels stacked vertically. Figure 2.3 shows the V-micro-jetmixer where the streams are crossed when entering the mixing region, while in the P-micro-jetmixer the channels are parallel. Simulations of the mixing behaviour of the straight inlet channels predict complete mixing of methane and oxygen within 30 μ s at a gas velocity of 15 m/s (Ehrfeld et al, 2000).

Figure 2.3: Two platelet designs for the microjet mixer (Ehrfeld et al, 2000)

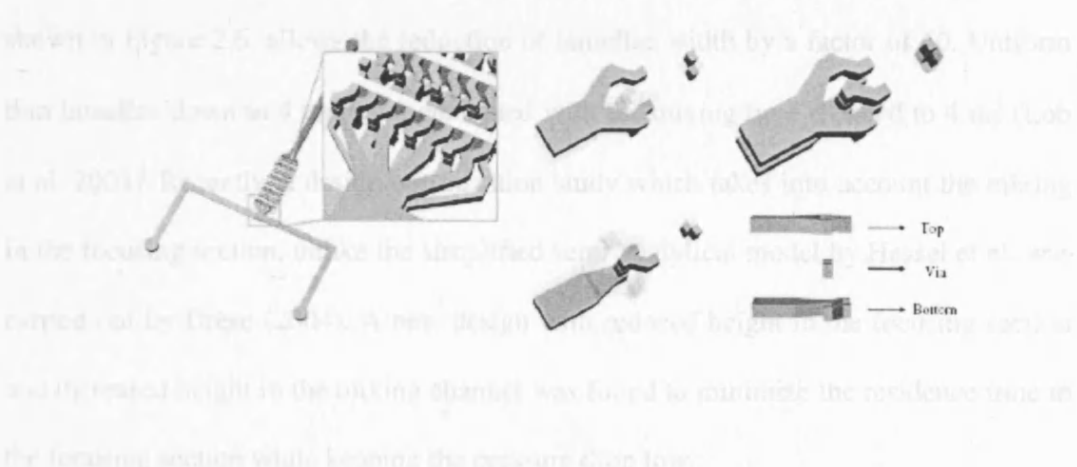


Zech et al (2000) characterised the mixing efficiency of the straight inlet channel mixers with complete mixing found to occur after about 800 μ m flow passage. The good mixing performance was due to the almost immediate transition from laminar to turbulent flow when entering the mixing zone, especially if the streams leaving the microchannels are crossed, due to the increased turbulence intensity (Ehlers et al, 2000).

StarLaminators, developed for high throughput applications (1 – 3.5 m^3/h) achieve multi-lamination via a stack of plates with star-like openings which when assembled, allow alternating flow injection (Figure 2.4). Due to the large internal opening and large throughput, the flow regime is typically turbulent such that a pre-layered flow is consecutively mixed by eddy formation (Ehrfeld et al, 2000).

Figure 2.4: StarLaminator from IMM (Werner et al, 2005)

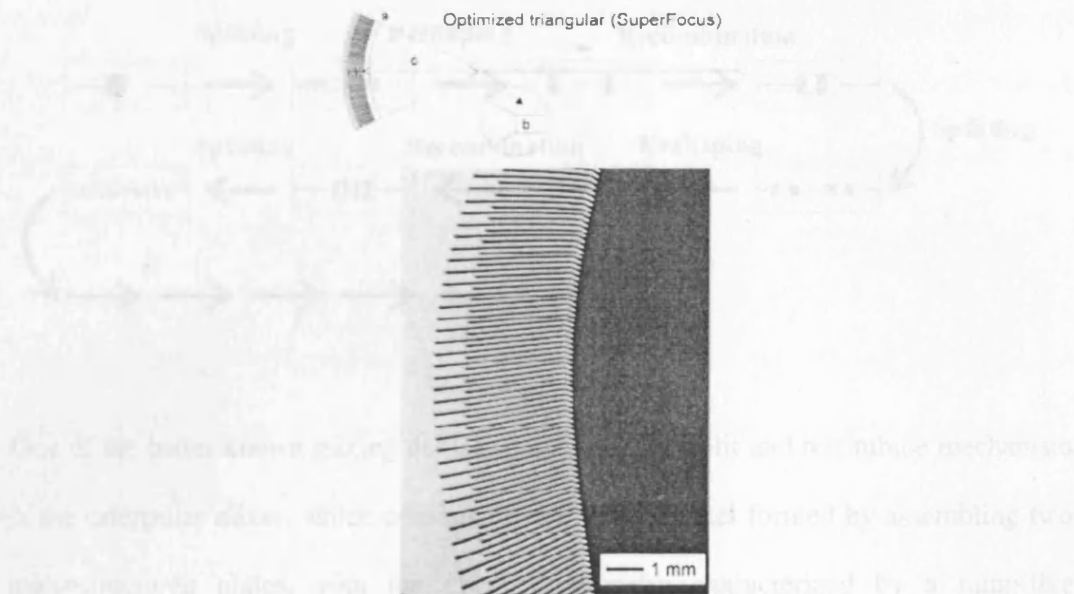
Recently, a three dimensional ‘chessboard mixer’ which consists of the top, via and bottom structures was described by Cha et al (2006). Two different flows are injected into the top and bottom channels and each flow is then divided into two sub-flows, of which one is again divided into separate channels through the ‘via’ channels before all flows are rejoined again like a chessboard (Figure 2.5). Improved mixing was obtained due to the increased interfacial area with 90 % mixing completed by the seventh stage for a 50 μm mixing channel.

Figure 2.5: Schematic diagram of the ‘Chessboard’ mixer (Cha et al, 2006)

2.6.4. Focusing Micromixers

Knight et al (1998) developed a micromixer capable of diffusive mixing in very short times, down to 10 μ s. This is achieved by hydrodynamic means; the fluid lamellae are further compressed by contacting two fluids of extremely different volumetric flow. The fluid of higher flow forms a thick lamellae due to volume conservation while the other fluid forms an ultra thin lamellae. The micromixer is a cross-like structure, with four rectangular channels of 10 μ m wide and 10 μ m deep. The inlet flow is introduced through a channel which narrows to 2 μ m at the intersection while the other fluid is fed through two channels perpendicular to the inlet channel. These side flows squeeze the inlet fluid into a thin stream that exits the intersection through the fourth channel.

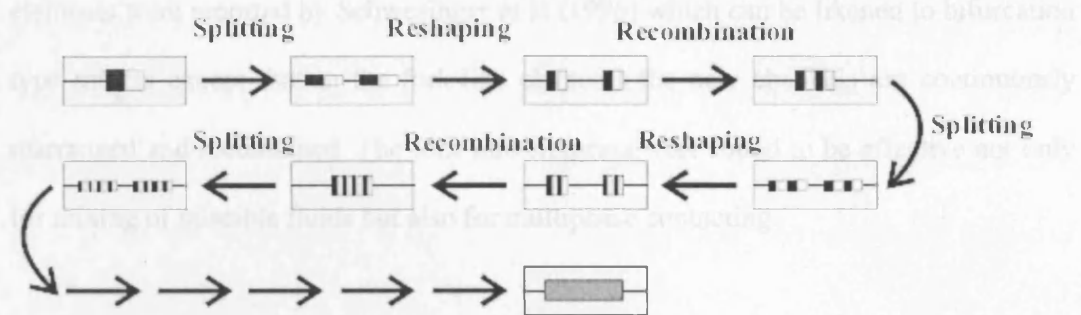
A similar concept where the flows are focussed using geometrical constraints has also been presented. Numerical and experimental investigations on the rectangular, triangular and slit shaped micromixer and an optimized version of the triangular mixing device (SuperFocus), confirmed the formation of a multilaminated flow pattern and lamella thinning by hydrodynamic and geometric focusing, leading to faster mixing times (Hessel et al, 2003; Hardt and Schonfeld, 2003). The SuperFocus micromixer, as shown in Figure 2.6, allows the reduction of lamellae width by a factor of 40. Uniform thin lamellae down to 4 μ m were generated with the mixing time reduced to 4 ms (Lob et al, 2004). Recently, a design optimization study which takes into account the mixing in the focusing section, unlike the simplified semi-analytical model by Hessel et al, was carried out by Drese (2004). A new design with reduced height in the focusing section and increased height in the mixing channel was found to minimize the residence time in the focusing section while keeping the pressure drop low.

Figure 2.6: Optimised SuperFocus micromixer (Hessel et al, 2003)

Veenstra et al (1999) constructed a T-type device which employs a similar concept. The mixer consists of a narrowing section which significantly reduces the diffusion distance compared to the wider channel, resulting in shorter mixing times. Other examples include a cyclone mixer made with feed inlets set on a circle allowing injection of feed into a cylindrical mixing chamber which enables fluid layers to be focussed by hydrodynamic and geometric means (Hardt et al, 2002).

2.6.5. Serial Lamination Micromixers

Split and recombine mixers create multi-laminating patterns in series by repeated splitting and recombination of fluid layers. Such an approach is attractive as it allows uniform mixing properties to be achieved under moderate pressure drop without the need for high fabrication requirements. This is illustrated in Figure 2.7.

Figure 2.7: Splitting-reshaping-recombination (SAR) mechanism

One of the better known mixing devices employing the split and recombine mechanism is the caterpillar mixer, which consists of one main channel formed by assembling two microstructured plates, with the channel geometry characterized by a ramp-like architecture. No additional fluid connecting channels are required between a splitting and recombining step, allowing large throughputs at lower pressure drop as well as facilitating cleaning. The mixing quality achieved at high volumetric flows with the caterpillar mixer was close to those achieved using the interdigital mixers.

A second generation optimized version of the caterpillar micromixer which allowed a vertically aligned multi lamination pattern to be achieved was recently reported by Schonfeld et al (2004). The mixing performance of the SAR caterpillar mixer was evaluated both theoretically and experimentally (Hardt et al, 2006) and found to achieve better mixing performance compared to simple T-micromixers and unlike chaotic mixers, has the advantage of almost identical mixing conditions over the whole channel cross section.

Comparison of the performance of the device with that of a straight channel with equivalent dimensions showed that mixing in this device can be up to 2 times faster.

Several different designs employing SAR principle have been reported. Fork-like elements were reported by Schwesinger et al (1996) which can be likened to bifurcation type mixers except that in the fork-like elements the new channels are continuously rearranged and recombined. The fork-like elements were found to be effective not only for mixing of miscible fluids but also for multiphase contacting.

Branebjerg et al (1996) reported a device with multiple flow splitting and recombination with a separation plate to support the fluid lamination by allowing the fluids to stack on each other without forming a fluid/fluid interface which may disturb lamination. Complete mixing was reported within 100 – 300 ms.

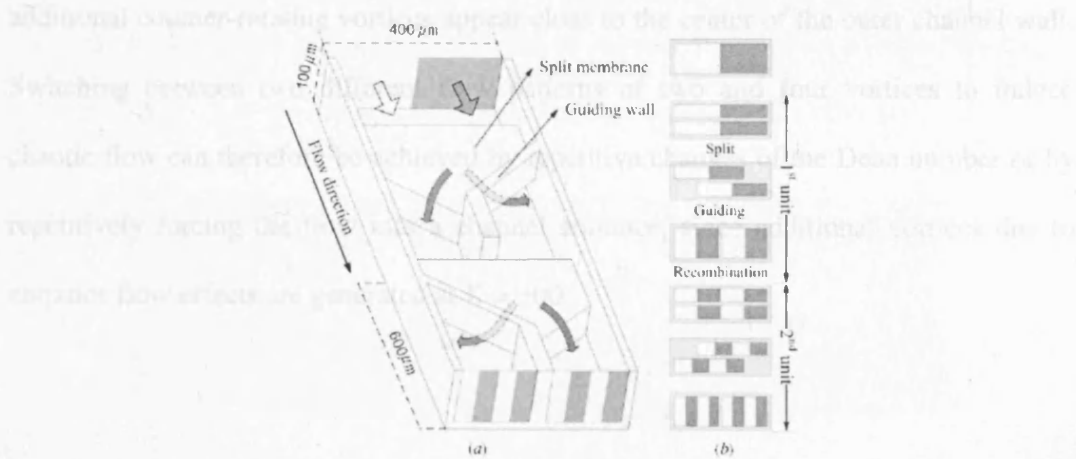
Mae et al (2004) reported two types of split and recombine mixing devices suitable for numbering up for mass production. Both devices consist of 11 stages of mixing elements; the number of elements decreases with increasing mixing stage in the first type while in the second type the number of elements per mixing stage remains constant. Each element consists of two holes for the incoming flow both of which are subsequently split into two streams. The four streams are then recombined into two streams before flowing out of the two outflow holes.

Munson and Yager (2004) developed a micromixing device in which the fluid layers are successively laminated. The two inlet fluids are split and then recombined along a plane perpendicular to the splitting plane successively, creating multiple striations. Comparison of the performance of the device with those of a straight channel with equivalent dimensions showed that mixing in this device can be up to 3 times faster.

Chen and Meiners (2004) constructed a mixing device which repeatedly folds the flow and exponentially increase the concentration gradients to enhance the mixing. In this device, the two fluid streams are combined, split out-of-plane, rotated in opposite directions and recombined, in a topologic structure akin to a Möbius band. Efficient mixing was achieved making this mixer suitable for mixing high molecular weight or high viscosity fluids.

A new split and recombine micromixer fabricated in PDMS was presented by Lee et al (2006). The flow is split horizontally by a PDMS membrane and the split streams are then arranged laterally by a guiding wall and expanded before the flows are recombined again, as shown in Figure 2.8. The mixing performance was evaluated both experimentally and numerically in the range $Re = 0.012 - 120$, with experimental results in good agreement with numerical results. At $Re = 0.6$, 90 % mixing was achieved by the seventh unit, increasing to 10 units for $Re = 120$, demonstrating the efficiency of this mixer for rapid mixing.

Figure 2.8: PDMS Split and recombine micromixer (Lee et al, 2006)



2.6.6. Secondary Flow Micromixers

One of the simplest methods for achieving secondary flow is by using curved microchannels. Helical flows in curved pipes and channels are characterized by a shift of the maximum in the velocity profile toward the outer channel wall accompanied by the occurrence of a pair of counter-rotating vortices known as Dean vortices.

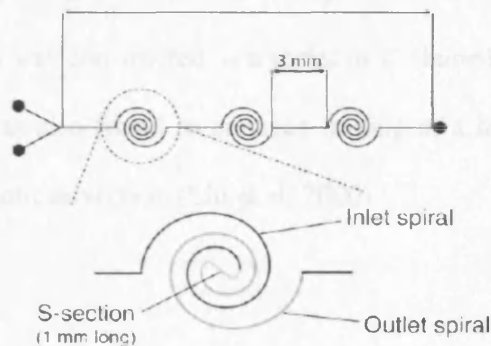
Howell et al (2004) constructed a mixer based on Dean vortices and studied the effects of flow velocity, aspect ratio and radius of channel curvature on the generation of Dean vortices. A pair of counter-rotating vortices is generated when fluid is directed around a curve. Vortices were observed at Re between 1 and 10, becoming stronger as the flow velocity is increased. Vortex formation is enhanced at higher aspect ratios and with lower radius of curvature. The Dean number, K is defined as:

$$K = Re \left(\frac{d}{R} \right)^{1/2} \quad [2.3]$$

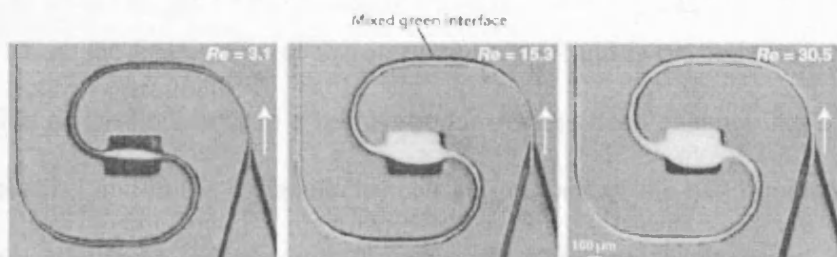
where d denotes the hydraulic diameter and R denotes the radius of curvature. A qualitative change in the secondary flow pattern is observed above a critical Dean number of about 140 (Jiang et al, 2004; Schonfeld and Hardt, 2004). For $K < K_c$, the secondary flow consists of two counter-rotating vortices whereas for $K > K_c$ two additional counter-rotating vortices appear close to the center of the outer channel wall. Switching between two different flow patterns of two and four vortices to induce chaotic flow can therefore be achieved by repetitive changes of the Dean number or by repetitively forcing the flow into a channel entrance, since additional vortices due to entrance flow effects are generated at $K > 300$.

Recently, a similar micromixer which uses Dean vortices was introduced (Sudarsan and Ugaz, 2006). The mixer consists of a channel which incorporates a series of spiral shaped sections along the flow path as shown in Figure 2.9 (a). The spiral arrangement of the channels result in increasingly stronger Dean flows as the fluid travels from the outer to inner regions of the spiral path where the radius of curvature is the smallest. The required mixing length decreases with increasing Re as stronger Dean vortices are generated. Replacing the central 'S' section with a wide straight section, as shown in Figure 2.9 (b) causes the formation of expansion vortices which can further enhance mixing.

Figure 2.9: (a) Schematic of a spiral microchannel incorporating 3 spiral segments (Sudarsan and Ugaz, 2006).



(b) Gray scale images depicting expansion of the mixed interface with increasing Re in a two-arc spiral channel incorporating expansion vortex effects.



At high flowrates, the fluid separates from the wall in a jet-like motion, when the fluid encounters this sudden expansion in cross sectional area. Simultaneously, a pair of vortices develops at the entrance to this expansion on either side of the jet stream which become asymmetric with increasing Re . The combined effects of transverse Dean vortices and expansion vortices result in rapid mixing, although these effects are not significant enough at lower flow rates.

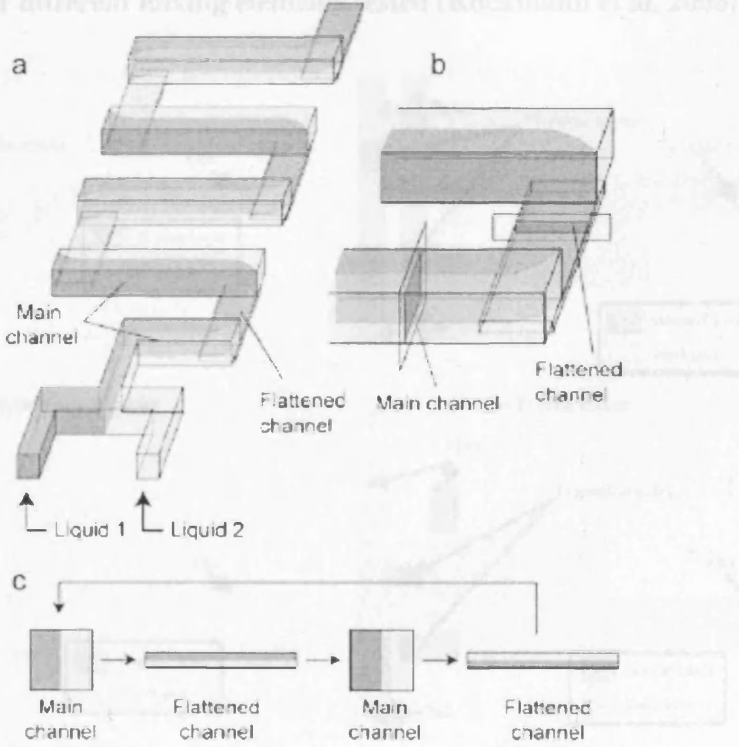
At sufficiently high Re , secondary flows can also be generated using bends and turns to enhance mixing (Kockmann et al, 2006). For example, the mixing in a zigzag microchannel was found to improve above a critical Reynolds number of 80, due to recirculations at the turns which induce a transversal component of the velocity. (Mengeaud et al, 2002). A three dimensional serpentine mixing channel fabricated in silicon and glass, which was constructed as a series of C-shaped segments positioned in perpendicular planes was also found to enhance mixing at a higher Reynolds number ($Re = 25-70$) due to chaotic advection (Liu et al, 2000).

A variation of the serpentine mixing channel, based on fluid twisting and flattening was introduced recently (Lee et al, 2005). This micromixer is constructed by repeating two microchannel segments consisting of a main channel and a flattened channel, placed perpendicularly with the flattened channel located below the main channel, as shown in Figure 2.10. At the intersection of these segments, the fluid is twisted as a result of the introduction of the liquids from a relatively narrow and deep channel into a wide and shallow channel and in the flattened channel the interface of the two liquids is directed horizontally allowing rapid mixing due to the small diffusional distance.

The perpendicular arrangement and difference in aspect ratios of the two segments were found to strongly influence the twisting of the fluid interface while increasing the flowrates somewhat enhanced twisting slightly. As expected, at low flowrates, mixing was complete within the first few turns whereas at higher flowrates, complete mixing was only achieved after a significantly higher number of turns attributed to longer residence time for diffusion to occur.

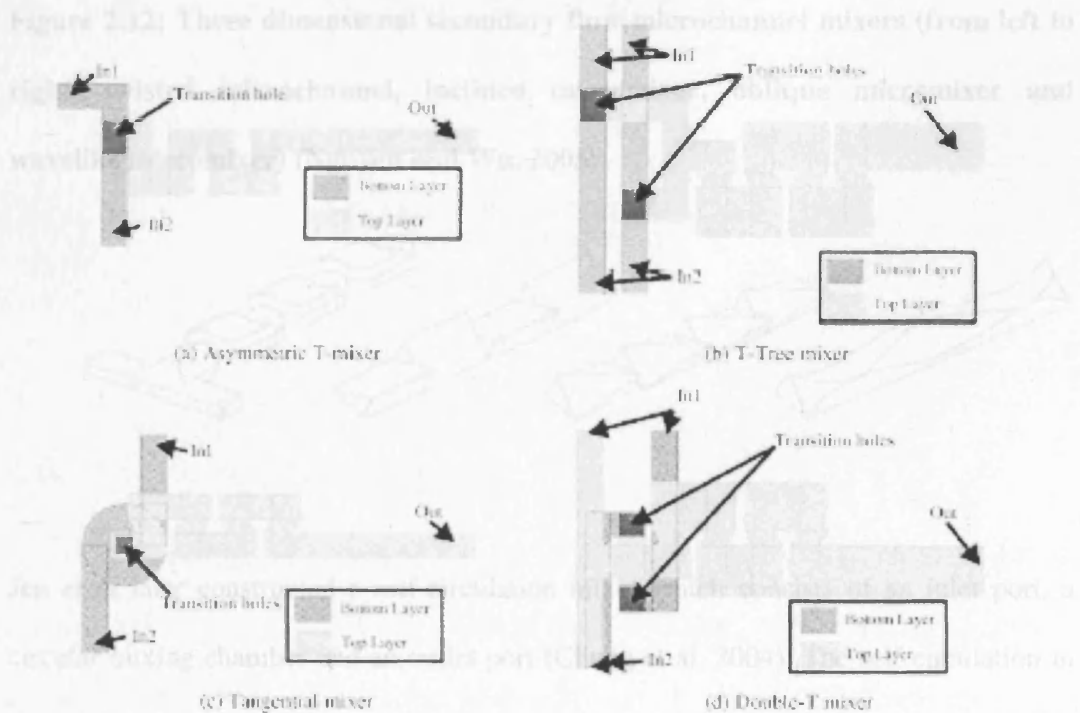
Figure 2.10: Schematic diagram showing the micromixer and the mixing principle (Lee et al, 2005)

Figure 2.11: Four different twisting elements tested (Kochmann et al, 2016)



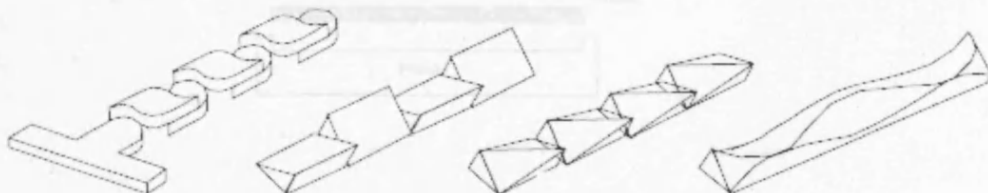
Following a detailed study on flow effects in a 90° bend and T-junction, Kockmann et al designed and tested four different combinations of mixing elements, namely the asymmetric T-mixer, T-tree mixer, tangential mixer and T-cascade mixer. These configurations have different inlet ‘contacting’ sections but are all followed by a series of 90° bends, not unlike a serpentine mixer, as shown in Figure 2.11. The tangential mixer was found to produce the best mixing performance. The mixing time for all four configurations were found to decrease with increasing Re and falls below 1 ms in the range $Re > 700-900$ (Kockmann et al, 2006; Kockmann et al, 2006).

Figure 2.11: Four different mixing elements tested (Kockmann et al, 2006)



Other three dimensional micromixers include a three dimensional twisted microchannel (first mixer on the left, Figure 2.12) which rotates and separates the two fluids by partitioning walls and generates smaller blobs exponentially (Park et al, 2004). The breakup process was found to enhance mixing even at low Reynolds number ($Re=1$) as it increases the interfacial area as well as produce a steep concentration gradient at the interface. Three types of twisted microchannels, the inclined, oblique and wavelike microchannels (Figure 2.12) have also been reported with an improved mixing performance of 31 % over the T-micromixer for the inclined micromixer (Jen et al, 2003).

Figure 2.12: Three dimensional secondary flow microchannel mixers (from left to right, twisted microchannel, inclined micromixer, oblique micromixer and wavelike micromixer) (Nguyen and Wu, 2005)



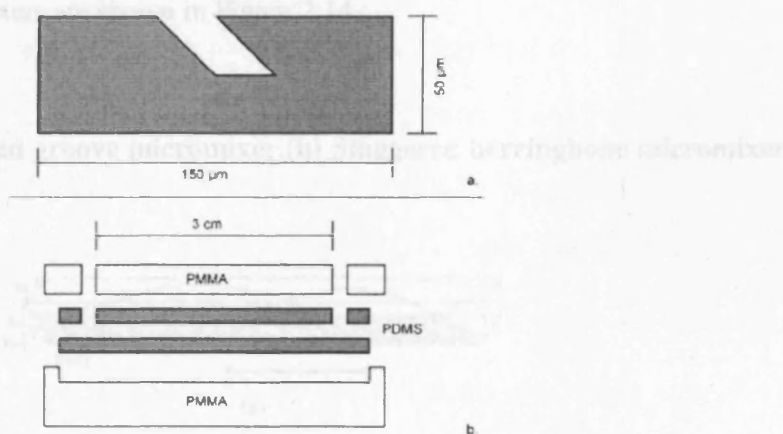
2.6.7. Grooved Micromixers

Traversing flow can be generated by placing microstructured objects within the flow Jen et al later constructed a self-circulation mixer which consists of an inlet port, a mixing chamber, an outlet port and an air inlet port (Chung et al, 2004). The self circulation in the mixing chamber is achieved by the forward and backward pumping of the working fluids. The mixer was found to enhance mixing especially at Re between 20 and 400.

secondary flow mixers, flow mixing is easier to achieve due to the large number of grooves on such planes.

A recirculating passive micromixer made from PDMS which uses a sawtooth structure (Figure 2.13) placed in the channel to generate transverse flows parallel to the length of the channel was recently reported (Nichols et al, 2006). Individual streamlines are accelerated or decelerated relative to other streamlines such that sections of fluid at different lengths of the channel can be brought into contact with each other.

Figure 2.13: Schematic of the structure of the microfluidic device. (a) Design of one sawtooth unit. (b) Cross section of the device. The gray areas indicate the PDMS device while the white areas are the housing made of PMMA (Nichols et al, 2006).

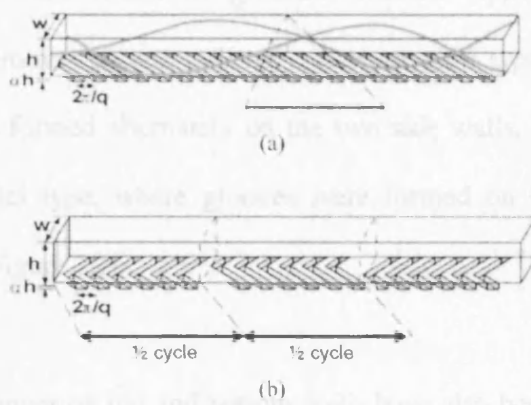


2.6.7. Grooved Micromixers

Transverse flow can be generated by placing microstructured objects within the flow passage on one side of the microchannels. Such structures include rips, grooves and staggered herringbones. By placing these structures on one side of the microchannel, flow circulations are generated which lead to an exponential increase of the specific interface, leading to improved mixing. While grooved microchannels fall under secondary flow mixers, these are discussed separately due to the large number of work on such mixers.

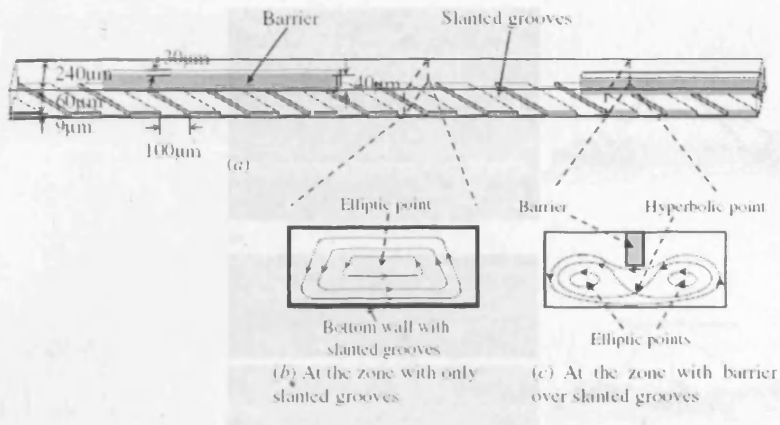
Johnson et al (2002) used grooves ablated on the bottom wall which induced lateral flow across the channel. Almost at the same time, Stroock et al (2002) reported using bas-relief structures on the floor of channels to induce transverse flows in the microchannel. Slanted grooves were tested and confirmed to induce transverse flows, which led to the design of a staggered herringbone structure to induce steady chaotic flows in the channel. The staggered herringbone was found to work well for Reynolds numbers from 1 to 100, up to Peclet numbers of 1×10^6 . Analytical models were derived for flows in both the slanted groove micro channel and staggered herringbone microchannel (Stroock and McGraw, 2004). Both slanted groove and staggered herringbone groove mixers are shown in Figure 2.14.

Figure 2.14: (a) Slanted groove micromixer.(b) Staggered herringbone micromixer (Stroock et al, 2002).



A similar type of mixer, called a barrier embedded chaotic micromixer (Figure 2.15) where three dimensional helical flows were generated by slanted grooves on the channel floor has also been reported (Kim et al, 2004). Barriers were periodically embedded on the top surface of the channel to impose spatially periodic perturbation on the helical flow, thereby generating alternating velocity fields. The mixing performance was found to give improved performance over slanted groove mixers.

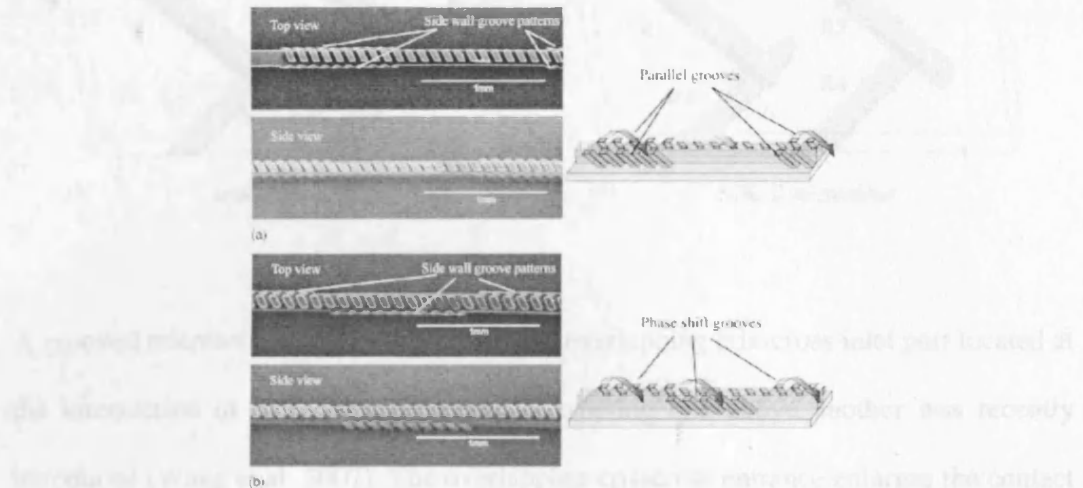
Figure 2.15: Barrier embedded micromixer (Kim et al, 2004) (a) Schematic view, (b) and (c) are cross-sectional velocity fields at two typical locations.



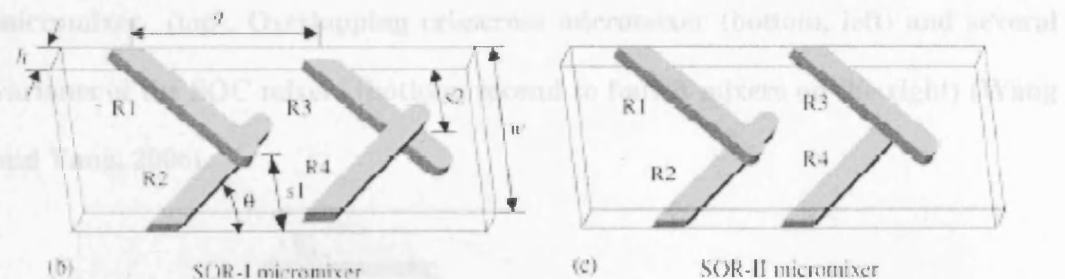
A novel method for fabricating micro-structures on the top and side walls of microchannels, based on a two-step inclined backside exposure using both sides of Cr patterned glass substrate has been developed (Sato et al, 2005). The microchannels with grooved side walls were found to generate efficient spiral flow compared to microchannels with grooves on one wall only. A phase-shift type mixer, i.e. where the slanted grooves were formed alternately on the two side walls, was found to perform better than the parallel type, where grooves were formed on both side walls. Both mixers are shown in Figure 2.16.

Micromixers with grooves on top and bottom walls have also been reported (Howell et al, 2005; Floyd-Smith et al, 2006), giving rise to vertically stacked vortices as well as the two counter rotating vortices observed in the staggered herringbone mixer. The mixers with grooves on both top and bottom walls were able to generate comparable mixing to those in a staggered herringbone mixer over a shorter relative channel length.

Figure 2.16: (a) Parallel grooved micromixers. (b) Phase-shift grooved micromixers (Sato et al, 2005)



Two similar micromixers, which consist of mixing segments made up of a microchannel section with two pairs of ridges which can be located either on the top of the channel or floor of the channel were recently reported (Fu et al, 2006). In the first mixer design SOR-I, half of each pair of ridges is located on opposite sides and the arrangement is switched from one pair of ridges to the next pair. The second mixer design SOR-II is similar, with half of each pair of ridges located on opposite sides of the channel, however, the arrangement is not switched from one pair to the next, i.e. all ridges on the left side are located on the top wall and all ridges on the right side are located on the floor of the channel. Both mixer designs are shown in Figure 2.17. Mixing was found to improve with increasing Re due to increased stretching and folding, with better performance observed in SOR-II. The stretching in SOR-II was also found to be higher than SOR-I at all Re .

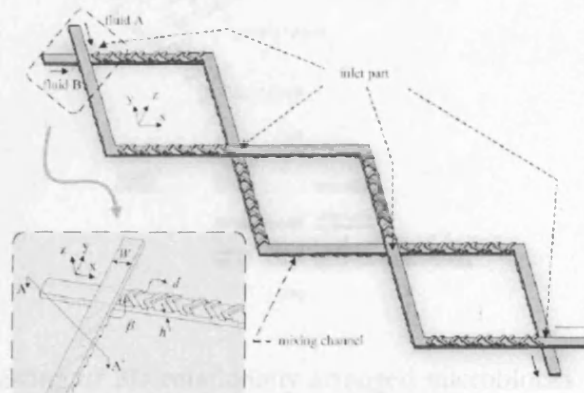
Figure 2.17: Staggered oriented ridges (Fu et al, 2006)

A grooved micromixer which incorporates an overlapping crisscross inlet port located at the intersection of two patterned channels crossing one above another was recently introduced (Wang et al, 2007). The overlapping crisscross entrance enlarges the contact area between the two mixing fluids and induces tumbling to generate a vertical component of flow. The mixing index of the crisscross mixer is 46 % better than that of the staggered herringbone mixer, increasing to 60 % if the grooves are positioned such that they are located nearer to the horizontal fluid interface.

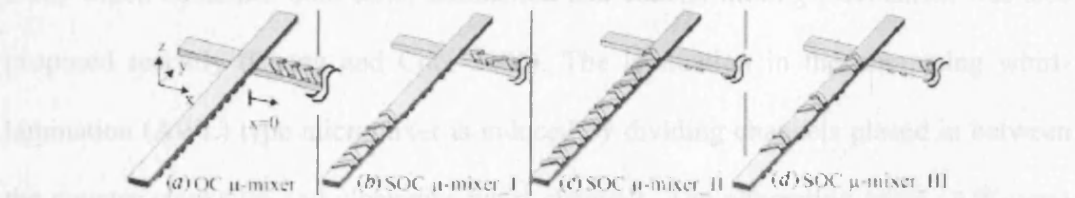
A variation of this mixer, the staggered overlapping crisscross mixer was also presented (Wang and Yang, 2006). Varied pattern arrangements were introduced, for example alternating the position of the grooves from top to bottom wall, switching the position of the leading edge of the grooves or a combination of both. The staggered overlapping crisscross mixers performed 21 % better than overlapping crisscross mixers. Both the overlapping and staggered mixing mechanisms with chaotic advection were overlapping crisscross and staggered overlapping crisscross micromixers are shown in recently introduced (Kim et al, 2005). The different kinds of successive arrangements of Figure 2.18.

Y-shape mixing units in two layers for continuous splitting and recombination while the overall 3D serpentine path of the microchannel induces tumbling effects at the corners, as shown in Figure 2.19. Ideal flow lamination is enhanced at higher Re due to flow advection effects with complete mixing achieved for a range of Re numbers.

Figure 2.18: Schematic diagram of a staggered overlapping crisscross (SOC) micromixer (top). Overlapping crisscross micromixer (bottom, left) and several variants of the SOC mixers (bottom, second to fourth mixers on the right) (Wang and Yang, 2006).



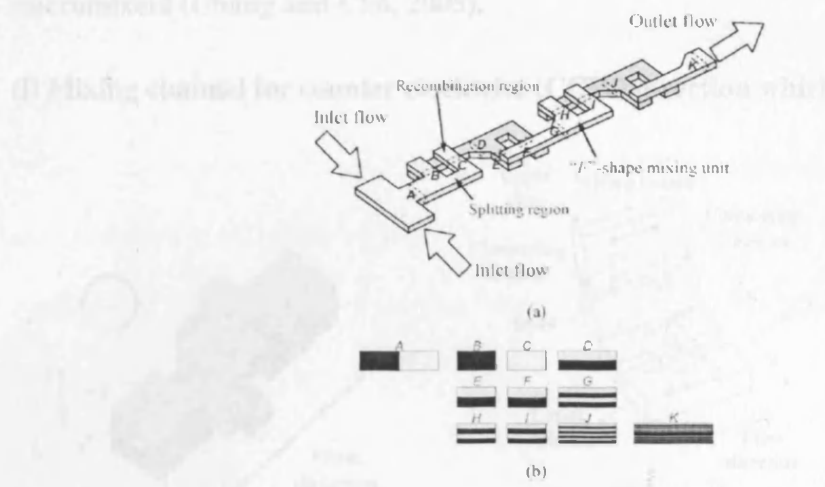
A micromixer consisting of staggered microchannels is shown in Figure 2.18 which combines both serial lamination and chaotic mixing mechanism was also proposed in 2006 by Wang and Yang. The schematic in the following will



micromixer, which is based on chaotic advection by staggered configuration of staggered crisscross and chaotic mixing channel, was also investigated.

2.6.8. Hybrid Micromixers

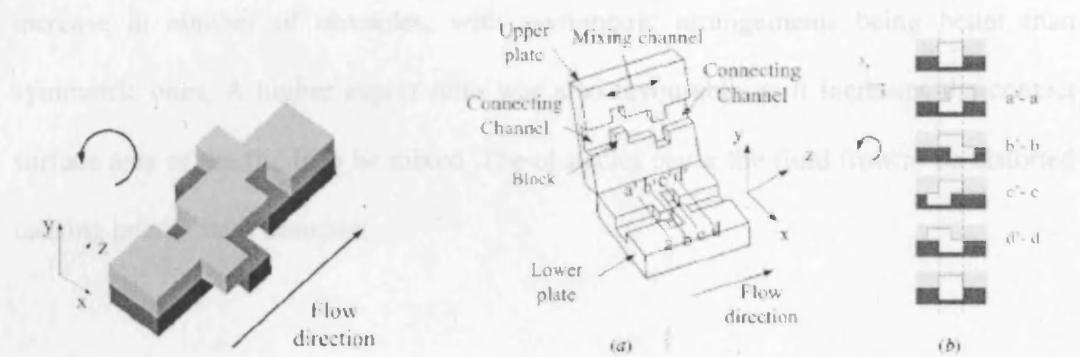
Recently several micromixers have been proposed which combine more than one micromixing mechanisms. For example, the serpentine laminating mixer (SLM), which combines both split and recombine mixing mechanism with chaotic advection was recently introduced (Kim et al, 2005). The mixer consists of successive arrangements of 'F'-shape mixing units in two layers for continuous splitting and recombination while the overall 3D serpentine path of the microchannel induces stirring effects at the corners, as shown in Figure 2.19. Ideal flow lamination is enhanced at higher Re due to flow advection effects with complete mixing achieved for a range of Re numbers.

Figure 2.19: Serpentine laminating mixer (Kim et al, 2005)

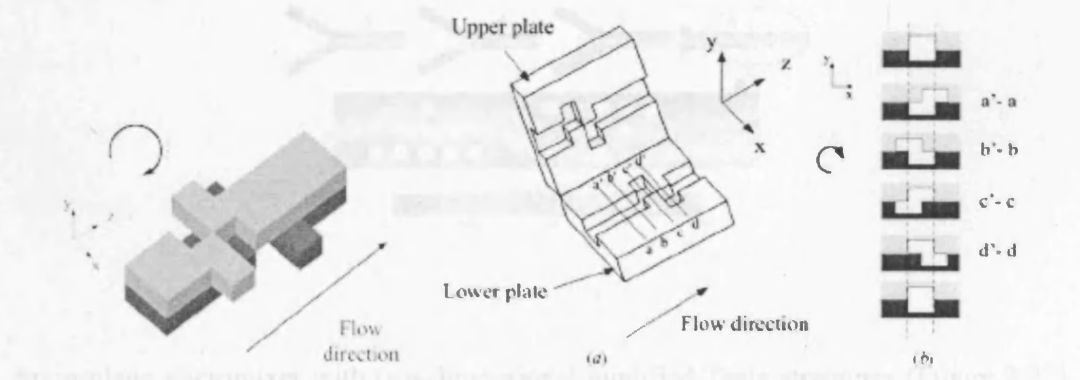
A micromixer consisting of 3D rotationally arranged microblocks (as shown in Figure 2.20) which combines both serial lamination and chaotic mixing mechanism was also proposed recently (Chang and Cho, 2005). The lamination in the alternating whirl-lamination (AWL) type micromixer is induced by dividing channels placed in between the counter clockwise and clockwise whirl channels. The alternating whirl (AW-type) micromixer, which is based on chaotic advection by alternating combination of counter clockwise whirl channel and clockwise whirl channel, was also investigated. Unsurprisingly, both micromixer types produce rapid mixing compared to plain channels, with mixing lengths of $2.8 - 5.8$ mm for $Re = 0.26 - 26$ for the AWL type, a 60 % reduction compared to mixing lengths of $7 - 17$ mm in the range $Re = 0.01 - 10$ for a mixer similar to the staggered herringbone mixer.

Figure 2.20: Alternating whirl (AW) and Alternating whirl-lamination (AWL) micromixers (Chang and Cho, 2005).

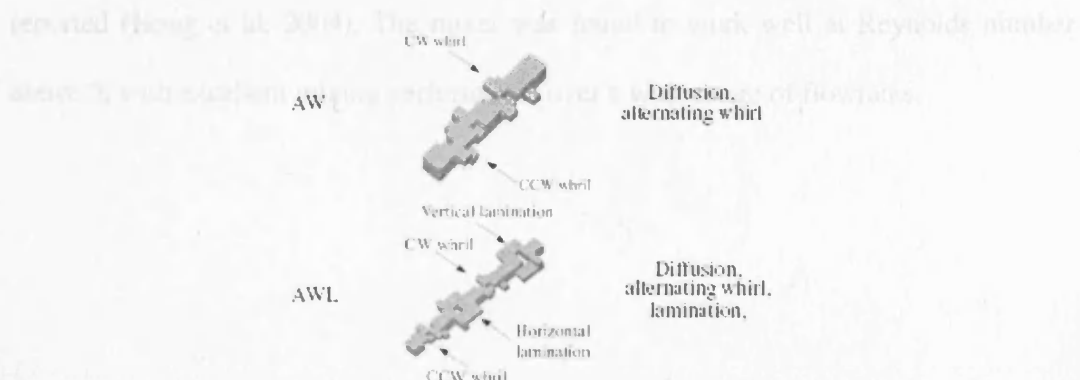
(i) Mixing channel for counter clockwise (CCW) direction whirls



(ii) Mixing channel for clockwise (CW) direction whirls



(iii) Structure of both AW and AWL micromixers.



2.6.9. Miscellaneous Micromixers

A microchannel with obstacle structures located on the microchannel floor, as shown in Figure 2.21 has been proposed (Wang et al, 2002). Mixing was enhanced with an increase in number of obstacles, with asymmetric arrangements being better than symmetric ones. A higher aspect ratio was also favourable as it increases the contact surface area of the fluids to be mixed. The obstacles cause the fluid flow to be distorted causing lateral mass transport.

Figure 2.21: Micromixer with obstacle structures (Wang et al, 2002)

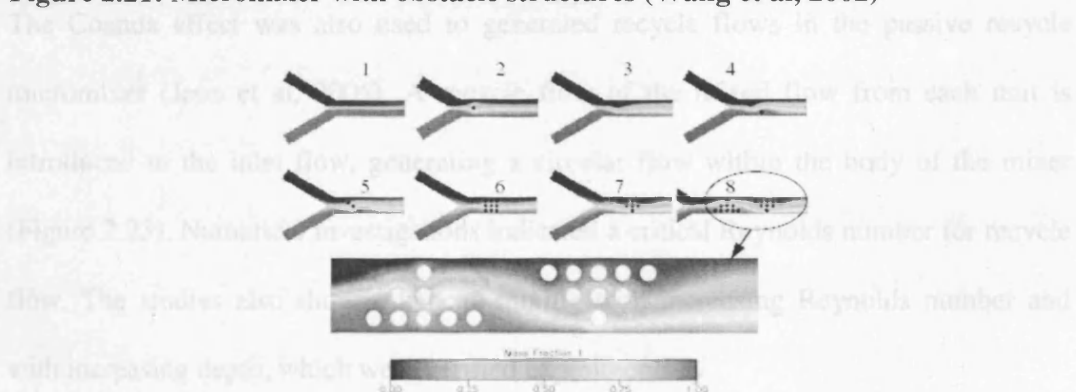
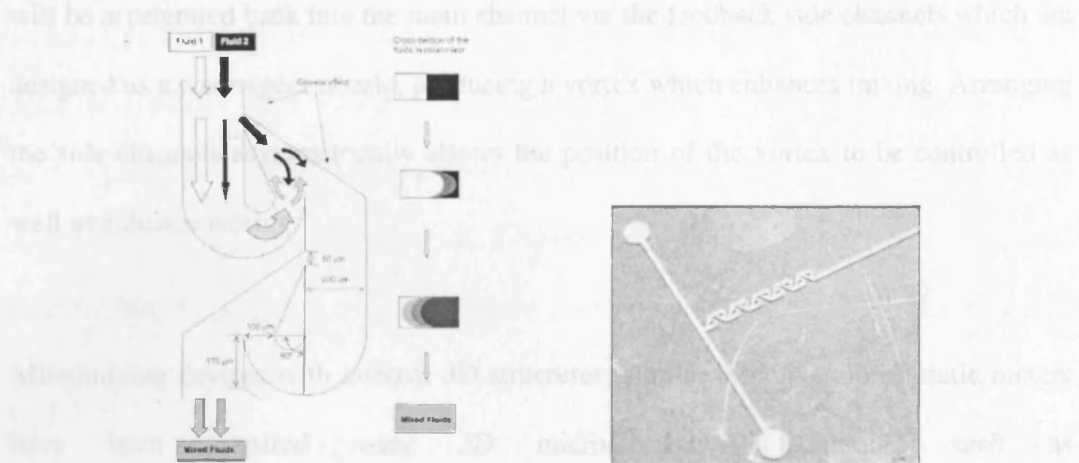


Figure 2.22: Schematic diagram of the passive recycle mixer (Jeon et al, 2005)

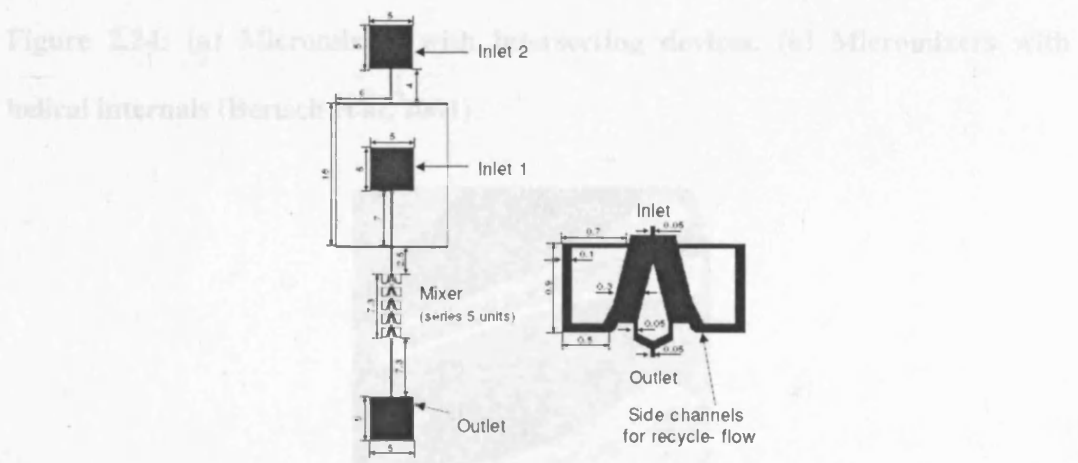
An in-plane micromixer with two-dimensional modified Tesla structures (Figure 2.22), which makes use of the Coanda effect to generate transverse dispersion has also been reported (Hong et al, 2004). The mixer was found to work well at Reynolds number above 5, with excellent mixing performance over a wide range of flowrates.

Figure 2.22: Schematic illustration of the mixing principle (left) and the Tesla micromixer (right) (Hong et al, 2004).



The Coanda effect was also used to generate recycle flows in the passive recycle micromixer (Jeon et al, 2005). A recycle flow of the mixed flow from each unit is introduced to the inlet flow, generating a circular flow within the body of the mixer (Figure 2.23). Numerical investigations indicated a critical Reynolds number for recycle flow. The studies also show enhanced mixing with increasing Reynolds number and with increasing depth, which were verified experimentally.

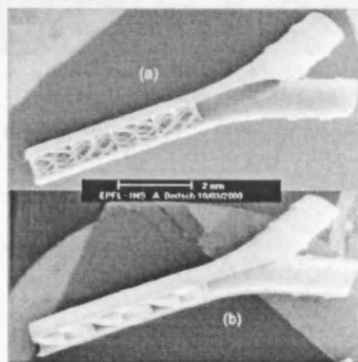
Figure 2.23: Schematic diagram of the passive recycle mixer (Jeon et al, 2005)



A new micromixer which incorporates feedback side channels on both sides of the main channel has also been proposed (Hung et al, 2005). At a critical Re number some fluid will be accelerated back into the main channel via the feedback side channels which are designed as a convergent nozzle, producing a vortex which enhances mixing. Arranging the side channels asymmetrically allows the position of the vortex to be controlled as well as enhance mixing.

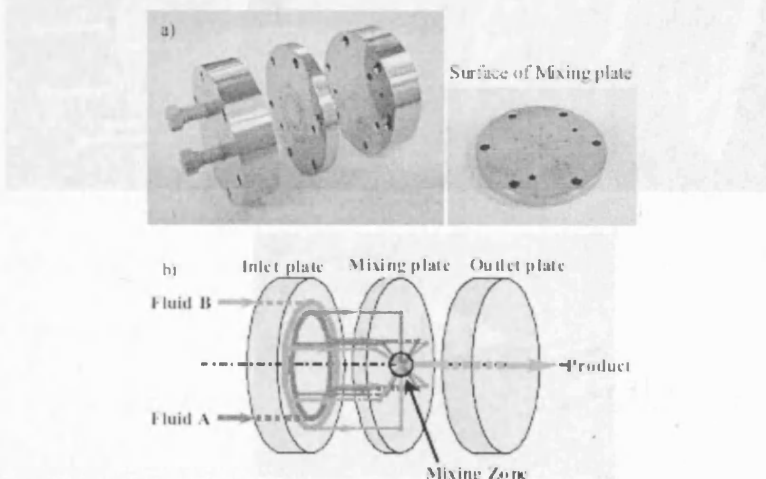
Micromixing devices with internal 3D structures, similar to conventional static mixers have been prepared using 3D microfabrication techniques such as microstereolithography using polymerization of a liquid resin (Bertsch et al, 2001). Two such structures were fabricated, one with intersecting internals and another with helical internals as shown in Figure 2.24. Mixing in the intersecting devices was achieved via manifold splitting and recombining of the flow, with good mixing efficiency. The helical device on the other hand performs mixing via flow stretching and folding, with a lower mixing efficiency. Better performance in the intersecting device was due to relatively good dispersion across the channel diameter.

Figure 2.24: (a) Micromixers with intersecting devices. (b) Micromixers with helical internals (Bertsch et al, 2001)



Recently, a new micromixer based on mixing by both kinetic energy and molecular diffusion was reported by Nagasawa et al (2005). The micromixer, constructed out of stainless steel consists of an inlet plate, a mixing plate and an outlet plate (Figure 2.25). Annular channels were fabricated on the inlet plates to feed two different fluids uniformly to the inlets of the microchannels on the mixing plate. The inlet channels are arranged in a circular arrangement, with different fluid fed alternately. The two fluids are then directed to the centre of the mixing plate where they are instantly mixed before being directed to the outlet flow. The mixing performance was attributed to the breaking of micro segments under high shear rates and instant molecular diffusion between micro segments. Increasing the number of fluid segments (by increasing the number of channels for dividing reactant fluids) decreases the size of the divided fluid segments and hence improves mixing. The mixing performance improved with increasing flowrate due to the combined effect of shorter diffusional distance and the confluence of multiple fluid segments (Aoki and Mae, 2006).

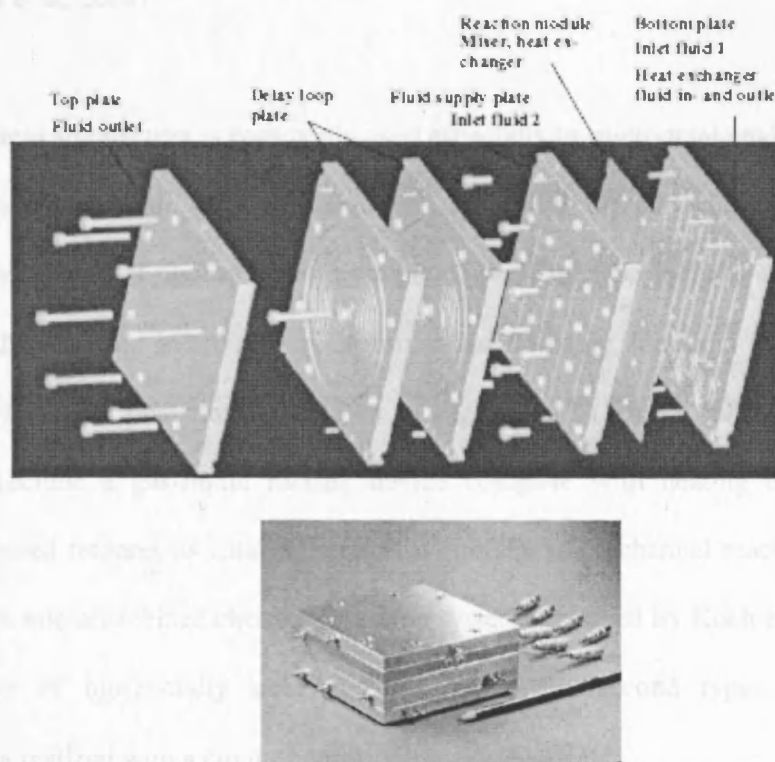
Figure 2.25: Micromixer based on collision of microsegments (Nagasawa et al, 2005) (a) The internal structure. (b) Schematic of flow in the micromixer.



2.6.10. Integrated Microreaction Systems

Miniaturised reaction systems frequently combine a number of microstructured devices and unit operations which allow chemical reactions to be performed effectively. Depending on the function and complexity, a vertical or horizontal architecture or hybrid integration scheme can be used to form a complete microchemical plant. In the vertical integration architecture, a microsystem may consist of several layers/sheets, each performing one or more functions. Layers are then stacked into a compact reactor assembly (Gavrilidis et al, 2002). The assembled microreaction system developed by the Institut für Mikrotechnik Mainz for the synthesis of a vitamin precursor with integrated static mixers, heat exchangers, reaction channels and delay loop is an example of a vertically integrated system as shown in Figure 2.26.

Figure 2.26: Vertically integrated microreaction system (Ehrfeld et al, 2000)

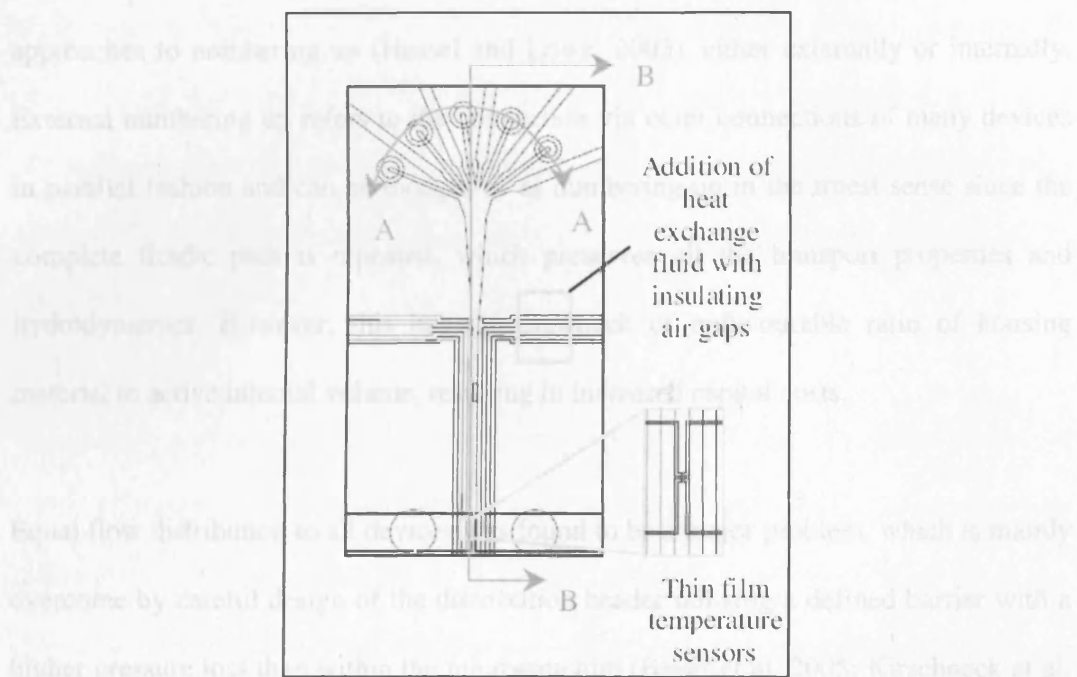


A modular design of such a reaction system allows for greater flexibility since it allows for multi step synthesis as well as variation in residence time simply by introducing additional microstructured plates (Ehrfeld et al, 2000). Other examples include a system for catalytic partial oxidation of methane, which combines a reaction zone, a reactant preheat section, a product quench section and a heat generation section in a multiple sheet planar arrangement (Tonkovich et al, 1998). Schmitt et al (2005) developed a ceramic plate heat exchanger for heterogeneous gas-phase reactions with integrated heat exchange in a similar manner.

With the horizontal architecture, various functions are integrated either on a single layer or via a fluid distribution unit on which various devices such as pumps, mixers and reactors can be mounted. The distribution unit contains channels which bring the fluid from one device to the next without the need for conventional tubing connections (Gavriliidis et al, 2002).

The horizontal architecture is commonly used especially in micro total analysis where it is desirable to have all the unit operations integrated on one chip. Examples of horizontally integrated microreaction systems of the first type include a liquid phase reactor with triangular interdigital micromixer and focusing zone and integrated heat exchanger for rapid heat transfer, shown in Figure 2.27 (Jensen, 2001). Other such examples include a gas-liquid mixing device complete with heating elements and microstructured features as catalyst support within the microchannel reactor (Losey et al, 2002). A micromachined chemical reaction system described by Koch et al (1999) is an example of horizontally integrated system of the second type, with fluidic connections realized with a circuit board.

Figure 2.27: Horizontally integrated microreaction system with a nozzle-type mixing component, using microlamination and hydrodynamics focusing and a two-channel, countercurrent flow heat exchanger (Jensen, 2001)



2.7. Microchemical Plant Concepts

Few microchemical plants have been used for real production, it comes as no surprise then that engineers lack the experience and systematic tools for design and control of microchemical plants. New approaches to process design have been proposed (Bayer et al, 2005) and the necessary process design steps for microstructured devices have been outlined (Kirschneck et al, 2005). Design and operational issues in microchemical plants have also been discussed (Hasebe, 2004). The design problem of microchemical plants can be classified into the design of the microdevice, and the design of the entire plant structure, which is described in this section.

2.7.1. Internal versus External Numbering-up

The increase in production rate in a microchemical plant can be achieved, at least in principle, by increasing the number of parallel operating units. There are two main approaches to numbering up (Hessel and Lowe, 2003), either externally or internally. External numbering up refers to the connection via outer connections of many devices in parallel fashion and can be thought of as numbering-up in the truest sense since the complete fluidic path is repeated, which preserves all the transport properties and hydrodynamics. However, this has the drawback of unfavourable ratio of housing material to active internal volume, resulting in increased capital costs.

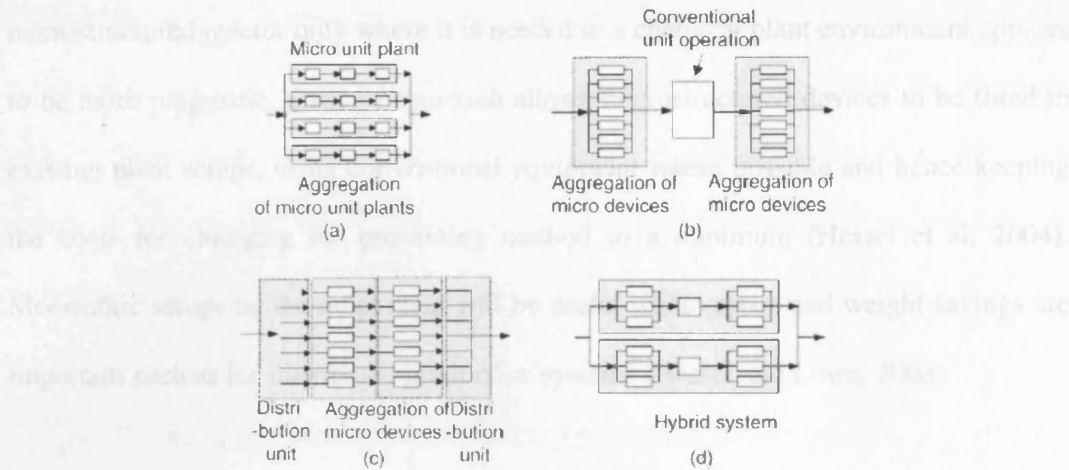
Equal flow distribution to all devices was found to be a major problem, which is mainly overcome by careful design of the distribution header utilising a defined barrier with a higher pressure loss than within the microstructure (Bayer et al, 2005; Kirschneck et al, 2005). Alternatively, equal flow distribution can be achieved by using instrumentation, which can be costly, limiting its use to only a small number of devices (Kirschneck et al, 2005). Internal numbering up, on the other hand refers to the parallel connection of functional elements only, rather than the complete device. These elements can then be grouped as a stack in a new housing which usually also includes a flow manifold and a collection zone. This allows for compact reactor architecture at reasonably high throughput. The drawback however is that a redesign of the fluidic path and possibly the functional element may be required, although this may be avoided by taking into consideration the method for scaling out at the beginning of the device design stage. Even so, there is no evidence that internally numbered up devices, such as a multiplate microchannel reactor will truly operate under identical conditions at all points in the interconnected structure (Bayer et al, 2005).

The problems of scaling-up production using microstructured devices have not yet been considered in detail; however, even at this early stage it is clear that internal numbering up has a clear advantage over external numbering up. Still, external numbering-up may be appropriate in certain situations for example if the scale-out factor is less than 10 since internal numbering up will require further development costs and time. Certain processes are also more amenable to external scale out, for example if the fluidic path needs to be set below a certain characteristic dimension to guarantee inherent safety (Hessel et al, 2004).

The challenge with internal numbering-up is to adapt and enlarge the device to achieve higher throughput without changing the microstructured fluid flow behaviour substantially. Fouling needs to be carefully avoided since there may be major difficulties with removal. Heat management will also demand more elaborate solutions to ensure uniformity across the entire scaled-out device.

2.7.2. Microplant Structures

The selection of an appropriate scale out method is clearly application specific, depending on among other things, the final production capacity required and the process conditions and sensitivity to specific process parameters. Many plant structures have been proposed, ranging from a completely monolithic approach where microfluidic components are used exclusively to a hybrid approach where conventional tools are mixed with microfluidic components. These have been classified into four main types (Hasebe, 2004), as shown in Figure 2.28.

Figure 2.28: Four types of plant structures (Hasebe, 2004)

Plant structure (a) represents external numbering-up of unit microplants. Structure (b) represents the multi-scale approach, where internally scaled out units are used in conjunction with conventional macro scale devices where possible. Structure (c) represents internally numbered-up microdevices, similar to that in structure (b), with a different flow pattern. A hybrid structure, shown in (d) represents a microplant consisting of internally numbered up microdevices and conventional macro scale equipment which is then scaled externally to achieve higher throughput.

Hasebe (2004) also outlined the main factors to be considered in selecting the optimal plant structure. For instance, if the residence time in the interconnection between devices can significantly affect the process performance and needs to be minimized, then structures (a) and (c) are better than (b). If operating conditions such as temperature is different in two different micro unit operations, then it is better not to aggregate these unit operations and hence structures (b) and (c) are preferred. Structure (a) offers flexibility of production rate while structures (b) and (c) offers ease of replacing unit operations, which facilitate replacement of deactivated catalytic reactors or clogged devices.

For microreactor plant construction, a multi-scale approach which incorporates a microstructured reactor only where it is needed in a chemical plant environment appears to be more pragmatic. Such an approach allows microstructured devices to be fitted in existing plant setups, using conventional equipment where possible and hence keeping the costs for changing the processing method to a minimum (Hessel et al, 2004). Monolithic setups on the other hand will be useful where space and weight savings are important such as for distributed production systems (Hessel and Lowe, 2003).

2.7.3. Instrumentation and Control

In laboratory bench top applications, the use of miniaturized temperature sensors in microreactors have been reported although in the main, most applications still involve conventional thermocouples. Contact-free measuring methods such as thermal imaging for monitoring temperatures and IR measurements for concentration profiles provide an alternative to using conventional measuring devices. Offline methods including chemical techniques for comparing competing reactions provide a useful way to characterize system performance (Hessel and Lowe, 2003).

One of the major setbacks attributed to the numbering-up approach is the complexity in monitoring and controlling various process parameters since there will be substantially more devices in a scaled out unit. However, there is a strong argument for alternative approaches to maintain optimal process conditions. For example, proper design of the scaled out device may be more reliable for ensuring equal flow distribution rather than relying on individual monitoring of flows.

Similarly, due to the good thermal efficiency found in microreactors, inline measurements of temperature may be unnecessary; rather, the control of the whole reactor may be more appropriate (Hessel and Lowe, 2003). Hasebe for example, suggested an indirect control system which controls the temperature of the fluids in the microstructured device via control of the thermal fluid temperature, hence avoiding the need for inline temperature measurement (Hasebe, 2004).

2.7.4. External Scale-out of Microreaction Systems

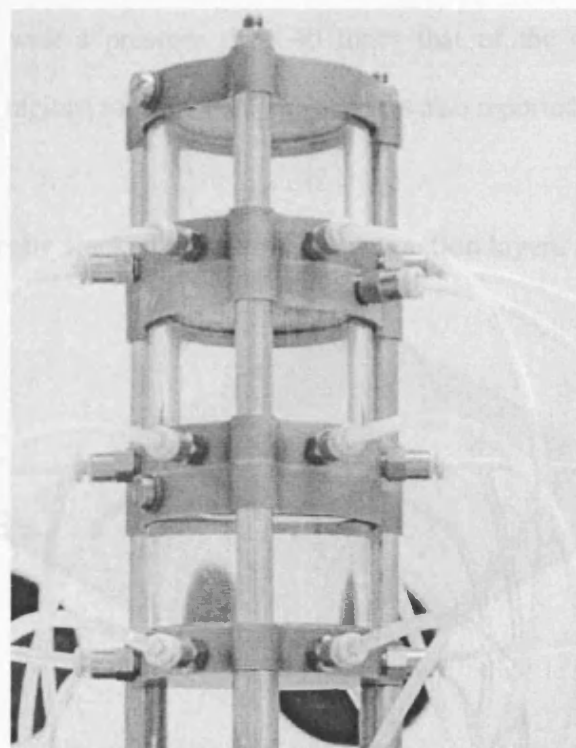
There are currently few detailed reports on the scale out of microreaction systems. A brief overview of some related reports is presented in the current and following sections. One of the first reports to address the issues in microreactor scale-up concerns the development of a turnkey multiple microreactor test station, which represents an external scaled out system (Quiram et al, 2000). The system includes microfabricated reactors as well as other MEMS components for fluidic control in a parallel array and highlights the difficulties in developing electrical and fluidic interfaces to microreactors.

Kobayashi et al (2005) used an assembly of nine palladium immobilized capillaries for the hydrogenation of 1-phenyl-1-cyclohexene. The uneven flow distribution resulted in a decrease in the yield; this was however compensated by immobilizing the Pd catalyst further, allowing the reaction to proceed with a quantitative yield.

A liquid flow splitting unit capable of splitting one reactant stream into six sub streams of equal portion by building up a pressure barrier was recently developed (Figure 2.29). The flow splitting unit consists of one inlet feed into a cylindrical tank with six outlets

each connected to a micromixer. With a sufficiently high pressure drop, the effect of mode of injection and tank geometrical parameters is minimized (Schenk et al, 2003). The device was subsequently applied for the synthesis of butyl acetamide from butylamine and acetyl chloride in THF using triethylamine as auxiliary base (Schenk et al, 2004). Liquid flow distribution was found to be governed by the precision of the fabrication process, with deviation from ideal flow distribution more pronounced than for non-reacting flows. This was attributed to the additional complexity of reacting systems with a higher tendency for fouling which then affects the flow splitting by increasing the pressure at the outlet.

Figure 2.29: Flow splitting unit for external scale-out (Schenk et al, 2004)

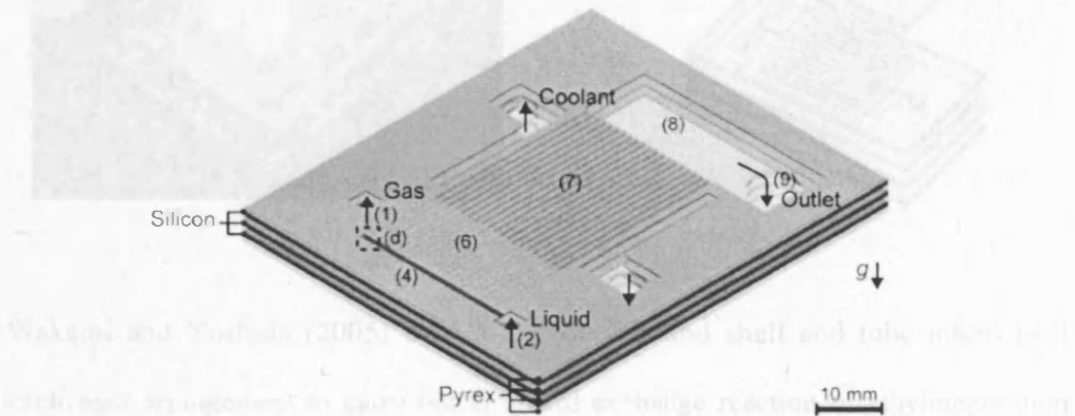


2.7.5. Internal Scale-out of Microreaction Systems

Examples of internally scaled out reaction systems include a falling film microreactor which consists of an array of parallel reaction channels for direct fluorination of toluene (Jahnisch et al, 2000) and a stainless steel modular multichannel gas/liquid microreactor for direct fluorination reactions (Chambers et al, 2005).

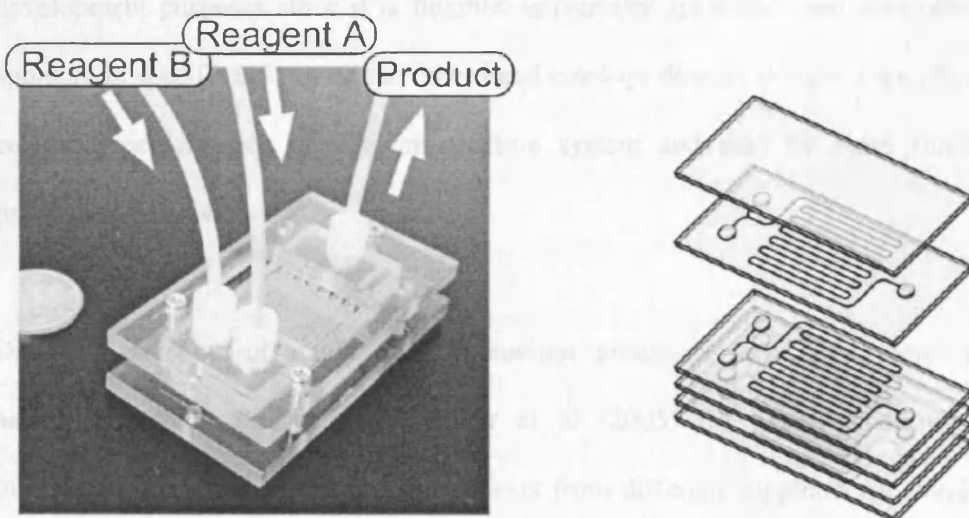
Recently, de Mas et al (2005) developed a scaled-out gas-liquid microreactor which consists of three vertically stacked reaction layers, as shown in Figure 2.30. Both gas and liquid distributors were designed to produce pressure drops that were a factor of 50 and 25 respectively, the pressure drop in the reaction channel. Later, a multichannel gas-liquid microreactor for ozonolysis of organic reagents, again using pressure drop channels designed with a pressure drop 40 times that of the downstream reaction channels and outlet regions for flow equipartition was also reported (Wada et al, 2006).

Figure 2.30: Vertically stacked gas-liquid microreaction layers (de Mas et al, 2005)



Kikutani et al (2002) developed a ‘pile-up’ microreactor with 10 vertically stacked reaction layers each with a single microchannel circuit (Figure 2.31). Flow distribution was achieved by using much larger cylindrical feed holes compared to the microchannels. The overall system size was minimised by using both sides of the glass plate, one etched with channels and the other as cover glass for the next plate. The amide formation reaction was carried out, with the yield in the single-layered chip nearly constant at 83 % at all flowrates tested, although in the pile-up reactor the yield dropped to 70 % with increasing flowrates. The decrease in reaction yield was attributed to uneven flow distribution and consequently a biased distribution of reactants.

Figure 2.31: Pile-up glass microreactors (Kikutani et al, 2002)



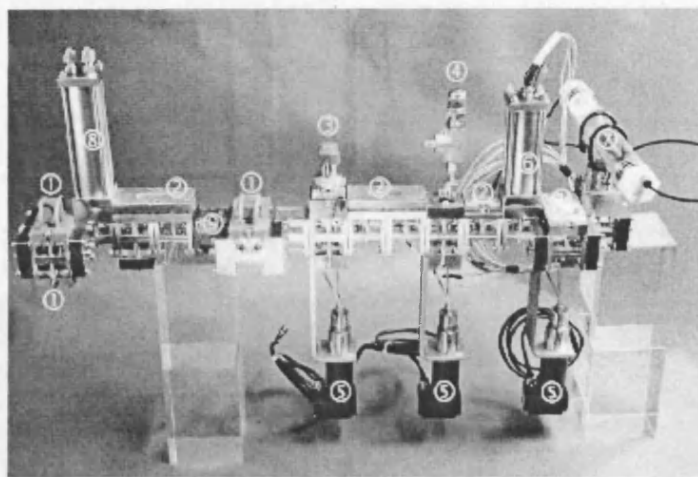
Wakami and Yoshida (2005) used a micromixer and shell and tube micro heat exchanger arrangement to carry out Grignard exchange reaction of ethylmagnesium bromide and bromopentafluorobenzene with a maximum product yield of around 95 %, although the flow distribution in the micro tubes was not studied. The setup was subsequently tested on a pilot plant with 14.7 kg product yield within 24 hours. More

recently, Iwasaki et al (2006) reported using a similar setup for the radical polymerization of methyl methacrylate which was also successfully tested on a pilot plant using 5 shell and tube reactors coupled by tube connectors.

2.7.6. Commercial Microreactor Setups

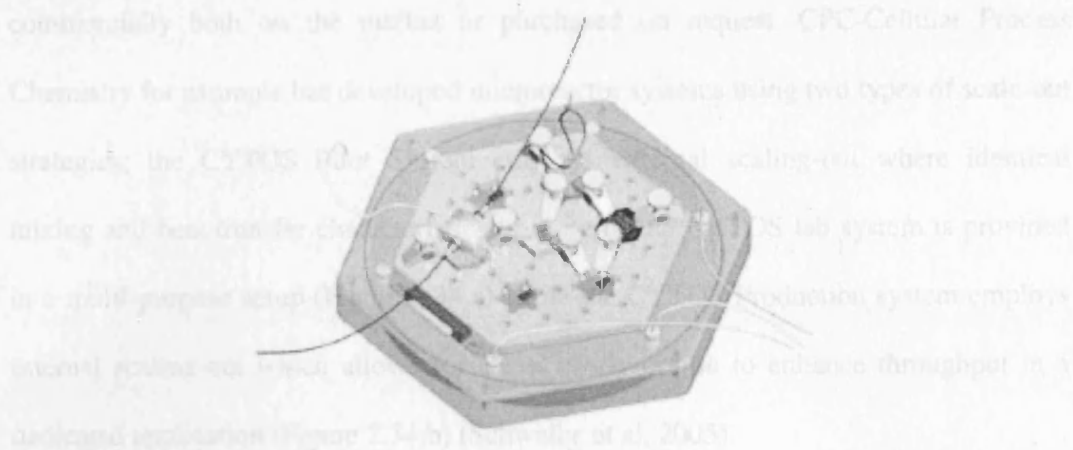
While previous research tended to focus on the application of individually designed microreactors for specific chemical problems, there has been an increasing trend on developing automated microreaction systems and modular microchemical processes based on toolkit concepts. A toolkit system where microchemical processes are set up using standardized microfluidic modules is attractive especially for process development purposes since it is flexible, universally applicable and controllable. An application specific system on the other hand employs devices designed specifically for enhanced performance of a given reaction system and may be more suitable for production purposes.

Different concepts of modular microreaction processes have been developed. A backbone system, described by Muller et al (2005) for example, allows fluidic interconnection of microfluidic components from different suppliers via standardized interfaces (Figure 2.32). The backbone consist of cube-like hollow elements which can be combined individually and flexibly in all directions, providing the flow paths for fluids as well as electrical conduits for power supply and signal transmission of sensors and actuators. Microstructured devices can be surface mounted onto this backbone to set up a microchemical process.

Figure 2.32: Modular fluidic backbone concept (Muller et al, 2005)

(1) heat exchanger, (2) mixer, (3) valve, (4) safety valve, (5) pump, (6) heated residence time module, (7) miser-settler extractor, (8) heated mixer-tube reactor and (9) thermal decoupler.

A multifunctional microreaction unit based on the toolkit concept developed by the Fraunhofer Alliance Moduler Microreaction Systems (FAMOS) allows microreaction processes to be set-up using up to 6 hexagonal microfluidic modules mounted and connected on a base plate with suitable fluidic and electronic interfaces for the interconnection of toolkit modules, complete with measurement data recording and connection to the macroscopic periphery (Figure 2.33). A temperature bath on which the base plate is mounted allows the temperature of the interconnections to be controlled while microfluidic modules can be individually heated or cooled using a heat exchange microstructure on the module. Integrated temperature sensors as well as infrared spectroscopic measurements allow temperature measurement and analytical information to be obtained (Keoschkerjan et al, 2004). The Modular Microreaction System offered by Ehrfeld Mikrotechnik operates in a similar manner, where various unit operations are performed in separate modules equipped with flow guiding micro structures which can be flexibly mounted on a base plate (Hessel et al, 2005).

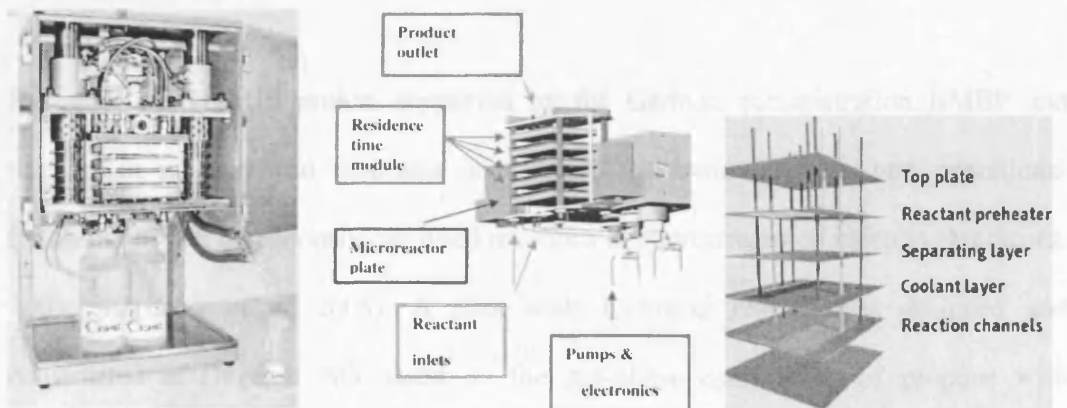
Figure 2.33: FAMOS microreaction system (Keoschkerjan et al, 2004)

While modular microreaction systems allow for fast changes of process setups and process parameters, additional automation is required for efficient and reliable parameter screening (Lobbecke et al, 2005). Ferstl et al (2004) developed an automated microreaction system with integrated microstructured sensors and analytical interfaces for systematic screening of process parameters as well as small-scale production in the kilogram range. The silicon microfluidic devices were integrated into cubical modules of identical shape and size to facilitate flexible interconnection of the devices. Each module is equipped with individual temperature control by both electrical heating and fluidic cooling and integrated pressure and/or temperature sensors. Pt 100¹ temperature sensors were used along with microstructured pressure and mass flow sensors fabricated in-house. The system allows inline analysis via IR or Raman spectroscopy. The process control system allows for systematic variation of process parameters by regulating and controlling the actuators.

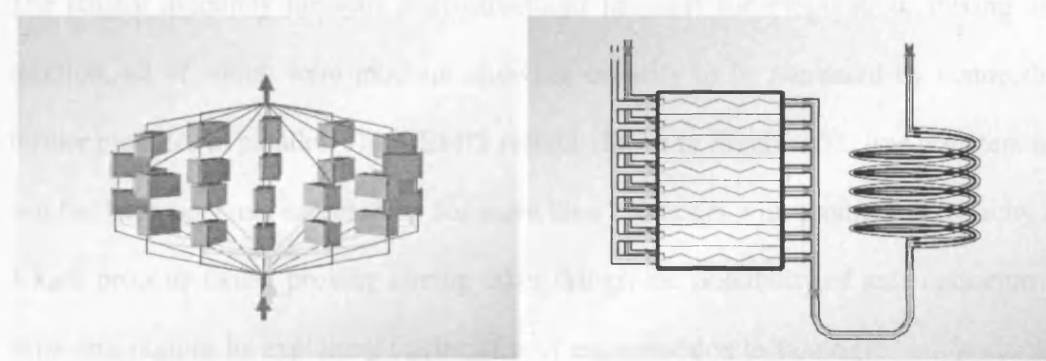
¹ Platinum temperature sensor with a resistance of $100\ \Omega$ at $0\ ^\circ\text{C}$.

In recent years, miniaturized reaction systems have been developed which are available commercially both on the market or purchased on request. CPC-Cellular Process Chemistry for example has developed microreactor systems using two types of scale-out strategies; the CYTOS Pilot System employs external scaling-out where identical mixing and heat transfer characteristics to those of the CYTOS lab system is provided in a multi-purpose setup (Figure 2.34 a) while the CYTOS Production system employs internal scaling-out which allows for a less costly option to enhance throughput in a dedicated application (Figure 2.34 b) (Schwalbe et al, 2005).

Figure 2.34: (a) CYTOS Lab System



(b) Fluidic scheme of the CYTOS Pilot System (left) and CYTOS Production System (right) (Schwalbe et al, 2005).



2.7.7. Microchemical Production Units

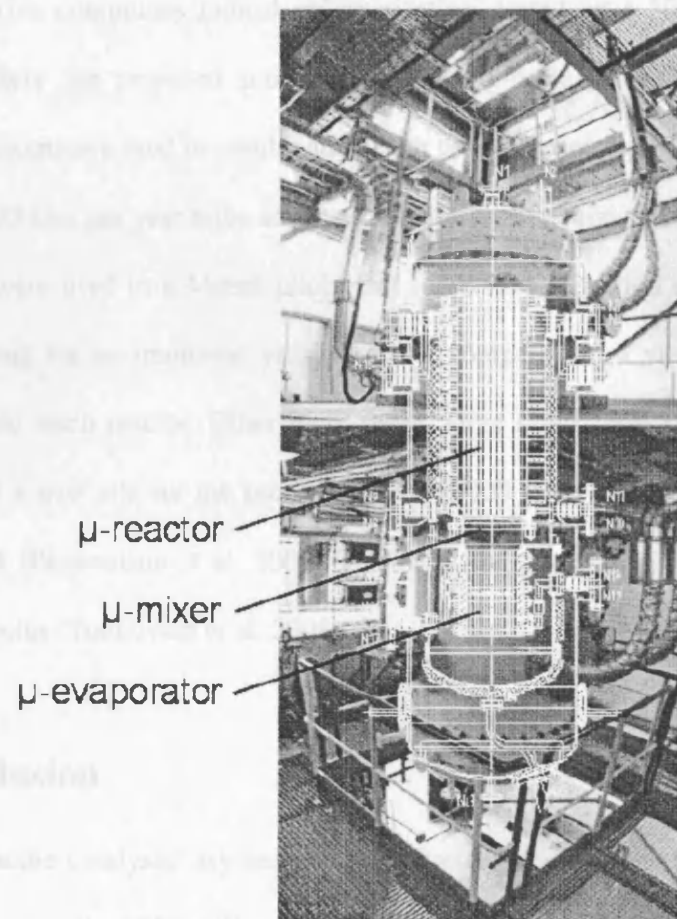
An example of the use of microchemical systems in manufacturing installations is for the synthesis of pigments with improved properties (Kim et al, 2002; Wille et al, 2004). A microreactor pilot plant was developed for Clariant utilizing three vertically stacked CYTOS production reactors embedded in one housing, with a capacity of up to 10 tonnes per annum. Reproducibility of the lab scale results in the pilot scale plant was demonstrated and strategies to overcome effects of long time operation such as fouling, coating and clogging of the microreactors were developed i.e. via a regular cleaning procedure. Details of other reactions which have been carried out in CYTOS systems are available elsewhere (Schwalbe et al, 2004; Schwalbe et al, 2005)².

Recently, the DEMIS project supported by the German administration BMBF and partners in industry and academia investigated the basic technical and operational feasibility of heterogeneously catalysed reactions in microstructured reactors (Markowz, 2003; Markowz et al, 2005). A pilot scale technical reactor was designed and constructed at Degussa AG based on the gas-phase epoxidation of propene with vaporised hydrogen peroxide as a model reaction.

The reactor assembly includes microstructured internals for evaporation, mixing and reaction, all of which were modular allowing capacity to be increased by connecting further modules in parallel. The DEMIS reactor shown in Figure 2.35, was 4 meters tall and has been operated successfully for more than 250 hours with production capacity of 1 kg/h propene oxide, proving among other things, the possibility of safe operation in explosive regions by exploiting the benefits of microreaction technology.

² Details also available on company website. www.cpc-net.com

Figure 2.35: External view of the DEMis reactor together with a schematic outline of the internals (Markowz et al, 2005)



2.6. Conclusions

Other commercial production units include the Velocys microchannel reactor for hydrogen production (Tonkovich et al, 2004), which combines the benefits of microreaction technology and novel engineered catalysts to create a compact, highly productive and thermally efficient system with multiple unit operations. A manifolding solution has been developed to achieve sufficient flow distribution with minimal pressure losses (Tonkovich et al, 2005). Plant and catalyst integration and manufacturing insights were also described (Tonkovich et al, 2005).

Although there has been a few industrial scale microchemical plants, detailed reports on these systems are relatively uncommon. Some of the earliest known large scale systems include the Axiva continuous radical polymerization, tested on a 50-tonnes per year pilot plant, where the proposed production scale pre-basic design consisted of 32 interdigital micromixers used in combination with tubular reactors enabling an acrylate capacity of 2000 tons per year to be achieved. Similarly, five mini mixer-tubular reactor arrangements were used in a Merck pilot plant for ketone reduction using a Grignard reagent, allowing for an improved yield of 92 % compared to a yield of 72 % in a production scale batch reactor. Other more recent large scale applications include the construction of a new site for the production of 150000 tonnes hydrogen peroxide by UOP and IMM (Pennemann et al, 2004) as well as for gas-to-liquids applications by FMC and Accentus (Tonkovich et al, 2005).

2.8. Conclusion

The poly-*L*-leucine catalysed asymmetric epoxidation of chalcone, first reported by Julia and Colonna in the 1980s, allows highly enantioselective chalcone epoxides to be produced in a triphasic system consisting of an organic phase, an aqueous phase and a gel-like solid phase. In recent years, several alternative reaction protocols employing the poly-*L*-leucine catalyst have been developed by Roberts et al, including a biphasic system, a mild system and a homogeneous system. A modified Julia-Colonna triphasic procedure which uses a phase transfer catalyst has also been reported. The different reaction protocols employ different alternative reactants as well as different forms of the catalyst, resulting in a range of reaction performance reported for the different protocols. Improvements in the physical properties and catalytic activity have been reported, via immobilization on suitable catalyst supports and developments in catalyst

preparation methods. A high degree of α -helix configuration and a minimum of 10 residues in the catalyst were found to effect good enantioselectivity, with the stereochemistry of the amino acid residues at the N-terminus playing a dominant role in determining the stereoselectivity of the reaction. The PLL catalyst behaves as an enzyme-like catalyst at low substrate concentrations, with the hydroperoxide species sequestered by the catalyst.

Microchemical processing offers several advantages over conventional processing including access to new reaction conditions, distributed point-of-use processing, faster process control and the opportunity to increase throughput by the numbering up approach. Microdevices offer the opportunity to precisely control the contacting of different fluid streams. The main methods developed for contacting fluids in passive microdevices include serial and parallel multilamination methods, hydrodynamic focusing methods, secondary flow mixers and more recently hybrid micromixers which combine several mixing methods in a single microdevice. These microdevices differ in mixing efficiency, throughput and ease of fabrication; the choice of microdevice is therefore application specific and is influenced by the following factors:

- Diffusional mixers (e.g. T-mixers) are generally easier to fabricate but may not be adequate for systems with low molecular diffusivity. A complicated 3D mixer design may be justified depending on the degree of mixing efficiency required.
- Parallel multilamination and focusing methods, which require small channel dimensions, may be more suitable for enhancing mixing in low throughput applications such as lab-on-a-chip devices due to the higher pressure drop associated with small channel dimensions.

- Secondary flow and serial lamination mixers, which allow for efficient mixing at larger channel dimensions may be more suitable for higher throughputs as well as systems with a tendency to foul.

Clearly, there has been considerable effort in developing new methods of contacting fluid streams more efficiently; on the other hand, not much effort has been directed at comparing and mapping suitable applications for the various devices. To aid the selection of a suitable microdevice, a quantitative comparison of the performance characteristics of the various microdevices would be beneficial.

Similarly, while considerable effort has been directed at developing integrated and automated microchemical systems, including commercial modular microreactor setups, few address the design aspects of microstructured reaction systems. Reports on scaled out production units are rare and even so, often do not address the choice of plant structure. A systematic and quantitative approach to selection and design of scaled out microchemical systems would be beneficial. Clearly, due to the lack of experience in designing such systems, much work needs to be done before a systematic approach can be outlined. The vast amount of literature available on microchemical systems demonstrates the interest in this growing field both from academia and industry. While the potential benefits of microchemical systems are obvious, it is perhaps less clear how much of an impact these will make on chemical processing as a whole e.g. whether it will find application in process development only or whether it could potentially change the nature of the chemical processing industry. Various issues including flow distribution, instrumentation and process control needs to be addressed before such an assessment can be made.

Chapter 3

Poly-*L*-leucine Catalysed Asymmetric

Epoxidation of Chalcone Protocol

Selection

N.B. This chapter has formed the basis for a conference paper “Reaction System Selection for Poly-*L*-leucine Catalysed Asymmetric Epoxidation of Chalcone“ for the 1st International Congress on Green Process Engineering, Toulouse 2007.

3.1. Introduction

There are various reaction protocols available for the asymmetric epoxidation of α,β -unsaturated ketones using polyamino acids as catalyst. As part of the investigation into continuous processing for the fine chemicals and pharmaceutical sectors, an appropriate protocol to be used as a case study needs to be selected. In this work, the method used to rank and select the most appropriate protocol is outlined. Only protocols involving chalcone as substrate and poly-*L*-leucine based catalysts were considered. This was because chalcone was commonly used as test substrate in the study of the Julia-Colonna epoxidation and hence there was substantially more information available from literature. While several other types of polyamino acids have been shown to match or even surpass the catalytic performance of poly-*L*-leucine for the epoxidation of chalcone, poly-*L*-leucine based catalysts (instead of other polyamino acids) were selected due to the commercial availability of the catalyst.

The asymmetric epoxidation of chalcone using poly-*L*-leucine based catalysts can largely be grouped into six major reaction protocols. These represent reaction protocols which employ different forms of the catalyst, the base or the oxidant. Clearly, this is a great simplification; the vast amount of literature on the reaction system carried out by various researchers means that for each identified protocol, there may be slight differences in terms of the actual catalyst (e.g. different initiator used for polymerization of the catalyst) or solvent used. A list of the six protocols reported in literature is shown in Table 3.1.

Table 3.1: Six major reaction protocols identified for poly-*L*-leucine catalysed asymmetric epoxidation of chalcone

	Reaction protocol¹	References
Triphasic protocol	Gel-like poly- <i>L</i> -leucine catalysts with substrate in organic phase, aqueous peroxide as oxidant and aqueous NaOH as base.	Colonna et al, 1983 Banfi et al, 1984 Itsuno et al, 1990 Dhanda et al, 2000 Geller et al, 2004 Geller et al, 2006 Berkessel et al, 2001 Bentley et al, 1998 Takagi et al, 2000
Biphasic protocol	Paste-like poly- <i>L</i> -leucine in a suitable organic solvent using anhydrous peroxide such as urea hydrogen peroxide as oxidant and organic base such as DBU.	Bentley et al, 1997 Geller et al, 2004 Baars et al, 2003 Bentley et al, 2001
Mild protocol	Poly- <i>L</i> -leucine in a 50:50 DME/Water solvent using sodium percarbonate as both oxidant and base.	Allen et al, 1999
Biphasic PaaSiCats protocol	Similar to biphasic protocol but using silica-supported poly- <i>L</i> -leucine with improved physical properties.	Yi et al, 2005
Homogeneous protocol	Similar to biphasic protocol but using soluble PEG supported poly- <i>L</i> -leucine.	Flood et al, 2001 Tsogoeva et al, 2002 Takagi et al, 2000 Kelly et al, 2004 Caroff, 2002 Mathew, 2003 Mathew et al, 2005
Triphasic with PTC protocol	Similar to triphasic protocol but with addition of phase transfer catalyst such as tetrabutylammonium bromide.	Lopez-Pedrosa et al, 2004

¹ Catalyst preparation methods differ resulting in varying catalytic activity. For details of methods as well as other alternative oxidants and bases, please refer to the references.

3.2. Evaluation of Reaction Systems

A suitable reaction system was selected from each of the six available reaction protocols for further evaluation:

1. Original Julia-Colonna triphasic system
2. Biphasic system
3. Mild system
4. Biphasic PaaSicats system
5. Homogeneous system
6. Triphasic with phase transfer catalyst system

The details of these six systems are provided in Table 3.2 and illustrated in Figure 3.1.

The six systems were evaluated to select a suitable process for the case study which can potentially be used to develop an optimal process suitable for large-scale manufacturing.

The selected route should ideally be cost efficient as well as safe, ecologically sound and robust. A quantitative approach was taken to aid decision-making due to the largely qualitative nature of these factors. A cost evaluation of the different routes was carried out. Additionally, a scoring system for both safety and environmental effects was used to quantify the inherent safety and environmental hazard of the routes. A scoring system was also used to evaluate the scaleability of the different routes based on potential scale-up obstacles identified. The methods used are detailed in the following sections.

Table 3.2: Details of the six reaction systems identified as potential candidates for the case study

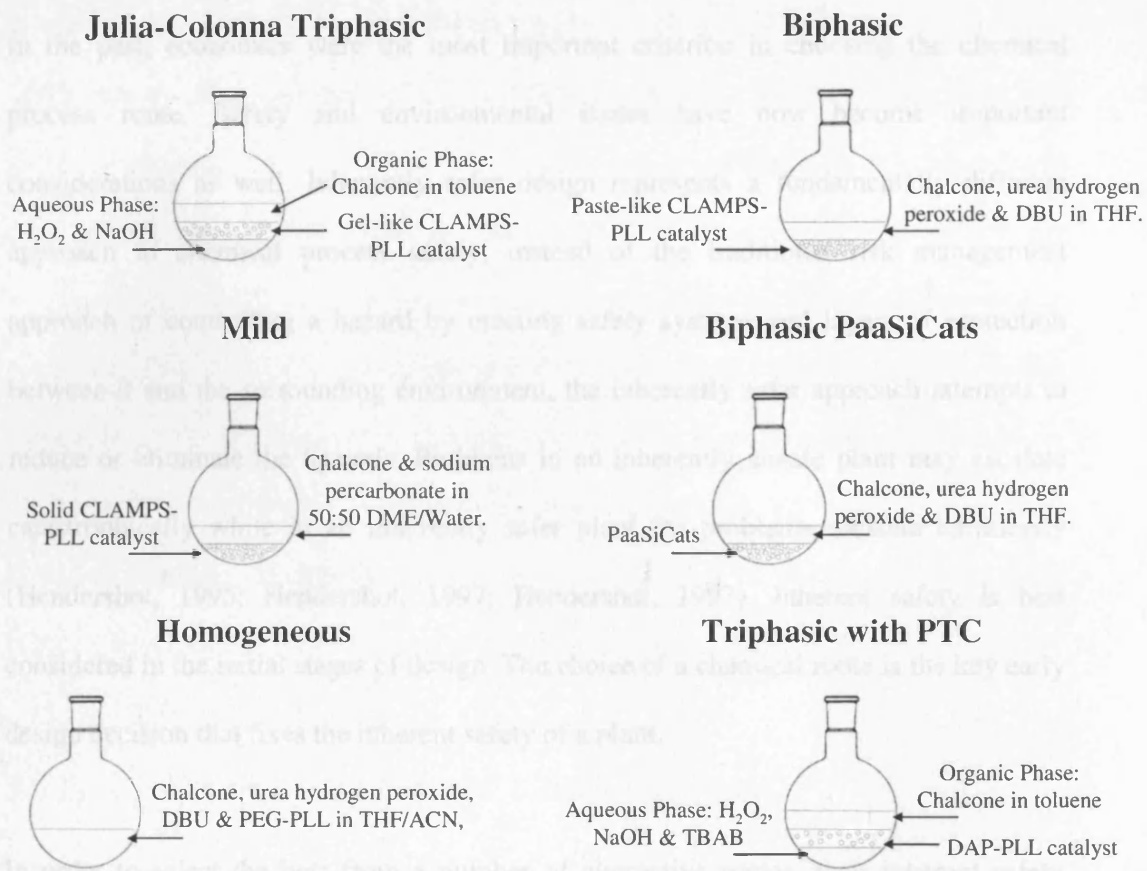
	Julia-Colonna Triphasic	Biphasic	Mild ²	Biphasic PaaSiCats ³	Homogeneous	Triphasic with PTC
Solvent	0.014 L Toluene	0.016 L THF	0.001 L DME 0.001 L Water	0.056 L THF	0.04 L THF 0.019 L ACN	0.016 L Toluene
Catalyst	0.8 g CLAMPS- PLL	2 g CLAMPS- PLL	2 g CLAMPS- PLL	8.65 g PaaSiCats	0.81 g PEG-PLL	2 g DAP-PLL
Oxidant	0.009 L H ₂ O ₂ (30 %)	1.2 mol equiv. NH ₂ CONH ₂ - H ₂ O ₂	1.5 mol equiv. Na ₂ CO ₃ ·1.5H ₂ O ₂	1.2 mol equiv. NH ₂ CONH ₂ - H ₂ O ₂	1.6 mol equiv. NH ₂ CONH ₂ - H ₂ O ₂	0.011 L H ₂ O ₂ (30 %)
Base	0.704 g NaOH	1.2 mol equiv. DBU	N/A	1.2 mol equiv. DBU	2.7 mol equiv. DBU	0.004 L NaOH
Phase transfer catalyst	N/A	N/A	N/A	N/A	N/A	0.11 mol equiv. Tetrabutylammonium bromide
Reaction type	Triphasic (Organic phase, gel-like catalyst and aqueous phase)	Biphasic (Organic phase and paste- like catalyst)	Biphasic (Miscible DME/Water and PLL catalyst)	Biphasic (Organic phase and granular solid catalyst)	Homogeneous	Triphasic (Organic phase, gel-like catalyst and aqueous phase)
Time (mins)	1080	30	30	30	16	7
Conversion (%)	90	90	95	95	87	99
Enantioselectivity (%)	95	95	95	95	95	94

1. All quantities are required amounts per gram of chalcone, unless stated otherwise.

2. 1.5 mol equivalents of Na₂CO₃·1.5H₂O₂ used as both oxidant and base.

3. Actual mass of poly-*L*-leucine used for PaaSiCats is ~ 1.97 g (6.68 g of Silica in 8.65 g of PaaSiCats)

Figure 3.1: Six reaction systems used in the case study



3.2.1. Cost Considerations

Selection of optimal route for scale-up is often driven by financial considerations. Cost estimates for production of 1 kg of required product were calculated for all six systems. Details of the calculations are provided in Appendix 3-1. For all routes considered the cost contribution of poly-*L*-leucine catalyst was found to be at least 96 %. It is therefore important to select the most economic route with high catalyst efficiency. The catalyst turnover is a measure of the efficiency of the catalyst and is defined here as,

$$\text{Catalyst turnover} = \frac{\text{Mass product}}{\text{Mass PLL} \cdot \text{time}} \quad [3.1]$$

3.2.2. Safety Considerations

In the past, economics were the most important criterion in choosing the chemical process route. Safety and environmental issues have now become important considerations as well. Inherently safer design represents a fundamentally different approach to chemical process safety; instead of the traditional risk management approach of controlling a hazard by erecting safety systems and layers of protection between it and the surrounding environment, the inherently safer approach attempts to reduce or eliminate the hazards. Problems in an inherently unsafe plant may escalate catastrophically while in an inherently safer plant the problems escalate harmlessly (Hendershot, 1995; Hendershot, 1997; Hendershot, 1997). Inherent safety is best considered in the initial stages of design. The choice of a chemical route is the key early design decision that fixes the inherent safety of a plant.

In order to select the best from a number of alternative routes, their inherent safety needs to be quantified. A method which has been developed as a tool to rank the inherent safety of routes was used to rank the various reaction systems (Edwards and Lawrence, 1993; Cave and Edwards, 1997). The inherent safety index is intended to aid decision-making at the route selection stage. As such, the index uses data that is available at the reaction selection stage, such as physical and chemical properties and expected process conditions that are available from laboratory or pilot plant developmental work. The following parameters were chosen for the scoring on the basis of the ready availability of data in the literature and at the initial stages of plant design: inventory, flammability, explosiveness, toxicity and yield.

Each reaction step in each route is given a score, which is the sum of the chemical score and the process score. The chemical score accounts for the properties of the chemicals involved in the step, in this case inventory, flammability, explosiveness and toxicity. The scores for all parameters are summed for each chemical present and the highest of these is taken as the chemical score. The process score accounts for the reaction conditions, that is the yield. Other process parameters such as temperature and pressure were not taken into account because all six reaction systems were conducted at ambient conditions. The total score for each step is the sum of the chemical and process scores for the step. The index for each reaction system is calculated by summing the scores obtained for each reaction step. All six reaction systems are essentially one-step processes therefore the sum of chemical and process scores for epoxidation is the score for the route. Details of the calculations are provided in Appendix 3-2.

3.2.3. Environmental Hazard Considerations

A method to quantify the environmental effects has also been developed () and was used to evaluate all six reaction systems for chalcone epoxidation. The environmental hazard index (EHI) is a dimensionless number, which indicates the potential environmental hazard of a route; the higher the EHI, the higher the hazard. The EHI estimates the maximum environmental harm which could be caused by a total loss of containment on a plant which implements the route, using only data about a route. This allows alternative chemical process routes to be ranked or screened if an acceptable threshold limit is set. The EHI is not location specific nor does it consider the circumstances leading to the release, as this information would probably not be known at the route selection stage. The EHI is not intended to be extremely accurate because at the route selection stage, not much data is available. The index is intended as a guide to allow the selection of routes based on environmental considerations.

The environmental hazard index is calculated by evaluating the damaging environmental effects of the chemical and the exposure (the quantity) of each chemical in the route. The environmental effect is represented by the specific environmental hazard index (SEHI), while the exposure of a chemical is the amount of the chemical available for release, which is the inventory of the chemical in the plant, Q . The EHI is based on the assumption that:

- The damage to the environment is proportional to the amount released.
- The damage due to a mixture is additive.

The EHI of a route is given by:

$$EHI = \sum_{i=1 \rightarrow n} Q_i \times SEHI_i, \quad \text{where } SEHI = SWHI + STHI \quad [3.2]$$

SEHI is calculated with reference to one tonne of the chemical and is defined as a function of the environmental concentration of a tonne of chemical i in the different environmental compartments and the toxicity of the chemical to the species present in the different environmental compartments. The SEHI is the sum of specific water hazard index (SWHI) and the specific terrestrial hazard index (STHI). SWHI represents the hazard to aquatic ecosystem associated with one tonne of a chemical released while STHI represents the hazard to the terrestrial ecosystem through food and water intake due to one tonne of the chemical released. Only the aquatic and terrestrial ecosystems were considered because in the event of a loss of containment, these are the ecosystems most affected. Both SWHI and STHI are based on three parameters, which are:

- Toxic effects: Toxicity of the chemical to the most sensitive species is taken to represent the ecosystem. Acute toxicity data such as LD_{50} and LC_{50} are used because they are more pertinent for a one-off loss of containment and because of the wider availability of data.

- Time period: Time basis is taken as 4 days due to better availability of data.
- Chemical distribution: Distribution of a chemical in the different environmental compartments is required in order to assess the effect of chemical toxicity upon the ecosystem. The predicted environmental concentrations (PEC) were calculated using Mackay's fugacity model (Mackay and Paterson, 1981) which gives the equilibrium concentration of a chemical in the different environmental compartments.

SWHI is calculated with reference to the aquatic organism with the lowest toxicity value and is given by:

$$SWHI_i = \frac{PEC_{wi} \times 10^6}{LC_{50_i}} \quad [3.3]$$

STHI is calculated for each terrestrial species for which LD₅₀ data is available. The most sensitive species is taken to represent the ecosystem. STHI is given by:

$$STHI = d \frac{[(TDI_{wx} PEC_{wi}) + (TDI_{fx} PEC_{si})]}{LD_{50_{si}} Wt_x} \times 10^9 \quad [3.4]$$

where,

LC₅₀ is the concentration of chemical *i* in water which kills 50% of a test population of the most sensitive species over a 96 hour period (mg/dm³),

LD₅₀ is the lethal dose of chemical *i* that kills 50% of the test population of species *x* (mg/kg),

PEC_{si} and PEC_{wi} are the predicted environmental concentration of chemical *i* in the soil and water respectively,

TDI_{fx} and TDI_{wx} are the total daily food and water intake of species *x* respectively (m³/day) and

Wt_x is the weight of species *x* (kg).

Details of these calculations are provided in Appendix 3-3.

3.2.4. Potential Scale Up Obstacles

Many processes suffer from a fall in reaction performance on scale up; this is due to the fact that chemical rate constants are scale independent while physical parameters and phenomena are scale-dependent (Caygill et al, 2006). Early identification of potential scale up obstacles allows for the selection of a potentially least problematic route for scale up as well as generation of possible alternatives to bypass these obstacles. All six reaction systems were screened for potential obstacles to scale-up based on available knowledge of each system (e.g. reaction time, side reactions etc).

3.3. Results and Discussion

3.3.1. Cost Evaluation

Figure 3.2 shows the relative cost and relative turnover values for all six systems which were computed by dividing the absolute values with the lowest value obtained. A relative value of 1 therefore represents the lowest cost and lowest catalyst turnover. The original Julia-Colonna triphasic system was found to be the most cost effective, with the lowest cost per kg product; however, the system was also found to have the lowest catalyst turnover values, which can be explained by the long reaction times employed. The Homogeneous system and Triphasic with phase transfer catalyst reaction systems were both found to be cost effective and efficient with two of the highest catalyst turnover values. The three other routes, which give reasonable catalyst efficiency, are the Biphasic, Mild and Biphasic PaaSiCats systems.

3.3.2. Safety and Environmental Effects

The safety and environmental scores for each route were computed and the scores were then divided by the lowest calculated score to obtain the relative safety and environmental scores. A relative score of 1 therefore represents the highest performance. From Figure 3.3, comparison of the safety scores shows that both the Mild system and Triphasic with phase transfer catalyst have the lowest score followed closely by the Original Julia-Colonna triphasic system. The Biphasic, Biphasic PaaSiCats and Homogeneous systems gave the higher safety scores mainly because of the use of THF as solvent, which is a volatile solvent, with a flash point of – 21.5°C (Source: Merck MSDS). While the Biphasic route also uses THF, it has a lower relative score of 1.2 due to its lower solvent inventory.

Comparison of the environmental scores shows that the Biphasic and Mild systems have the lowest scores. The environmental score for the Biphasic system can be attributed to both the lower specific environmental hazard index (SEHI) of THF and the lower solvent inventory compared to the other systems which also employ THF. Similarly, the Mild system has a lower environmental score due to its low solvent inventory, even though the SEHI of DME was the highest among all three solvents. This is followed closely by both the Triphasic with phase transfer catalyst and the Original Julia-Colonna triphasic system; this is attributed to the fact that both systems employ Toluene which has an intermediate SEHI value, as solvent, with a relatively low inventory. Biphasic PaaSiCats and Homogeneous systems scored the highest relative environmental scores. The main reason for the higher score is the significantly higher solvent inventory for these two reaction systems compared to the other systems.

Figure 3.2: Comparison of relative cost and catalyst turnover among the six reaction protocols, as identified below.

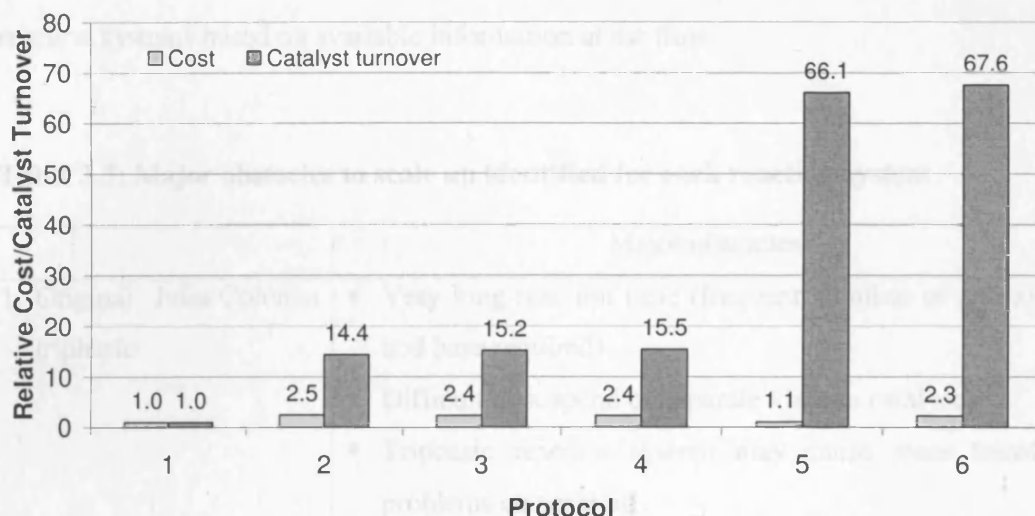
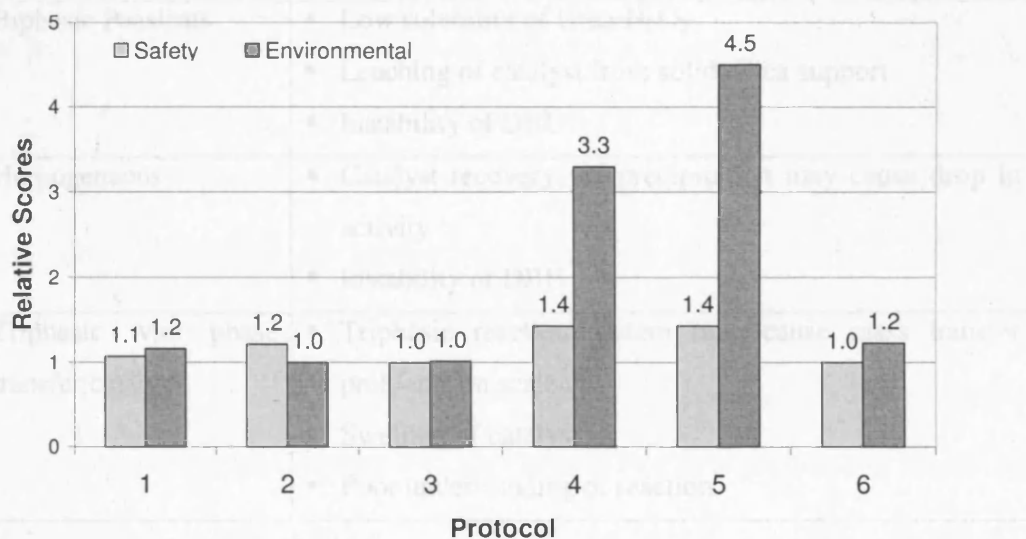


Figure 3.3: Comparison of relative safety and environmental scores among the six reaction protocols, as identified below.



1. Original Julia-Colonna triphasic system
2. Biphasic system
3. Mild system
4. Biphasic Paasicats system
5. Homogeneous system
6. Triphasic with phase transfer catalyst system

3.3.3. Potential Scale Up Obstacles

Table 3.3 details the major potential scale up obstacles identified for each of the six reaction systems based on available information at the time.

Table 3.3: Major obstacles to scale up identified for each reaction system

	Major obstacles
1. Original Julia-Colonna triphasic	<ul style="list-style-type: none"> ▪ Very long reaction time (frequent addition of peroxide and base required) ▪ Difficult to suspend or separate viscous catalyst ▪ Triphasic reaction system may cause mass transfer problems on scale up
2. Biphasic	<ul style="list-style-type: none"> ▪ Difficult to suspend or separate viscous catalyst ▪ Low solubility of Urea-H₂O₂ ▪ Instability of DBU
3. Mild	<ul style="list-style-type: none"> ▪ Teratogenic effects of DME
4. Biphasic Paasicats	<ul style="list-style-type: none"> ▪ Low solubility of Urea-H₂O₂ ▪ Leaching of catalyst from solid silica support ▪ Instability of DBU
5. Homogeneous	<ul style="list-style-type: none"> ▪ Catalyst recovery via precipitation may cause drop in activity ▪ Instability of DBU
6. Triphasic with phase transfer catalyst	<ul style="list-style-type: none"> ▪ Triphasic reaction system may cause mass transfer problems on scale up ▪ Swelling of catalyst ▪ Poor understanding of reaction

3.4. Conclusion

The six reaction systems are listed again below and the logic for selecting a suitable reaction system for the case study follows.

1. Original Julia-Colonna triphasic system
2. Biphasic system
3. Mild system
4. Biphasic Paasicats system
5. Homogeneous system
6. Triphasic with phase transfer catalyst system

The most economically feasible reaction systems are the ones with lowest cost and highest catalyst turnover. The systems with the lowest catalyst efficiency and highest cost can be ruled out leaving reaction systems 3, 4, 5 and 6 which were relatively indistinguishable in terms of cost, although it is clear that systems 5 and 6 have superior catalyst efficiency.

From the evaluation of obstacles to scale-up, system 3 is ruled out due to the teratogenic effects of the solvent in reaction system 3 making it unsuitable for large-scale manufacturing. A comparison of the safety scores of reaction systems 4, 5 and 6 with all other systems shows that the safety scores for these reaction systems are quite favourable, with only a slightly higher score compared to the lowest score available. The main reason for the higher scores for routes 4 and 5 is the use of THF as solvent. As a general rule of thumb, solvents with flash point above 18°C are avoided, but this is not expected to be a major issue, as THF is a very commonly used solvent. Comparison of the environmental scores again indicates higher scores for Routes 4 and 5. However, the higher scores are predominantly due to higher solvent inventory; moreover a comparison of actual scores indicates the difference in environmental scores of the six reaction systems is very small.

By comparing the results of the evaluations of cost, safety, environmental and potential obstacles to scale-up and keeping in mind the relative importance of each aspect, it is clear that the Homogeneous system offers the most cost effective performance while the Triphasic with phase transfer catalyst system offers the best performance in terms of safety and environmental hazards. However, at the time of making the selection decision, not much information was available about the Triphasic with phase transfer catalyst system; additionally, kinetic data was available for the Homogeneous system, tipping the balance heavily in favour of the Homogeneous system. The other feasible alternative is the Biphasic PaaSiCats system, as no major obstacles to scale-up can be envisaged. The use of Toluene and THF as solvents for these systems have the advantage of being easily recyclable, allowing for the possibility of reduction in waste solvents generated.

Chapter 4

Batch and Continuous Small Scale

Reaction Systems

N.B. This chapter has formed the basis for the paper “Batch versus continuous mg-scale synthesis of chalcone epoxide with soluble polyethylene glycol poly-l-leucine catalyst “,
Journal of Molecular Catalysis A: Chemical, Vol 263, Issue 1 - 2, 2007.

4.1. Introduction

Batch reactors have been the dominant workhorse in the pharmaceutical and fine chemicals industry for decades, due to their flexibility and versatility for cost-effective manufacture of small quantities of chemicals with short product life-times. This is in contrast to the bulk chemicals industry where dedicated continuous plants find widespread application as they offer the potential for lower manufacturing costs, improved safety, reduced variation in product quality (due to better control of reaction conditions) and reduction in down-time from batch to batch processing or plant reconfiguration. The increasing competitiveness in the pharmaceutical industry has intensified the search for more efficient and economical production processes. This, coupled with recent developments in microreaction technology has fuelled interest in continuous processing (de Mello and Wootton, 2002; Thomas, 2003; Boswell, 2004; Schwalbe et al, 2005; Roberge et al, 2005).

Microreactors typically have sub millimeter characteristic dimensions and hold-up volumes in the micro liter range. The high surface to volume ratio in such a miniaturized system facilitates intensified heat and mass transfer and precise control of operating conditions, expanding the range of chemistries resulting in better yield and selectivity. Microreaction technology could potentially revolutionize the pharmaceutical industry as it combines the benefits of continuous processing with some of the flexibility required by the industry. Additionally, it also allows for potential savings in R&D costs and time, by rapid scale-up via numbering up.

In recent years, various types of reactions have been tested in microreactors which exploit the benefits offered by microreaction technology to enhance performance. A substantial number of these relate to liquid phase organic synthesis, demonstrating the growing interest to exploit microreactors for fine chemicals production (Fletcher et al, 2002; Haswell and Watts, 2003; Feng et al, 2004; Wakami and Yoshida, 2005; Hessel and Lowe, 2005; Watts and Haswell, 2005). In this work, the poly-*L*-leucine catalysed epoxidation of chalcone reaction is investigated. It allows access to highly enantioselective chalcone epoxides that are reactive intermediates used in the pharmaceutical industry (Adger et al, 1997; Bentley et al, 1997; Bentley et al, 1998; Cappi et al, 1998; Carde et al, 1999; Porter et al, 1999; Porter and Skidmore, 2000; Bentley et al, 2001; Lauret and Roberts, 2002; Carrea et al, 2004; Kelly and Roberts, 2004; Carrea et al, 2004; Carrea et al, 2004).

The use of poly-*L*-leucine as a catalyst for epoxidation of chalcone was first reported by Julia and Colonna in 1980, in a triphasic reaction system with the chalcone substrate in a water-immiscible organic solvent such as hexane or toluene, aqueous sodium hydroxide containing hydrogen peroxide as oxidant and base and the insoluble gel-like polyamino acid as catalyst (Julia et al, 1980; Julia et al, 1982; Colonna et al, 1983; Banfi et al, 1984). However, this system did not gain widespread popularity because of the lengthy reaction time and difficulty in recovering the gel-like catalyst. Later, a nonaqueous biphasic system was reported, in which the aqueous sodium hydroxide and hydrogen peroxide were replaced with organic base and anhydrous urea-hydrogen peroxide. This improved reaction times to around 30 minutes but the paste-like form of the catalyst remained difficult to handle (Bentley et al, 1997). A “mild” biphasic system employing sodium percarbonate as both oxidant and base was also reported

which diminishes the background epoxidation, resulting in improved enantioselectivity (Allen et al, 1999). Immobilisation of the solid catalyst on silica (Geller and Roberts, 1999; Dhanda et al, 2000) improved physical properties for handling, while tethering the catalyst to polyethylene-glycol allowed for the employment of homogeneous reaction conditions (Flood et al, 2001; Kelly et al, 2004). More recently, a modified triphasic procedure has been reported, in which addition of a phase transfer catalyst in the original triphasic procedure improved reaction rates rapidly (Geller et al, 2004; Geller et al, 2004).

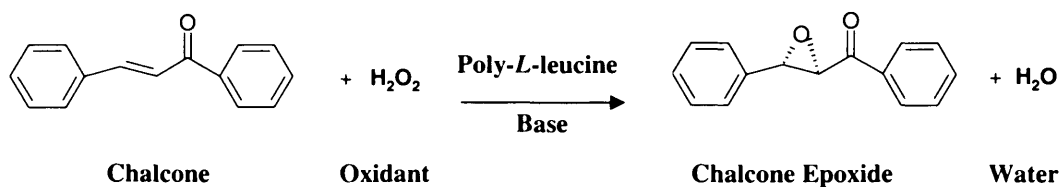
From all the above reaction systems, the one selected is the polyethylene glycol-poly-*L*-leucine catalysed asymmetric epoxidation of chalcone, a liquid phase reaction in a mixed tetrahydrofuran (THF) and acetonitrile (ACN) solvent with urea-hydrogen peroxide as oxidant and 1,8-diazabicyclo[5.4.0]undec-7-ene (DBU) as base to deprotonate the oxidant as depicted in Scheme 4.1. The reaction is strongly affected by the choice of solvent used. Acetonitrile was found to enhance the background reaction while THF appears to prevent the background reaction (Caroff, 2002). A THF:ACN ratio of 2.15 was selected for the reaction system to allow for comparisons of our experimental results with those from earlier kinetic studies which were carried out in a THF:ACN ratio of 2.15 (Mathew, 2003). Experimental results from these kinetic studies indicate a conversion of 87 % and enantioselectivity of > 95 % in 16 minutes at 23.1°C and at base case initial concentrations as shown in Table 4.1.

Table 4.1: Base case initial concentrations of reactants

PLL	13.47	g/l
Peroxide	0.132	mol/l
Chalcone	0.0802	mol/l
DBU	0.22	mol/l

All the reactants are completely soluble in mixed THF/ACN, except for urea-hydrogen peroxide which leaves behind an insoluble solid, after the hydrogen peroxide is extracted with organic solvent (Mathew, 2003).

Scheme 4.1



This chapter describes the transfer of the reaction from a batch to continuous mode. For this purpose, batch and continuous experimental studies were carried out to help establish a protocol for a continuous system with similar performance characteristics as the batch process.

4.2. Experimental

4.2.1. Analytical Conditions

Chiral HPLC analyses were performed on a Jasco liquid chromatograph equipped with the chiral column Chiraldapak® AD (VWR International). The mobile phase was 10% ethanol in hexane. The flowrate was set at 1.0 ml/min and the UV detector at 254 nm. The oven temperature was set at 10°C and the sample was injected manually with a Rheodyne 7725i injection valve.

4.2.2. Determination of Peroxide Concentration

The peroxide concentration was determined using the procedure by Gonsalves et al (1991). Each 0.5 ml aliquot was treated with 15 ml glacial acetic acid and 5 ml saturated potassium iodide solution and left in the dark for approximately 10 minutes. The resulting solution was then titrated against 0.1 M sodium thiosulphate until a light yellow solution was obtained. A drop of starch solution was then added and the titration with 0.1 M sodium thiosulphate continued until a clear solution was obtained. All the chemicals were obtained from Sigma-Aldrich. The concentration of H_2O_2 was determined from this titration value based on the stoichiometric equations below:



4.2.3. Batch Experimental Procedure

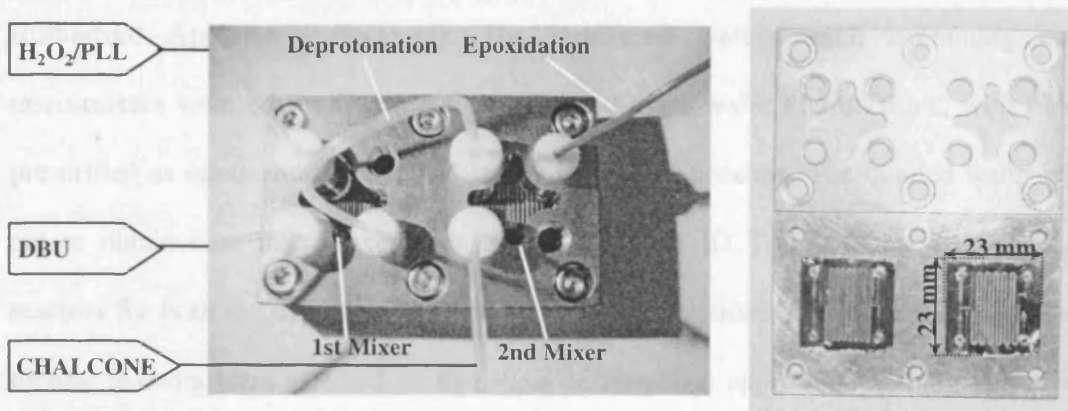
A batch of mixed solvents was prepared keeping the THF:ACN ratio at 2.15 v/v. A solution of hydrogen peroxide was prepared by stirring 3 g of urea-hydrogen peroxide (Lancaster Synthesis) in 20 ml of mixed THF/ACN for approximately 1 hour. The mixture was then filtered to remove the undissolved solids and the clear solution was used in the reaction. This solution was titrated regularly and its concentration remained around 1 M. A 3.0 mol/l chalcone solution (Lancaster Synthesis) was also prepared. For every batch reaction, approximately 0.42 g of PEG-poly-*L*-leucine catalyst (Lancaster Synthesis) was used. The catalyst was dissolved in mixed THF/ACN and the peroxide and DBU (Lancaster Synthesis) solutions were then added to this. The mixture was stirred for approximately 30 minutes and the reaction was initiated by adding the chalcone solution. The reactor is maintained at 30 °C by placing it in a water bath. After

16 minutes, a reaction sample was taken and quenched with saturated aqueous sodium sulphite solution (Sigma-Aldrich). The organic phase was diluted with ether, evaporated to dryness and the residue redissolved in 10% v/v ethanol in hexane for HPLC analysis.

4.2.4. Continuous Experimental Procedure

An XP 3000 Modular Digital Pump (Cavro) with three 50- μ l syringes was used to pump solutions of chalcone, peroxide and catalyst with DBU. Three solutions were prepared: a 0.16 mol/l chalcone solution, a 0.53 mol/l peroxide solution and a PLL/DBU solution of 53.88 g/l PLL and 0.88 mol/l DBU. Two micromixer chips were used to bring the reagents into contact. They are shown in Figure 4.1 and consist of a 100 μ m T-type micromixer channel (first section) followed by a larger serpentine delay loop channel (second section), dimensions of which are given in Table 4.2. The experimental setup used is shown in Figure 4.2.

Peroxide and PLL/DBU flows of 5 μ l/min each joined in the first micromixer chip and entered a 0.3 ml Teflon tubular reactor with 30 minutes residence time. Subsequently, a 10 μ l/min chalcone flow joined the combined streams in the second micromixer and entered a 0.32 ml Teflon tubular reactor with a total residence time of 16 minutes. The micromixers and Teflon tubular reactor were maintained at a temperature of 30°C by placing them in a water bath. The reaction was quenched at the reactor outlet by collecting the outlet flow in a stirred vial containing sodium sulphite as quench.

Figure 4.1: Assembled continuous flow reactor and mixing chips used in this work**Figure 4.2: Experimental setup for continuous epoxidation experiments****Table 4.2: Channel dimensions of the mixing chips**

Dimensions	First Chip		Second Chip	
	1 st section	2 nd section	1 st section	2 nd section
Width (μm)	100	300	100	600
Depth (μm)	300	300	300	300
Length (mm)	~20	~288	~20	~198

The microreactor chips were fabricated by photolithography and deep reactive ion etching (DRIE) on 4" silicon wafers at the Central Microstructure Facility (CMF, Rutherford Appleton Laboratory). The structured wafers, each containing nine micromixers were covered with a Corning 7740 glass wafer (1 mm thick, with holes pre-drilled as inlets and outlets) and sealed by anodic bonding. The bonded wafer was cut to obtain nine micromixers per wafer. 0.75 mm ID Teflon tubes were used as reactors for both the deprotonation and epoxidation reactions. The dimensions of these tubular reactors were selected so that their performance approximated plug flow. For plug flow to be applicable the following criteria must be met (Raja et al, 2000):

$$\frac{d}{L} \ll \text{Re}_d \text{Sc} \ll \frac{L}{d} \quad [4.3]$$

For a 0.75 mm ID tube the length required for a 0.32 ml reactor volume is 0.724 m. In this case $\text{Re}_d \text{Sc} = 78.4$ based on chalcone molecular diffusivity of $7.22 \times 10^{-9} \text{ m}^2/\text{s}$, while the values of $\frac{d}{L}$ and $\frac{L}{d}$ are 0.001 and 966 respectively. Wilke and Chang correlations were used to estimate the binary diffusivity of chalcone in pure THF and pure acetonitrile while the method of Tang and Himmelblau was used to estimate diffusivity in a pair of mixed solvents (Perry and Green, 1997). The calculations to estimate the diffusivity values are shown in Appendix 4-1.

4.3. Batch Experiments

4.3.1. Effect of Solvent Premixing

The batch reaction was initially carried out by first extracting the urea-hydrogen peroxide into pure acetonitrile. This was then pre-stirred with the DBU and poly-*L*-leucine catalyst in THF for 30 minutes for deprotonation and the reaction was initiated by adding a solution of chalcone dissolved in THF, taking care to ensure that the THF to acetonitrile ratio was always maintained at 2.15 (Mathew, 2003). This protocol gave a conversion of 96.0 % (\pm 1.2 %)¹ and enantioselectivity of 90.2 % (\pm 1.1 %) at 30°C and 16 minutes reaction time.

Two main problems were apparent with this initial batch procedure. Extraction of hydrogen peroxide from urea-hydrogen peroxide using pure acetonitrile (while using pure THF for all other reactants) limited the maximum peroxide concentration to 0.132 mol/l, due to the need to maintain the THF: ACN ratio at 2.15. This ruled out the possibility of further optimising the reaction for improved yields and production rate. Additionally, this also resulted in formation of a white precipitate on addition of hydrogen peroxide in acetonitrile solution to the reaction mixture in THF (Mathew, 2003).

A new reaction protocol was devised in which a large batch of mixed THF and acetonitrile was prepared with a THF: ACN ratio of 2.15. This batch of mixed solvent was then used to prepare all reagent solutions as well as for extracting urea-hydrogen peroxide, therefore allowing a larger range of peroxide concentrations to be used while

¹ These are values of the standard deviation, as a measure of the reproducibility of the experiments.

also avoiding formation of precipitate, which could potentially cause clogging of continuous equipment. In the early stages of setting up the experiments, the existing water bath in the lab was only capable of operating at temperatures above ambient conditions (heating only). For this reason, to ensure isothermal conditions, the experiments were carried out at a temperature of 30°C which allows for a reasonably fast rate while avoiding potentially damaging operating conditions to catalyst lifetime (the catalyst is a polypeptide, which denatures at high temperatures).

A base case batch experiment using the modified procedure with premixed THF and ACN at 30°C, with prestir (deprotonation) time of 30 minutes resulted in a conversion of 94.9 % ($\pm 2.6 \%$) and enantiomeric excess of 90.3 % ($\pm 0.5 \%$) in 16 minutes, close to those obtained with the initial procedure, without formation of white precipitate, hence making the reaction feasible for continuous processing. The current procedure allows scope for further optimising the reaction in a single continuous unit prior to numbering up, as we are now able to increase the peroxide concentration to higher levels.

4.3.2. Effect of Deprotonation Time

The first step of the reaction involves a pre-reaction equilibrium. The concentration of the reactive species, which is the peroxy anion, is determined by the chemical equilibrium process:



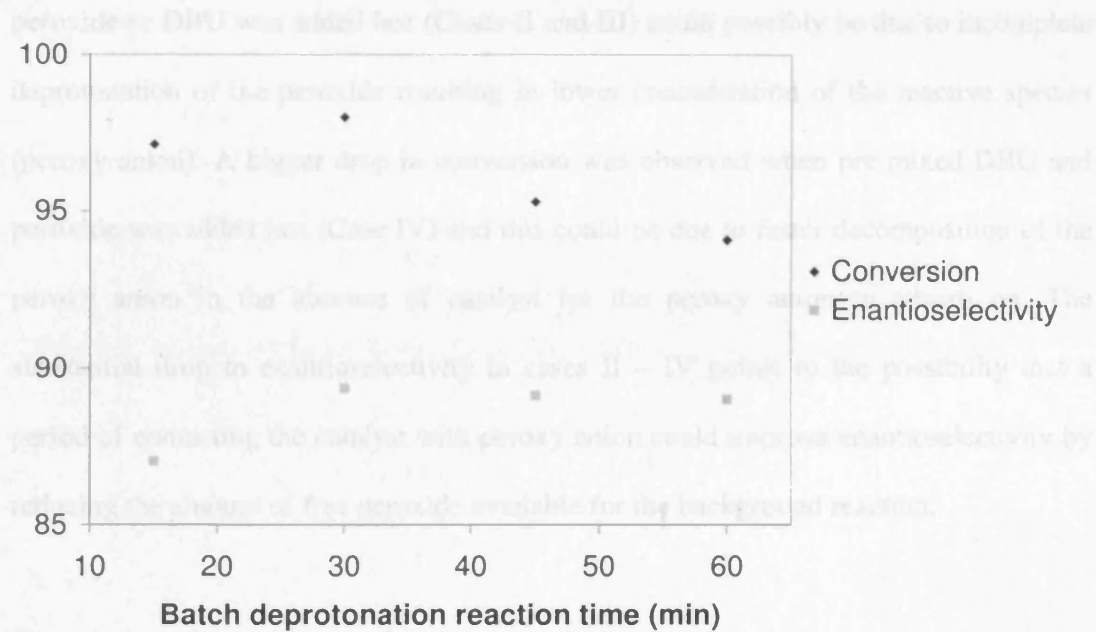
It was estimated that near complete deprotonation was achieved with the peroxide and DBU concentrations used, with final peroxy anion concentrations in excess of the stoichiometric requirements ($pK_a H_2O_2 = 11.75$, $pK_a DBU = 12$) (Carrea et al, 2004).

However, data on the rate at which the equilibrium concentration is reached was not available. A further complication exists, as hydrogen peroxide is prone to decomposition under basic conditions. To ensure that the initial concentration of the reactive species is constant, the effect of varying deprotonation reaction time was examined. The batch experiments were carried out with varying deprotonation reaction time, from 15 minutes to 60 minutes, to check for the optimum deprotonation reaction time.

From Figure 4.3, the conversion was observed to be highest at a deprotonation time of 30 minutes, and drops when the deprotonation time was increased further. The enantioselectivity however, increases to about 89 % after 30 minutes, and remains fairly constant even when the deprotonation time was increased further. The difference may be due to different initial peroxy anion concentrations; at lower deprotonation time, deprotonation reaction is incomplete resulting in lower peroxy anion concentration, while at longer deprotonation time, deprotonation reaction is complete but peroxy anion starts to decompose due to the alkaline reaction conditions.

The improvement in enantioselectivity from 15 minutes to 30 minutes and subsequent stabilisation after 30 minutes point to the possibility that a period of stirring the catalyst and peroxide prior to start of reaction may lead to improved enantioselectivity as it allows the peroxy anion to adsorb on the catalyst, reducing the amount of free peroxide available for the background reaction. However, the improvement of around 2 % is probably not significant enough for such a conclusion to be drawn.

Figure 4.3: Conversion and enantioselectivity of the chalcone epoxidation as a function of deprotonation time (conditions: base case with premixed THF/ACN at 30°C)



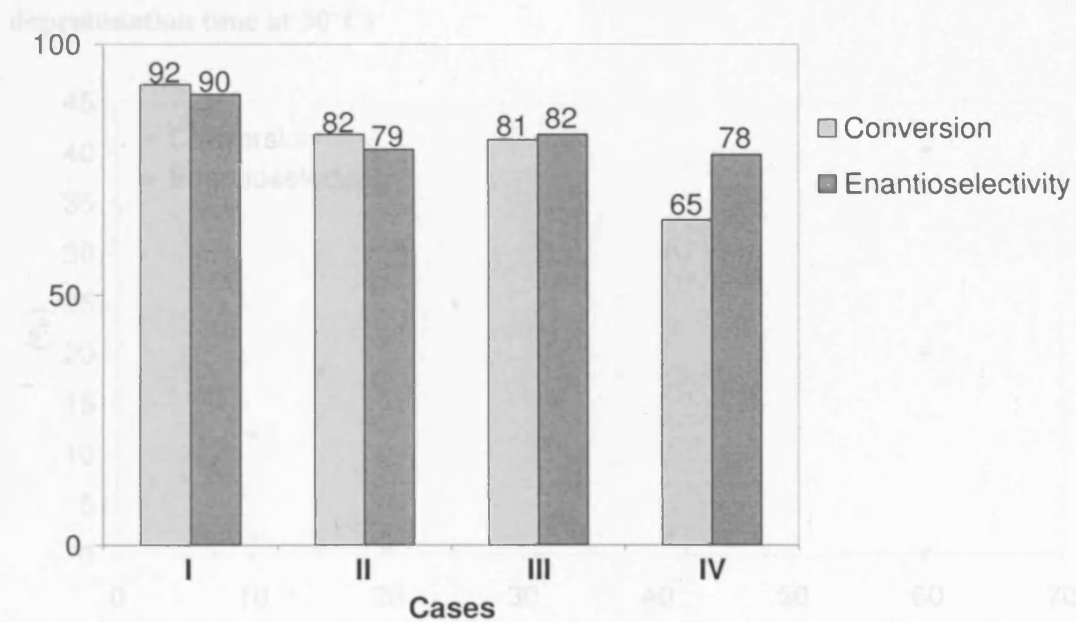
4.3.3. Effect of Reactant Addition Sequence

The effect of the order of reactant addition on the reaction performance was also investigated. The following cases were examined:

- I. Catalyst, peroxide and DBU pre-stirred for 30 minutes followed by addition of chalcone solution to start the reaction.
- II. Catalyst, chalcone and DBU pre-stirred for 30 minutes followed by addition of peroxide solution to start the reaction.
- III. Catalyst, chalcone and peroxide pre-stirred for 30 minutes followed by addition of DBU to start the reaction.
- IV. Catalyst solution pre-stirred with chalcone for 30 minutes. The peroxide solution was simultaneously pre-stirred with DBU, for 30 minutes. The two solutions were then mixed to start the reaction.

The results show a significant change in conversion and enantioselectivity when the sequence of reactant addition was varied (see Figure 4.4). The drop in conversion when peroxide or DBU was added last (Cases II and III) could possibly be due to incomplete deprotonation of the peroxide resulting in lower concentration of the reactive species (peroxy anion). A bigger drop in conversion was observed when pre-mixed DBU and peroxide was added last (Case IV) and this could be due to faster decomposition of the peroxy anion in the absence of catalyst for the peroxy anion to adsorb on. The substantial drop in enantioselectivity in cases II – IV points to the possibility that a period of contacting the catalyst with peroxy anion could improve enantioselectivity by reducing the amount of free peroxide available for the background reaction.

Figure 4.4: Conversion and enantioselectivity of the chalcone epoxidation for various reactant addition sequences. For details see text. (Conditions: with premixed THF/ACN, 30 minutes pre-stir prior to epoxidation reaction at 30°C)



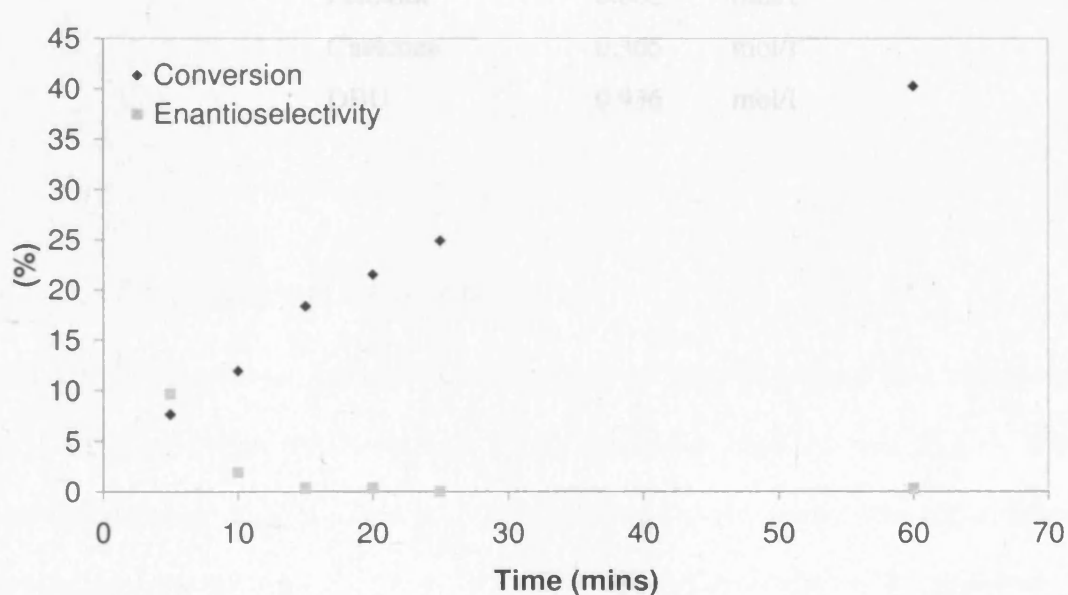
4.3.4. Background Reaction

The background reaction refers to the rate of the epoxidation reaction in the absence of poly-*L*-leucine catalyst. The rate of background reaction was examined at base case conditions in the absence of the catalyst with a 30 minutes deprotonation time before chalcone is added to start the reaction. The conversion of chalcone after 16 minutes was approximately 19 % (see Figure 4.5).

Table 4.3: Initial concentrations of reactants at background base conditions

Peroxide	0.0791	mol/l
Chalcone	0.0763	mol/l
DBU	0.21	mol/l

Figure 4.5: Conversion and enantioselectivity for chalcone epoxidation in the absence of catalyst (Conditions: premixed THF/ACN with 30 minutes deprotonation time at 30°C)



4.3.5. Effect of Higher Concentrations

With the original procedure i.e. extraction of peroxide using pure acetonitrile and then mixing this with other reactants dissolved in pure THF, the peroxide concentration was limited to a maximum value of 0.132 mol/l. However, with the new reaction procedure, where a large batch of mixed solvents at a THF: ACN ratio of 2.15 is prepared beforehand and all reactants dissolved with this solvent, a higher peroxide concentration can be used in the reaction. This is an attractive feature since it allows the reaction to be intensified, if the concentrations of all reagents (which were previously limited by the available peroxide concentration) could be increased while keeping the relative quantities of each reagent constant. A batch experiment was carried out at around 6 times base case concentrations as shown in Table 4.4. Conversion was nearly complete (98.2 % \pm 2.1 %) within 5 minutes, with enantioselectivity of around 83.9 % (\pm 0.2 %).

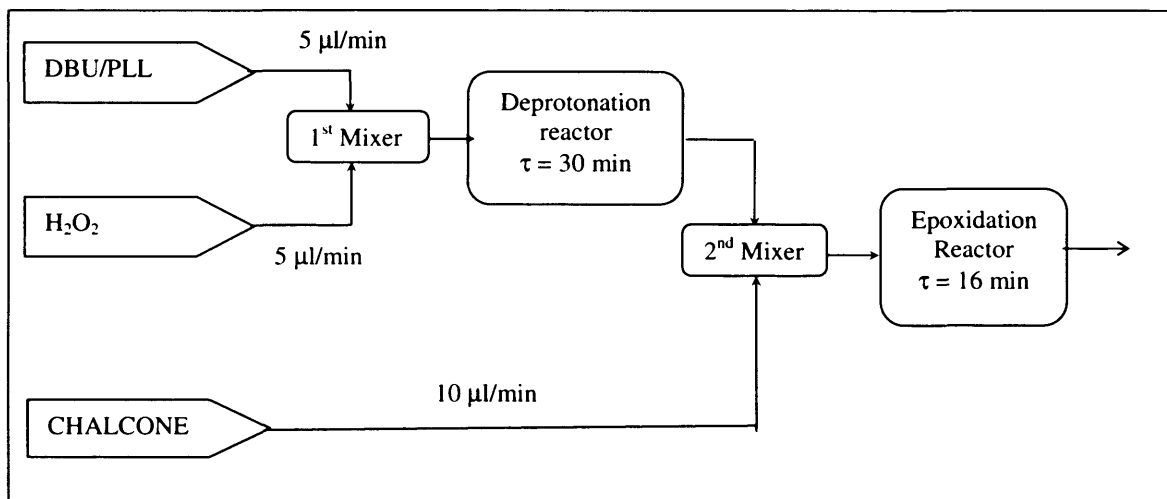
Table 4.4: Initial concentrations of reactants used at 6 x base case concentrations

PLL	60.73	g/l
Peroxide	0.602	mol/l
Chalcone	0.365	mol/l
DBU	0.936	mol/l

4.4. Continuous Experiments

Having established the reaction protocol from the batch runs, the reaction was then performed in a continuous setup (see Figure 4.6) at inlet reactor concentrations at base case conditions (see Table 4.1). Based on the results obtained from the batch reaction experiments, the continuous system was designed so that peroxide, poly-*L*-leucine catalyst and DBU were mixed first before entering the deprotonation tubular reactor with 30 minutes residence time. At the exit of the deprotonation reactor, the mixture was subsequently mixed with chalcone solution to start the reaction before entering the epoxidation reactor.

Figure 4.6: Flow diagram of continuous experimental setup



4.4.1. Background Reaction

Blank experimental runs i.e. epoxidation reaction without the catalyst were carried out in a 0.32 ml Teflon tubular reactor. The conversion obtained was 28.4 % with enantioselectivity of 0 %. This is comparable with results from batch experiments, where the conversion obtained was 19 %. The higher conversion can be attributed to longer residence time in the continuous setup due to presence of dead volumes.

4.4.2. Catalysed Reaction

The conversion and enantioselectivity obtained for the continuous reaction system were 73.6 % and 83.1 % respectively, much lower than those obtained from the batch system. This was thought to be due to incomplete mixing as the length required for complete mixing of the substrates was calculated earlier based on diffusivity values for chalcone. Given the polymeric nature of the PEG-poly-*L*-Leucine catalyst, it is expected that the diffusivities could be significantly lower than that for chalcone. The average molecular weight of the PEG-poly-*L*-Leucine was assumed to be around 7000 (average molecular weight of PEG is 5000, while the poly-*L*-Leucine chain was assumed to contain 15 Leucine monomers) (Caroff, 2002). An empirical equation for estimating diffusivity of a polymeric solution is given by Sherwood et al (1975) :

$$D(\text{cm}^2/\text{s}) = 2.74 \times 10^{-5} (\text{MolecularWeight})^{-\frac{1}{3}} \quad [4.5]$$

Using this equation and for an average molecular weight of 7000, the molecular diffusivity of PEG-poly-*L*-leucine can be estimated to be $1.432 \times 10^{-10} \text{ m}^2/\text{s}$. This is a reasonable estimate as the diffusivity of polyethylene glycol with an average molecular weight of 15500 was reported by Brandrup et al (1967) as $6 - 8 \times 10^{-11} \text{ m}^2/\text{s}$. The Fourier Number is defined as

$$Fo = \frac{D_{ab}t}{d_c^2} \quad [4.6]$$

For substantial to complete mixing, the Fourier number should be in the range ($0.1 < Fo < 1$) (Gobby et al, 2001). The mixing length can be calculated by multiplying the average velocity with the mixing time. The length, L for complete mixing (at $Fo = 1$) can be obtained from:

$$L_{Mix} = \frac{Fo \cdot d_c^2 \cdot \bar{u}}{D_{ab}} \quad [4.7]$$

The mixing lengths were recalculated for the first and second mixing chips, and were found to be inadequate. For a characteristic dimension, $d_c=100 \mu\text{m}$, the required mixing lengths for the first and second chips are 388 mm and 776 mm respectively. If the larger channel dimensions (in the second section) of the two chips are taken as characteristic length, this results in an even larger mixing length. In comparison, the required mixing lengths calculated based on chalcone diffusivity are 7.7 mm and 15.4 mm for the first and second micromixing chips respectively (see Table 4.5) well within the available mixing length. This indicates that all other reagents except poly-*L*-leucine are well mixed (chalcone is expected to have lower molecular diffusivity compared to the other reagents due to its larger molecular size).

Table 4.5: Calculated required mixing lengths in the first and second micromixing chips based on poly-*L*-leucine and chalcone diffusivities

	Molecular Diffusivity (m^2/s)	Mixing length at $\text{Fo} = 1$ (mm)	
		First micromixer	Second micromixer
Chalcone	7.219×10^{-9}	7.7	15.4
Poly- <i>L</i> -leucine	1.432×10^{-10}	388	776

As the calculations indicate insufficient mixing, an experimental run using IMM Standard Slit Interdigital Micromixers was carried out. The two inlet feed streams come into contact in the interdigital mixing element, creating a multi-laminated outlet flow with characteristic lamellae dimensions of $40 \mu\text{m}$. The regular flow pattern created by multi-lamination is combined with geometric focusing and subsequent volume expansion which speeds up liquid mixing of the multi lamellae and leads to jet mixing².

² Details of the IMM Slit Interdigital Micromixer can be found at <http://www.imm-mainz.de>

The results however were similar to those obtained with the chip T-micromixers (see Table 4.6). The mixing time required based on lamellae width of 40 μm was estimated and shown in Table 4.7 (based on multi-lamination effect only. Semi-analytical calculation of mixing time was not possible due to complex interplay between focused interlamellae diffusion and jet mixing). With hindsight, the IMM mixers are probably not very good substitutes as the materials of construction of the mixing elements (Nickel on Copper for the first micromixer and Silver on Copper for the second micromixer) are known to catalyse peroxide decomposition.

Table 4.6: Comparison of reaction performance with different micromixers

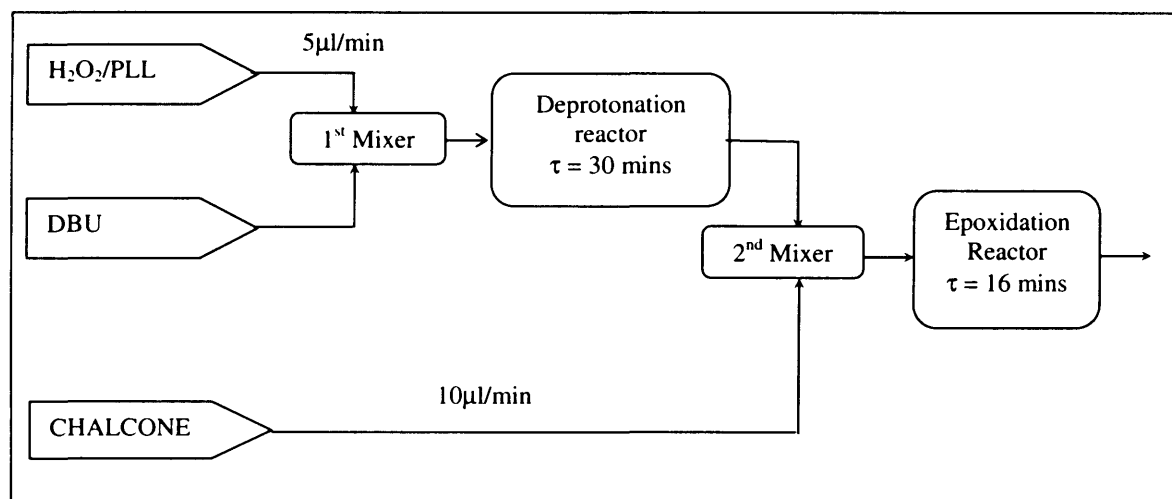
	T-micromixers	IMM Micromixers
Conversion	73.6 %	75.8 %
Enantioselectivity	83.1 %	84.1 %

Table 4.7: Calculated required mixing time for IMM Slit Interdigital Micromixer based on poly-*L*-leucine and chalcone diffusivities. Values in brackets are for characteristic dimension of 100 μm for comparison.

	Molecular Diffusivity (m^2/s)	Mixing time at $\text{Fo} = 1$ (s)
Chalcone	7.219×10^{-9}	0.22 (1.39)
Poly- <i>L</i> -leucine	1.432×10^{-10}	11.2 (69.8)

The setup was then modified such that the peroxide was pre-mixed with the catalyst as shown in Figure 4.7. This would allow the peroxide to be well dispersed with the catalyst molecule and adsorb on the catalyst on deprotonation instead of decomposing. Furthermore, the lack of free peroxy anions would reduce the background reaction rate. This modification resulted in conversion of 94.6 % ($\pm 0.4\%$) and enantioselectivity of 89.7 % ($\pm 0.3\%$), closely matching those obtained in the batch experiments.

Figure 4.7: Modified flow arrangement of continuous experimental setup



For near complete reaction, the production rate of this setup is approximately 1 g/day, making it suitable for bench-scale production of milligram quantities of chalcone epoxide. In comparison, CPC-System's CYTOS Lab System with an internal volume of 1.1 ml is designed to handle flowrates of 0.2 to 40 ml/min, for production of the initial 40 g and up to kilogram quantities of product (Schwalbe et al, 2004; Schwalbe et al, 2005). This easily meets the target for small scale production to supply the pre-clinical and clinical phase I studies, where delivery time for kilogram quantities is in the order of 4 – 6 months (Roberge et al, 2005).

While the production rate can be easily increased by increasing the number of reactors operating in parallel, clearly, for the existing unit to achieve the higher end of the production range, the reaction rate needs to be enhanced further. Numbering up may indeed prove beneficial for rapid scale-up; recent efforts to scale-up a modified triphasic epoxidation to 100 g substrate level have suffered from scale-up related problems, with significant increase of the overall reaction time (Gerlach and Geller, 2004). A continuous chemzyme membrane reactor for PEG-poly-*L*-leucine catalysed epoxidation of chalcone in pure THF had showed a decrease in reaction performance, when the reactor is operated for long times (Tsogoeva et al, 2002).

4.5. Conclusion

Batch experiments were carried out for the poly-*L*-leucine catalysed asymmetric epoxidation of chalcone using the standard batch procedure developed at University of Hull, achieving a conversion of 96.0 % and enantioselectivity of 90.2 %. A new procedure using premixed solvent was developed which allows for higher peroxide concentrations to be used and prevented the formation of a white precipitate. This new procedure resulted in a conversion of 94.9 % and enantioselectivity of 90.3 %. The effect of varying the deprotonation time was examined and the optimal deprotonation time of 30 minutes was established. The effect of reactant addition sequence was also examined and found to affect the performance substantially. These results indicate the importance of the deprotonation time and the decomposition of peroxide and suggest that the peroxide is sequestered by the catalyst. Background reaction was found to be relatively slow, with a conversion of only 19 %. Increasing the concentrations of all reactants while maintaining the same reactant concentration ratios resulted in a drop in enantioselectivity although complete conversion was achieved within 5 minutes.

Initial continuous experiments in which a mixture of PEG-poly-*L*-leucine and DBU was fed with a peroxide solution resulted in a drop in both conversion and enantioselectivity values compared to batch experiments, although the continuous background reaction achieved higher conversion (attributed to a slightly longer residence time). It was found that mixing needed to be enhanced as mixing by diffusion alone would require a very long channel due to the low molecular diffusivity of PEG-poly-*L*-leucine. The mixing problem was circumvented by feeding a mixture of peroxide and PEG-poly-*L*-leucine to the reactor system instead of feeding them separately. In this way, the peroxide adsorbed on the catalyst as soon as it is deprotonated, reducing the amount of free peroxide for the background reaction or decomposition. It may also be possible to improve the system further by reduction of the deprotonation reaction time, as the performance difference for 15 minutes and 30 minutes are not significant and are well within limits of experimental error. A continuous system, by appropriate optimization and scale out provides the opportunity for higher throughputs.

Chapter 5

Design of a Continuous Microstructured Reactor for Chalcone Epoxidation

5.1. Introduction

Having established a suitable continuous protocol and identified important process parameters (such as the deprotonation time and enhanced mixing performance) for the chalcone epoxidation reaction in Chapter 4, the next step then is to design a suitable microstructured reactor for the system. This chapter will therefore describe the issues and considerations for the design of a continuous reaction system for chalcone epoxidation and is structured as follows.

With a view to scale-up this system via the numbering-up approach at a later stage, the choice of plant structure will be considered first since this influences the device design and fabrication. The rate equations for this reaction system are then introduced and the experimental results of both batch and continuous reactions are compared to the predicted values from the mathematical models using the rate equations provided, in order to gain confidence on the applicability of the rate equations for design purposes. The detailed design of a single reaction unit is then considered, including provision of mixing, residence time and heat management. Finally, selection of a suitable material of construction will also be considered.

5.2. Design Basis and Motivation

There is currently a lack of knowledge and experience in the design and scale-out of a microchemical plant. As an emerging field, there is often a large degree of freedom and choices available in design. The following list of desirable features for a microstructured multi-scale chemical plant was defined to guide in assessing suitable designs for the system.

- Simple constructional principle, as they are relatively easy to fabricate.
- Flexibility in numbering up
- Simple assembly/disassembly and cleaning,
- Robust/not prone to fouling
- High throughput with non excessive energy expenditure (low pressure drop)
- Great variability to choice of constructional material.

With a view to scale up the system at a later stage, the structure of the scaled-out system was considered as a first step, since this can influence the device design and fabrication significantly. A basic requirement of reactor design is the ability to reproduce the results obtained from small scale at a larger scale. Establishing the 'plant' structure at an early stage then allows both the single system and the scaled out system to be as similar as possible in terms of the fluidic connections between unit operations.

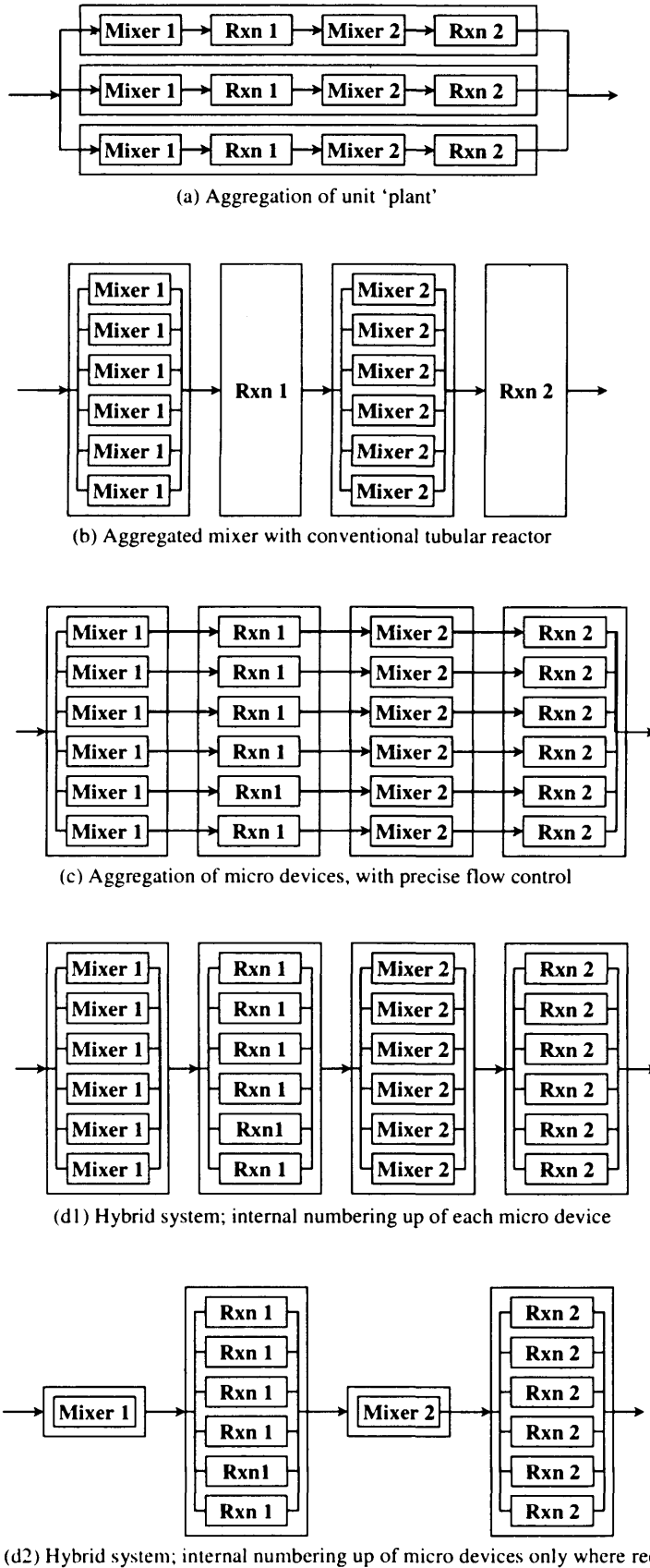
There is a vast number of possible plant structures for a given process, since the system can be numbered up internally or externally or indeed a combination of both approaches. Additionally, a decision could be made to use a conventional macro scale equipment for a particular unit operation where appropriate.

There are four main types of plant structures as shown in Figure 2.28. The reaction system is essentially a two-step process, consisting of the deprotonation reaction and the epoxidation reaction. Several possible scale-out structures analogous to the main structures identified in Figure 2.28, is shown in Figure 5.1 for the selected two-step reaction system.

Structure (a) in Figure 5.1, which represents external scaling out of a unit plant was selected as it offers the following advantages over other structures:

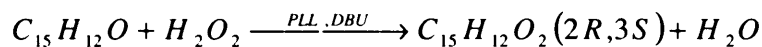
- The reaction system is a homogeneous system where reaction starts on contact of the two fluid streams in the mixer. Structure (a) allows better control of the time for material to transfer from one unit operation to the other since it minimises residence time in distribution headers, which is crucial as batch experimental results conducted earlier had indicated an optimal deprotonation time of 15 - 30 minutes.
- Flexibility in production rates as this can be adjusted by simply increasing or decreasing number of units in operation.

Figure 5.1: Possible scale-out structures for chalcone epoxidation

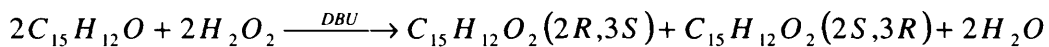


5.2.1. Rate Equations

The rate equations are necessary for design purposes for ensuring that appropriate residence time is provided for the microstructured reactor. Chalcone is epoxidised to (2R,3S)-chalcone epoxide, in the presence polyethylene glycol-poly-L-leucine (PEG-PLL) as catalyst, hydrogen peroxide extracted from urea-hydrogen peroxide adducts as oxidant and 1,8-diazabicyclo[5.4.0]undec-7-ene as base. The solvent is a mixed Tetrahydrofuran (THF) and Acetonitrile (ACN) solvent, with a THF: ACN ratio of 2.15.



The competing background epoxidation occurs in the absence of PEG-PLL catalyst, with chalcone epoxidised to both (2R,3S)-chalcone epoxide and (2S,3R)-chalcone epoxide, resulting in a racemic product.



The following ranges of reactant concentrations were used in the kinetic study to derive the rate equations (Mathew, 2003):

Table 5.1: Reactant concentration ranges used for kinetic studies

Reagent	Concentration range
PEG-PLL	7.94 – 22.96 g/l
Chalcone	0.014 – 0.1788 mol/l
Peroxide	0.034 – 0.14 mol/l

The average heat of reaction was found to be - 111 kJ/mol. The rate equations for both the main and competing reactions at 23.1°C are as shown below, with the values of the kinetic constants indicated in Table 5.2 (Mathew, 2003):

$$\text{Rate}_{PLL-\text{Catalysed}} = \frac{k [\text{Cata}] [\text{Chalcone}] [\text{H}_2\text{O}_2]}{(1 + K_{\text{Chalcone}} [\text{Chalcone}] + K_{\text{H}_2\text{O}_2} [\text{H}_2\text{O}_2])} \quad [5.1]$$

$$\text{Rate}_{Background} = k_{BG} [\text{Chalcone}] [\text{H}_2\text{O}_2] \quad [5.2]$$

where,

k is the rate constant,

$[\text{Cata}]$ is the catalyst loading in g/l,

$[\text{Chalcone}]$ is the chalcone concentration in mol/l,

$[\text{H}_2\text{O}_2]$ is the hydrogen peroxide concentration in mol/l.

Table 5.2: Values for kinetic constants used in the rate equations for both catalysed and background chalcone epoxidation

K (l ² /g.mol.min)	K_{Chalcone} (l/mol)	$K_{\text{H}_2\text{O}_2}$ (l/mol)	k_{BG} (l/mol.min)
0.143	2.172	1.092	0.132

To gain an understanding of how useful these equations are for predicting reaction performance in the microstructured reactor, it would be useful to compare the predicted performance with experimental results obtained to date. The experimental results obtained for this reaction system so far is summarised in Table 5.3, to allow for comparison with predicted results with mathematical models using the rate equations described earlier.

At base case initial concentrations and conditions, as shown in entry 1, the conversion and enantioselectivity obtained from batch runs were 87 % and 95 % respectively (Mathew, 2003). On increasing the temperature to 30°C (entry 2), the conversion increased to 94.9 % while the enantioselectivity was around 90.3 %. Increasing reagent concentrations (keeping relative ratios of reagents constant) at 30°C resulted in complete conversion within 5 minutes but with a sharp drop in enantioselectivity to 84 % (entry 3). In comparison, running the reaction in continuous mode using the continuous protocol at 23.1°C and 30°C resulted in a performance comparable to that in batch mode (entries 4 and 5 respectively). The difference in enantioselectivity between batch and continuous runs at 23.1°C can be explained by the fact that the catalysts used in these two runs were of a different batch.

Table 5.3: Conversion and enantioselectivity values at various reaction conditions.

Entry	Chalcone (mol/l)	H ₂ O ₂ (mol/l)	PLL (g/l)	DBU (mol/l)	time (min)	T (°C)	Conversion (%)	Ee ^c (%)
1 ^a	0.0802	0.132	13.47	0.22	16	23.1	87.0	> 95.0
2	0.0802	0.132	13.47	0.22	16	30.0	94.9	90.3
3	0.3650	0.602	60.73	0.94	5	30.0	98.2	83.9
4 ^b	0.0802	0.132	13.47	0.22	16	23.1	88.4	88.8
5 ^b	0.0802	0.132	13.47	0.22	16	30.0	94.6	89.7

a. Results from kinetic studies carried out by Blackmond and Mathew. The enantioselectivity was initially measured several times and assumed to be constant thereafter (Mathew, 2003).

b. Results obtained from continuous mode in this work.

c. Enantiomeric excess. See equation [5.5].

In Chapter 4, the initial batch process was improved to prevent formation of precipitate and allow the reaction to be transferred to a continuous flow process. Following that, a continuous reaction protocol was established and several design issues were identified. Based on these findings, a single continuous reactor comprising of two mixer-reactors in series for the deprotonation and epoxidation reactions is designed in this chapter with the following requirements:

- i. Base case initial concentrations
- ii. Base case operating temperature of 23.1 °C, as well as for a temperature range of 15 – 35 °C
- iii. Mixing needs to be enhanced to ensure complete mixing prior to reaction, due to the low diffusivity of PEG-PLL.
- iv. Optimal deprotonation of peroxide by DBU in the presence of PEG-PLL in 15 – 30 minutes, prior to entering the epoxidation reactor.
- v. Peroxide and PEG-PLL should be premixed as one feed to the deprotonation reactor, while DBU and chalcone solutions at set concentrations were fed as separate feeds into the deprotonation and epoxidation reactor respectively.

5.2.2. Production Rate

The main concern for selecting the production rate was the cost of running the reaction continuously due to the high cost of the catalyst. Assuming a scale-out factor of 10, a rough estimate of the cost of catalyst required for running the reactions at base case initial concentrations and 23.1 °C for 16 minutes residence time at reactor unit volumes of 0.32 ml, 3.2 ml and 32 ml were evaluated and compared.

To simplify the calculations, the conversion was assumed to be complete, based on earlier continuous experimental results (entry 4, Table 5.3). These are shown in Table 5.4.

Table 5.4: Estimate of cost of catalyst using different reactor volumes

	Reactor Unit Volumes (ml)		
	0.32	3.2	32
Product flow per unit (mol/min) ^a	0.0000016	0.000016	0.00016
Daily production per unit (kg/day) ^b	0.0005	0.005	0.052
Daily production per 10 units (kg/day)	0.005	0.05	0.52
Catalyst required per unit (g/day)	0.39	3.88	38.79
Cost of catalyst per unit (£/day) ^c	7.76	77.59	775.87
Catalyst required for 10 units (g/day)	3.9	38.8	387.9
Cost of catalyst for 10 units (£/day)	78	775.9	7758.7
Estimated yearly production rate (kg/year) ^d	1.66	16.58	165.76

a. For a residence time of 16 minutes at base case initial concentrations and T = 23.1

°C, assumed complete conversion.

b. Molecular weight of chalcone epoxide = 224.26, 1 day = 24 hours

c. Cost of catalyst is £ 20/g.

d. Assumed 320 operating days per year

The 32 ml unit reactor volume was ruled out due to the excessive costs incurred. Both 0.32 ml and 3.2 ml unit reactor volumes were deemed acceptable, with 0.32 ml unit reactor volume preferred as it is then feasible to run at prolonged runs without cost constraints. Running the reaction for a period of 5 residence time only, sufficiently long to achieve steady state conditions, would reduce the cost of catalyst to only 16 % of the daily catalyst costs. The corresponding design flowrate for a 0.32 ml unit is 3.33×10^{-10} m³/s.

5.3. Mathematical Models

Batch reactor and laminar tubular reactor models were set up in gPROMS using the rate equations in section 5.2.1 to allow for comparison with experimental results from Chapter 4. A laminar slit flow reactor model was also set up to ensure sufficient residence time is provided and to predict the effect of reactor geometry on reaction performance for design purposes. The deprotonation reaction was not taken into account since the rate equation was not available; however, provided sufficient residence time is available, the final concentration of the peroxy anion will be the same (for base case conditions). The required residence time for the deprotonation reaction was established experimentally in Chapter 4.

5.3.1. Batch Reactor Model

For a constant volume batch reactor, the mole balance is given by:

$$\frac{dC_n}{dt} = -r_n \text{ for } n \text{ components in the reaction system.} \quad [5.3]$$

For $n = 5$ components in the system, the change in concentration due to reaction for each component is given by:

Table 5.5: Change in component concentration due to reaction

$$\begin{aligned}
 -r_{\text{Chalcone}} &= -\text{Rate}_{\text{PLL-Catalysed}} - \text{Rate}_{\text{Background}} \\
 -r_{\text{Peroxide}} &= -\text{Rate}_{\text{PLL-Catalysed}} - \text{Rate}_{\text{Background}} \\
 -r_{\text{product}} &= \text{Rate}_{\text{PLL-Catalysed}} + \frac{1}{2} \text{Rate}_{\text{Background}} \\
 -r_{\text{Byproduct}} &= \frac{1}{2} \text{Rate}_{\text{Background}} \\
 -r_{\text{Water}} &= \text{Rate}_{\text{PLL-Catalysed}} + \text{Rate}_{\text{Background}}
 \end{aligned}$$

The conversion, X after a time period t , was calculated from:

$$X = \frac{C_{Chalcone,t=0} - C_{Chalcone,t=t}}{C_{Chalcone,t=0}} \quad [5.4]$$

The enantioselectivity, S was calculated from:

$$S = \frac{C_{product,t=t} - C_{Byproduct,t=t}}{C_{product,t=t} + C_{Byproduct,t=t}} \quad [5.5]$$

5.3.2. Laminar Tubular Reactor Model

Laminar flow in tubular reactors is characterized by a parabolic velocity profile:

$$V_z(r) = 2\bar{u} \left(1 - \frac{r^2}{R^2}\right) \quad [5.6]$$

As a result of this parabolic velocity profile, laminar flow reactors in general have concentration and temperature gradients in both the radial and axial direction. The material balance in a laminar flow tubular reactor at steady state conditions is given by [5.7]. The change in concentration of component n due to reaction, \mathfrak{R}_n is as shown in

Table 5.5.

$$V_z(r) \frac{\partial C_n}{\partial z} = D_n \left[\frac{\partial C_n}{\partial z^2} + \frac{1}{r} \frac{\partial C_n}{\partial r} + \frac{\partial^2 C_n}{\partial r^2} \right] + \mathfrak{R}_n \quad [5.7]$$

For a reactor with radius R and length L, the dimensionless form of [5.7], shown in [5.8] is obtained by introducing the following dimensionless spatial coordinates:

$$\zeta = \frac{r}{R} \quad \xi = \frac{z}{L}$$

$$2(1 - \zeta^2) \frac{\partial C_n}{\partial \xi} = \left(\frac{D_n \tau}{R^2} \right) \left[\left(\frac{R^2}{L^2} \right) \frac{\partial^2 C_n}{\partial \xi^2} + \frac{1}{\zeta} \frac{\partial C_n}{\partial \zeta} + \frac{\partial^2 C_n}{\partial \zeta^2} \right] + \mathfrak{R}_n \tau \quad [5.8]$$

where

D_n = Molecular diffusivity (m²/s)

τ = mean residence time (s)

The boundary conditions used are as follows:

1) Across entire cross section, $\zeta = 0$ to 1,

At the inlet, $\xi = 0$,

$$C(n,0, \zeta) = C_{n0}$$

At the outlet, $\xi = 1$ (assume gradients are small)

$$\frac{\partial C_n}{\partial \xi} = 0$$

2) Across the entire length of the reactor, $\xi = 0$ to 1

At $\zeta = 0$, (symmetry in cross flow direction)

$$\frac{\partial C_n}{\partial \zeta} = 0$$

At the wall, $\zeta = 1$, (solid tube without transpiration)

$$\frac{\partial C_n}{\partial \zeta} = 0$$

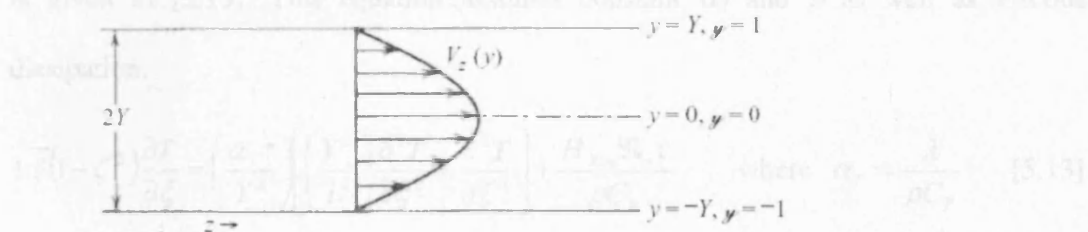
Both conversion and enantioselectivity values were computed from [5.4] and [5.5] using mixing cup average outlet concentrations due to the presence of radial variation in concentration. The mixing cup average outlet concentration was computed from (Nauman, 2002):

$$C_{n,mix} = 4 \int_0^1 C_n(\zeta, z) [1 - \zeta^2] \zeta \, d\zeta \quad [5.9]$$

5.3.3. Laminar Slit Flow Reactor Model

Channels fabricated onto a planar surface do not generally have a circular cross section but a rectangular cross-sectional area which is better represented by slits. Slit flow, which occurs between closely spaced parallel plates provides good mixing due to much smaller achievable slit heights, compared to those achieved using conventional tubular designs. Figure 5.2 below illustrates pressure-driven flow between flat plates. The downstream direction is z . The cross-flow direction is y , with $y = 0$ at the centerline and $y = \pm Y$ at the walls so that the channel height is $2Y$. Suppose the slit width (x-direction) is very large so that the sidewall effects are negligible.

Figure 5.2: Pressure driven flow between parallel plates with both plates stationary



The axial velocity profile for laminar, Newtonian fluid of constant viscosity in a slit is given by:

$$V_z(y) = 1.5\bar{u} \left(1 - \frac{y^2}{Y^2} \right) \quad [5.10]$$

The material balance in a laminar slit flow reactor at steady state conditions with negligible side-wall effects is given by [5.11]. The change in concentration of component n due to reaction, \mathfrak{R}_n is as shown in Table 5.5.

$$V_z(y) \frac{\partial C_n}{\partial z} = D_n \left[\frac{\partial^2 C_n}{\partial z^2} + \frac{\partial^2 C_n}{\partial y^2} \right] + \mathfrak{R}_n \quad [5.11]$$

For a reactor with height $2Y$ and length L , the two independent variables z and y can be scaled with length L and half-height Y respectively. We define two new independent variables $\xi = \frac{z}{L}$ and $\zeta = \frac{y}{Y}$ so that they both have a range from 0 to 1. Substituting the new variables and [5.10] into equation [5.11]:

$$1.5(1 - \zeta^2) \frac{\partial C_n}{\partial \xi} = \left(\frac{D_n \tau}{Y^2} \right) \left[\left(\frac{Y^2}{L^2} \right) \frac{\partial^2 C_n}{\partial \xi^2} + \frac{\partial^2 C_n}{\partial \zeta^2} \right] + \mathfrak{R}_n \tau \quad [5.12]$$

where

$\left(\frac{D_n \tau}{Y^2} \right)$ can be taken as Pe^{-1} , where Pe is the radial Peclet number

Heat diffuses much like mass and is governed by similar equations. The energy balance is given in [5.13]. This equation assumes constant α_T and ρ as well as viscous dissipation.

$$1.5(1 - \zeta^2) \frac{\partial T}{\partial \xi} = \left(\frac{\alpha_T \tau}{Y^2} \right) \left[\left(\frac{Y^2}{L^2} \right) \frac{\partial^2 T}{\partial \xi^2} + \frac{\partial^2 T}{\partial \zeta^2} \right] + \frac{H_{Rvn} \mathfrak{R}_n \tau}{\rho C_p} \quad \text{where } \alpha_T = \frac{\lambda}{\rho C_p} \quad [5.13]$$

The boundary conditions used are as follows:

1) Across the entire cross section, $\zeta = 0$ to 1

At the inlet, $\xi = 0$,

$$C(n, 0, \zeta) = C_{n0}$$

$$T(0, \zeta) = T_{in}$$

At the outlet, $\xi = 1$, (assume gradients are small)

$$\frac{\partial C_n}{\partial \xi} = 0, \quad \frac{\partial T}{\partial \xi} = 0$$

2) Across the entire reactor length $\xi = 0$ to 1

At $\zeta = 0$, (symmetry in cross flow direction)

$$\frac{\partial C_n}{\partial \zeta} = 0, \quad \frac{\partial T}{\partial \zeta} = 0$$

At the wall, $\zeta = 1$, (solid tube without transpiration)

$$\frac{\partial C_n}{\partial \zeta} = 0, \quad T = T_{wall} \text{ for fixed wall temperature, } \frac{\partial T}{\partial \zeta} = 0 \text{ for adiabatic conditions}$$

The inside wall temperature was assumed to be equal to the outside wall temperature because of the small wall thickness. Similarly, the conversion and enantioselectivity values were calculated using the mixing cup average concentration which can be computed from:

$$C_{n,mix} = 1.5 \int_0^1 C_n(\zeta, z) [1 - \zeta^2] d\zeta \quad [5.14]$$

5.3.4. Accuracy of Numerical Method

All three reactor models were coded and solved using gPROMS on Windows XP with Pentium IV 3.00 GHz CPU and 512 MB of RAM. The gPROMS scripts for all three reactor models can be found in Appendices 5-1, 5-2 and 5-3. For both the laminar tubular flow reactor and slit flow reactor models, second order orthogonal collocation (OCFEM) over 20 finite elements was adopted for the radial direction. The axial domain was discretised using centered finite differences (CFDM) of second order over a uniform grid of 150 intervals. For a reporting interval of 0.01, the batch reactor model took less than 1 s to solve while the laminar tubular and slit flow reactor models took 86 s and 154 s to solve respectively for the discretisation parameters described above.

Increasing the number of grid points improves the accuracy of the solution albeit with increased computational time. The models were solved using different orders of approximation and numbers of discretisation intervals/elements to check for the accuracy of the solution. The results are shown in Table 5.6. An improvement in the accuracy of the solution is expected with the doubling of either the order of approximation or number of discretisation intervals/elements. However, as seen in Table 5.6, the differences in the results obtained were not substantial. The current parameters are therefore used since these allow for a faster solution.

Table 5.6: Solution of the gPROMS models using different number of grid points

	Conversion	Enantioselectivity
Laminar tubular reactor		
Base case ^a	88.26 %	92.42 %
Fourth order CFDM	88.25 %	92.42 %
300 discretisation intervals	88.28 %	92.42 %
40 finite elements	88.28 %	92.42 %
Third order OCFEM	88.27 %	92.42 %
Slit flow reactor		
Base case ^a	89.57 %	92.41 %
Fourth order CFDM	89.56 %	92.41 %
300 discretisation intervals	89.58 %	92.41 %
40 finite elements	89.59 %	92.41 %
Third order OCFEM	89.58 %	92.41 %

a. Second order OCFEM over 20 finite elements in the radial direction, second order CFDM over 150 discretisation intervals in the axial direction.

5.3.5. Comparison with Experimental Results

The results of the batch and continuous experimental runs in Table 5.3 were compared to those predicted by the models and shown in Figures 5.3 and 5.4, to gain confidence on the applicability of the rate equations for estimating the required residence time for the microstructured reactor.

It appears that the rate equations give a fairly reliable prediction of the rate of reaction at base case conditions, with experimental conversion values at 23.1°C and 30 °C within 3 % and 6 % of predicted values respectively. The experimental enantioselectivity values were within 5 % of predicted values at base case at both 23.1 and 30 °C. In the case of higher reagent concentrations, while the predicted conversion matches the experimental values (complete reaction within 5 minutes), the predicted enantioselectivity value was higher than experimental values by ~13 %.

The difference between predicted and experimental values could possibly be due to different catalytic activity from using different catalyst batches. From the results in Table 5.3, it is observed that the conversions increase with increasing temperature, as expected. However, temperature effects on the rates of both the catalysed and background reactions are not captured; hence the predicted conversion is slightly lower than experimental values at 30 °C. Similarly, the effect of temperature on relative rates of catalysed and background reactions are not captured so the predicted enantioselectivities are not reliable.

Another possible reason is the assumption made during the kinetic studies where the enantioselectivity was assumed constant even when reactant concentrations were varied (Mathew, 2003). The rate equations therefore do not capture the effect of varying concentrations on the relative rates of the catalysed and background epoxidations, as the main cause of the drop in enantioselectivity is due to an increase in the rate of the background epoxidation rate relative to the rate of the catalysed epoxidation.

An important point to note is that since the rate equations are based on the concentration of peroxide rather than peroxy anion, which is the active species, the rate equations may not be accurate if the deprotonation time is varied since this means that a different initial concentration of the active species is used. The presence of an optimal deprotonation time suggests that the initial concentration of the active species is determined by both the extent of deprotonation and decomposition of peroxide and if optimal deprotonation time is not provided, the conversion values predicted by the rate equation could be very far off the mark since this means the initial concentration of the active species is not close to the concentration of peroxide used.

Figure 5.3: Experimental and predicted values of conversion and enantioselectivity in a batch reactor.

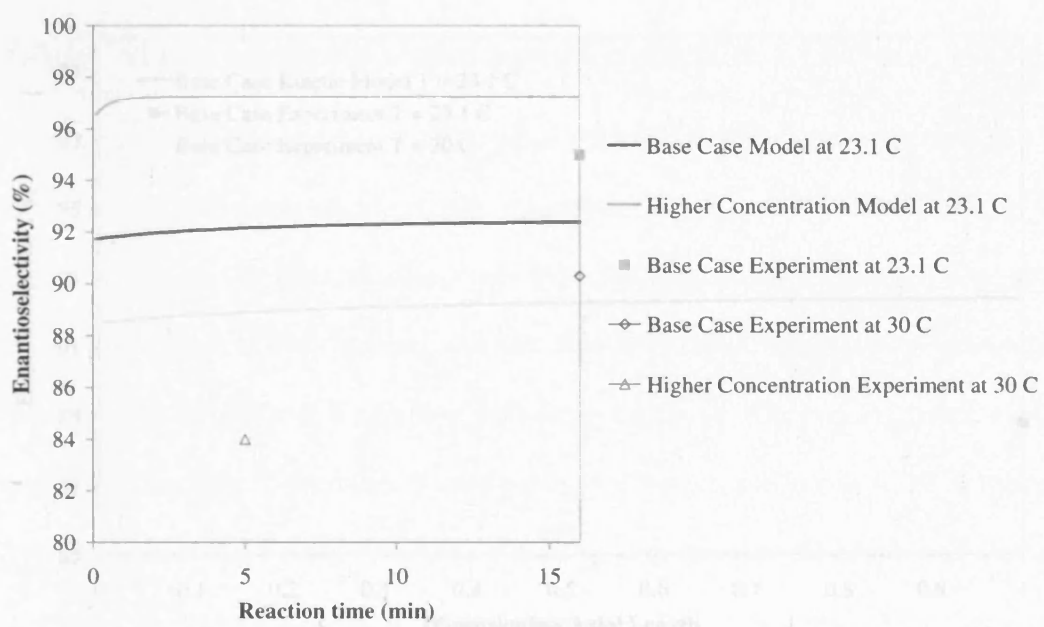
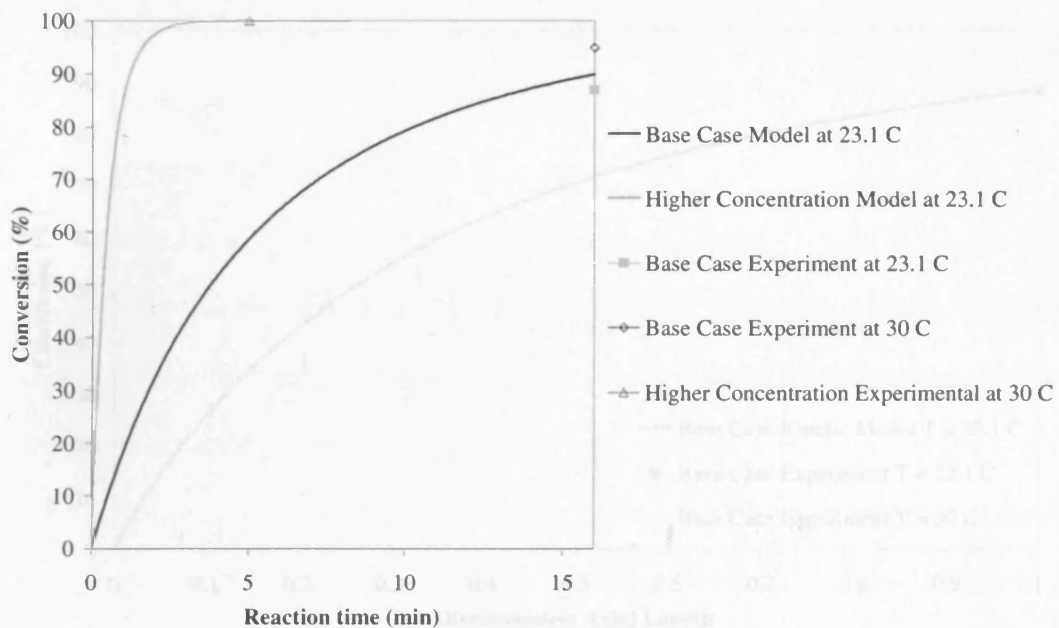
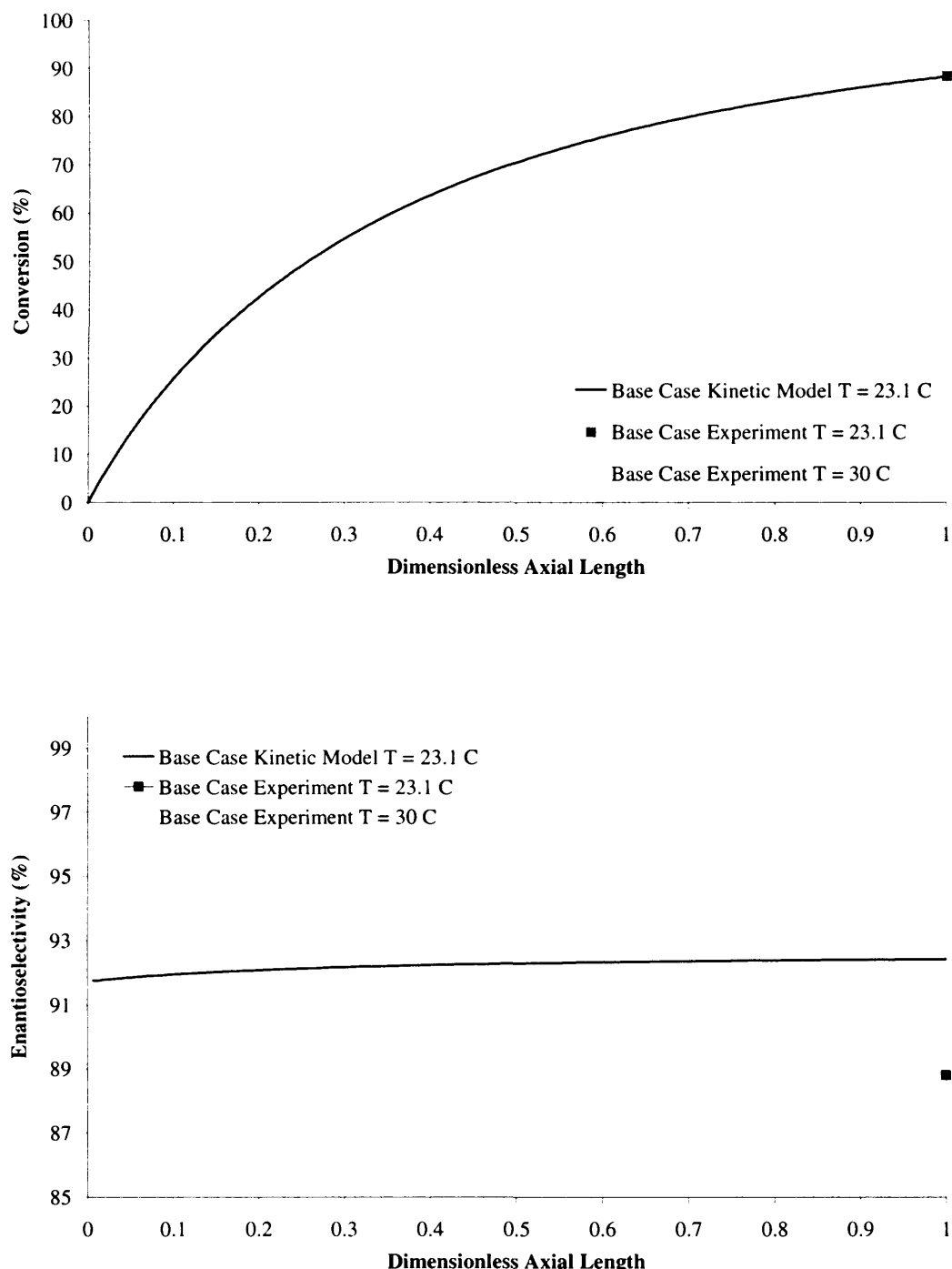


Figure 5.4: Predicted and experimental conversion and enantioselectivity values in a continuous tubular reactor



5.4. Design of Single Reaction Unit

The main considerations in designing the single reaction unit are:

- Provision of sufficient mixing
- Provision of residence time for reaction to occur
- Heat management

As diffusional mixing was found to be insufficient in Chapter 4, methods for enhancing mixing were screened and a suitable method selected. A residence time channel was also sized to provide sufficient residence time for the reaction to complete and this was dimensioned appropriately to ensure a tight residence time distribution. Heat management was less crucial in this case, due to the low expected adiabatic temperature increase. The main concern is therefore on providing isothermal reaction conditions for the system.

5.4.1. Mixer Device Screening and Selection

The simplest micromixer is the T-micromixer where two streams are combined at a T-junction and sufficient residence time is provided downstream of the junction for complete mixing. Mixing typically occurs by molecular diffusion only and depending on the diffusivity of the reactants and the rate of reaction, this may be acceptable. However, for reactants with very low diffusivity values or with very fast reactions the rate of mixing in a T-micromixer may not be acceptable and needs to be enhanced. Several methods have been shown to enhance mixing for continuous reaction systems (Ehrfeld et al, 2000; Stroock et al, 2002; Hessel et al, 2003; Jiang et al, 2004; Schonfeld et al, 2004) including interdigital multilamination, split and recombine, geometric focussing and chaotic mixing methods.

As a first step in selecting a suitable mixing device, the required diffusional mixing times in a T-mixer with a characteristic length of 100 μm were calculated for both chalcone and poly-L-leucine. For chalcone and poly-L-leucine molecular diffusivities of 1×10^{-9} and 1×10^{-11} m^2/s respectively, the diffusional mixing times were calculated as follows:

$$t_{\text{Chalcone}} = \frac{l^2}{D} = \frac{(1 \times 10^{-4})^2}{1 \times 10^{-9}} = 10\text{s} \quad [5.15]$$

$$t_{\text{PLL}} = \frac{l^2}{D} = \frac{(1 \times 10^{-4})^2}{1 \times 10^{-11}} = 1000\text{s} \quad [5.16]$$

The reaction time constants are essentially the half time of the reactions under consideration. In the case of the PLL catalysed epoxidation, there are 2 reactions:

- i. the poly-L-leucine catalysed reaction
- ii. the background reaction.

The initial concentrations of chalcone and peroxide are $C_{A0} = 0.0802 \text{ mol/l}$ and $C_{B0} = 0.132 \text{ mol/l}$ respectively. To simplify the calculations, assume $C_{A0} = C_{B0}$. The rate equations for both catalysed and background reactions are then simplified to:

$$\frac{dC_A}{dt} = \frac{-k \cdot \text{Cat} \cdot C_A^2}{1 + (K_{H2O2} + K_{Chalc})C_A} \quad [5.17]$$

$$\frac{dC_A}{dt} = -k_{BG} \cdot C_A^2 \quad [5.18]$$

Rearranging and integrating [5.17] and [5.18] from C_{A0} to $0.5 C_{A0}$ to evaluate the half time of the reactions:

$$\int_{C_{A0}}^{0.5C_{A0}} \left(\frac{1 + (K_{H2O2} + K_{Chalc})C_A}{-k \cdot \text{Cat} \cdot C_A^2} \right) dC_A = \int_0^t dt \quad [5.19]$$

$$\int_{C_{A0}}^{0.5C_{A0}} \frac{1}{-k_{BG} \cdot C_A^2} dC_A = \int_0^t dt \quad [5.20]$$

The catalysed and background reaction time constants were then evaluated from [5.21] and [5.22].

$$t = \left[\frac{1}{k \cdot Cat} \left(\frac{1}{C_A} \right) - \left(\frac{K_{H2O2} + K_{Chalc}}{k \cdot Cat} \right) \ln C_A \right]_{C_{A0}}^{0.5C_{A0}} \quad [5.21]$$

$$t = \frac{1}{k_{BG}} \left[\frac{1}{C_A} \right]_{C_{A0}}^{0.5C_{A0}} \quad [5.22]$$

The reaction time constants calculated at two initial concentrations (Cases 1 and 2) for both catalysed and background reactions are shown below in Table 5.7. The smaller value of the reaction time constants for both catalysed and background reactions were then used to compute the ratio of diffusional mixing time constants to the reaction time constants.

Table 5.7: Reaction time constants for catalysed and background reactions at two different initial concentration values

Catalysed reaction time constants		
	Case 1: $C_{A0} = 0.0802 \text{ mol/l}$	Case 2: $C_{A0} = 0.132 \text{ mol/l}$
K	$0.143 \text{ l}^2/\text{g.mol.min}$	$0.143 \text{ l}^2/\text{g.mol.min}$
K_{H2O2}	1.092 l/mol	1.092 l/mol
K_{Chalc}	2.172 l/mol	2.172 l/mol
Cat	13.47 g/l	13.47 g/l
$t_{1/2}$	7.65 minutes	5.11 minutes
Background reaction time constants		
K_{BG}	0.132 l/mol.min	0.132 l/mol.min
$t_{1/2}$	94.5 minutes	57 minutes

The calculated ratio of diffusion mixing time to reaction time constants for both catalysed and background reactions are presented in Table 5.8. A comparison of the catalysed and background reaction time constants shows that the catalysed reaction is much faster than background reaction. However, at a characteristic length scale of 100 μm , the catalysed reaction is diffusion controlled (based on PLL diffusion time). From [5.23], a characteristic diffusion length $L_d \sim 55 \mu\text{m}$ is required for the PLL diffusion rate to at least equal the catalysed reaction rate. This represents a convection length, L_c of 34 m for a design flowrate of $3.33 \times 10^{-10} \text{ m}^3/\text{s}$.

Table 5.8: Calculated reaction and mixing time constants

Catalysed reaction time constant	5.11 minutes (307 s)
Background reaction time constant	57 minutes (3420 s)
Chalcone diffusion time ($l=100 \mu\text{m}$)	10 s ($D = 1\text{e}^{-9}$)
PLL diffusion time ($l=100 \mu\text{m}$)	1000 s ($D = 1\text{e}^{-11}$)
Ratio of mixing time to catalysed reaction time constants	$\frac{\text{Diffusion}_{PLL}}{\text{Rate}_{PLL-\text{Catalysed}}} = 3.25$
Ratio of mixing time to background reaction time constants	$\frac{\text{Diffusion}_{Chalcone}}{\text{Rate}_{Background}} = 2.92 e^{-3}$

$$L_d = \sqrt{Dt} \quad [5.23]$$

$$L_c = \bar{u}t \quad [5.24]$$

For minimal mixing effect on selectivity, the diffusion time should be smaller than the catalysed reaction time. A mixer capable of complete mixing within several seconds is sufficient for the system to be in the reaction-controlled region (see Table 5.8).

At a ratio of diffusion to reaction time constants of 0.01, the diffusion time required would be 3.1 s, which (from equation 5.23) corresponds to a characteristic length of 5.5 μm which is clearly not feasible with a simple T-micromixer due to excessive pressure drop at such low dimensions. This means that simple mixing by diffusion is insufficient and needs to be enhanced by other methods.

Of the various methods for enhancing mixing, the following three methods were viewed as most suitable for production purposes, as they meet most of the desirable features identified in section 5.2.

- i. Curved Channels
- ii. Staggered Herringbone
- iii. Split and Recombine Caterpillar mixer

Enhancement by chaotic flow is preferred due to the exponential increase in intermaterial surface area generated while allowing high throughputs at minimal pressure drop. Of the first two mixers, which are both chaotic, the curved channel is more attractive compared to the staggered herringbone mixer due to the ease of fabrication.

5.4.1.1. Curved Channel Mixer

Two dimensionless groups characterizing such flows are the Reynolds number, Re and the Dean Number, K .

$$\text{Re} = \frac{ud}{v} \quad [5.25]$$

$$K = \text{Re} \sqrt{\frac{d}{R}} \quad [5.26]$$

where

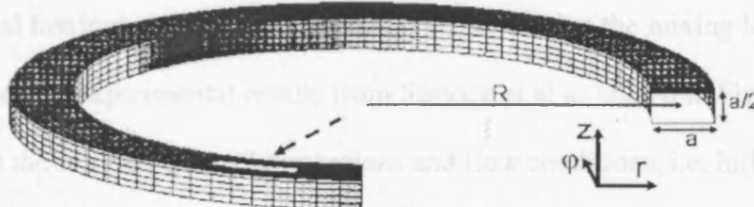
d denotes the hydraulic diameter,

R , the mean radius of curvature

u , the fluid velocity

and ν , the kinematic viscosity.

Figure 5.5: Curved channel mixer (Schonfeld and Hardt, 2004)



A qualitative change in the secondary pattern is observed for Dean numbers above a critical value K_c of around 140. For $K < K_c$, the secondary flow consists of two counter-rotating vortices whereas for $K > K_c$, two additional counter-rotating vortices appear close to the center of the outer channel wall. To achieve a relatively strong helical flow with the vortex centres shifted towards the outer channel wall, the Dean number should be at least 100 (Jiang et al, 2004).

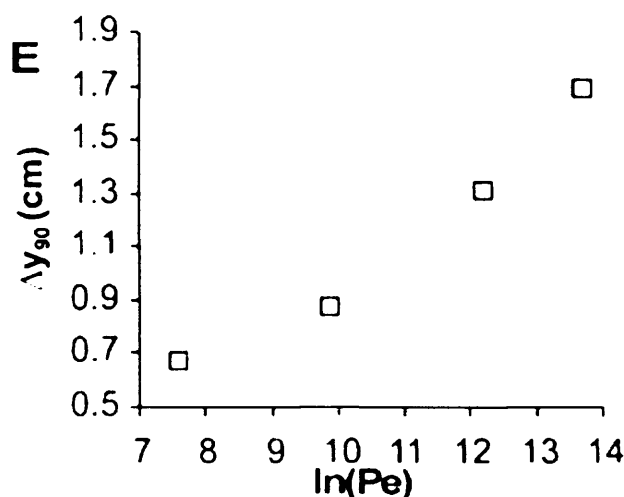
Taking a minimum value of $R = d$, the Dean number for a range of channel hydraulic diameters at a design flowrate of $3.33 \cdot 10^{-10} \text{ m}^3/\text{s}$ were evaluated. From Table 5.9, for Dean number to exceed the minimum value of 100 required for the formation of secondary flow, a channel with a maximum hydraulic diameter of $6 \mu\text{m}$ is required, which clearly would cause problems with clogging and high pressure drops.

Table 5.9: Calculated Dean number for a range of channel hydraulic diameters

	Hydraulic diameter (μm)	Radius(μm)	Dean Number
1	100	100	7
2	50	50	14
3	15	15	46
4	10	10	69
5	6	6	115

5.4.1.2. Staggered Herringbone Mixer

The staggered herringbone was evaluated next by estimating the mixing length and time required based on experimental results from Stroock et al as shown in Figure 5.6. It was found that at the selected channel dimensions and flow conditions, i.e. $\ln(\text{Pe}) \sim 10.3$ (see Table 5.10), the mixing length required is ~ 0.9 cm with corresponding mixing time of only 0.5 s.

Figure 5.6: Length for 90 % mixing versus $\ln(\text{Pe})$ (Stroock et al, 2002)

5.4.1.3. IMM Split and Recombine Mixer

The data for the split and recombine mixer was calculated based on a standard caterpillar split and recombine mixer from IMM with 8 mixing stages at a length of 13.5 mm. The lamella width is halved at each stage, therefore after 8 stages, lamella width is calculated from [5.27] and the corresponding diffusional mixing time is calculated from [5.28]. Compared to the first two mixers, the split and recombine mixer is relatively more complicated to fabricate and generates a slower increase in intermaterial surface area.

$$l = \frac{\text{width}}{2^8} = \frac{8.4 \times 10^{-4}}{2^8} = 3.28 \times 10^{-6} \text{ m.} \quad [5.27]$$

$$t_{\text{mix}} = \frac{l^2}{D_{\text{PLL}}} = \frac{(3.28 \times 10^{-6})^2}{1 \times 10^{-11}} = 1.1 \text{ s} \quad [5.28]$$

5.4.1.4. Conclusion

The curved channel while extremely attractive due to its simple constructional principle was eventually ruled out, as at the design flowrate, chaotic flow is only generated at a maximum hydraulic diameter of 6 μm , which could potentially cause problems with clogging. The IMM split and recombine mixer was not selected because the mixing time required is estimated to be more than double that of the staggered herringbone mixer with a more complex geometry to fabricate. The staggered herringbone mixer was therefore selected and used for enhancing mixing in the system as it allows rapid mixing with high throughput, low pressure drop and relatively simple construction. A summary of the three evaluated mixers is presented in Table 5.10.

A detailed numerical study of the staggered herringbone mixer is presented in Chapter 6, where the required length for complete mixing is computed. The computed mixing length is 1.3 and 1.5 cm for the first and second mixer respectively; however, the mixer was designed with sufficient margin to ensure complete mixing and flexibility for slightly higher flows. The final mixer design is summarised in Table 5.11.

Table 5.10: Details of the three mixer types evaluated.

	Curved Channel	Staggered Herringbone	Split and Recombine
Channel Width (μm)	6	200	840
Channel Height (μm)	6	85	840
Hydraulic diameter (μm)	6	133	840
Velocity (m/s)	9.3	0.02	4.72E-04
Reynolds Number	115	5	0.82
Peclet Number	694444	29240	4960
Dean Number	115	-	-
Mixing Length (m)	-	0.009	-
Mixing time (s)	-	0.5	1.1 ²

² This refers to time required after 8 stages.

Table 5.11: Details of staggered herringbone mixer design

Channel width, w (μm)	200
Channel height, h (μm)	85
Groove depth, 2αh (μm)	31
Groove period, 2π/q (μm)	100
Angle, θ	45°
Grooves/half cycle	6
Length per cycle (mm)	1.516
Number of cycles	26
Total mixer length (mm)	40

5.4.2. Dimensioning of Reactor Channel

Flows in microchannels are typically laminar, with a parabolic flow profile. The velocity gradient across the rectangular channel, with zero velocity near the wall and high velocity at the centreline, causes a gradient in composition across the depth of the channel, as molecules near the wall undergo complete conversion while those near the centreline have a much shorter reaction time. Molecular diffusion tends to alleviate this gradient, hence the channels can be dimensioned appropriately to minimise the composition gradient so that the flow behaves more like a plug flow reactor. A rectangular cross-sectional channel with small height (slit flow) provides good mixing across the cross section of the channel.

From equation [4.3] in Chapter 4, for plug flow to be applicable the following criteria must be met (Raja et al, 2000):

$$\frac{d}{L} \ll \text{Re}_d \text{ Sc} \ll \frac{L}{d}, \quad \text{where } \text{Re}_d \text{ Sc} = \frac{\rho u d}{\mu} \frac{\mu}{\rho D_n} = \frac{u d}{D_n} \quad [4.3]$$

The lower bound ensures that the axial diffusive transport over the length scale L is negligible compared to axial convective transport, while the upper bound ensures that there are no radial variations. Rearranging [4.3], we get

$$Pe_r = \frac{ud^2}{D_n L} \ll 1 \quad \text{for negligible radial concentration gradients}$$

$$Pe_z = \frac{uL}{D_n} \gg 1 \quad \text{for negligible axial diffusive transport.}$$

For a slit reactor, d is replaced by $2Y$, the depth of the slit and the Pe_r becomes:

$$Pe_r = \frac{uY^2}{D_n L} = \frac{Y^2}{D_n \tau} \ll 0.25$$

Recall the dimensionless convective-diffusive equation for a slit flow reactor [5.12]:

$$1.5(1 - \zeta^2) \frac{\partial C_n}{\partial \xi} = \left(\frac{D_n \tau}{Y^2} \right) \left[\left(\frac{Y^2}{L^2} \right) \frac{\partial^2 C_n}{\partial \xi^2} + \frac{\partial^2 C_n}{\partial \zeta^2} \right] + \mathfrak{R}_n \tau \quad [5.12]$$

The slit flow analogue of the Hagen-Poiseuille equation, which was used in [5.12], is valid only if $Y \ll W$, so that edge effects are unimportant (Bird et al, 2002). Given the relatively long residence time required, this means there is a trade-off between maximising the effects of diffusion (reduce Y as much as possible which increases the total length) and minimising the pressure drop and footprint of the reactor (reduce total length). The reaction channel was sized to allow for 16 minutes residence time at a total volume of 0.32 ml. This was because at a total volume of 3.2 ml, the length required to provide 16 minutes reaction time becomes excessively long (for a similar cross sectional area, the required length is 10 times that of a 0.32 ml reactor).

The reaction channels should ideally be dimensioned to fulfil the following criteria:

- For negligible side-wall effects, the dimensions were selected such that $\frac{Y}{W} < 0.1$.
- $\frac{1}{Pe_r} = \frac{D_n \tau}{Y^2} \gg 4$
- $Pe_z = \frac{uL}{D_n} \gg 1$

For a rectangular channel, the pressure drop can be calculated from the equation:

$$\Delta P = \frac{128\mu L Q}{\pi D_E^4} \quad [5.29]$$

where Q and L represents the volumetric flowrate and channel length. D_E the equivalent diameter for a rectangular channel with width w and height h can be calculated from:

$$D_E = \left(\frac{128wh^3}{\pi K} \right)^{1/4} \quad [5.30]$$

where K is a constant, the value of which is dependent on the ratio w/h (Perry and Green, 1997).

Table 5.12: K values for different channel width to height ratios

w/h	1	1.5	2	3	4	5	10	∞
K	28.45	20.43	17.49	15.19	14.24	13.73	12.81	12

The minimum channel length required at different channel widths were determined and listed in Table 5.13. The change in pressure drop with the listed values of channel equivalent diameter in Table 5.13 is shown in Figure 5.7.

Table 5.13: Dimensions of 0.32 ml reaction channel at different channel widths

Width (μm)	Depth (μm)	Length (mm)	D_E (μm)	$\frac{1}{Pe_r}$	Pe_z
500	83	7680	171.2	44.2	7.7×10^8
1000	170	1920	348.5	11.1	4.8×10^7
2000	330	480	681.9	2.8	3.0×10^6
3000	500	213	1030.5	1.2	5.9×10^5
4000	500	160	1114.9	1.2	3.3×10^5

Shallow channels (for example at 83 and 170 μm) allow for high values of Pe_r^{-1} but result in excessively long reaction channels. The length can be reduced (at such low values of channel depth) by increasing the channel width; however a channel that is too wide may result in unnecessary dead volumes. Narrow channels are also preferred as they minimise the expansion from a mixer width of 200 μm . The criteria for selecting the reactor channel dimension was driven mainly by the decision to adhere to a maximum footprint of 85 mm x 110 mm (approximately the size of 2 credit cards).

The effect of several different values of Pe_r^{-1} at channel width of 2000 μm on the conversion is shown in Figure 5.8. It can be seen that the conversion improves with increasing Pe_r^{-1} up to $Pe_r^{-1} = 2$, beyond which the improvement in conversion is only marginal. For this reason, the 2000 μm wide channel was selected even though the Pe_r^{-1} was below 4 as it allows for a reasonable reactor length to be used. The selected reaction channel dimensions for both the deprotonation reaction and epoxidation reaction are shown in Table 5.14 below.

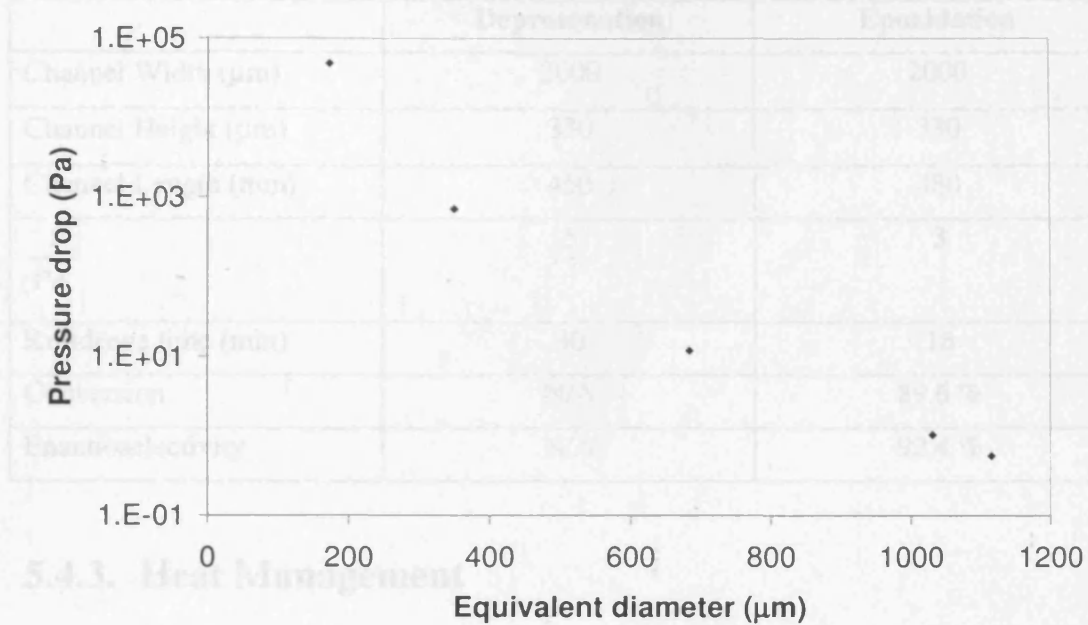
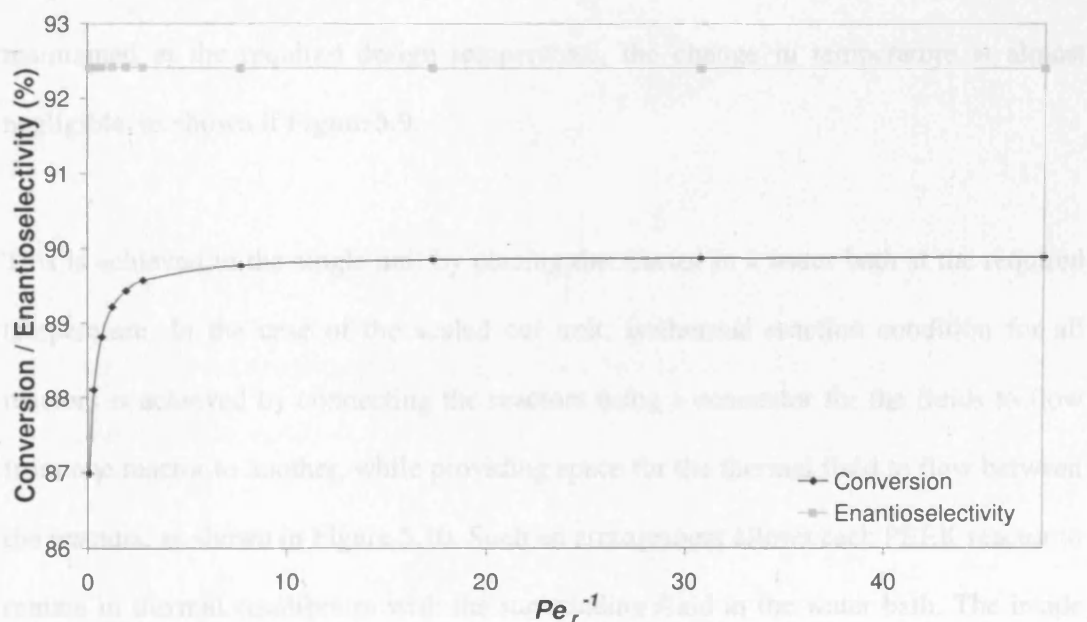
Figure 5.7: Change in pressure drop with channel equivalent diameter**Figure 5.8: Effect of $\frac{1}{Pe_r}$ on conversion and enantioselectivity**

Table 5.14: Reaction Channel dimensions

	Deprotonation	Epoxidation
Channel Width (μm)	2000	2000
Channel Height (μm)	330	330
Channel Length (mm)	450	480
$\frac{1}{Pe_r}$	5	3
Residence time (min)	30	16
Conversion	N/A	89.6 %
Enantioselectivity	N/A	92.4 %

5.4.3. Heat Management

The reaction was found not to be very highly exothermic, with the average heat of reaction measured at around 111 kJ/mol. Consequently, the calculated adiabatic temperature rise is minimal at only 4.9 K. However, if the inside wall temperature was maintained at the required design temperature, the change in temperature is almost negligible, as shown in Figure 5.9.

This is achieved in the single unit by placing the reactor in a water bath at the required temperature. In the case of the scaled out unit, isothermal reaction condition for all reactors is achieved by connecting the reactors using a connector for the fluids to flow from one reactor to another, while providing space for the thermal fluid to flow between the reactors, as shown in Figure 5.10. Such an arrangement allows each PEEK reactor to remain in thermal equilibrium with the surrounding fluid in the water bath. The inside wall temperature was assumed to be equal to the outside wall temperature due to the thin wall layers used (< 2 mm).

Figure 5.9: (a) Adiabatic temperature rise and (b) temperature profile at constant wall temperature, both shown here for a design temperature of 23.1°C.

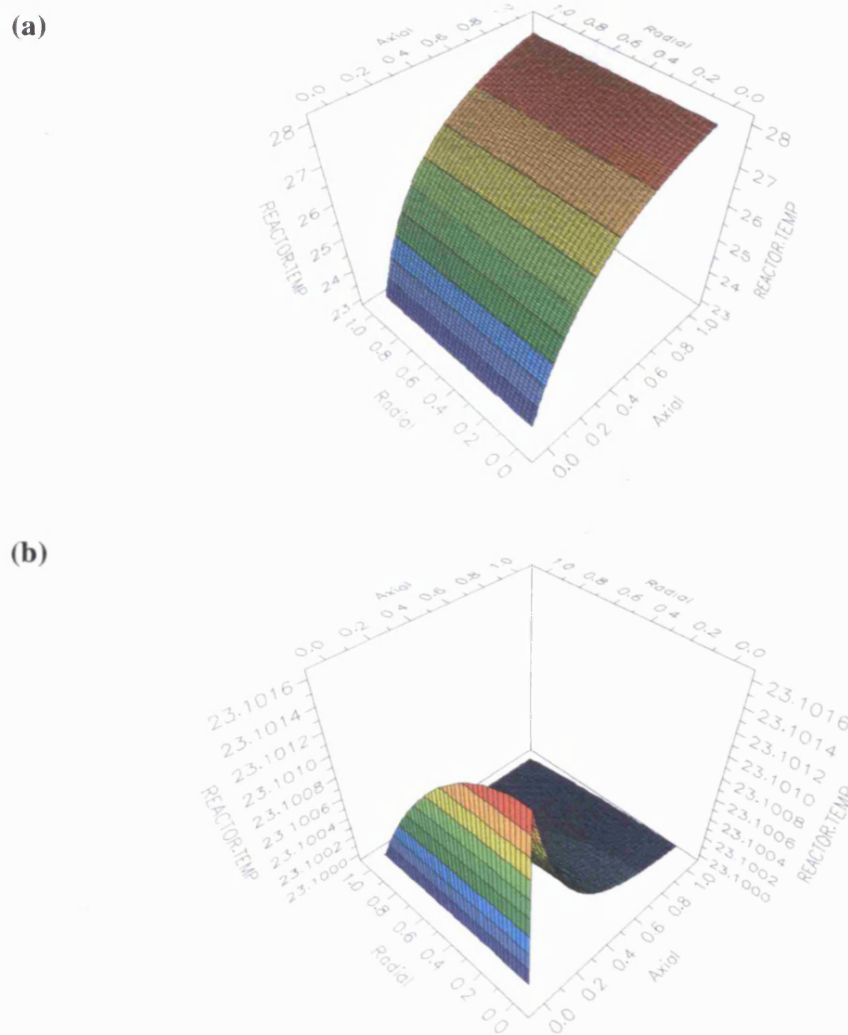
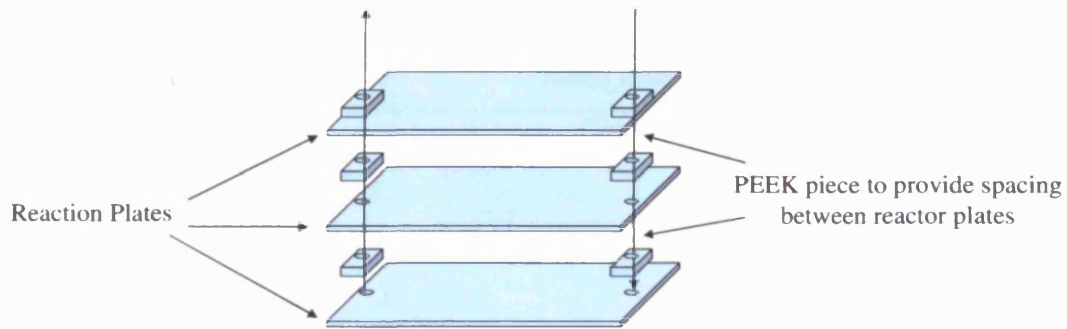


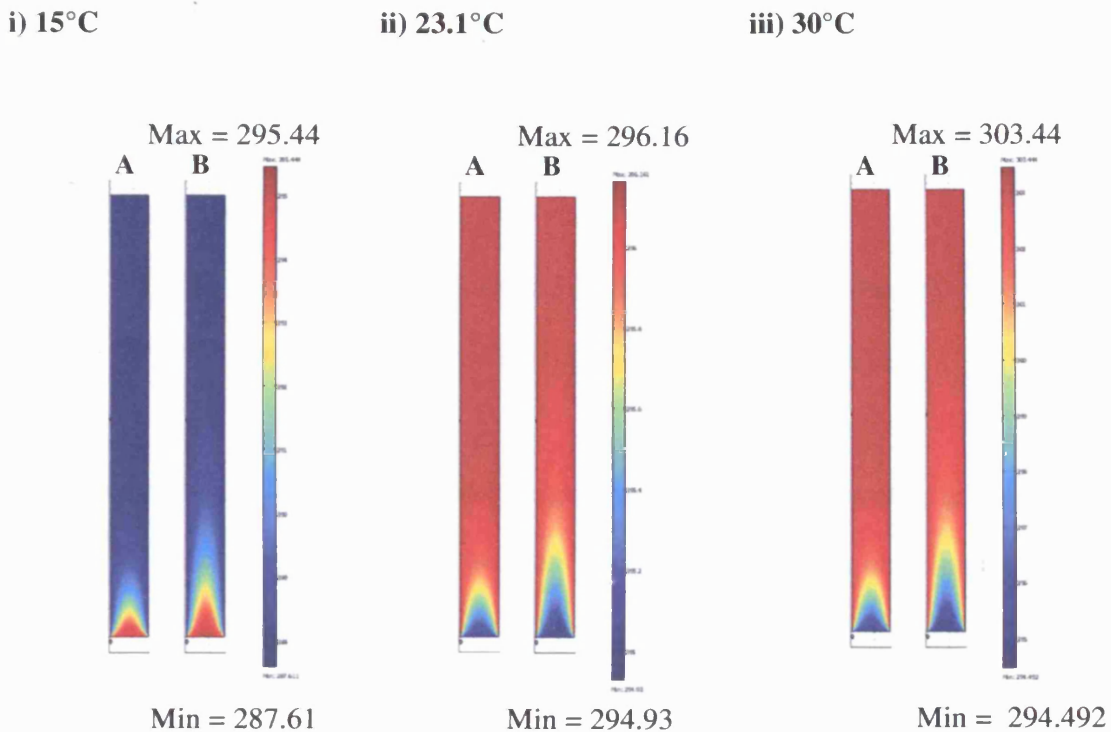
Figure 5.10: Arrangement of scaled out reaction reactors to maintain isothermal conditions in all reactors



A FEMLAB simulation was carried out to ensure that sufficient length is provided for the entering fluids to be heated/cooled to the desired design temperatures prior to contacting. A 1 mm long section of the reactant inlet was simulated, assuming an inlet temperature of 295 K. The simulated geometry and fluid properties are shown in Table 5.15. The temperature profile for design temperatures 15, 23.1 and 30 °C are shown in Figure 5.11, which clearly shows that at constant inside wall temperature, the inlet fluids were heated/cooled to desired design temperature within a very short distance.

Table 5.15: Channel geometry and fluid properties used in FEMLAB simulation

Simulated channel geometry (inlet to mixer section)		
Width (μm)	100	
Depth (μm)	85	
Length (mm)	1	
Fluid properties		Case
	A	B
Density (kg/m ³)	837.73	837.73
Viscosity (Pa s)	0.0004051	0.0004051
Cp (J/kg.K)	1933.5	1933.5
Thermal Conductivity (W/(m.K))	0.14855	0.14855
Inlet velocity (m/s)	9.804 x 10 ⁻³	0.0196
Temperature range (°C)	15 – 30	15 - 30
Boundary Conditions		
Inlet	T = inlet temperature	
Side walls	Thermal insulation	
Top and bottom walls	Fixed wall temperature	
Exit	Convective Flux	

Figure 5.11: Temperature profile of inlet fluids

5.4.4. Materials

Advances in microfabrication techniques mean that microdevices are no longer confined to silicon and are now available in glass, stainless steel, ceramics, polymers such as PMMA, Mylar, polycarbonate, PDMS, COC and PET, alloys and graphite. A review on the production and characteristics of microreactors made of photo-structurable glass Foturun is given by Dietrich et al (2005). A similar review on the potential applications of plastics and polymers as substrate materials in microfluidic applications is also available (de Mello, 2002). The reaction conditions for chalcone epoxidation can be quite harsh due to the choice of reaction solvents such as Tetrahydrofuran and Acetonitrile, which are both incompatible with various materials. The basic condition due to the presence of the organic base DBU further aggravates the situation.

The choice of material of construction should ideally fulfill the following criteria:

- Relatively low cost
- Appropriate chemical compatibility, thermal and electrical properties
- Superior optical properties
- Easily machinable and applicable to mass replication technologies
- Facile bonding and encapsulation of the structured substrate

While for production purposes, a robust material such as stainless steel is generally preferred, for the purpose of this study, stainless steel was ruled out due to the excessive costs involved. Glass, which is inert and has good optical properties, was also ruled out due to the excessive fabrication costs involved. Acrylic which has good optical properties and is relatively inexpensive to fabricate could not be used as it is not chemically compatible with THF and Acetonitrile. PEEK which is chemically compatible with THF and Acetonitrile below 70°C was finally selected as it is relatively inexpensive and is amenable to mass replication. Evidently there are downsides compared to stainless steel, however, in this case the choice was constrained by practical costs considerations. A similar design was also fabricated in acrylic for flow visualisation purposes.

Both the PEEK and Acrylic reactors were fabricated by Epigem Limited, UK using photolithographic methods for microstructures (< 150 µm deep and 300 µm wide) and machining methods for larger mili scale structures. SU-8, an epoxy-based negative photoresist has been gaining popularity as a material of choice for fabrication of microfluidics due to its superior chemical and mechanical properties and ease of fabrication using either x-ray or UV based LIGA process (Song et al, 2004). The

fabrication process at Epigem uses an SU-8 layer spin coated on a substrate (which can be PEEK or Acrylic), where the micro structures are patterned on the SU-8 layer and are therefore completely surrounded by SU-8. The milli scale structures, on the other hand consist of both substrate and SU-8. The reactors are bonded via diffusion bonding using SU-8. The CAD drawing for the reactor layout and PEEK fittings for external fluidic connections are presented in Appendix 5-4.

For the PEEK microstructured reactor design, channel depths of 85 μm for both mixer and reactor channels were etched onto one substrate while the herringbone grooves and reactor channel depth of 245 μm were etched/machined onto another substrate. The two sides are then aligned and bonded together to give a total depth of 85 μm in the micromixer section and 330 μm in the reactor channel section. A microscope photograph of the two sides focussing on the section where the micromixers expand to the reactor entrance is shown in Figure 5.12.

An unbonded microchannel plate etched with SU-8 layer spin coated on PEEK was placed in a solution containing urea-hydrogen peroxide in THF/ACN and DBU and was stirred overnight, with regular replacement of the peroxide and DBU solution (as DBU causes the peroxide to decompose). The depth of the open channel at two different locations (A & B) was measured before and after the tests and did not indicate any major changes. The channel depths were measured using an Olympus BX60 microscope as the difference in the instrument dial reading when the focussing was varied from a point in the channel to another point at the top of the channel. The pictures taken from the microscope along with the depth measurements are shown in Figure 5.13.

Figure 5.12: Microscope photograph of unbonded PEEK reactor (a) Matching PEEK plates which after bonding forms the reactor (b) Herringbone grooves etched on SU-8.

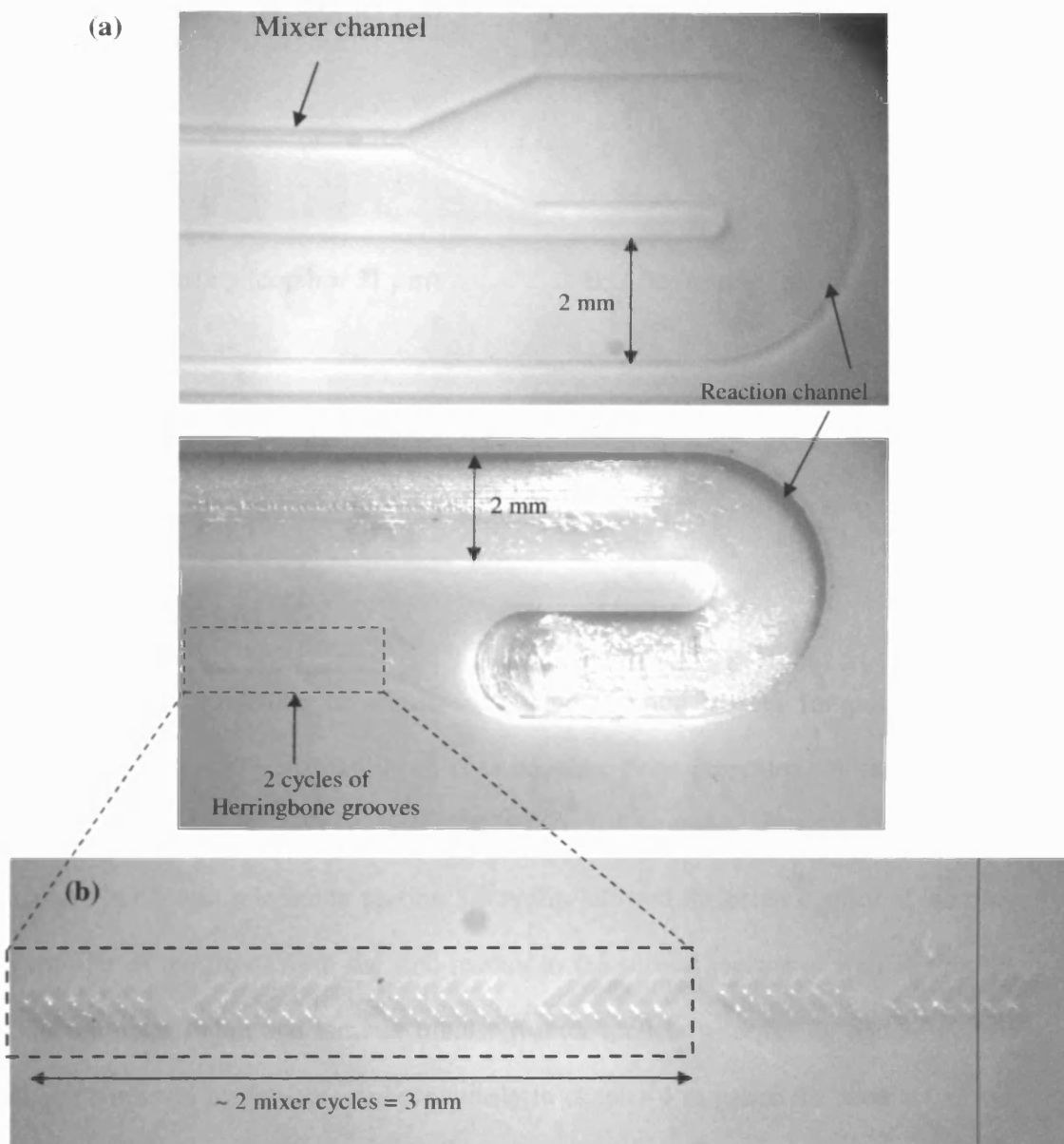


Figure 5.13: Pictures of unbonded SU-8 on PEEK microchannel before and after testing with urea-hydrogen peroxide and DBU in THF/ACN.

A. Before testing (depth = 47 μm)

A. After testing (depth = 48 μm)

B. Before testing (depth = 51 μm)

B. After testing (depth = 53 μm)

5.5. Conclusion

The design and modelling of a microstructured reaction system for poly-*L*-leucine catalysed asymmetric epoxidation of chalcone has been presented. With a view to potentially scale out the system, an external scale-out structure of the microstructured reaction system was selected in section 5.2 as this allowed for better control of the time for transfer of the fluids from the first reactor to the second reactor as well as flexible production rate. Batch and laminar tubular reactor models were set up and compared with experimental results obtained previously in chapter 4 to gauge the accuracy of the model. The rate equations were found to predict the conversion fairly accurately, although enantioselectivity values were less accurate. The ratio of diffusional mixing time to reaction time constants for both the catalysed and background reactions were computed and compared. The catalysed reaction was found to be diffusion-controlled and hence mixing by diffusion alone is not sufficient.

The performance and characteristics of the curved channel mixer, staggered herringbone mixer and split and recombine mixer were compared and the staggered herringbone mixer was selected to enhance the mixing, as it allows rapid mixing with high throughput and lower pressure drop as compared to a plain channel, with a relatively simple construction. A detailed study of the staggered herringbone mixer is presented in Chapter 6.

The reactor channel was dimensioned accordingly to maximise the effects of molecular diffusion so that it approximates that of a plug flow reactor as closely as possible, without excessive length. Sufficient channel lengths were provided at the fluid inlets prior to contacting to ensure all inlet reactants were at the desired design temperatures. Suitable materials of constructions were screened and SU-8 spin coated on a PEEK substrate was selected due to its high chemical resistance and low cost of fabrication. The next step is to test the validity of the design and this is presented in chapter 7.

Chapter 6

Design and Characterisation of Staggered Herringbone Mixer

N.B. This chapter has formed the basis for a poster titled “Numerical Study of Mixing in a Staggered Herringbone Mixer”, presented at the International Conference on Microreaction Technology, Potsdam 2006.

6.1. Introduction

In recent years, microfluidic systems have gained widespread applications in a number of fields such as analytical chemistry, high-throughput synthesis and microchemical processing. One aspect of microfluidic systems that have attracted considerable interest is the mixing of fluids in miniaturized systems. Fluid flows in miniaturized systems are characterized by low values of Reynolds Number ($Re = \rho u l / \mu$). At low Re number, the flow is laminar with parabolic velocity profile and mixing occurs only by molecular diffusion. The characteristic length scales in microfluidic applications are frequently of the order of several hundred microns, which allow rapid mixing by molecular diffusion alone. Examples of such mixers include the T-type and Y-type micromixers (Gobby et al, 2001; Wong et al, 2004). However, in cases where the molecular diffusivity is very low (in biotechnology applications for example, molecular diffusivity for proteins are typically around $10^{-11} \text{ m}^2/\text{s}$), mixing by molecular diffusion becomes very slow, requiring lengths of up to several metres for complete mixing to occur.

Various micromixer designs have been reported, these include various flow lamination mixers such as interdigital micromixers (Hessel et al, 2003; Hardt and Schonfeld, 2003; Lob et al, 2004), split and recombine mixers (Hessel et al, 2003; Schonfeld et al, 2004), geometric focusing mixers (Hessel et al, 2003; Hardt and Schonfeld, 2003; Drese, 2004; Lob et al, 2004), secondary flow micromixers (Mengeaud et al, 2002) and chaotic mixers (Liu et al, 2000; Jen et al, 2003; Jiang et al, 2004). Detailed reviews of the various types of micromixers are available elsewhere (Hardt et al, 2005; Hessel and Lowe, 2005; Hessel et al, 2005; Nguyen and Wu, 2005).

Chaotic micromixers, where the fluid volumes are stretched and folded over the cross section of the channel, are particularly effective for reducing the mixing length. The stretching and folding of fluid volumes proceed exponentially as a function of the axial distance travelled, accelerating the diffusion by increasing the interfacial area for mass transfer and decreasing the striation thickness over which diffusion must occur for complete homogenization. One of the earliest reports on chaotic micromixers was based on placing microstructured objects within the flow passage on one side of the microchannel walls (Stroock et al, 2002; Johnson et al, 2002). Bas-relief structures, such as oblique ridges and staggered herringbones on the floor of channels were used to induce steady chaotic flows in the slanted groove and staggered herringbone micromixers respectively (Stroock et al, 2002). The staggered herringbone offered superior mixing performance at low Re numbers, low resistance to flow and is relatively easy to fabricate using planar lithographic methods. It was found to work well for Reynolds numbers from 1 to 100 and for Peclet numbers of up to 1×10^6 , with the required mixing length increasing only logarithmically with the Peclet number.

The flow patterns in bas-relief structured channels have been studied extensively. A number of numerical studies have been carried out on grooved microchannel mixers which looked at effects of various geometric parameters on mixing performance. Many of the numerical approaches used for characterising mixing performance are based on methods used for macro-scale static mixers such as the coefficient of variance, intensity of segregation, stretching histories, poincare sections, rate of strain tensor, number of striations and residence time distributions (Hobbs and Muzzio, 1997; Hobbs and Muzzio, 1998; Hobbs et al, 1998).

Wang et al (2003) evaluated the slanted groove micromixer using a computational fluid dynamics (CFD) package to simulate the 3D velocity field for particle tracking purposes as well as to study two-fluid mixing. Streaklines from slanted groove microchannels twist in a helical shape, indicating folding and stretching of fluids. Poincare maps¹ were generated by advecting one or a series of passive particles through a series of periodic planes located at the end of each mixing segment and each position of the particle which hits this plane was then recorded. The Poincare map obtained indicated an increase in flow irregularity on increasing the groove aspect ratio, with particle trajectories circling around the flow axis. By counting the dots per circle in the Poincare map, the length required for one complete recirculation was computed, which was then used as a basis for evaluating mixing performance. The length required for one complete recirculation decreased exponentially with increasing groove aspect ratio. The mean helicity², measured from the angle between the longitudinal channel axis and the interfacial line of two fluid streams shifted by the helical flow pattern, was found to be independent of flow velocity and was a function of geometric parameters only, especially the aspect ratio of grooves.

¹ In the study of dynamical systems, Poincare maps are used essentially to describe how points on a plane (the Poincare section) in phase space which is transversed by a periodic or almost periodic orbit of the flow get mapped back onto the plane by the flow. Regular patterns indicate non chaotic flow whereas jumbled patterns indicate the presence of chaotic behaviour.

² The helicity, H_n in a flow is a measure of the extent of corkscrew like motion in the flow, and is defined as $H_n = \frac{u \cdot \omega}{|u||\omega|}$ (Rosaguti et al, 2005).

Schonfeld and Hardt (2004) simulated the helical flows produced in the slanted groove micromixer. The relative transverse velocities as a function of the vertical position were evaluated and found to be in good agreement with experimental results (Stroock et al, 2002). At varying values of α (the ratio of the groove half height to the channel height), the maximum relative transverse velocities obtained was in good agreement with experimentally obtained values and analytical approximations up to $\alpha < 0.45$ (Stroock et al, 2002). Double-sided structured channels were found to increase the relative transverse velocity significantly. The relative transverse velocities were also found to be independent of Reynolds number.

Aubin et al (2003) compared the flow pattern and mixing behaviour in both the slanted groove micromixer and staggered herringbone mixers using CFD and particle tracking methods. Quantitative methods commonly used for characterization of mixing performance in macro-scale static mixers were presented and used to quantify the mixing quality in both types of mixers. Better mixing was achieved in the staggered herringbone micromixer due to the formation of two helical flows, with alternating small and large vortices rotating in opposite directions. Calculation of variance of the dispersion of particle tracers and the mean stretching of fluid filaments were found to be good methods for characterizing the mixers while the rate of strain tensor appeared not to be well adapted for the mixers studied.

More recently, Aubin et al (2005) studied the effects of geometric parameters such as groove depth, number of grooves per cycle and groove width on the mixing quality. An alternative method for characterizing the mixing performance was introduced, which is based on a statistical method called nearest neighbour analysis. Other methods for

characterising the mixing performance include measurement of the maximum striation thickness as a function of mixer length and the residence time distribution. Mixing quality was improved with deeper and wider grooves, but was relatively unaffected by the number of grooves per cycle. Residence time distribution was improved compared to Poiseuille flow, although wider grooves were observed to give rise to dead volumes in the microchannel.

Simple analytical models have been derived for the flow behaviour in both slanted groove and staggered herringbone micromixers (Stroock et al, 2002; Stroock and McGraw, 2004). Poincare maps and mixing simulations using the models indicate the existence of an optimal degree of asymmetry, p (fraction of channel width occupied by the wide arm of the herringbones) for the herringbone grooves in the interval $\frac{7}{12} < p < \frac{2}{3}$.

For a fixed value of the ratio of transverse to axial velocity, a minimum axial length per half-cycle was required, below which mixing is poor. Improvement in the residence time distribution compared to Poiseuille flow was also reported, although it was noted that the model does not capture the effects of dead volume due to the presence of grooves.

Kang and Kwon (2004) compared the flow characteristics in slanted groove, staggered herringbone and barrier embedded slanted groove micromixers using a coloured particle tracking method. Transverse velocity vector plots at different downstream locations as well as Poincare maps obtained for all three micromixers indicated chaotic flow for both staggered herringbone and barrier embedded micromixers, but no notable chaotic mechanism was observed for slanted groove micromixers, in agreement with results reported earlier (Wang et al, 2003). Particle tracers were labelled with a specific colour

and the particle trajectories tracked for 20 periodic units. The coloured particle distributions were then used to evaluate the mixing quality both qualitatively as well as quantitatively, using a new method based on mixing entropy. The staggered herringbone was found to give the best mixing performance.

Liu et al (2004) presented a numerical study of mixing pure water and a solution of glycerol in water, in both the 3-D serpentine and staggered herringbone mixers. The effect of different fluid physical properties was examined by varying the amount of glycerol in the glycerol/water solution φ (i.e. the mass fraction of glycerol in water) at two different Reynolds number, $Re = 1$ and $Re = 10$. The mixing performance at both Re , measured via a mixing index, decreased with increasing φ , although the variation in mixing index was smaller at higher Re . Tracer particles initially located at two-fluid interface were advected inside the mixer and the distribution of tracer particles at the outlet cross section were more or less identical at different Re and at different φ . Inspection of the cross-section mixing concentration profiles obtained from the numerical simulation revealed that the breakdown and deformation of the interface between the two fluids at $Re = 1$ and $Re = 10$ were similar and independent of φ , although the gray intensity (which represents the mixedness of the two fluids) at lower Re (at all φ) was more uniform than the corresponding picture at higher Re . This was due to the longer residence time available for diffusional mixing at lower Re . The gray intensity gradually turned less uniform with increasing φ , at both Re , due to lower diffusivity values. Unlike the 3-D serpentine mixers, the flow advection in the staggered herringbone mixer was not enhanced with increasing Re , in agreement with experimental observation (Stroock et al, 2002).

Yang et al (2005) presented a numerical study of the effects of geometric parameters such as depth ratio of the grooves, asymmetry index, groove intersection angle and upstream to downstream channel width ratio on the mixing performance of the staggered herringbone mixer. Two dominant mechanisms of mixing were identified; the stretching and folding of the interface due to the vortical motions of flow at the groove's side edge and the increase in contact area between the two fluids due to underside fluid transportation. The groove depth ratio and asymmetry index were found to be the most relevant. Results from a pressure loss analysis indicated better mixing with higher groove flow rate, which can be achieved by decreasing the asymmetry index and increasing the depth ratio of the groove.

The effect of the groove asymmetry and the number of grooves per half cycle on the mixing performance was also investigated by Li and Chen (2005), using the Lattice-Boltzmann method. The optimal value for the above geometric parameters were found to be 0.6 for the groove width fraction (a measure of the groove asymmetry) and 5 -6 grooves per half cycle.

The velocity generated by the grooves in a staggered herringbone mixer and the effect of varying Re on the generation of cross channel flow and mixing have been investigated in detail by Hassell and Zimmerman (2006). Three representative geometries were evaluated; a single herringbone groove, a channel section representing one continuous herringbone cycle and a third representing a system in which the orientation of the grooves were constantly switched. As Re is increased, the amount of entrained fluid in the groove decreases and the fluids in the groove move further across the groove before re-entering the bulk channel flow at the channel edges. Increasing the

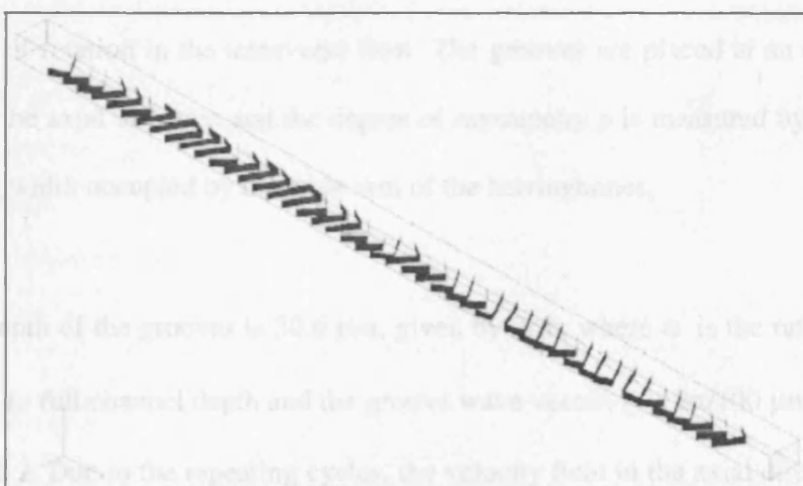
groove depth results in increased fluid entrainment in the grooves leading to an increase in non-axial velocity component in the bulk flow, in agreement with earlier studies (Aubin et al, 2005). Successive grooves resulted in an increase in the non-axial velocity components and a 14 % increase in fluid entrainment in grooves compared to the case of the single groove. The fluid flow in the bulk channel flow was found to exhibit low helicity which increases slightly at higher Re.

Recently an alternative method for characterizing and quantifying the degree of mixing was presented by Camesasca et al (2005). The Shannon entropy S, which has been previously employed for a variety of practical applications in polymer processing, was used to compare the mixing performance in a plain microchannel, a slanted groove microchannel as well as the staggered herringbone micromixer. The staggered herringbone mixer was shown to perform better than the slanted groove mixer, with no mixing observed in the plain channel, as expected. The method can also be applied to experimental data; using experimentally derived pictures of the mixer cross section for the staggered herringbone mixer, the change in entropy with increasing number of cycles was compared to the values obtained numerically, with excellent agreement in both values.

Camesasca et al (2006) presented an alternative way to pattern ridges on the walls of a simple straight channel to achieve chaotic mixing. Three types of non-periodic patterns were generated using the Weierstrass fractal function to position the tip of 'V' grooves on the bottom channel wall and the performance of these mixers was compared to a design which was similar to the staggered herringbone mixer. Qualitative analysis of the cross-sectional velocity field along the length of the channel as well as pathlines of

particle trajectories and trajectory ‘beams’ confirm the presence of chaotic flow for all four mixers. Evaluation of Lyapunov exponents allowed for a limited assessment of mixing behaviour while entropic analysis allowed a more global characterization of mixing performance. Two of the new mixers designed were found to be more efficient than the one based on the staggered herringbone mixer. Generalized fractal dimensions associated with the interface of the two fluids to be mixed were computed for all four mixer designs and the results were consistent with results from entropic mixing analysis.

Figure 6.1: 3D geometry of one of the channels with asymmetric V-shaped ridges using the Weierstrass function to generate the position of the ‘V’ groove on the bottom wall.



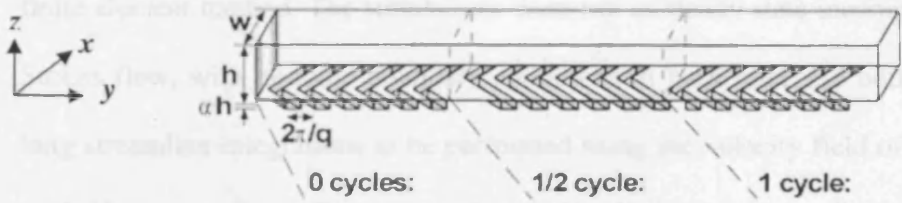
In the current work, the flow behaviour of the staggered herringbone mixer is studied using computational fluid dynamics and particle tracking methods. Several methods which were previously reported for characterising the mixing performance in macro-scale static mixers were used such as the coefficient of variance of the distribution of particle tracers and the stretching histories of the particles. The geometric mean stretch

computed from the stretching histories is then used to compute the minimum mixing length required for complete mixing, by taking into account the rate of striation reduction and diffusional penetration distance.

6.2. Numerical Methods

The mixer geometry used was kept consistent with that reported by Stroock et al (2002). The channel width is 200 μm and the channel height is 85 μm . The staggered herringbone mixer is composed of several mixing cycles in series. Each mixing cycle is composed of two sets of herringbone grooves which are asymmetric with respect to the centre of the channel in the axial direction. The orientation of the asymmetric herringbones is switched between each half cycle, allowing a corresponding switch in the center of rotation in the transverse flow. The grooves are placed at an angle θ with respect to the axial direction and the degree of asymmetry p is measured by the fraction of channel width occupied by the wide arm of the herringbones.

The full depth of the grooves is 30.6 μm , given by $2\alpha h$, where α is the ratio of groove half-depth to full channel depth and the groove wave vector, q is $2\pi/100 \mu\text{m}^{-1}$, as shown in Figure 6.2. Due to the repeating cycles, the velocity field in the axial direction can be assumed to be periodic and hence the velocity field in one mixing cycle can be obtained and reused repeatedly for successive cycles. Details of the mixer geometry and fluid properties are summarised in Table 6.1 below.

Figure 6.2: Staggered Herringbone Mixer (from Stroock et al, 2002)**Table 6.1: Mixer geometry and fluid properties**

Mixer	
Channel Width, w	200 μm
Channel Depth, h	85 μm
Length per cycle	1.516 mm
Number of grooves per cycle	12
Relative groove depth (α)	0.18
Wave Vector, q	$2\pi/100 \mu\text{m}$
Groove Asymmetry	2/3
θ	45°
Fluid Properties	
Density	1200 kg/m^3
Viscosity	0.067 Pa s

6.2.1. Velocity Field

The 3D-velocity field for one complete mixing cycle was computed using COMSOL Multiphysics which is a commercial multiphysics modelling software based on the finite element method. The simulations were run as steady state incompressible Navier-Stokes flow, with periodic boundary conditions at both inlet and outlet. This enables long streamline integrations to be performed using the velocity field of a single mixing cycle if entrance flow effects are neglected. No slip boundary conditions were applied at all other channel walls. The volumetric flow through the mixer was set by specifying a pressure drop and setting the pressure at the outlet equal to the pressure at the inlet minus the pressure drop. The number of mesh elements in the model is 30712 and the simulations were performed on Windows XP with Pentium IV 3.00 GHz CPU and 2 GB of RAM.

Evaluation of mixing performance is typically carried out by simultaneously solving the Navier-Stokes and continuity equations for the velocity field and the convection-diffusion equations for the concentration profiles in the mixer. However, this approach introduces artificial diffusive fluxes due to discretisation errors, especially for liquid/liquid mixing (Jiang et al, 2004; Schonfeld and Hardt, 2004). Lagrangian particle tracking methods, where the trajectories of massless tracer particles are computed have been used to characterize the mixing performance, to avoid numerical diffusion problems (Hobbs and Muzzio, 1997; Hobbs and Muzzio, 1998; Hobbs et al, 1998; Aubin et al, 2003; Wang et al, 2003; Kang and Kwon, 2004; Aubin et al, 2005). The 3-D velocity field was first computed as described above. Streamline integration of the velocity field, which will be described in the following section, then allows the particle trajectories in the micromixer to be computed.

6.2.2. Particle Tracking Computations

6.2.2.1. Particle Trajectories

The particle trajectories in the herringbone mixer were obtained by solving the vector equation of motion for each particle:

$$\frac{d\vec{x}}{dt} = v(x) \quad [6.1]$$

where \vec{x} is the particle position vector, $v(x)$ is the particle velocity vector and t is the time. For a particle at a given location (x, y, z) , the particle velocity is obtained by interpolating the velocity field from the solution of the Navier-Stokes and continuity equations. The COMSOL particle tracking algorithm was modified to allow for the velocity field obtained in a single mixing cycle to be utilised over successive mixing cycles. The algorithm to achieve this was set up as follows:

- i) Based on the particle axial position and mixer length per cycle, establish in which cycle number the particle is located.
- ii) Determine the equivalent position in the first mixing cycle (where the velocity field solution is available)
- iii) Interpolate the velocity field solution to obtain the velocity at that position
- iv) Calculate new position by solving [6.1].

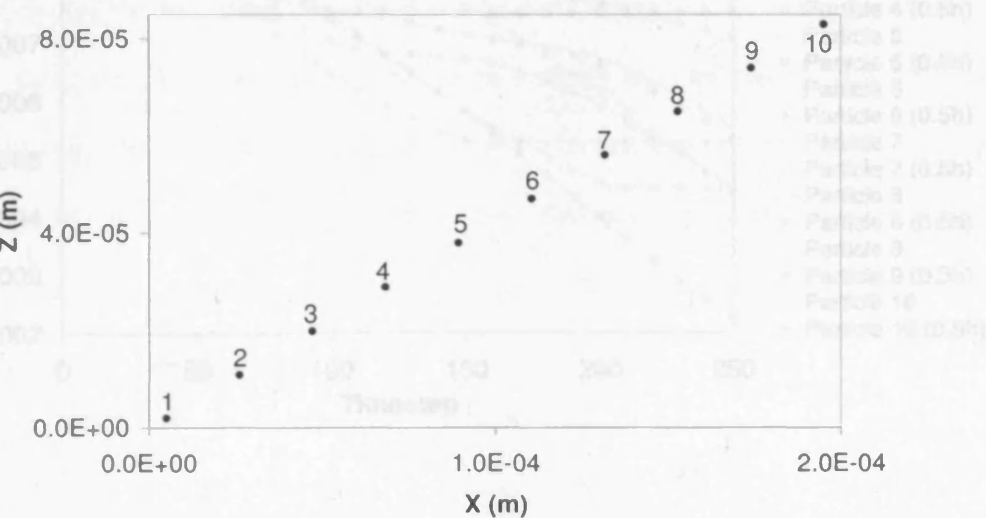
The particle is moved to a new position down the channel length at every time step, information about the new coordinates is stored and the procedure repeated for the specified number of time steps. A standard fourth order Runge-Kutta method with fixed time steps was used. The size of the time step was selected carefully to avoid losing particles (too big a time step will result in the particle moving to a position outside the solution domain and the particle is then ‘lost’) while at the same time avoiding

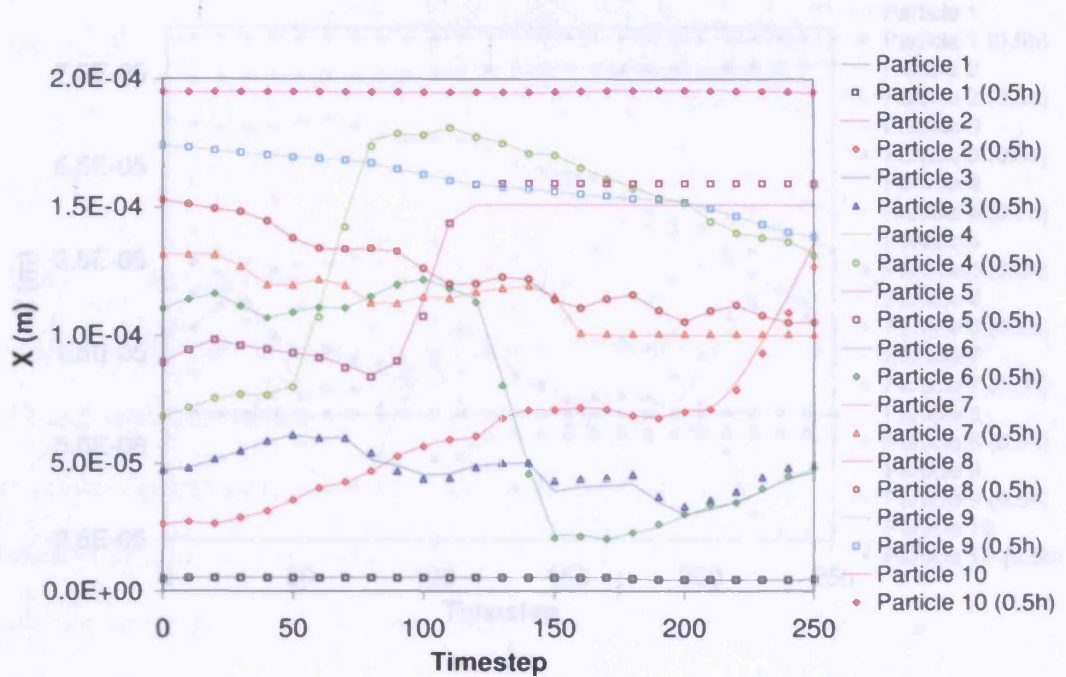
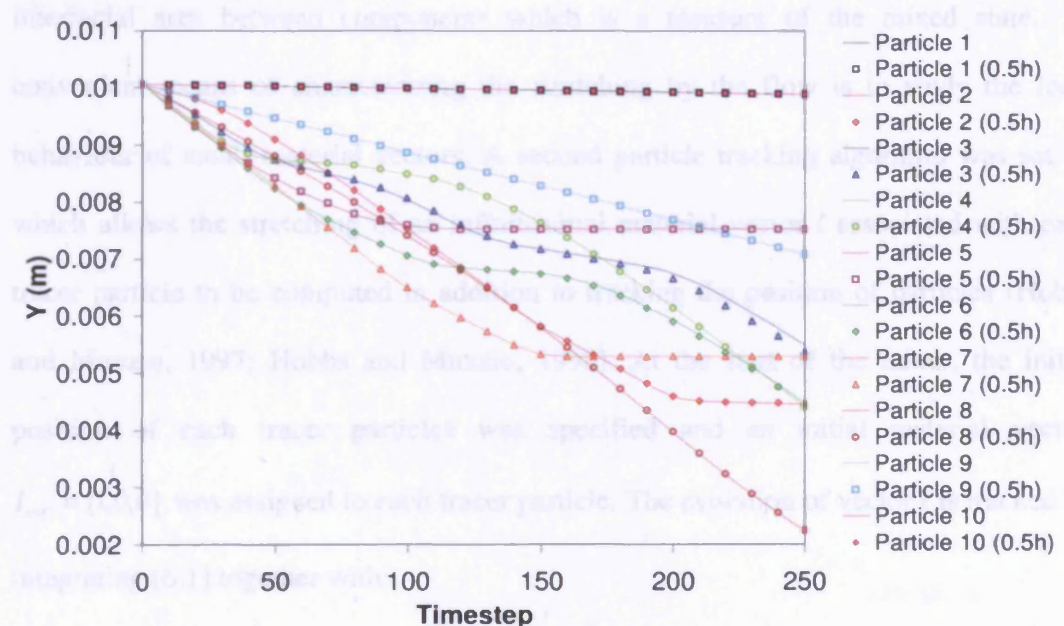
excessive computation time. The coordinates of the particle at the end of every mixing cycle were recorded. Figure 6.3 shows particle trajectories for 10 particles initially located across the mixer cross section computed at the selected time step, $h = 0.1$ s and at half the time step, $0.5h = 0.05$ s.

As shown in Figure 6.3, the selected time step is reasonably accurate as the computed trajectory at half the initial time step is not substantially different in most cases. Particles located in the middle of the channel were observed to show the biggest difference in computed particle trajectory, due to the bigger change in velocities in these areas. However, even in these cases the difference in particle coordinate values were only about 4 % relative to channel dimensions and so the initial time step was selected to avoid excessive computation time. The Matlab code for the particle tracking algorithm can be found in Appendix 6-1.

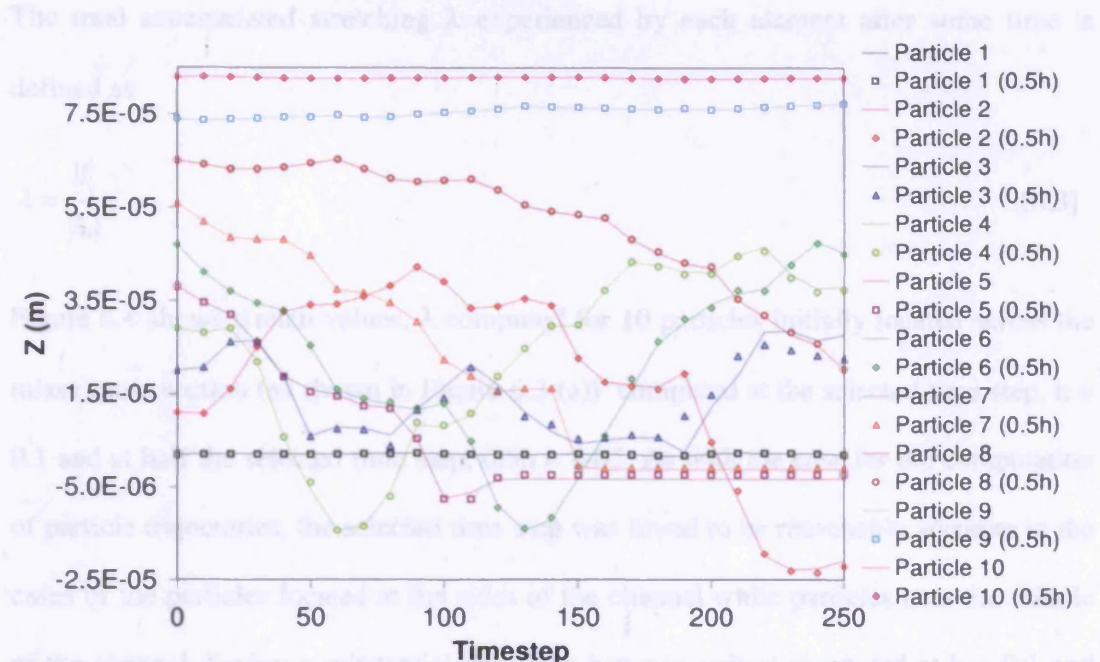
Figure 6.3: Computed particle trajectories at a time step of $h = 0.1$ and 0.05 , for 10 different initial locations.

a) Initial location of 10 particles



b) Particle trajectories in the x-direction**6.2.2.3. Stretching****c) Particle trajectories in the y-direction**

d) Particle trajectories in the z-direction



6.2.2.2. Stretching

The stretching of material lines and surfaces by a flow is useful for determining the interfacial area between components which is a measure of the mixed state. A convenient means of characterizing the stretching by the flow is to study the local behaviour of small material vectors. A second particle tracking algorithm was set up which allows the stretching of an infinitesimal material vector l associated with each tracer particle to be computed in addition to tracking the position of particles (Hobbs and Muzzio, 1997; Hobbs and Muzzio, 1998). At the start of the mixer, the initial position of each tracer particles was specified and an initial material vector, $l_{t=0} = [1,0,0]$ was assigned to each tracer particle. The evolution of vector l is tracked by integrating [6.1] together with:

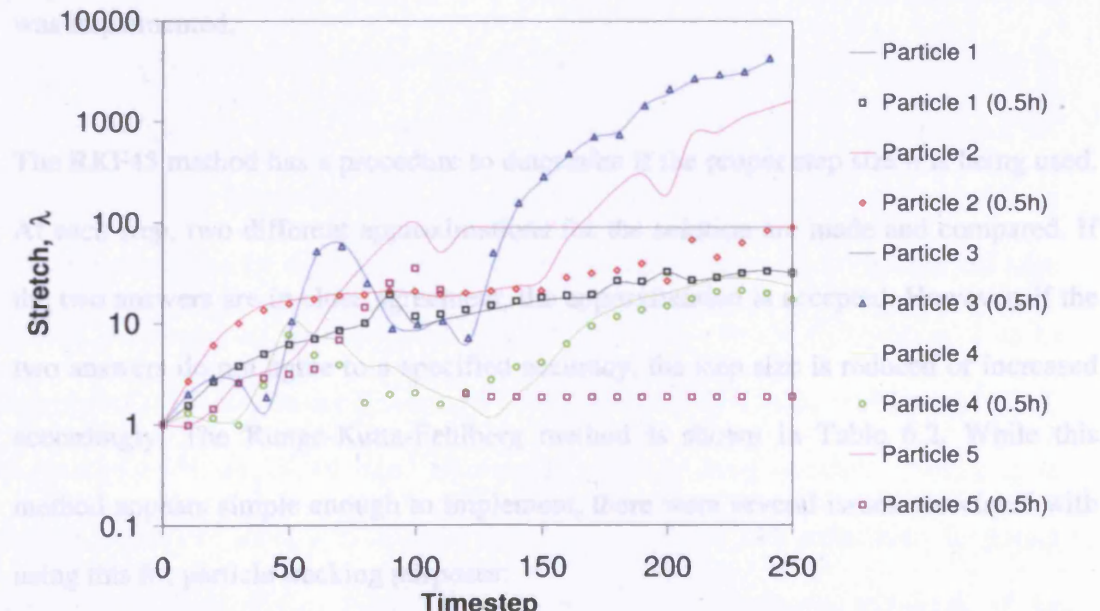
$$\frac{d(l)}{dt} = (\nabla v)^T \cdot l \quad [6.2]$$

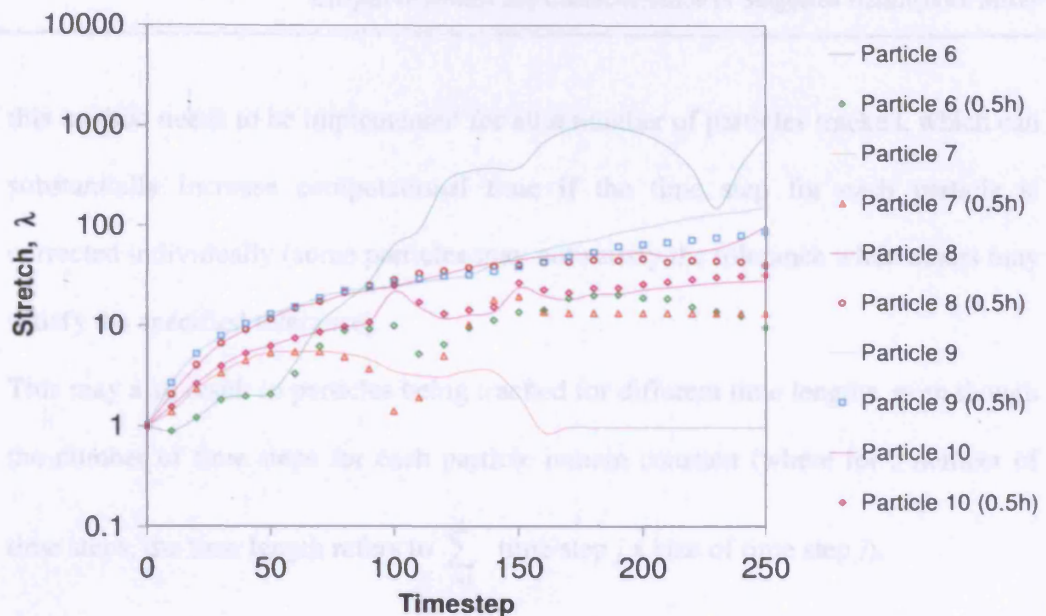
The total accumulated stretching λ experienced by each element after some time is defined as

$$\lambda = \frac{|l|}{|l_0|} \quad [6.3]$$

Figure 6.4 shows stretch values, λ computed for 10 particles initially located across the mixer cross section (as shown in Figure 6.3 (a)) computed at the selected time step, $h = 0.1$ and at half the selected time step, $0.5h = 0.05$. As with the case for the computation of particle trajectories, the selected time step was found to be reasonably accurate in the cases of the particles located at the sides of the channel while particles near the middle of the channel display a substantial deviation between values computed at $h = 0.1$ and $0.5h = 0.05$.

Figure 6.4: Computed stretch values at a time step of $h = 0.1$ and 0.05 , for 10 different initial locations.





One way of improving the accuracy of the computation is by repeating the exercise above i.e. solving the problem twice, using step sizes h and $h/2$ and comparing the answers at the mesh points corresponding to the larger step size. However, this requires a significant amount of computation for the smaller step size and must be repeated if the agreement is not good enough. To resolve this problem, the Runge-Kutta-Fehlberg method (RKF45) (Mathews and Fink, 2004) which is an adaptive time stepping method, was implemented.

The RKF45 method has a procedure to determine if the proper step size h is being used. At each step, two different approximations for the solution are made and compared. If the two answers are in close agreement, the approximation is accepted. However, if the two answers do not agree to a specified accuracy, the step size is reduced or increased accordingly. The Runge-Kutta-Fehlberg method is shown in Table 6.2. While this method appears simple enough to implement, there were several issues associated with using this for particle tracking purposes:

- this method needs to be implemented for all n number of particles tracked, which can substantially increase computational time if the time step for each particle is corrected individually (some particles may not satisfy the tolerance while others may satisfy the specified tolerance).
- This may also result in particles being tracked for different time lengths, even though the number of time steps for each particle remain constant (where for z number of time steps, the time length refers to $\sum_{j=1}^z$ time step $j \times$ size of time step j).
- To satisfy the desired accuracy, the step size may also be reduced such that the total time length tracked is very small. This will cause fewer particles to be advected to the end of the 8 mixing cycles and hence affect the computation of mean stretch values at the end of each mixing cycle, since the mean stretch value is then computed from a smaller number of particles.

To address these issues, the following steps were taken. The algorithm was set up such that at every time step, the optimal step size for each particle was computed. If all particles satisfy the specified tolerance, the solution is accepted. However, if some of the particles do not satisfy the specified tolerance, the step size is modified for all particles using the minimum of all optimal step sizes computed. This ensures that all particles are tracked for the same total time lengths and reduced the computational time required, compared to modifying the step size for each particle individually. Due to limited available computational memory, a minimum step size value was also specified, which requires balancing the need to improve accuracy using as small a time step as possible on the one hand, with the need to track the particles for a sufficiently long total time length to maximise the number of particles that can be advected to the end of the mixing cycle.

Table 6.2: Runge-Kutta-Fehlberg Method (RKF45)

Each step requires the use of the following six values:

$$k_1 = hf(t_k, y_k)$$

$$k_2 = hf(t_k + \frac{1}{4}h, y_k + \frac{1}{4}k_1)$$

$$k_3 = hf(t_k + \frac{3}{8}h, y_k + \frac{3}{32}k_1 + \frac{9}{32}k_2)$$

$$k_4 = hf(t_k + \frac{12}{13}h, y_k + \frac{1932}{2197}k_1 - \frac{7200}{2197}k_2 + \frac{7296}{2197}k_3)$$

$$k_5 = hf(t_k + h, y_k + \frac{439}{216}k_1 - 8k_2 + \frac{3680}{513}k_3 - \frac{845}{4104}k_4)$$

$$k_6 = hf(t_k + \frac{1}{2}h, y_k - \frac{8}{27}k_1 + 2k_2 - \frac{3544}{2565}k_3 + \frac{1859}{4104}k_4 - \frac{11}{40}k_5)$$

An approximation to the solution using a Runge-Kutta method of order 4 is made from:

$$y_{k+1} = y_k + \frac{25}{216}k_1 + \frac{1408}{2565}k_3 + \frac{2197}{4101}k_4 - \frac{1}{5}k_5$$

A better value for the solution is determined using a Runge-Kutta method of order 5:

$$z_{k+1} = y_k + \frac{16}{135}k_1 + \frac{6656}{12825}k_3 + \frac{28561}{56430}k_4 - \frac{9}{50}k_5 + \frac{2}{55}k_6$$

The optimal step size (sh) is determined by multiplying the scalar s with the current step size h. The scalar s is calculated from

$$s = \left(\frac{tol \cdot h}{2|z_{k+1} - y_{k+1}|} \right)^{1/4}$$

For 4100 particles, the maximum number of time steps that can be used which still allows all data associated with each particle to be stored was determined to be 6000. The minimum step size was set such that 4100 particles can be tracked for a minimum total time length of 2 residence times (in an 8 cycle micromixer) to maximize the number of particles that have advected to the end of the mixer. The algorithm can be summarised as follows:

- i) At each time step, two different approximations for the solution are made, y_{k+1} , using a Runge-Kutta method of order 4 and z_{k+1} , using a Runge-Kutta method of order 5. The scalar s for all n particles is computed.
- ii) If $s > 1$ for all particles, the first approximation (y_{k+1}) is accepted.
- iii) If any of computed $s < 1$, then the optimal step size sh is computed from the minimum of all s values, s_{min} . The larger of the two values, $s_{min}h$ and h_{min} (the specified minimum step size) is then used to compute the solution for all particles using the Runge-Kutta method of order 4.

The Matlab code for the stretching computations using the Runge-Kutta-Fehlberg method can be found in Appendix 6-3.

6.3. Results and Discussions

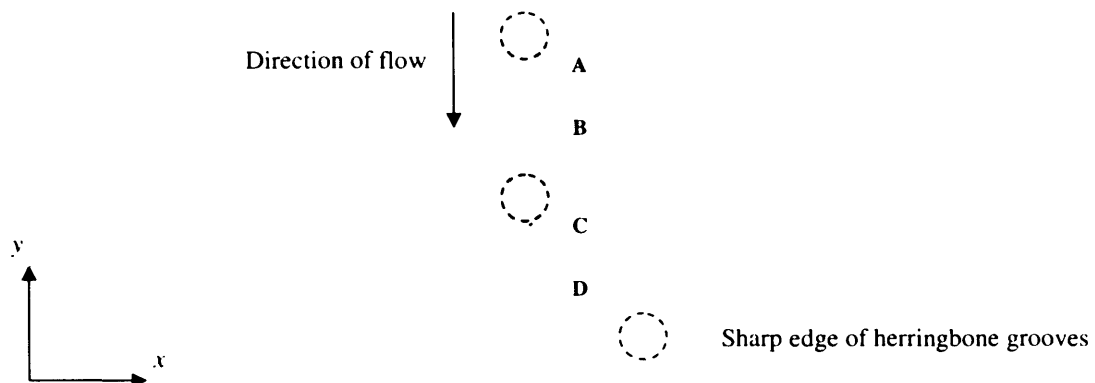
6.3.1. Flow Patterns

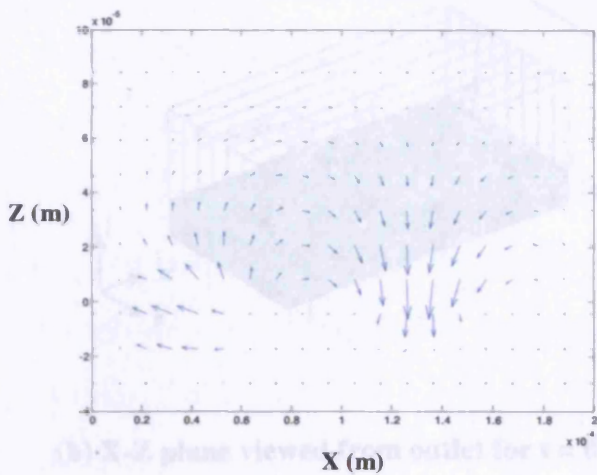
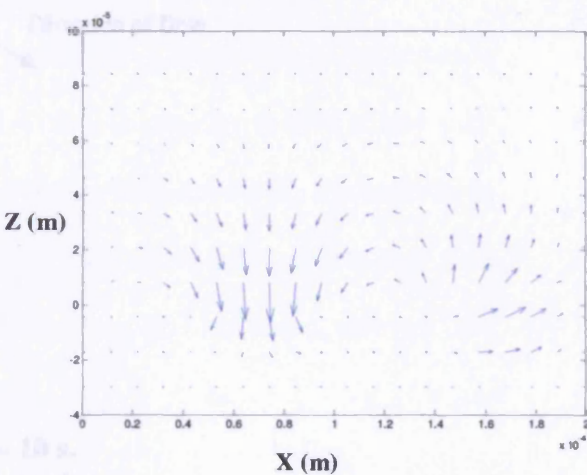
The cross-sectional velocity vector plots at various locations along one mixing cycle at $Re = 0.01$, as indicated in Figure 6.5(a), are shown in Figure 6.5(b). The flow patterns are complex with a strong transverse component. As the flow moves along in the axial direction, two counter rotating vortices are produced, consisting of one large vortex and one small vortex. The two vortices meet over the sharp edge (at $X = 1.3$ for locations A & B and $X = 0.7$ for locations C & D) of the herringbone grooves (see Figure 6.5) and

alternate periodically depending on the direction of asymmetry of the herringbone grooves. The maximum and minimum velocities in the x, y and z directions are also indicated in Figure 6.5, where the negative sign represents flow in the opposite direction. Figure 6.6 shows the particle trajectories at 10 sample points initially located across the mixer cross section. The particle trajectories show small scale helical motion similar to the results of Wang et al (2003), which indicates folding and stretching of fluids. The herringbone grooves aid mixing not only by creating secondary helical flow but also by 'ditch mixing' where fluid from one side of the channel is transported to the opposite side of the channel in the grooves and rolls out from the grooves at the side edge back into the main flow in the channel (Bennett and Wiggins, 2003). This results in increased contact area between the two fluids that enhance mixing. Mixing in the staggered herringbone mixer is therefore enhanced by both the strong transverse flow which stretches and folds the fluid interface and increased contact area by ditch mixing.

Figure 6.5: Cross-sectional velocity vector plots at various axial positions for $Re = 0.01$

(a) Axial position of the cross-sectional velocity vector plots

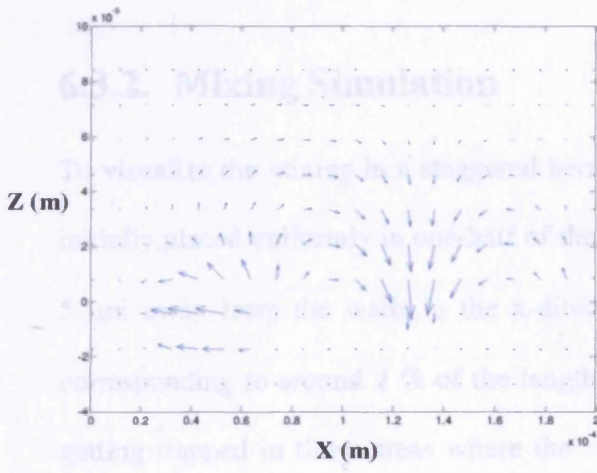
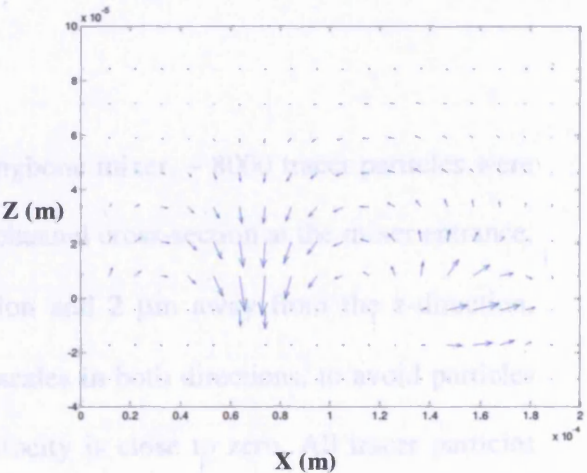


(b) Velocity vector plots
Section A

Section C

Velocity (m/s)
Max
Min

X	1.401 x 10 ⁻⁴	-3.021 x 10 ⁻⁴
Y	3.78 x 10 ⁻³	-8.832 x 10 ⁻⁶
Z	2.297 x 10 ⁻⁴	-5.225 x 10 ⁻⁴

Velocity (m/s)
Max
Min

X	2.779 x 10 ⁻⁴	-1.114 x 10 ⁻⁴
Y	3.772 x 10 ⁻³	-9.597 x 10 ⁻⁶
Z	2.363 x 10 ⁻⁴	-4.864 x 10 ⁻⁴

Section B

Section D

Velocity (m/s)
Max
Min

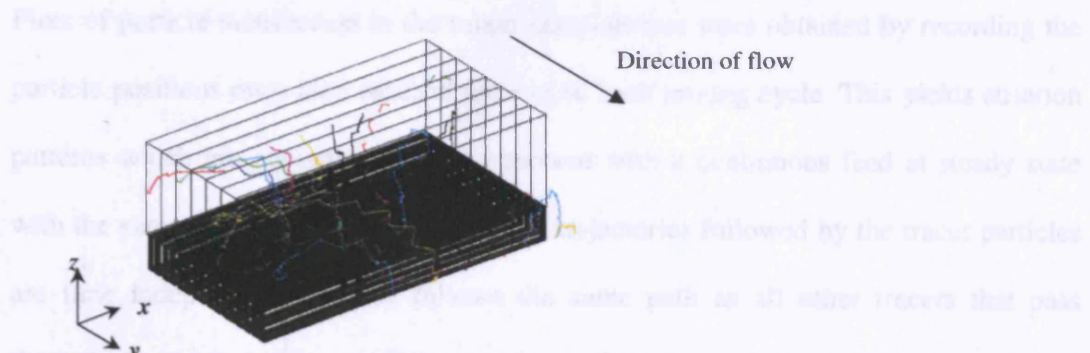
X	1.342 x 10 ⁻⁴	-3.588 x 10 ⁻⁴
Y	3.785 x 10 ⁻³	-2.339 x 10 ⁻⁵
Z	2.125 x 10 ⁻⁴	-4.324 x 10 ⁻⁴

Velocity (m/s)
Max
Min

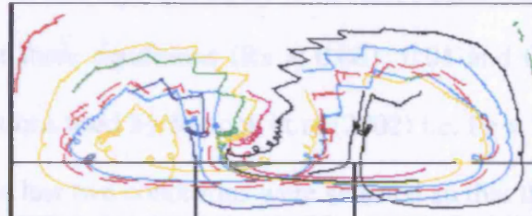
X	3.41 x 10 ⁻⁴	-1.419 x 10 ⁻⁴
Y	3.778 x 10 ⁻³	-1.068 x 10 ⁻⁵
Z	2.094 x 10 ⁻⁴	-5.018 x 10 ⁻⁴

Figure 6.6: Particle trajectories of 10 samples points at $Re = 0.01$

(a) Particle trajectories at 10 different initial locations along 8 mixing cycles for $t = 0 - 10$ s



(b) X-Z plane viewed from outlet for $t = 0 - 10$ s.



The time simulations were carried out for $Re = 0.01$, 0.03 , 0.05 , 0.08 , 1 and 10 . The Reynolds numbers $Re = 0.01$, 0.03 , 0.05 , 0.08 correspond to the three displacement conditions 0.0001 , 0.0003 , 0.0005 , 0.0008 and 0.0012 of Figure 5.8. The last two cases ($Re = 1$ and 10) correspond to a larger range of Reynolds number and are evaluated. X and Z sizes used for all cases are shown in Table 6.1.

6.3.2. Mixing Simulation

To visualize the mixing in a staggered herringbone mixer, ~ 8000 tracer particles were initially placed uniformly in one-half of the channel cross-section at the mixer entrance, $5 \mu\text{m}$ away from the walls in the x -direction and $2 \mu\text{m}$ away from the z -direction, corresponding to around 2 % of the length scales in both directions, to avoid particles getting trapped in those areas where the velocity is close to zero. All tracer particles were released simultaneously and the position of the tracer particles was tracked along the mixer length as described in Section 6.2.2.1.

The tracer particles travel along the mixer length at different speeds due to the Poiseuille flow profile and the presence of dead volumes in the herringbone grooves. Plots of particle distribution in the mixer cross-section were obtained by recording the particle positions once they reached the end of each mixing cycle. This yields striation patterns which are equivalent to that observed with a continuous feed at steady state with the same initial conditions because the trajectories followed by the tracer particles are time independent; a tracer follows the same path as all other tracers that pass through the same starting position regardless of its time of introduction (Stroock and McGraw, 2004).

The mixing simulations were carried out at the following conditions: $Re = 0.001, 0.01, 0.03, 1$ and 10 . The first three conditions ($Re = 0.001, 0.01$ and 0.03) correspond to three experimental conditions used by Stroock et al (2002) i.e. $Pe = 20000, 200000$ and 900000 in Figure 5.6. The last two conditions were selected so that the effect of a larger range of Reynolds number can be evaluated. The step sizes used for all cases are shown in Table 6.3.

Table 6.3: Step sizes used for all simulation cases

Cases	Time step sizes (s)	Number of time steps
Re 0.001	0.1	4000
Re 0.01	0.01	4000
Re 0.03	0.002	4000
Re 1	7.2×10^{-5}	4000
Re 10	7.2×10^{-6}	4000

The mixer cross-sectional plots at $Re \sim 0.01$ at the mixer inlet and at various locations downstream of the entrance are shown in Figure 6.7. The simulation plots were compared to published experimental confocal micrographs at the same conditions (Stroock et al, 2002) and the evolution of striation patterns can be seen to be qualitatively similar, indicating that the numerical simulation method used can capture the flow phenomena accurately. Small differences between the simulation and experimental micrographs can be attributed to the fact that the computed velocity field assumes identical fluid properties for the two inlets to be mixed as this allows the velocity field to be used repeatedly over successive mixing cycles while in practice this was clearly not the case. Additionally, the simulation plots do not take into account molecular diffusion effects.

The cross-sectional plots at the same axial positions were observed to be qualitatively similar at all Re , with no major differences in the patterns of the tracer particles. The flow advection in a staggered herringbone mixer was found to be independent of Reynolds number, as shown in Figure 6.8 and hence non-inertial in origin, which is in agreement with other numerical studies on the staggered herringbone mixer (Stroock and McGraw, 2004; Liu et al, 2004) as well as experimental results where the flow patterns was found to be qualitatively similar up to $Re = 100$ (Stroock et al, 2002).

Figure 6.7: Comparison of the evolution of particle tracer positions along the mixer length with confocal micrographs of an actual staggered herringbone mixer. Both the simulation plot and experimental confocal micrographs were obtained at $Re = 0.01$.

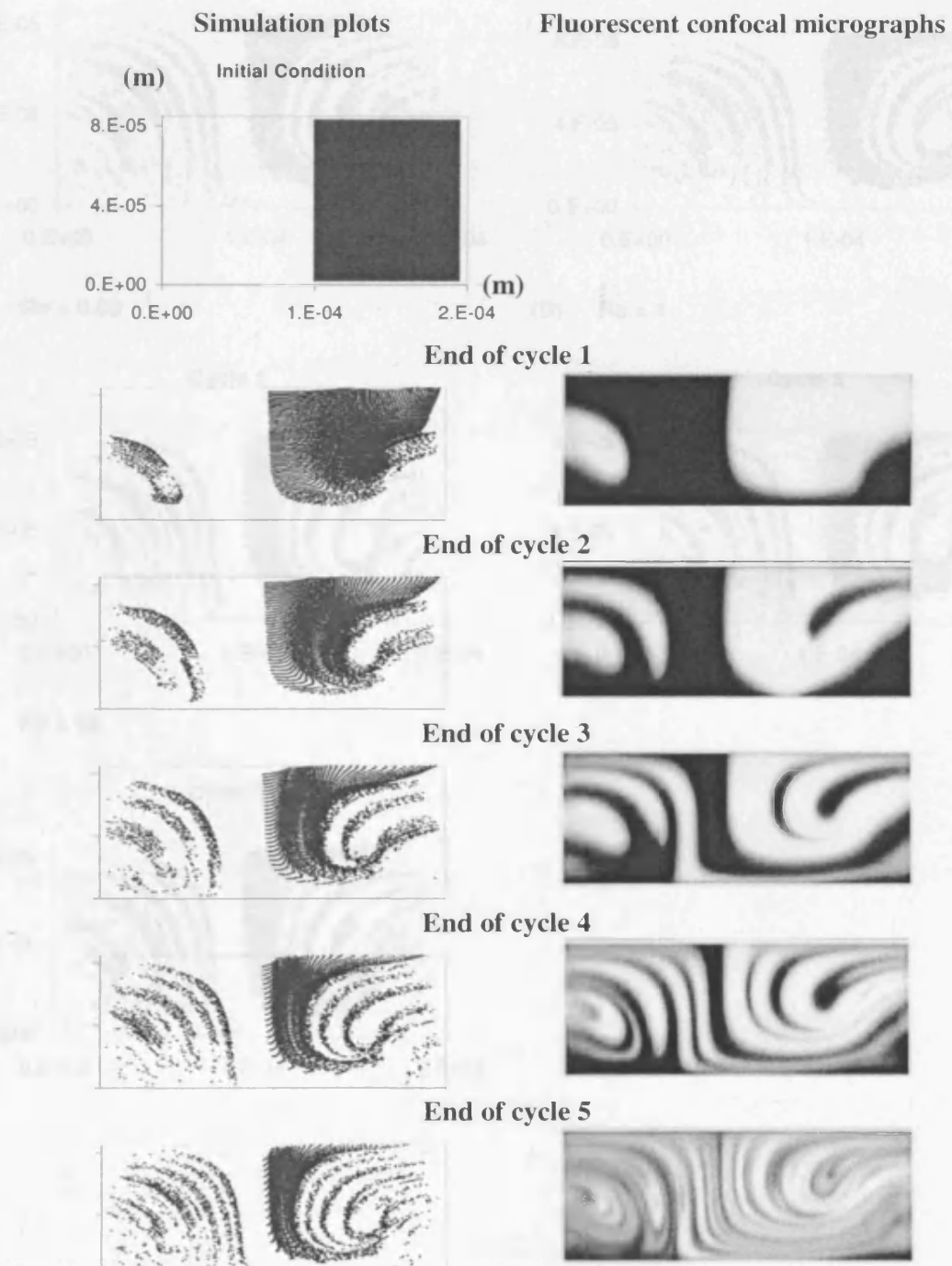
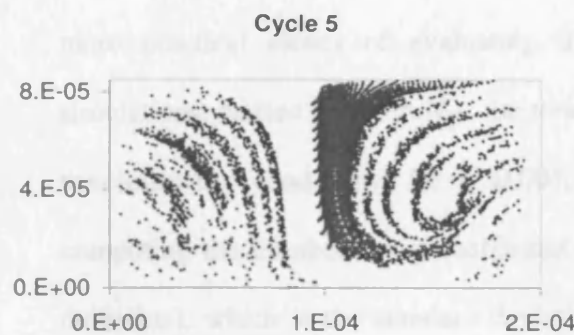
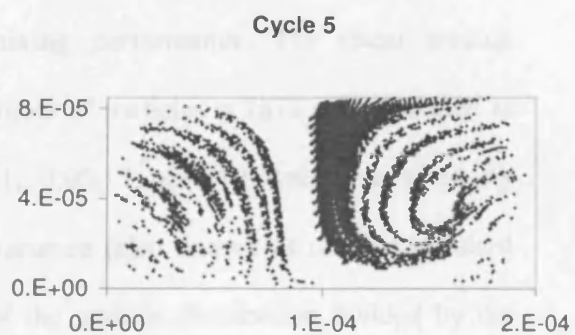
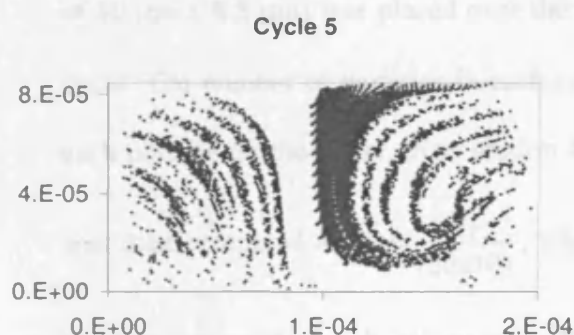
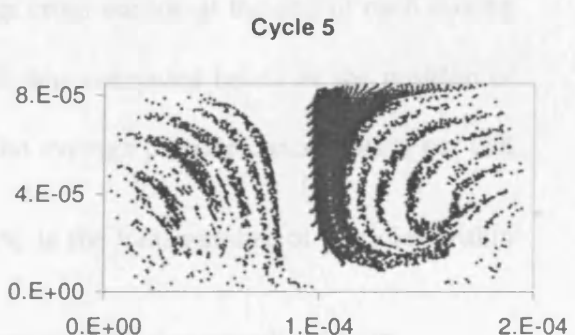
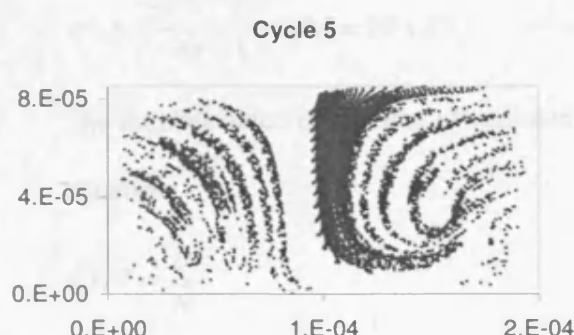


Figure 6.8: Comparison of particle distribution cross-sectional plots at the end of cycle 5, at $Re = 0.001, 0.01, 0.03, 1$ and 10 .

(A) $Re = 0.001$ (B) $Re = 0.01$ (C) $Re = 0.03$ (D) $Re = 1$ (E) $Re = 10$ 

6.3.3. Coefficient of Variance

While the mixing simulations allowed for a good qualitative assessment of mixing in a staggered herringbone mixer, a quantitative description of the mixing quality affords a more practical means of evaluating the mixing performance. The tracer mixing simulations, carried out with N_{T0} , the total number of particles = 7872 and evaluated at the following conditions: $Re = 0.001, 0.01, 0.03, 1$ and 10 were quantified by computing the number-based coefficient of variance (also known as relative standard deviation), which is the standard deviation of the particle distribution divided by the mean. A 20×10 X-Z grid of equal-sized cells (each cell with approximate dimensions of $10 \mu\text{m} \times 8.5 \mu\text{m}$) was placed over the mixer cross section at the end of each mixing cycle. The number of particles in each cell, N_i was computed based on the position of each particle on the mixer cross section and the average particle concentration per cell

was then computed as $\bar{N} = \frac{N_T}{(20 \times 10)}$, where N_T is the total number of particles within

the grid at the end of each mixing cycle. The variance σ^2 was calculated from:

$$\sigma^2 = \frac{\sum_{i=1}^M (N_i - \bar{N})^2}{M - 1}, M = 20 \times 10 \quad [6.4]$$

The number based coefficient of variance (COV) was then computed from the following equation:

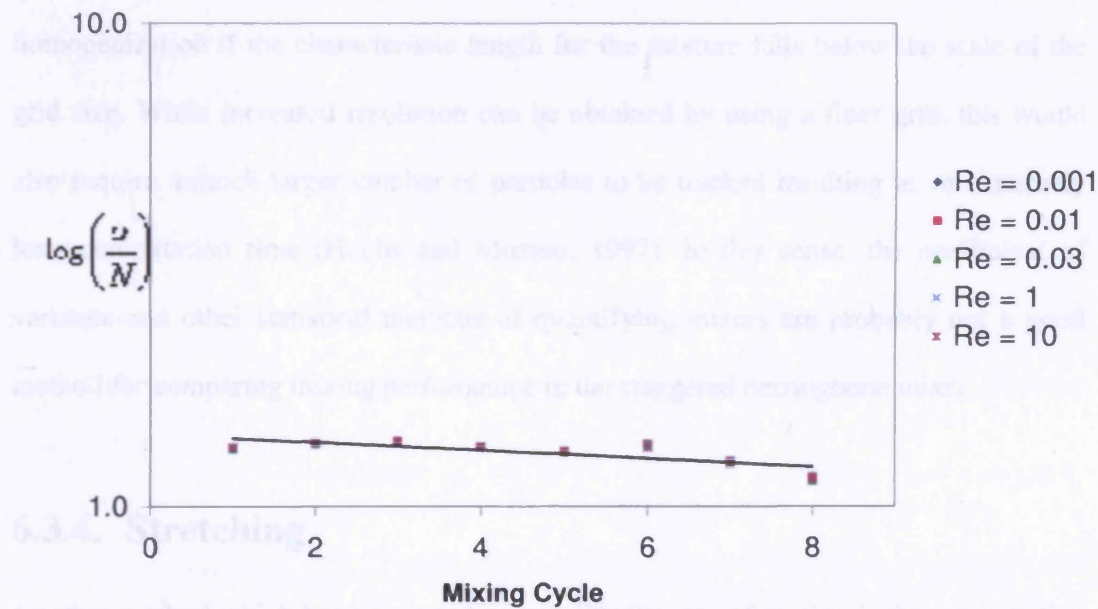
$$COV = \frac{\sigma}{\bar{N}} \quad [6.5]$$

When the COV is zero, an ideal homogenization of the mixture is obtained. The coefficient of variance at different mixing cycles can be fitted to an equation of the form:

$$\frac{\sigma}{\bar{N}} = A \exp(-Bx), \quad x = \text{mixing cycle number} \quad [6.6]$$

The coefficient B represents the rate of decrease of the coefficient of variance per mixing cycle and provides a simple quantitative estimate of the mixing rate while the coefficient A represents the coefficient of variance of the unmixed inlet stream. The results of the coefficient of variance plotted against the number of mixing cycles at different Reynolds number is shown in Figure 6.9.

Figure 6.9: Change in coefficient of variance with number of mixing cycles at $Re = 0.001$ to 10 (All data points at different Re overlap).



The calculated coefficient of variance gradually decreases with increasing number of cycles at all values of Re . The change in coefficient of variance with increasing number of cycles at $Re = 0.001$ to 10 were observed to be very similar. The value of the coefficient B was $\sim 0.023 \pm 0.002$ in all cases considered, indicating little difference in mixing rates. This is consistent with the qualitative evaluation of the striation patterns formed, which were observed to be independent of Re .

The total number of particles at each mixer cross-section gradually decreases from the initial number of particles released at the inlet resulting in decreasing number of tracked points with increasing mixer cycle, which affects the accuracy of the calculations. This is due to increasingly more particles being left behind in the cycle grooves, as a result of the dead volumes in the mixer. The number of tracked points reduced by an average of 201 particles every cycle, which represents an average reduction of 6 % per cycle.

Additionally, the grid size used in the calculation may limit the resolution of mixture homogenization if the characteristic length for the mixture falls below the scale of the grid size. While increased resolution can be obtained by using a finer grid, this would also require a much larger number of particles to be tracked resulting in an extremely long computation time (Hobbs and Muzzio, 1997). In this sense, the coefficient of variance and other statistical methods of quantifying mixers are probably not a good method for comparing mixing performance in the staggered herringbone mixer.

6.3.4. Stretching

Another method which has been used to quantify the rate of mixing is the computation of the stretching histories along with the trajectories of a set of material elements placed within the flow (Hobbs and Muzzio, 1997; Hobbs and Muzzio, 1998; Aubin et al, 2003). This method has been employed in evaluating the mixing and chaotic behaviour in two-dimensional, time periodic flows as well as three-dimensional static mixers.

The key to effective mixing is in producing the maximum amount of interfacial area between two initially segregated fluids in the minimum amount of time. The amount of intermaterial surface generated in a region is directly proportional to the amount of stretching experienced by fluid elements in that region; regions with high rates of stretching provide good mixing while regions with low rates of stretching provide poor mixing. The distance between striations, however, is inversely proportional to the surface area. Hence, the rate of stretching and folding affects the rate of micromixing by both reducing the striation thickness (and hence the diffusional distance) and increasing the interfacial area for interdiffusion of components (Ottino and Wiggins, 2004).

Chaotic flow is associated with an exponential rate of stretching and folding, resulting in a corresponding decrease in the axial length required for complete mixing. Stretching computations can be used to evaluate the chaotic behaviour and hence mixing efficiency in the mixers, which for a time periodic system, can be expressed by the Lyapunov

exponent, $\delta = \lim_{t \rightarrow \infty} \frac{\ln \lambda}{t}$ (Khakhar et al, 1987; Aubin et al, 2003). The stretching computations can also be used to characterize the distribution of mixing intensities from the distribution of stretching magnitudes in the mixer flow (Khakhar et al, 1987; Hobbs and Muzzio, 1997; Hobbs and Muzzio, 1998).

For the stretching calculations, 4100 particles were placed uniformly across the channel cross section at the mixer entrance, 5 μm away from the channel walls in the x-direction and 2 μm away in the z-direction. The tracer particle position and the accumulated length stretch were tracked along the mixer length as described in Section 6.2.2.2. The initial and minimum time step specified for all simulation cases are shown in Table 6.4.

Table 6.4: Initial and minimum time step sizes for all simulation cases

Cases	Initial step size (s)	Minimum step size (s)
Re 0.001	0.05	0.025
Re 0.01	0.005	0.0025
Re 0.03	0.001	0.0005
Re 1	3.6×10^{-5}	1.8×10^{-5}
Re 10	3.6×10^{-6}	1.8×10^{-6}

At every periodic plane, both the tracer particle position and the components of the stretch vector were recorded. The geometric mean stretching values for all N tracer particles was computed at every periodic plane from

$$\lambda_{g,50} = \left(\prod_{i=1}^N \lambda_i \right)^{\frac{1}{N}} \quad [6.7]$$

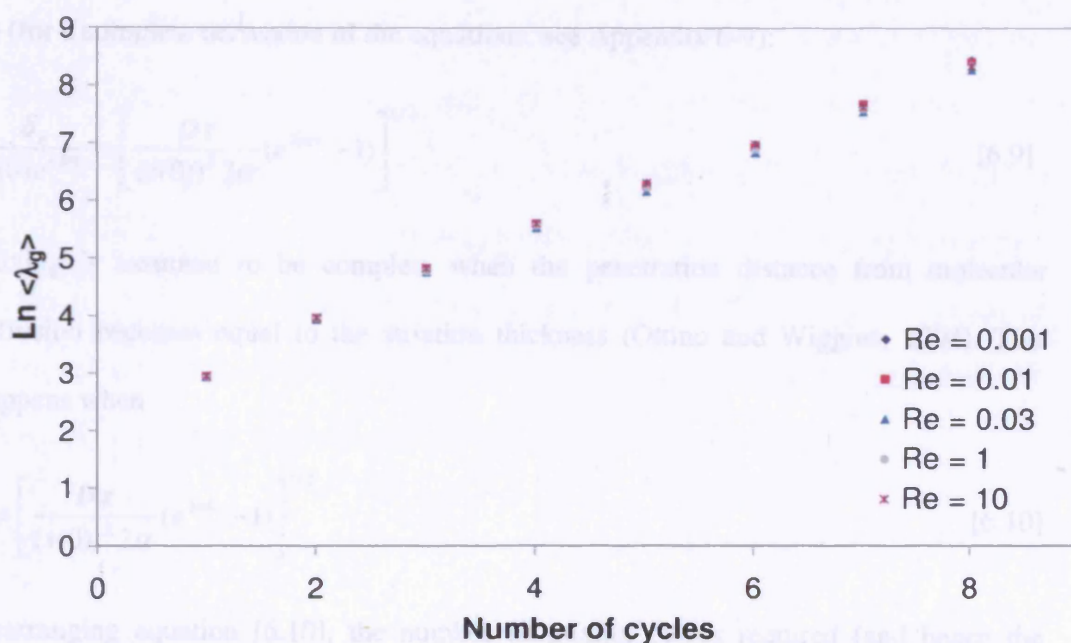
The specific stretch per period, α_{50} for a spatially periodic flow, which is the direct analog of the Lyapunov exponent, δ for a time periodic flow (Hobbs and Muzzio, 1997; Hobbs and Muzzio, 1998; Aubin et al, 2003), was computed from:

$$\alpha_{50} = \lim_{n \rightarrow \infty} \left[\frac{1}{n} \ln \lambda_{g,50} \right], n = \text{period} \quad [6.8]$$

The logarithm $\ln \lambda_{g,50}$ is plotted against the number of mixing cycles in Figure 6.10 for the following conditions: Re = 0.001, 0.01, 0.03, 1 and 10. In chaotic flows, the value α_{50} tends to positive limit values implying exponential stretching and growth of inter-material area (on average) while in regular flows this value tends to zero (Khakhar et al, 1987). The values of α_{50} at different Reynolds number were obtained from the gradients of the plots in Figure 6.10.

The mean stretch, $\lambda_{g,50}$ increases exponentially with the number of mixing cycles at every Reynolds number considered. The values of α_{50} were found to be similar with no distinct trend with respect to Re, while the values of α_{50} showed a greater particular trend with respect to Re with $\alpha_{50} = 0.75 \pm 0.01$ in all cases.

Figure 6.10: $\ln\langle\lambda_{g,50}\rangle$ vs number of mixing cycles at various Re (Data points at the 50% mixing length, α_{50})



It is clear from the results of the mixing simulations in Figure 6.8 that the form of the flow remains qualitatively the same at different Re number, which is in agreement with published findings (Stroock et al, 2002; Stroock and McGraw, 2004; Liu et al, 2004). The difference in mixing uniformity at various Pe number observed in Figure 5.6 can then be attributed to the effects of molecular diffusion and hence to compute the required length for complete mixing, the role of molecular diffusion must also be considered.

Recall that the exponential stretching of fluid elements accelerate mixing in two different ways, that is by reducing the striation thickness and by generating a greater interfacial area for molecular diffusion. For a spatially periodic flow, the penetration distance due to molecular diffusion increases along the mixer length while the striation thickness is reduced from $s(0)$ to $s(N)$, according to the stretching function, α . The ratio of penetration distance to striation thickness evolves along the mixer length according to (for a complete derivation of the equations, see Appendix 6-9):

$$\frac{\delta_x}{s(0)e^{-\alpha N}} = \left[\frac{D\tau}{(s(0))^2 2\alpha} (e^{2\alpha N} - 1) \right]^{1/2} \quad [6.9]$$

Mixing is assumed to be complete when the penetration distance from molecular diffusion becomes equal to the striation thickness (Ottino and Wiggins, 2004). This happens when

$$1 = \left[\frac{D\tau}{(s(0))^2 2\alpha} (e^{2\alpha N} - 1) \right]^{1/2} \quad [6.10]$$

Rearranging equation [6.10], the number of mixing cycles required (and hence the mixing length) for complete mixing is determined from:

$$N = \frac{\ln\left(\frac{(s(0))^2 2\alpha}{D\tau} + 1\right)}{2\alpha} \quad [6.11]$$

$$y = N \cdot L_{\text{cycle}} \quad [6.12]$$

The required mixing lengths (y_{50}) computed using the mean stretch values (α_{50}) are shown in Figure 6.11 along with mixing lengths obtained experimentally by Stroock et al (2002). The mixing lengths calculated using the specific stretch per period were observed to be different from those derived experimentally.

This can be due to the following:

- the experimentally derived values are based on measurements in the central 50 % of the cross sectional area, where striation thickness reduction can be seen to be much slower than say, at the bottom or sides of the channel. Additionally, the experimentally derived mixing lengths were determined for 90 % mixing.
- The specific stretch per period used to compute the mixing lengths was derived from the mean stretch values in each period (this represents rate of increase in the mean stretch values with increasing mixing cycle), when in reality there exists a log-normal distribution of stretch values (Ottino and Wiggins, 2004), as shown in Figure 6.12. The scatter plots represent the probability density calculated from frequency data for the stretch values at various mixing cycles while the smooth lines represent normal distribution curves fitted using the computed mean and standard deviation values. The normal distribution is defined as the distribution with density:

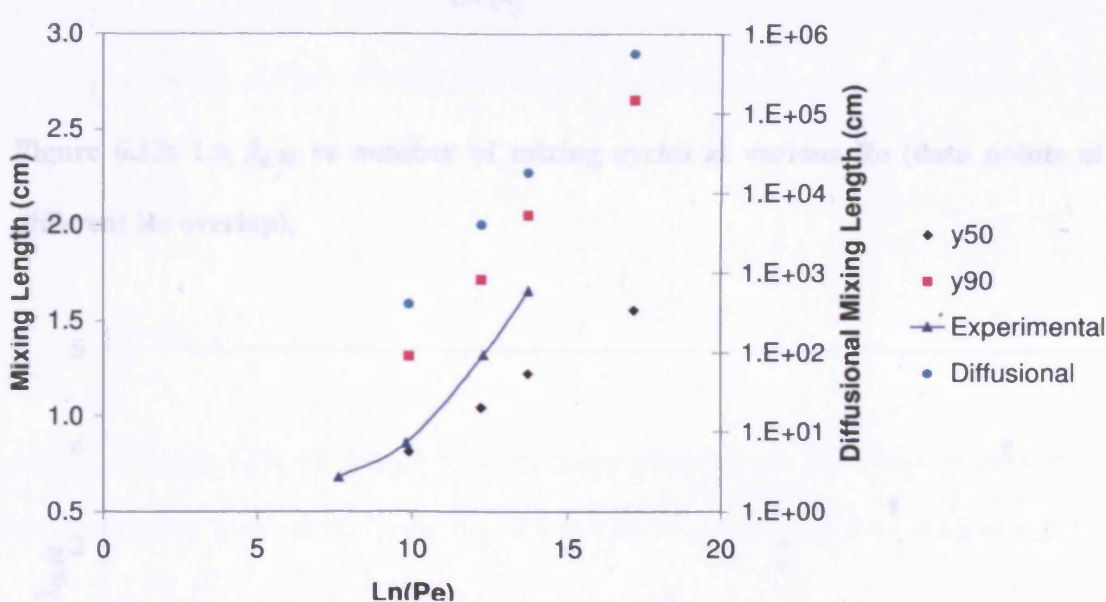
$$f(x) = \frac{1}{\sigma\sqrt{2\pi}} e^{-\frac{1}{2}\left(\frac{x-\mu}{\sigma}\right)^2} \quad [6.13]$$

where x represents $\ln(\lambda)$, μ represents the mean and σ represents the standard deviation.

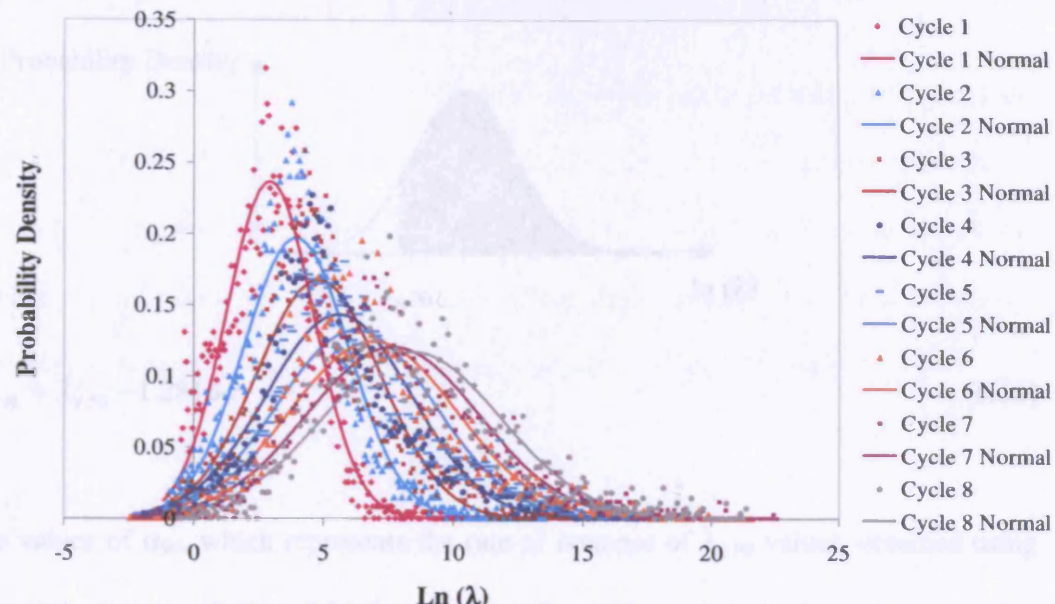
- As demonstrated in Figure 6.4, the accuracy of the computed stretch values can be sensitive to the time step used. While this problem may be alleviated using a smaller time step and implementing adaptive time-step control, there is a tradeoff between using an infinitely small time step to improve accuracy and running the simulation for a sufficiently long time to ensure a substantial number of particles are advected to the end of the mixing cycles (smaller time step means that for the same run time, the particles may not reach the same axial distance downstream of the entrance, resulting in smaller sample size).

In the design of mixers, it is of interest to ensure that the mixer length provided can achieve sufficient mixing. One way of doing this which avoids the problems mentioned above is by using a method which allows a conservative estimate of required mixing length to be made. This can be done by replacing the geometric mean stretching $\lambda_{g,50}$, which represents the cut-off point at which 50 % of the stretch values have a higher value, with a lower cut-off point in which at least 90 % of the stretch values are higher. Using the z-score³, this lower cut-off point was determined to be at 1.2816 times the standard deviation below the mean, as illustrated in Figure 6.14.

Figure 6.11: Computed and experimentally derived mixing lengths versus $\ln(\text{Pe})$



³ The z-score for a value y of a data set is the distance that y lies above or below the mean, measured in units of the standard deviation. The z-score is defined as $z = \frac{y - \mu}{\sigma}$, where μ is the mean and σ is the standard deviation. The cut-off point was determined from a table of Normal Curve Areas (Mendenhall and Sincich, 1995)

Figure 6.12: Log-normal distribution of stretch values at $Re = 0.01$.

This coefficient $\lambda_{g,90} = 0.45 \pm 0.01$ for all data from Figure 6.12, given a conservative mixing length value and can be thought of as the value where 90% mixing is achieved.

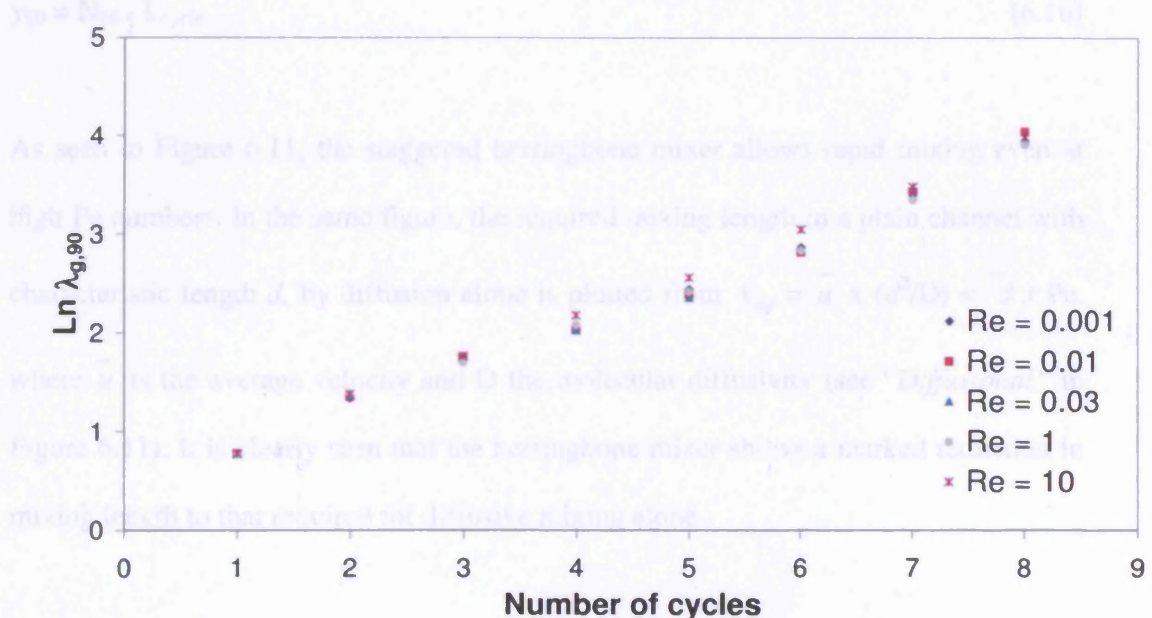
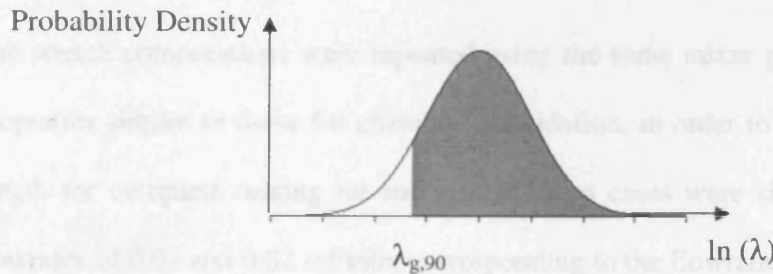
Figure 6.13: $\ln \lambda_{g,90}$ vs number of mixing cycles at various Re (data points at different Re overlap).

Figure 6.14: Cut-off point above which 90 % of computed stretch values are higher

$$\lambda_{g,90} = \lambda_{g,50} - 1.2816\sigma \quad [6.14]$$

The values of α_{90} , which represents the rate of increase of $\lambda_{g,90}$ values, obtained using this method ($\alpha_{90} = 0.43 \pm 0.01$ for all cases, from Figure 6.13), gives a conservative mixing length value and can be thought of as the point where 90% mixing is achieved.

$$N_{90} = \frac{\ln\left(\frac{(s(0))^2 2\alpha_{90}}{D\tau} + 1\right)}{2\alpha_{90}} \quad [6.15]$$

$$y_{90} = N_{90} \cdot L_{cycle} \quad [6.16]$$

As seen in Figure 6.11, the staggered herringbone mixer allows rapid mixing even at high Pe numbers. In the same figure, the required mixing length in a plain channel with characteristic length d , by diffusion alone is plotted from $y_{dif} = \bar{u} \times (d^2/D) = d \times Pe$, where \bar{u} is the average velocity and D the molecular diffusivity (see “Diffusional” in Figure 6.11). It is clearly seen that the herringbone mixer shows a marked reduction in mixing length to that required for diffusive mixing alone.

6.3.5. Mixer Design for Chalcone Epoxidation

The stretch computations were repeated using the same mixer geometry but with fluid properties similar to those for chalcone epoxidation, in order to determine the required length for complete mixing for the system. Two cases were simulated, at volumetric flowrates of 0.01 and 0.02 ml/min, corresponding to the flowrates in the first and second mixer sections respectively. The fluid properties used are listed in Table 6.5.

Table 6.5: Fluid properties of chalcone epoxidation reaction

Density (kg/m ³)	837.7
Viscosity (Pa s)	0.0004051
Molecular diffusivity (m ² /s)	8 x 10 ⁻¹¹

Figure 6.15 shows the change in values of $\ln \lambda_{g,50}$ and $\ln \lambda_{g,90}$ with increasing mixing cycles. In both cases the values of α_{50} and α_{90} obtained were very similar. The final results are tabulated in Table 6.6.

Figure 6.15: $\ln \lambda_{g,50}$ and $\ln \lambda_{g,90}$ vs number of mixing cycles (data points at different Re overlap).

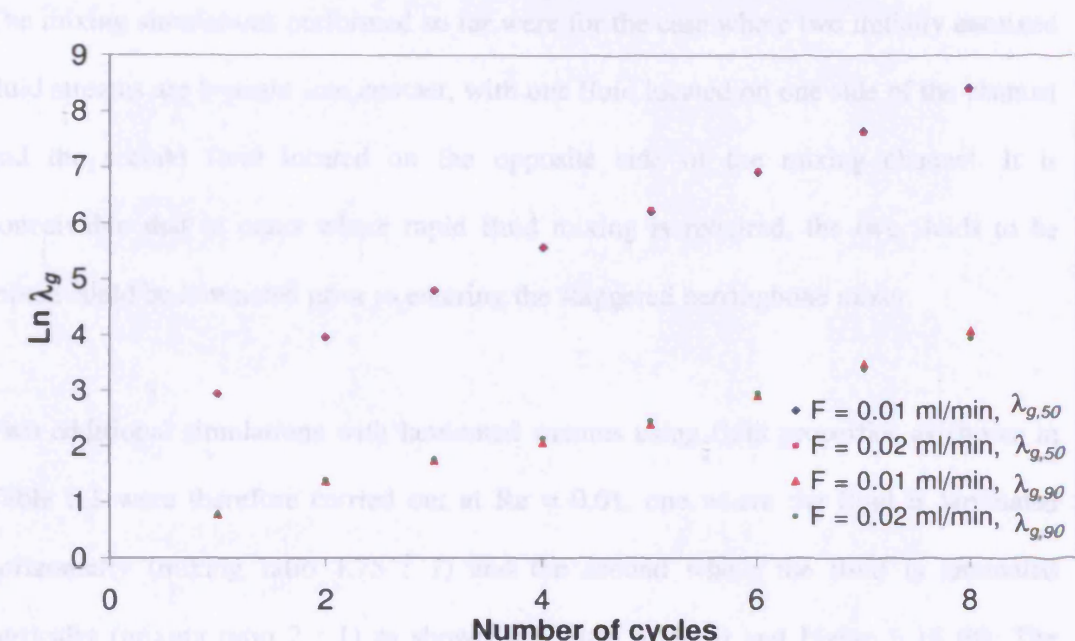


Table 6.6: Results of stretching computation for chalcone epoxidation conditions

	0.01 ml/min	0.02 ml/min
Specific stretch based on $\lambda_{g,50}, \alpha_{50}$	0.76	
Specific stretch based on $\lambda_{g,90}, \alpha_{90}$	0.44	
Number of mixing cycles based on $\lambda_{g,50}, N_{50}$	5.5	6
Number of mixing cycles based on $\lambda_{g,90}, N_{90}$	8.8	9.9
Mixing length based on $\lambda_{g,50}, y_{50}$ (cm)	0.84	0.91
Mixing length based on $\lambda_{g,90}, y_{90}$ (cm)	1.33	1.5

6.3.6. Laminated Inlets

The mixing simulations performed so far were for the case where two initially unmixed fluid streams are brought into contact, with one fluid located on one side of the channel and the second fluid located on the opposite side of the mixing channel. It is conceivable that in cases where rapid fluid mixing is required, the two fluids to be mixed could be laminated prior to entering the staggered herringbone mixer.

Two additional simulations with laminated streams using fluid properties as shown in Table 6.1 were therefore carried out at $Re = 0.01$, one where the fluid is laminated horizontally (mixing ratio 1.75 : 1) and the second where the fluid is laminated vertically (mixing ratio 2 : 1) as shown in Figure 6.16 (a) and Figure 6.16 (b). The simulation with laminated streams were not repeated at other Re numbers, since the striation patterns formed were shown in section 6.3.2 to be independent of Re . The striation patterns formed with increasing number of cycles are also shown in Figure 6.16.

Figure 6.17 compares the striation patterns formed by the end of cycle 5 for both lamination cases with the striation patterns formed in a regular unlaminated fluid stream. Laminated inlets clearly show much thinner striation patterns by the end of cycle 5, particularly in the case of vertical lamination compared to regular unlaminated inlet streams.

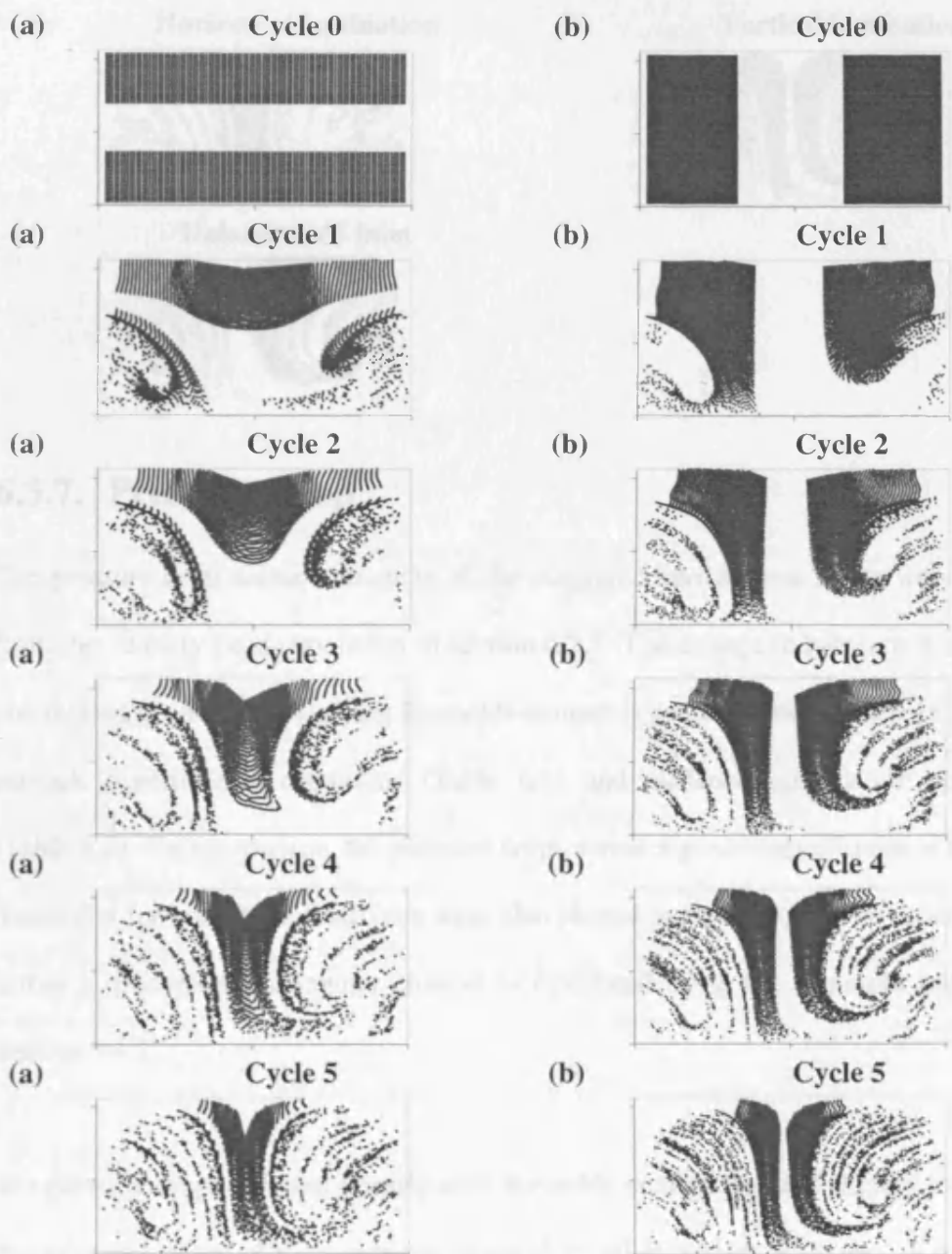
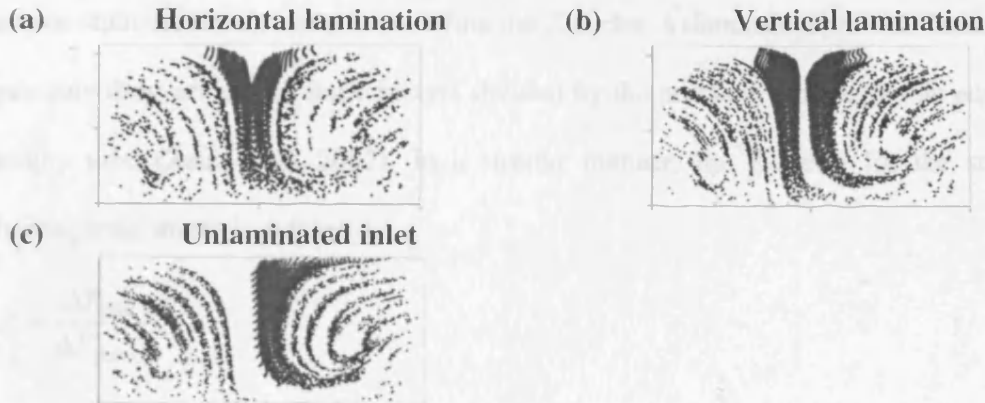
Figure 6.16: Evolution of striation patterns with mixing cycles for laminated inlet**streams at $Re = 0.01$. (a) Horizontal lamination. (b) Vertical lamination.**

Figure 6.17: Comparison of striation patterns at the end of Cycle 5. (a) Horizontal Lamination. (b) Vertical Lamination. (c) regular unlaminated inlet



6.3.7. Pressure Drop

The pressure drop across one cycle of the staggered herringbone mixer was obtained from the velocity field simulation in section 6.2.1. The change in pressure drop across one mixing cycle with increasing Reynolds number is presented in Figure 6.18, for both Stroock experimental conditions (Table 6.1) and chalcone epoxidation conditions (Table 6.5). For comparison, the pressure drops across a grooveless channel of the same dimension for both these conditions were also plotted in Figure 6.18. The pressure drop across a grooveless rectangular channel is calculated using the equations outlined in Section 5.4.2.

The pressure drop increased linearly with Reynolds number and was slightly lower than the pressure drop in a grooveless channel at all Reynolds number. It has been previously reported that the presence of grooves effectively weakens the no-slip condition, resulting in lowering of the pressure drop compared to that in a simple grooveless channel (Bennett and Wiggins, 2003). The groove type, groove depth and number of grooves per cycle have negligible effect on the pressure drop although the

width of the grooves appear to have a stronger effect on pressure drop (Aubin et al, 2003; Aubin et al, 2005). A common approach used when considering pressure drop across static mixer elements is to define the Z-factor, a dimensionless ratio based on the pressure drop across the static mixers divided by the pressure drop across an equivalent empty tube (Zalc et al, 2002). In a similar manner, the Z-factor for the staggered herringbone mixer is defined as:

$$Z = \frac{\Delta P_{SHM}}{\Delta P_{channel}} \quad [6.17]$$

ΔP_{SHM} represents the pressure drop across one cycle of the staggered herringbone mixer while $\Delta P_{channel}$ represents the pressure drop in an equivalent grooveless channel, calculated from [5.29]. The change in Z-factor with increasing Reynolds number is shown in Figure 6.19.

The Z-factor computed was below 1 and remained fairly constant at 0.926 up to $Re = 10$, rising to 0.94 at $Re = 100$ as inertial effects become increasingly important. These results further demonstrate the potential benefits of using the staggered herringbone mixer to enhance mixing, as unlike static mixing elements, the presence of the grooves reduce the energy costs compared to a plain channel. The change in friction factor, calculated from [6.18], is plotted against the Reynolds number in Figure 6.20 using ΔP values obtained from the COMSOL simulations.

$$f = \frac{w\Delta P}{2\rho u^2 L} \quad [6.18]$$

The friction factor decreases linearly with Reynolds number and can be approximated as

$$f \approx \frac{43}{Re} \quad [6.19]$$

This allows the pressure drop across one mixing cycle to be estimated using [6.18].

Figure 6.18: Change in ΔP across one mixing cycle with Reynolds number

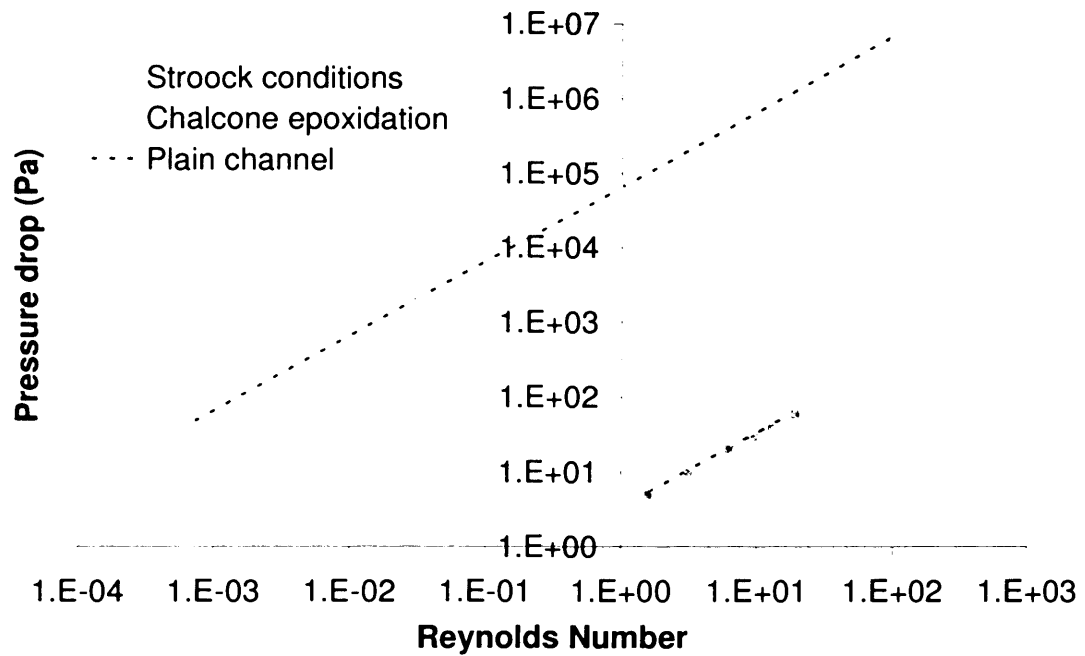


Figure 6.19: Change in Z-factor values with increasing Reynolds number

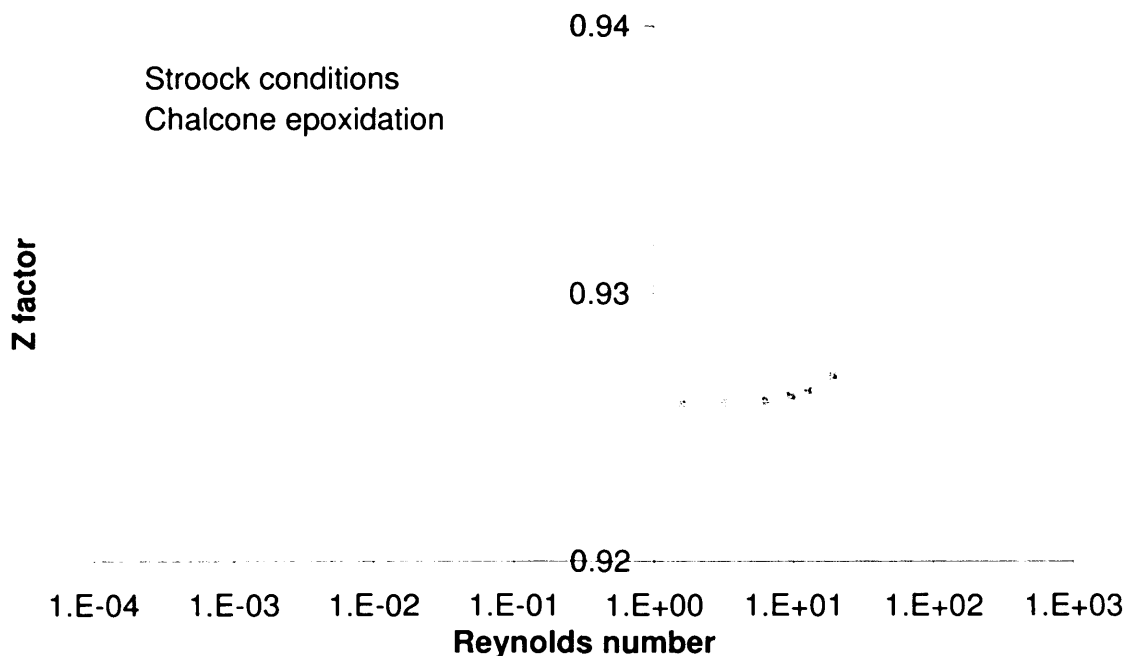
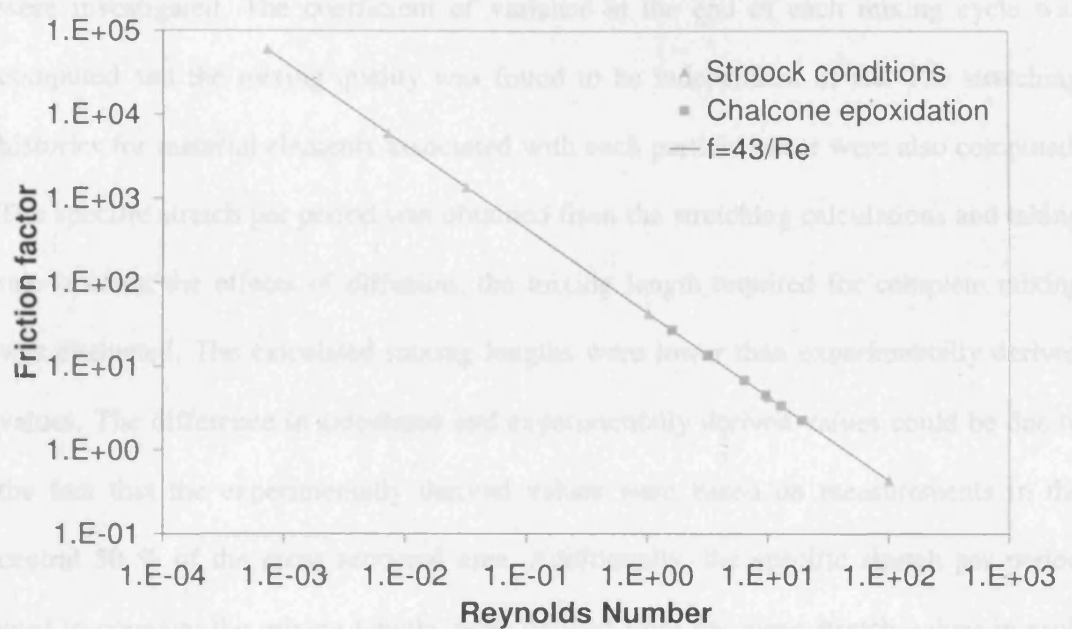


Figure 6.20: Change in friction factor with Reynolds number

6.4. Conclusions

The mixing performance of the staggered herringbone mixer was evaluated numerically at $Re = 0.001-10$. The velocity field was obtained via CFD simulations. Particle tracking methods were used to quantify the mixing performance to avoid numerical diffusion problems. Mixing is enhanced in the staggered herringbone mixer by the formation of a double helical flow in the mixer which alternates from one side of the channel to the other depending on the asymmetry of the herringbone grooves as well as by ditch mixing, where fluid from one side of the channel is transported to the opposite side via the grooves, resulting in increased contact area for mixing. The particle distribution at the end of every mixing cycle was obtained for all cases and the striation patterns were found to be qualitatively similar to published work.

Several methods to quantify the mixing performance of the staggered herringbone mixer were investigated. The coefficient of variance at the end of each mixing cycle was computed and the mixing quality was found to be independent of Re . The stretching histories for material elements associated with each particle tracer were also computed. The specific stretch per period was obtained from the stretching calculations and taking into account the effects of diffusion, the mixing length required for complete mixing was evaluated. The calculated mixing lengths were lower than experimentally derived values. The difference in calculated and experimentally derived values could be due to the fact that the experimentally derived values were based on measurements in the central 50 % of the cross sectional area. Additionally, the specific stretch per period used to compute the mixing lengths were derived from the mean stretch values in each period, while in practice, there exists a log-normal distribution of stretch values. Using α_{90} , which represents the rate of increase of $\lambda_{g,90}$ values (cut-off point for λ_g in which 90% of the computed stretch values are higher), allowed for a conservative estimate of required mixing length to be made. Using this method, it was feasible to design the staggered herringbone mixers for both the deprotonation and epoxidation micro-structured reactors. The required mixer lengths for the deprotonation and epoxidation mixers were found to be 1.33 cm and 1.5 cm respectively. This work shows that it is possible to design chaotic mixers by CFD simulations with a higher level of confidence.

Chapter 7

Chalcone Epoxidation Reaction in a

Microstructured PEEK Reactor

7.1. Introduction

The previous chapters described the methods used to design a continuous microstructured reactor for the poly-*L*-leucine catalysed epoxidation of chalcone. The design was carefully selected to satisfy the requirements of the reaction system. It allows for flexible production rate by increasing the number of reactors operating in parallel. As demonstrated in chapter 4, the selected reactor volume was found to easily meet the target for small scale production. However, in order to maximise the production rate, the reaction rate needs to be enhanced as much as possible. This chapter describes the experimental work using the fabricated reactor to test the validity of the design as well as to examine the effects of various parameters, to enhance reaction performance.

7.2. Experimental

7.2.1. Reactor Configuration

A picture of the open (unbonded) fabricated reactor is presented in Figure 7.1 while Figure 7.2 shows the assembled single reactor in both PEEK and Acrylic.

Figure 7.1: View of the unbonded microstructured PEEK plate

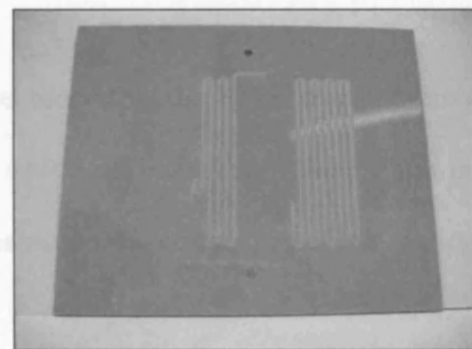
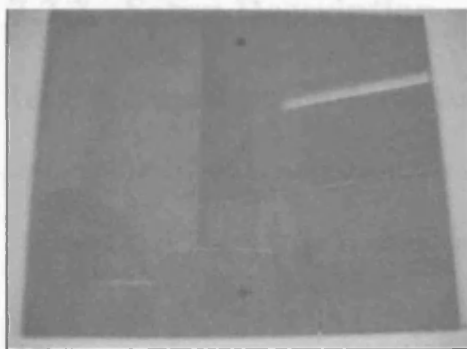
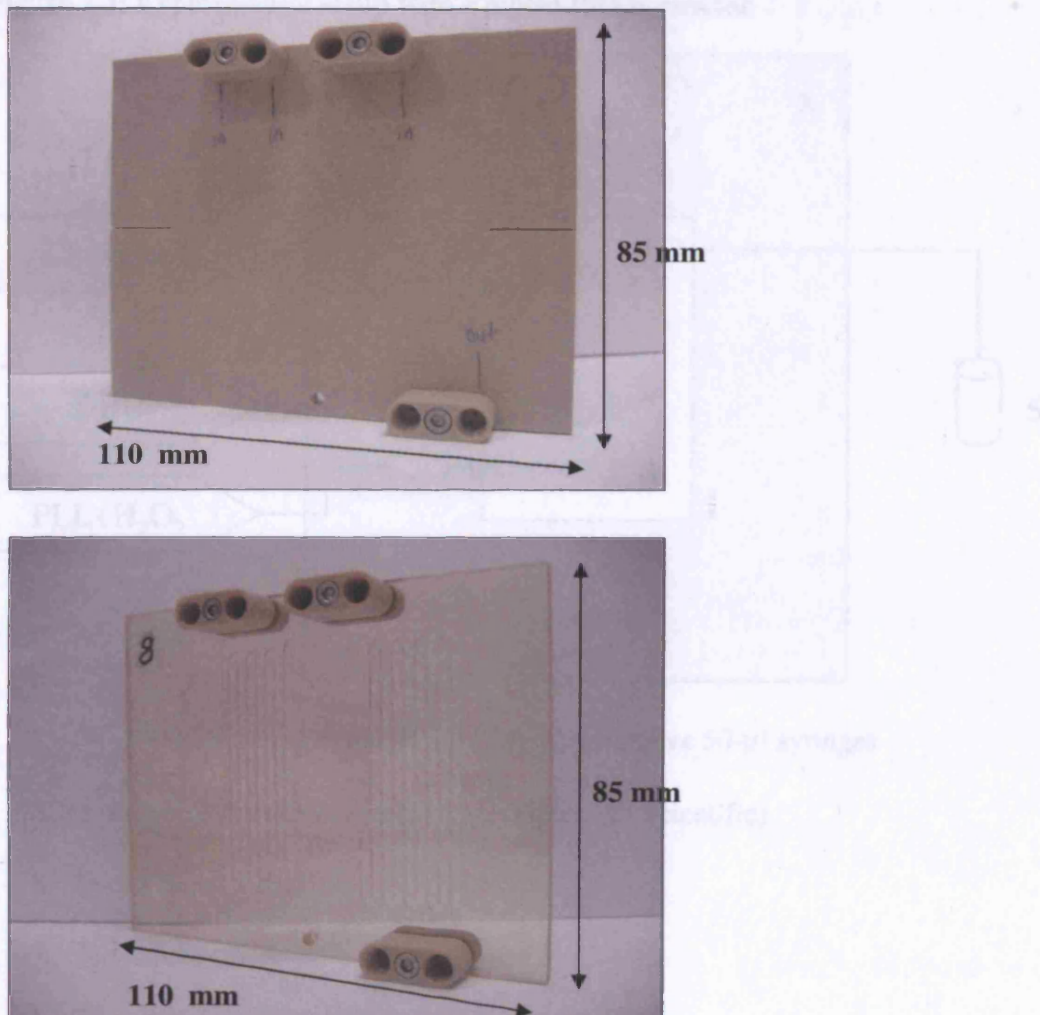
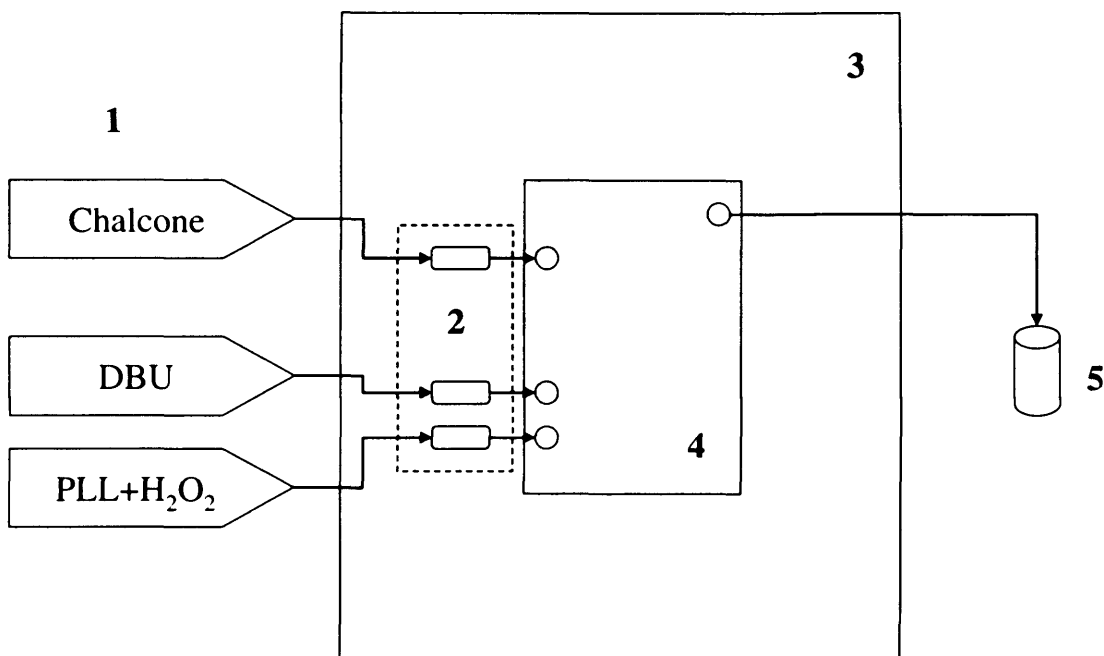


Figure 7.2: Assembled PEEK and Acrylic microstructured reactors

7.2.2. Setup Description

The reactor used for the epoxidation reaction was a PEEK reactor (Cetco) with three 50 ml PTFE jacketed beakers. The experimental setup and procedures used for testing the PEEK reactor were similar to those described in section 4.2, with the additional inclusion of three 2 μ m porosity stainless steel filters at the reactant inlet streams to prevent clogging of the reactor.

Microstructured substrates were placed in a housing of 20 μ m depth, in the first unstructured rectangular reactor on the PEEK reactor, and ensured a 0.3 ml delay loop with 30 minutes residence times.

Figure 7.3: Experimental setup with Epigem PEEK reactor

1. XP 3000 Modular Digital Pump (Cavro) with three 50- μ l syringes
2. 2 μ m porosity stainless steel filters (Upchurch Scientific)
3. Water Bath (Huber)
4. Epigem PEEK Reactor
5. Stirred vial for sample collection

As shown in Figure 7.3, an XP 3000 Modular Digital Pump (Cavro) with three 50- μ l syringes was used to pump solutions of chalcone, DBU and catalyst with peroxide. Three solutions were prepared: a 0.16 mol/l chalcone solution, a 0.88 mol/l DBU solution and a PLL/peroxide solution of 53.88 g/l PLL and 0.53 mol/l peroxide. Three inline stainless steel filters were connected at all three reactant inlets. DBU and PLL/peroxide solutions were pumped at a flowrate of 5 μ l/min each, to the first staggered herringbone mixer on the PEEK reactor and entered a 0.3 ml delay loop with 30 minutes residence time.

Subsequently, a 10 μ l/min chalcone flow joined the combined streams in the second staggered herringbone mixer on the PEEK reactor in a 0.32 ml delay loop with a total residence time of 16 minutes, resulting in reactant concentrations at the inlet of the epoxidation reactor of 0.080 mol/l chalcone, 0.22 mol/l DBU, 13.47 g/l PLL and 0.132 mol/l peroxide. The PEEK reactor was maintained at the desired temperature by placing it in a water bath. The reaction was quenched at the reactor outlet by collecting the outlet flow in a stirred vial containing sodium sulphite as quench.

Clogging of the reactors was found to be a major issue and in initial scouting work, the PEEK reactors lasted only for several runs before clogging. Some of the PEEK reactors were also found to leak at relatively low flowrates, with maximum allowable flowrates not exceeding 0.02 ml/min in some cases. To alleviate these problems, the maximum flowrate was set at 0.02 ml/min, just sufficient for running the reaction.

The reactors were flushed with the solvent (THF/ACN) prior to running the reactions as well as after running the reactions. This was to prevent contacting the reactants dissolved in organic solvent with water, which may cause solids to precipitate out due to insolubility of the reactants in water. While PEEK is chemically compatible with THF, some swelling of PEEK may occur if it is in contact with THF for prolonged periods. After each run, the reactors were flushed with the solvent followed by water to minimise contact with THF.

7.3. Results and Discussions

7.3.1. Base Case

The Epigem PEEK reactor was tested with the poly-*L*-leucine catalysed asymmetric epoxidation of chalcone at base case conditions (Table 4.1). The base case epoxidation in the PEEK reactor at 23.1°C resulted in an average conversion of 86.7 % with an enantioselectivity value of 87.6 %, as shown in Table 7.1. This compares well with both the values predicted using the slit flow reactor model as well as with experimental results obtained using a continuous tubular reactor at the same reaction conditions (see Chapter 5). The experimental conversion values were within 3 % from predicted values.

Table 7.1: Comparison of base case chalcone epoxidation in PEEK reactor at 23.1°C and 16 minutes residence time with other reactors and models under similar operating conditions.

	Conversion (%)	Conversion Difference	Enantioselectivity (%)	E.e. Difference
Epigem PEEK reactor	86.7	2.9	87.6	4.8
Slit flow reactor model	89.6		92.4	
Continuous tubular reactor	88.4	0.1	88.8	3.6
Continuous tubular model	88.3		92.4	
Batch (Hull) ^a	87.0	2.9	> 95.0	- 2.6
Batch reactor model	89.9		92.4	

a. Batch experiments carried out at University of Hull (Mathew, 2003).

The predicted enantioselectivity values for both continuous experiments were larger than experimental values although the experimental values were still within 5 % of the predicted values. In the case of the batch values, the predicted enantioselectivity was lower than experimental values; it has to be noted however that the enantioselectivity value for batch experiments of 95 % (Mathew, 2003) was an assumed value (the enantioselectivity was established in the initial runs but was not evaluated for subsequent experimental runs carried out as it was assumed to be constant).

7.3.2. Blank Runs

Blank runs were carried out on the PEEK reactor to determine if there are any other effects that could catalyse peroxide decomposition in the reactor. A solution of 0.53 mol/l peroxide and 53.88 g/l PLL was prepared and used in the blank runs. DBU was not added as it is known to catalyse the decomposition of the peroxide. Both inlet and outlet peroxide concentrations were determined using the methods described in section 4.2.2. and determined to be at around 0.5 mol/l, indicating the absence of any other agents that could significantly catalyse peroxide decomposition.

7.3.3. Effect of Temperature

The effect of reaction temperature on both the catalysed and background reactions was investigated. The effect of reaction temperatures, studied in the range 15-35 °C on the performance of a similar system in pure THF has previously been reported (Carrea et al, 2004; Carrea et al, 2004) where the rate of reaction at 35 °C was reported to be 64 % higher than that at 15 °C. The performance of both catalysed and background reactions were investigated at three different temperatures, 15, 23.1 (base case) and 30°C.

It is expected that lower temperatures may improve enantioselectivity as it may slow down the background reaction compared to the catalysed reaction. However, lower temperatures are also expected to result in lower overall reaction rate. Increasing reaction temperature is expected to increase overall reaction rate, however, as the temperature is increased beyond a specific temperature, the relative rate of background reaction to catalysed reaction is expected to increase, since the catalyst is essentially a tertiary amine which can denature at high temperatures. This will have the effect of lowering enantioselectivity at higher temperatures.

The effect of reaction temperature on reaction performance is shown in Figure 7.4 and Figure 7.5. The conversion remains fairly constant as the temperature was raised from 15 to 23.1°C, increasing very slightly from 85.7 to 86.7 % but decreased to 77 % when the temperature was raised to 30°C. Similarly, the enantioselectivity remained fairly constant up to 23.1°C at around 87.5 ± 0.1 % but dropped to 84.5 % when the temperature was raised to 30°C.

This is in contrast to the performance achieved in a continuous tubular reactor (see Table 5.3, Chapter 5) where the conversion increased slightly from 88.4 % to 94 % while the enantioselectivity remained fairly constant at around 89 % when the temperature was increased from 23.1 to 30°C. The change in performance of the catalysed reaction in a tubular reactor from 23.1 to 30°C is also plotted in Figures 7.4 and 7.5. These results suggest that at 30°C, something seems to be happening in the PEEK reactor which causes the performance to deteriorate.

It was observed during the experiments that at higher temperatures, the outlet stream contained more bubbles than at lower temperatures. These bubbles are believed to form from the decomposition of peroxy anion, which is accelerated at higher temperatures. It is possible that these bubbles may cause formation of gas plugs within the reactor. Unlike tubular reactors, where the gas plugs are pushed along to the exit, the thin slits may cause the gas plugs to stagnate within the reactor creating dead volumes and hence shorter residence time resulting in lower conversion values.

This appears to be confirmed by similar results observed for the background reaction in the PEEK reactor, as shown in Figure 7.6. The background conversion increased from 20.3 % to 31.8 %, as expected, when the temperature was raised from 15 to 23.1°C, but showed a slight decrease to 31.5 % as the temperature was raised to 30°C. The smaller drop in conversion at 30°C for the background reaction compared to the catalysed reaction may be due to lower peroxide decomposition rates in the absence of the catalyst as the bubbling effect was also noticeably larger in the presence of the catalyst.

Figure 7.4: Effect of temperature on catalysed reaction conversion in PEEK reactor¹

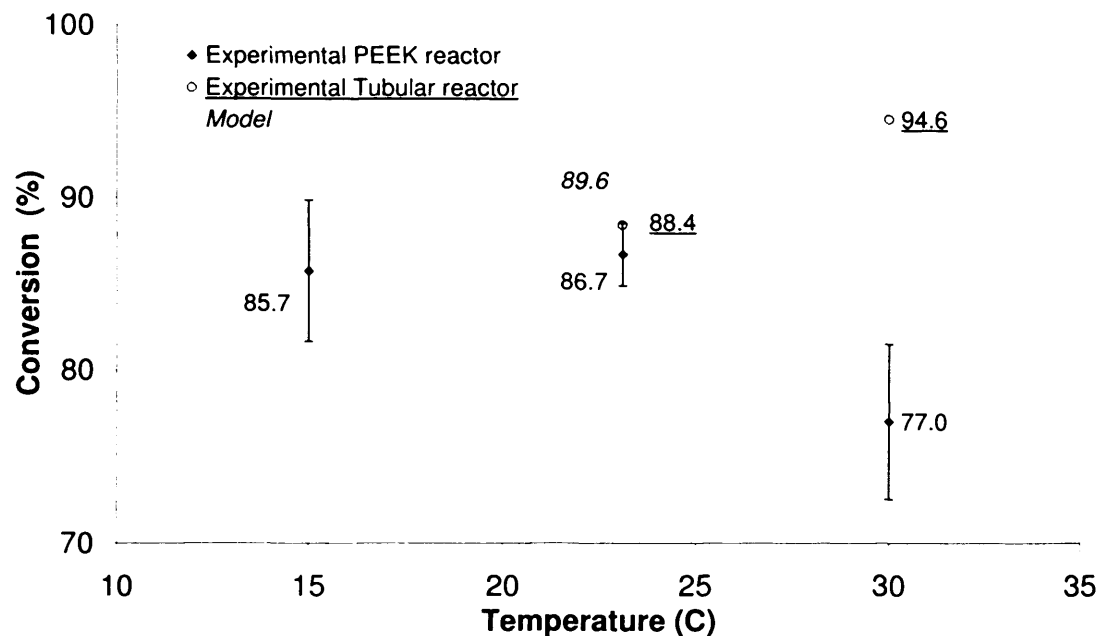
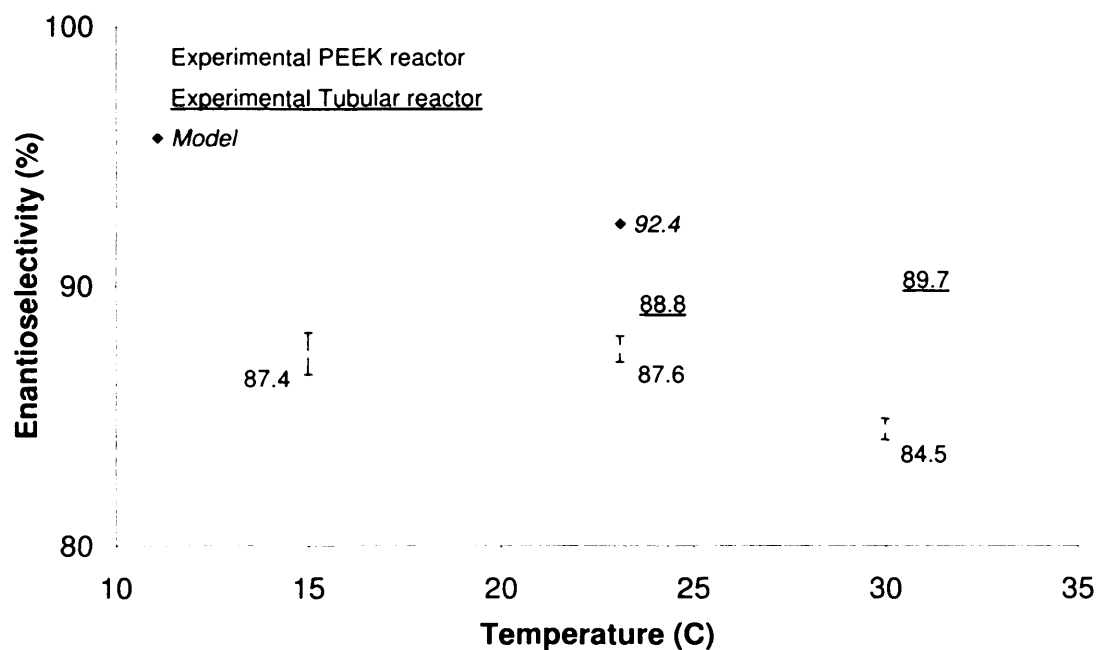
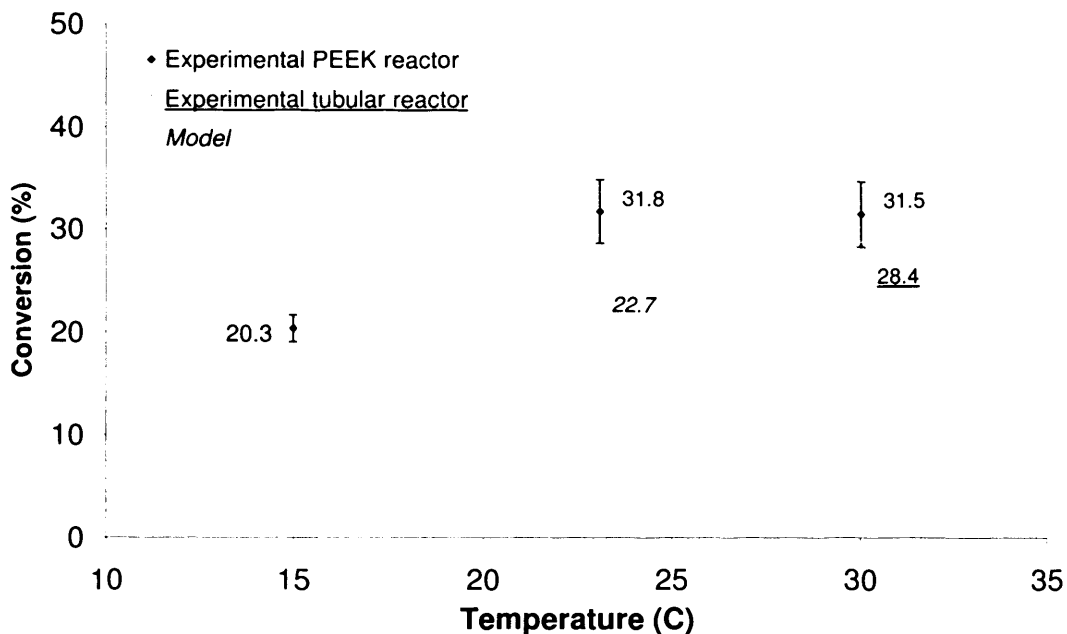


Figure 7.5: Effect of temperature on catalysed reaction enantioselectivity in PEEK reactor



¹ Error bars represent standard errors, SE calculated as $SE = \sigma / \sqrt{N}$ where σ is the standard deviation for N , the sample size.

Figure 7.6: Effect of temperature on background reaction in PEEK reactor

7.3.4. Effect of Chalcone Concentration

The effect of chalcone concentration on both conversion and enantioselectivity of the catalysed reaction was also examined. In addition to base case experiments, the catalysed reaction was carried out at two other chalcone concentrations while the concentrations of all other reactants were maintained at base case concentrations, as shown in Table 7.2.

Table 7.2: Initial concentrations of reactants used to study the effect of [Chalcone].

	Lower concentration	Base case	Higher concentration
PLL (g/l)	13.47	13.47	13.47
Peroxide (mol/l)	0.132	0.132	0.132
Chalcone (mol/l)	<i>0.0401 (0.5 x base case)</i>	<i>0.0802</i>	<i>0.1604 (2 x base case)</i>
DBU (mol/l)	0.22	0.22	0.22

The changes in conversion and enantioselectivity with a change in chalcone concentration are shown in Figures 7.7 and 7.8 respectively. The predicted values are also shown in dashed lines. The conversion gradually decreased from 87.9% to 64.5 % as the chalcone concentration was increased from 0.0401 to 0.1604 mol/l, displaying the same trend predicted by the model. However, unlike the model, the conversion decreased only very slightly from a chalcone concentration of 0.0401 to 0.0802 mol/l. The enantioselectivity on the other hand, gradually increased from 82.5 % to 88.0 % as the chalcone concentration was increased, while the model predicted a somewhat constant enantioselectivity.

The higher predicted conversion values at all chalcone concentrations is likely due to higher catalytic activity in the batch of catalyst used to determine the rate equations, as catalytic activity has been observed to differ slightly from batch to batch. The smaller change in experimentally obtained conversion compared to predicted conversion, as the chalcone concentration is increased from 0.0401 mol/l to 0.0802 mol/l can be attributed to experimental error.

The predicted enantioselectivity on the other hand, was observed to display a different trend to that obtained experimentally. The values of enantioselectivity are primarily determined by the relative rates of catalysed and background reactions. The higher predicted values of enantioselectivity at all chalcone concentrations can similarly be attributed to a difference in catalytic activity since a higher catalytic activity (in the batch used to determine the rate equations) would improve enantioselectivity.

The difference between the predicted trend in enantioselectivity compared to experimentally observed trend can be attributed to the fact that the rate equation for the background reaction was obtained in the absence of the catalyst while in the presence of the catalyst this reaction is slowed down considerably, possibly due to the lack of free perhydroxyl ions, consistent with the view that the perhydroxyl ions are sequestered by the poly-*L*-leucine catalyst (Lopez-Pedrosa et al, 2004). As the chalcone concentration is increased, the model predicts a decrease in the relative rate of catalysed to background reaction as seen in Figure 7.9 and hence a decrease in enantioselectivity. However, due to perhydroxyl ion sequestration by the catalyst, the background reaction is hindered and only the catalysed reaction rate will increase with an increase in chalcone concentration, resulting in improved enantioselectivity.

Figure 7.7: Effect of chalcone concentration on conversion in PEEK reactor

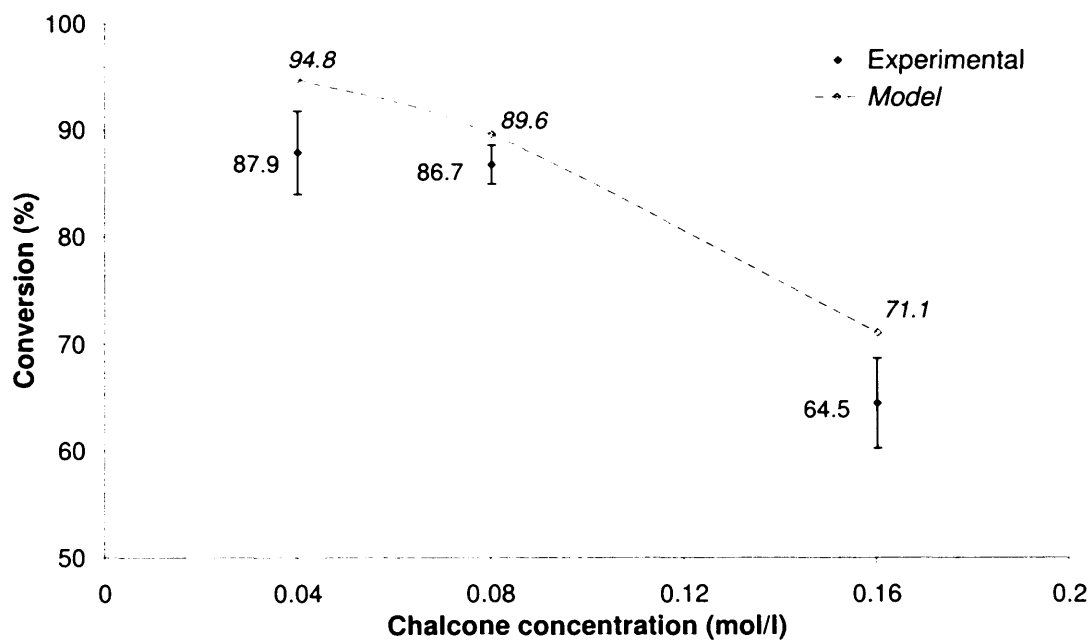


Figure 7.8: Effect of chalcone concentration on enantioselectivity in PEEK reactor

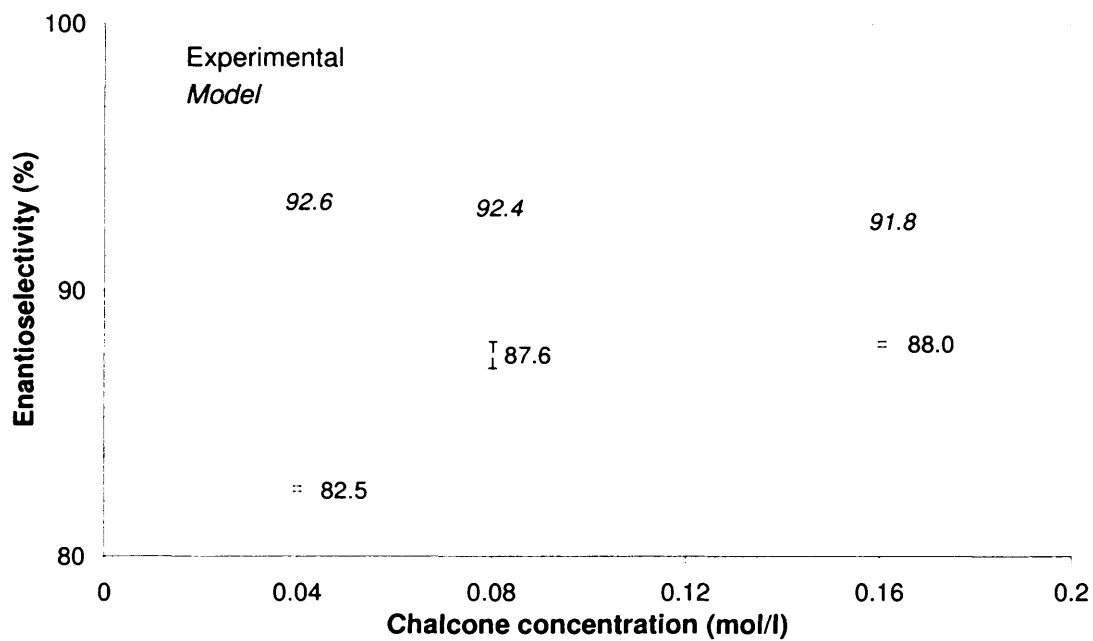
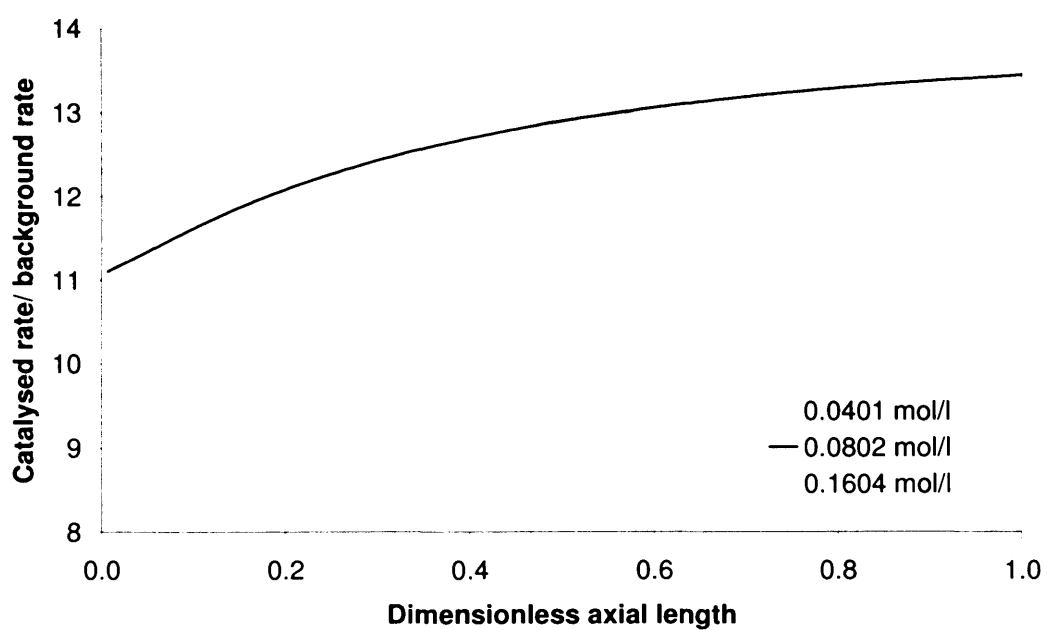


Figure 7.9: Predicted effect of chalcone concentration on ratio of catalysed to background reaction rates.



7.3.5. Effect of Peroxide Concentration

The effect of peroxide concentration on the catalysed reaction was investigated at two conditions in addition to base case experiments, one at half the base case peroxide concentration and the other at nearly double the base case peroxide concentrations (~1.9 times). The concentrations of all other reactants were maintained at base case concentrations, as shown in Table 7.3. The higher peroxide concentration was limited to only 1.9 times base case peroxide concentrations by the peroxide solubility. Unlike batch conditions, where the peroxide concentration could be increased up to a maximum of ~ 6 times base case concentration, under continuous flow conditions, a doubling in the reactor peroxide concentration required an increase in the parent solution concentration by more than 8 times base case peroxide concentrations, beyond the peroxide solubility in the solvent.

Table 7.3: Initial concentrations of reactants used to study the effect of $[H_2O_2]$.

	Lower concentration	Base case	Higher concentration
PLL (g/l)	13.47	13.47	13.47
Peroxide (mol/l)	<i>0.066 (0.5 x base case)</i>	<i>0.132</i>	<i>0.246 (1.9 x base case)</i>
Chalcone (mol/l)	0.0802	0.0802	0.0802
DBU (mol/l)	0.22	0.22	0.22

The changes in conversion and enantioselectivity with a change in peroxide concentration are shown in Figures 7.10 and 7.11 respectively. The conversion increased from 71.8 % to 86.7 % and then decreased to 69.7 % as the peroxide concentration was increased from 0.066 mol/l to 0.246 mol/l, in contrast with a predicted increase from 61 % at 0.066 mol/l peroxide to 89.6 % and 99.2 % with increasing peroxide concentration.

The enantioselectivity on the other hand showed a slight decrease from 91 % to 87.6 % and then decreased sharply to 63.8 % at 0.246 mol/l, in contrast with the predicted decrease from 92.6 % at 0.066 mol/l peroxide to 91.8 % at 0.246 mol/l peroxide.

The deviation from expected performance can be explained by the fact that the reactive species is not the peroxide itself but rather the perhydroxyl ion (OOH^-) and the change in reactive species concentration with a change in peroxide concentration was not captured by the model. The concentration of the reactive species at the start of the reaction is dependent on the concentrations of both the peroxide and DBU as well as the residence time in the deprotonation reactor. The deprotonation of peroxide increases the concentration of the reactive species while the base catalysed decomposition of peroxide (Evans and Upton, 1985) decreases the concentration of the reactive species. The base catalysed decomposition of peroxide is given by [7.1] and the corresponding rate equation has been shown to be of type [7.2].



$$\text{Rate}_{\text{decomposition}} = k [\text{H}_2\text{O}_2][\text{OOH}^-] \quad [7.2]$$

These factors suggest an optimum condition may exist where the concentration of the reactive species is maximised. An estimate of the equilibrium perhydroxyl ion concentration for all three experimental conditions is shown in Table 7.4 (calculations are provided in Appendix 7-1). The deprotonation was assumed to be instantaneous; however as actual data on the rate of deprotonation was not available, the equilibrium perhydroxyl ion concentration represents the maximum expected concentration, with actual perhydroxyl ion concentration possibly lower than this value. Several different reactant concentration ratios are also provided in Table 7.4 to aid analysis of the experimental results.

Table 7.4: Equilibrium perhydroxyl ion concentration and various reactant ratios at different peroxide concentrations

$[H_2O_2]$	$\frac{[DBU]}{[H_2O_2]}$	$[OOH^-]$	$\frac{[OOH^-]}{[H_2O_2]}$	$\frac{[OOH^-]}{[Chalcone]}$	$\frac{[PLL]}{[OOH^-]}$
0.066	3.33	0.0555	0.841	0.69	243 g/mol
0.132	1.67	0.0933	0.707	1.16	144 g/mol
0.246	0.90	0.1326	0.54	1.65	102 g/mol

At peroxide concentration of 0.066 mol/l, the equilibrium perhydroxyl concentration was found to be only 0.0555 mol/l and equivalent to around 0.7 of the chalcone concentration. The conversion was therefore limited to around 71.8 % by the available perhydroxyl ion concentration. The conversion value predicted by the model however, was much lower at 61 %. At peroxide concentration of 0.246 mol/l, a sharp drop in conversion to 69.7 % was observed in contrast to the predicted increase in conversion to 99.2 %. This can be explained by looking at the fraction of perhydroxyl ions formed from hydrogen peroxide (fourth column, Table 7.4). As the peroxide concentration is halved from 0.246 mol/l to 0.132 mol/l and halved again to 0.066 mol/l, the fraction of perhydroxyl ions formed increased from 0.54 to 0.841, indicating that the actual perhydroxyl ion concentration was lower than that implied by the model.

Other possible explanations for the drop in conversion at 0.246 mol/l peroxide concentration include incomplete deprotonation (longer time required to reach equilibrium concentration) and the base catalysed decomposition of peroxide (Evans and Upton, 1985), which increases with increasing perhydroxyl ion concentration as shown in equation [7.2] and may result in increased formation of oxygen bubbles which can reduce the residence time in the reactor.

Both predicted and experimental enantioselectivity values decrease with increasing peroxide concentration, although the predicted values were higher than the experimental values in all cases. The higher enantioselectivity values at all peroxide concentrations can be explained in part by the higher catalytic activity of the catalyst batch used for the kinetic studies. The big decrease in experimental enantioselectivity value at peroxide concentration of 0.246 mol/l is due to the increased availability of free peroxide, because of the lower ratio of perhydroxyl ion concentration to catalyst concentration. The higher rate of background reaction to rate of catalysed reaction implies that substrate saturation of the catalyst has been reached and therefore any further increase in peroxide concentration would only increase the background reaction. The huge discrepancy between experimental and predicted results is also attributed to the fact that this concentration falls outside the range of concentration for the kinetic studies (which was limited to a maximum peroxide concentration value of 0.14 mol/l).

Figure 7.10: Effect of peroxide concentration on conversion in PEEK reactor

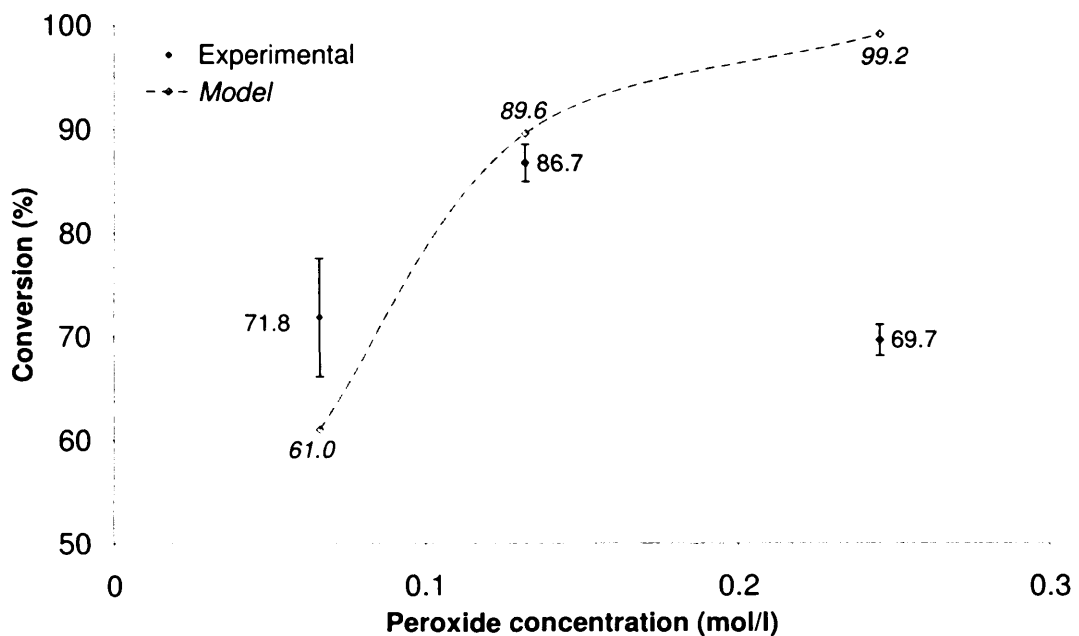
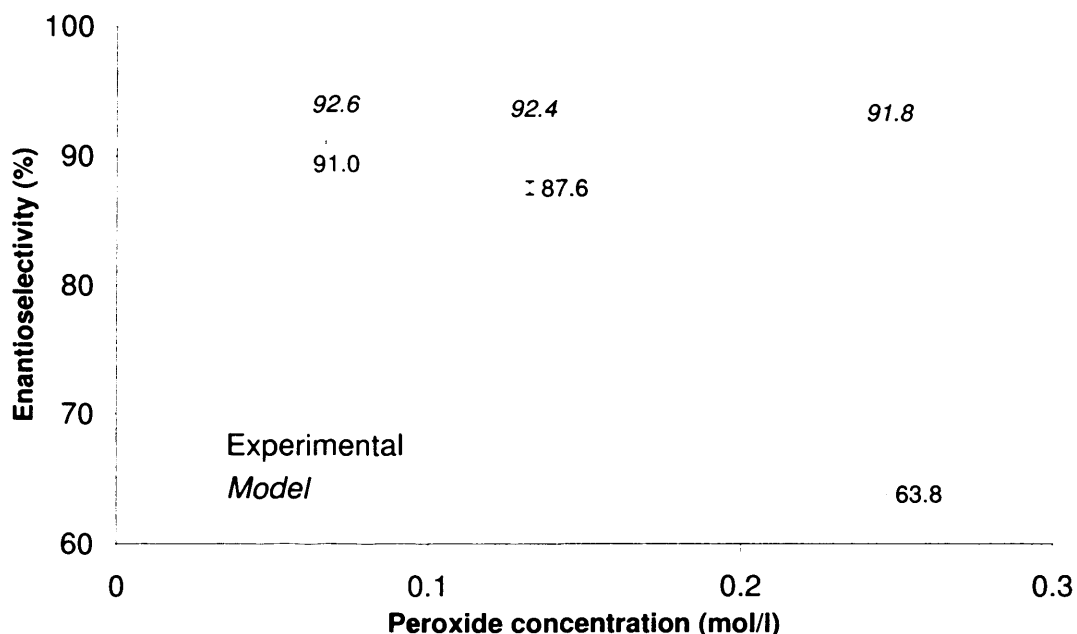


Figure 7.11: Effect of peroxide concentration on enantioselectivity in PEEK reactor



7.3.6. Effect of DBU Concentration

The effect of DBU concentration on the performance of the catalysed reaction was also examined at two additional DBU concentrations. The reactant concentrations used are shown in Table 7.5. The DBU concentration was expected to affect the reaction performance in a similar manner as the peroxide concentration, as they both influence the concentration of the reactive species. The estimated equilibrium concentrations of perhydroxyl ion at all three DBU concentrations are shown in Table 7.6. The changes in conversion and enantioselectivity with a change in DBU concentration are shown in Figures 7.12 and 7.13 respectively.

Table 7.5: Initial concentrations of reactants used to study the effect of [DBU]

	Lower concentration	Base case	Higher concentration
PLL (g/l)	13.47	13.47	13.47
Peroxide (mol/l)	0.132	0.132	0.132
Chalcone (mol/l)	0.0802	0.0802	0.0802
DBU (mol/l)	<i>0.11 (0.5 x base case)</i>	0.22	<i>0.44 (2 x base case)</i>

Table 7.6: Equilibrium perhydroxyl ion concentrations at different DBU concentrations

[DBU]	$\frac{[DBU]}{[H_2O_2]}$	[OOH ⁻]	$\frac{[OOH^-]}{[H_2O_2]}$	$\frac{[OOH^-]}{[Chalcone]}$	$\frac{[PLL]}{[OOH^-]}$
0.11	0.83	0.0685	0.519	0.85	197 g/mol
0.22	1.67	0.0933	0.707	1.16	144 g/mol
0.44	3.33	0.111	0.841	1.38	121 g/mol

At DBU concentration of 0.11 mol/l, conversion was only 45.1 %, even though the estimated equilibrium perhydroxyl ion concentration was 0.85 times the chalcone concentration. In comparison, a conversion of 71.8 % was achieved when the equilibrium perhydroxyl ion concentration was 0.69 times the chalcone concentration (see Table 7.4). In both cases, the reduction in either DBU or peroxide concentration resulted in a limiting equilibrium perhydroxyl ion concentration, yet in the latter case the conversion achieved was much higher. At lower DBU concentration of 0.11 mol/l, the lower conversion of 45.1 % was not due to a limiting equilibrium perhydroxyl ion concentration but possibly due to a lower rate of deprotonation resulting in lower concentration of the reactive species.

The lower enantioselectivity of 74.7 % compared to base case could also be explained by the slower rate of deprotonation, which would lead to fewer perhydroxyl ions sequestered by the poly-*L*-leucine catalyst by the time the catalyst/peroxide mixture enters the epoxidation reactor. As the DBU concentration is increased to 0.22 mol/l, both conversion and enantioselectivity increased to 86.7 % and 87.6 % respectively. Both of these can be attributed to faster deprotonation rate. As with the case of peroxide concentration, complete conversion was not achieved even though the equilibrium perhydroxyl ion is now in excess of the chalcone concentration and this is mainly due to insufficient residence time for complete reaction (complete conversion was not predicted by the model using actual peroxide concentrations). The increase in enantioselectivity even at a lower ratio of catalyst to equilibrium perhydroxyl ion concentration, further suggests a faster deprotonation rate (compared to DBU concentration of 0.11 mol/l), reducing the concentration of free peroxide.

As the DBU concentration was increased to 0.44 mol/l, the conversion decreased slightly to around 85.8 % while enantioselectivity was reduced to 82.7 %. The slight decrease in conversion values may well be due to experimental error. However given that the reduction in enantioselectivity values is larger than experimental error this decrease can be attributed to an increase in the rate of decomposition of perhydroxyl ions due to the increased concentration of free perhydroxyl ions. The concentration of free perhydroxyl ions is expected to increase due to the lower ratio of perhydroxyl ion concentration to catalyst concentration as well as the faster rate of deprotonation at 0.44 mol/l DBU. The lower enantioselectivity is similarly explained by the increase in the amount of free peroxide for background reaction.

Figure 7.12: Effect of DBU concentration on conversion in PEEK reactor.

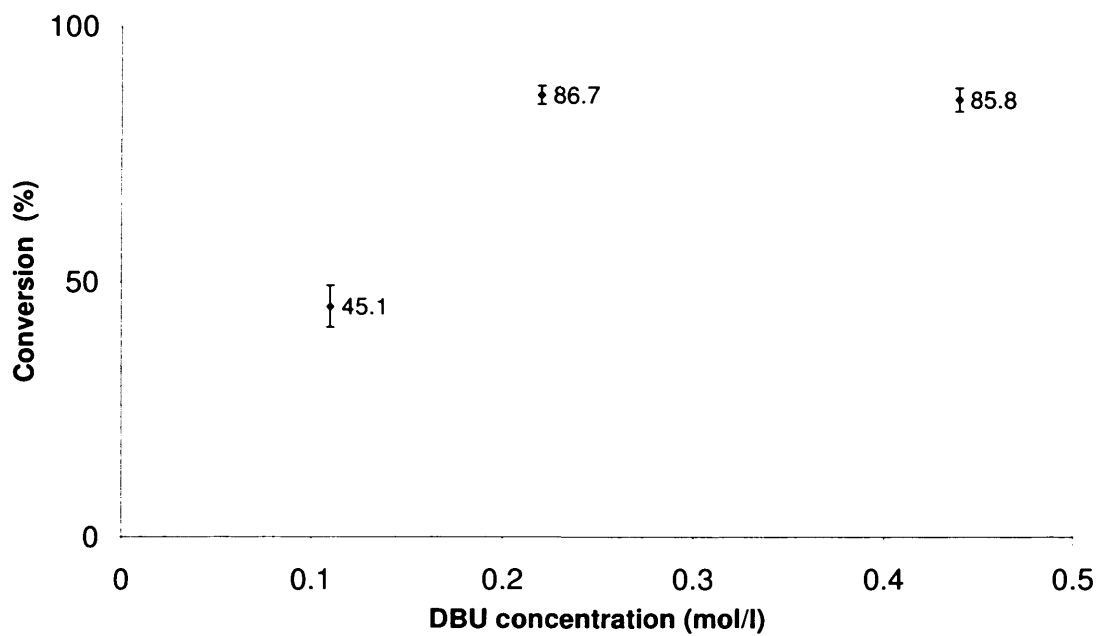
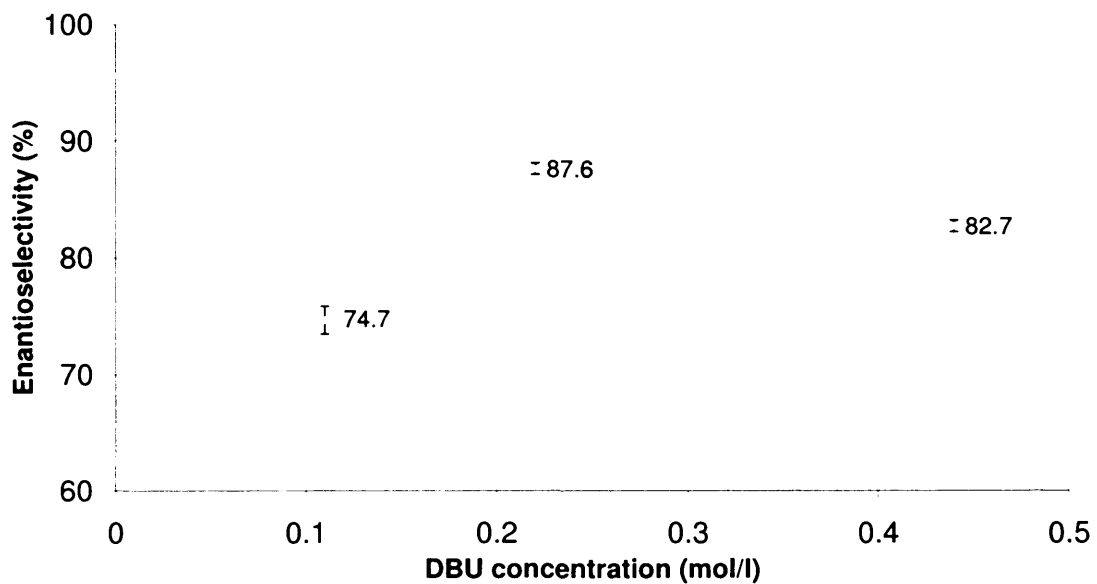


Figure 7.13: Effect of DBU concentration on enantioselectivity in PEEK reactor.



7.3.7. Effect of Catalyst Concentration

The effect of catalyst concentration was examined at two other catalyst concentrations in addition to the base case concentration as shown in Table 7.7. The change in conversion with catalyst concentration is shown in Figure 7.15 while the change in enantioselectivity is shown in Figure 7.16.

Table 7.7: Initial concentrations of reactants in the study of the effect of [PLL]

	Lower concentration	Base case	Higher concentration
PLL (g/l)	6.74 (0.5 x base case)	13.47	20.21 (1.5 x base case)
Peroxide (mol/l)	0.132	0.132	0.132
Chalcone (mol/l)	0.0802	0.0802	0.0802
DBU (mol/l)	0.22	0.22	0.22

The conversion increased from 51.5 % to 86.7 %, displaying a similar trend to predicted values when the catalyst concentration was increased from 6.74 g/l to 13.47 g/l. On increasing the catalyst concentration further to 20.21 g/l, the conversion decreased to 75.8 % in contrast to a predicted increase in conversion to 95.5 %. Similarly, the enantioselectivity values increased from 71.4 % to 87.6 % but then decreased to 85.7 %, in contrast with values predicted by the model.

The reductions in both conversion and enantioselectivity values with a decrease in catalyst concentration are in line with expectations, since the relative rate of the catalysed to background reaction rate will decrease due the slowing of the catalysed reaction rate, reducing the conversion and enantioselectivity. The conversion and enantioselectivity values predicted by the model at 6.74 g/l catalyst concentration were 75.2 % and 85.8 % respectively, much higher than the experimental values.

The higher predicted values at both 6.74 and 13.47 g/l catalyst can again be partly attributed to higher catalytic activity of the catalyst used in the kinetic study. Additionally, the catalyst concentration of 6.74 g/l does not fall within the catalyst concentration range used in the kinetic studies.

The decrease in experimental conversion and enantioselectivity values at catalyst concentration of 20.21 g/l in contrast to the predicted values of 95.5 % and 94.9 % respectively can be attributed to incomplete mixing in the reactors, due to a decrease in molecular diffusivity and an increase in viscosity of the reaction mixture. As the catalyst concentration was increased the catalyst solution was observed to be more viscous. For an epoxidation reactor catalyst concentration of 20.21 g/l, the corresponding catalyst concentration in the deprotonation reactor would be 40.42 g/l. Given the average density of the THF/Acetonitrile solvent is 837.73 kg/m³, the weight fraction of the catalyst in the solution is only about 0.05 and hence can be classified as a dilute polymeric solution (see Figure 7.14, Cussler, 1997).

Figure 7.14: Diffusion of high polymers (Cussler, 1997)

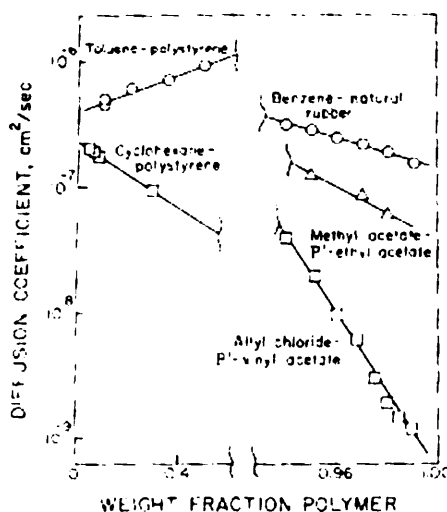


Figure 7.15: Effect of PLL concentration on conversion in PEEK reactor

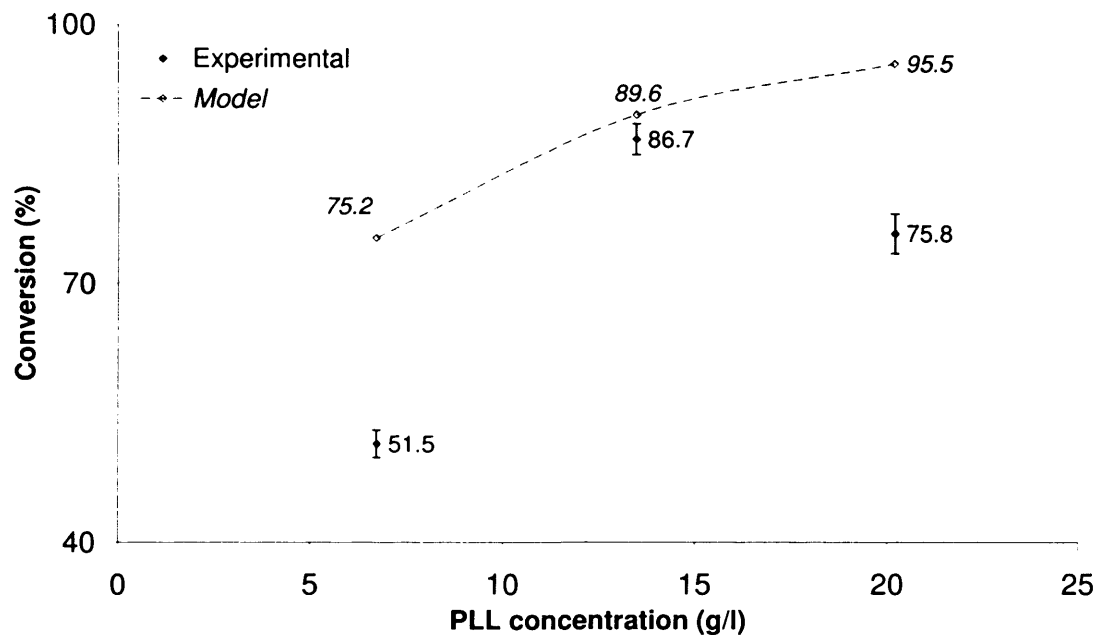
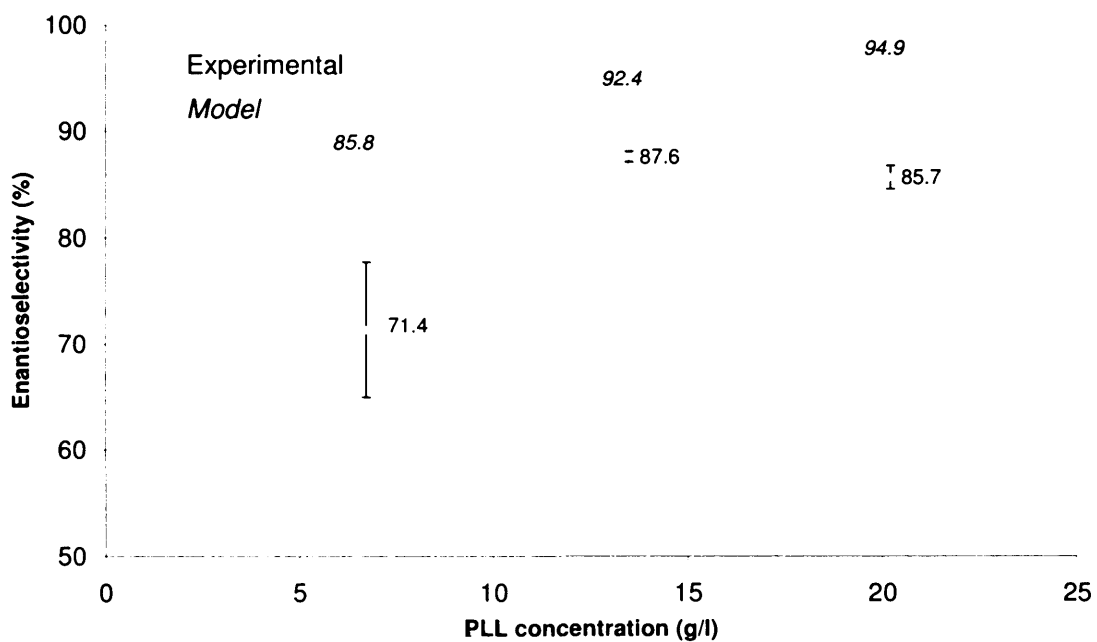


Figure 7.16: Effect of PLL concentration on enantioselectivity in PEEK reactor



In general, solutions of proteins are not treated as polymeric solutions; however the catalyst in this case is tethered on polyethylene glycol with a much larger molecular weight (molecular weight of polyethylene glycol with 82 monomers ~ 5084 compared to molecular weight of 15 monomers of *L*-leucine of 1965) and hence can be treated as a dilute polymeric solution. The diffusion coefficient in a dilute polymeric solution is given by (Li and Gainer, 1968):

$$D = D_0(1 - \alpha\phi) \quad [7.3]$$

where

D is the diffusion coefficient of the solute in the polymer solution

D_0 is the diffusion coefficient of the solute in pure solvent

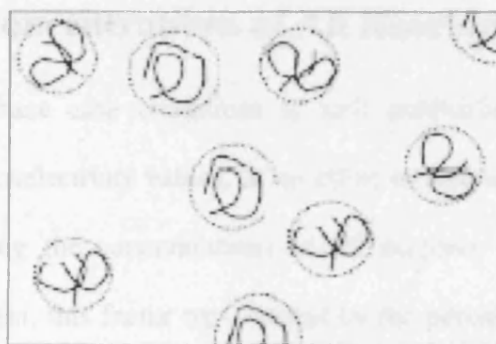
α is a parameter which describes the geometric shape of the polymer molecule. Its value is always greater than unity and is 1.5 for spherical shapes and polymer molecules.

ϕ is the volume fraction of the polymer in solution.

From [7.3], as the catalyst concentration is increased the diffusivity is decreased, although in general this decrease in diffusivity is not expected to be as huge as the increase in relative viscosity (Li and Gainer, 1968). This decrease in diffusivity (not calculated since the volume fraction of the polymer in solution is not known) could affect the conversion by reducing the rate at which the reactants come into contact. The lower enantioselectivity value could be explained by the slower diffusivity, however the higher catalyst to perhydroxyl ion concentration (amplified due to lower perhydroxyl ion concentration and increased catalyst concentration) should compensate for this effect.

Since the viscosity of a solution usually increases drastically when a small amount of polymer is dissolved in it (Li and Gainer, 1968), the poor performance at high catalyst concentration is more likely due to incomplete mixing caused by the increased viscosity. In a dilute polymer solution, the polymers can be regarded as spheres (coils) with a certain radius of gyration (R_g) which depends on the number of monomers per polymer (N), as illustrated in Figure 7.17 (Kozer et al, 2006).

Figure 7.17: Polymer coils in solution (Kozer et al, 2006)



For a suspension of rigid spheres, the effective viscosity, μ_{eff} is given by the Einstein equation (Bird et al, 2002)

$$\mu_{\text{eff}} = \mu_0 (1 + 2.5\phi) \quad [7.4]$$

in which μ_0 is the viscosity of the suspending medium and ϕ is the volume fraction of the spheres. As seen from equation [7.4], the effective viscosity can increase substantially with an increase in the volume fraction of polymer ϕ . The effective viscosity was not calculated, as calculation of the volume fraction requires knowledge of the radius of gyration R_g which was not known.

The large increase in viscosity will lead to a high viscosity ratio between the fluids to be mixed, which can cause a deviation in velocity profile from Poiseuille flow, which increases with increasing viscosity ratio (Kim et al, 2004). Using micro PIV (Particle Image Velocimetry) measurements of two fluid flow in a Y-shape microchannel at high viscosity ratios, the high viscosity fluid was found to occupy a larger portion of the cross sectional area. The high viscosity ratio is likely to also affect the velocity profile and mixing behaviour in the staggered herringbone mixer.

7.3.8. Higher Concentrations of All Reactants

The performance at base case conditions is well established, with relatively good conversion and enantioselectivity values. In an effort to increase the rate of production, the effect of increasing the concentrations of all reagents by the same factor was investigated. Once again, this factor was limited by the peroxide concentration to only about ~ 1.9 times base case conditions due to the reasons described in section 7.3.5. The concentrations of the reagents used in the experiment are shown in Table 7.8.

Table 7.8: Initial concentrations of reactants at higher reagents concentrations

	Base case	Higher concentration
PLL (g/l)	13.47	25.03
Peroxide (mol/l)	0.132	0.245
Chalcone (mol/l)	0.0802	0.149
DBU (mol/l)	0.22	0.41

As shown in Figure 7.18, the conversion decreased from 86.7 to 80.4 % in contrast to a predicted increase from 89.6 % to 99.7 %. The enantioselectivity shown in Figure 7.19, decreased from 87.6 to 78.8 % compared to a predicted increase from 92.4% to 95.3%. The difference between experimental and predicted results can be similarly explained by incomplete mixing due to the lowering of solute diffusivities and increase in viscosity of reaction mixture with an increase in the catalyst concentration, as described in section 7.3.7. However, while the catalyst concentration was even higher at 25.03 g/l in this case, (compared to 20.21 g/l in section 7.3.7), the conversion obtained was higher (although not substantially higher) than that obtained previously (75.8 %) while the enantioselectivity obtained was lower than the 85.7 % achieved previously.

Figure 7.18: Effect of higher concentrations of all reactants on conversion

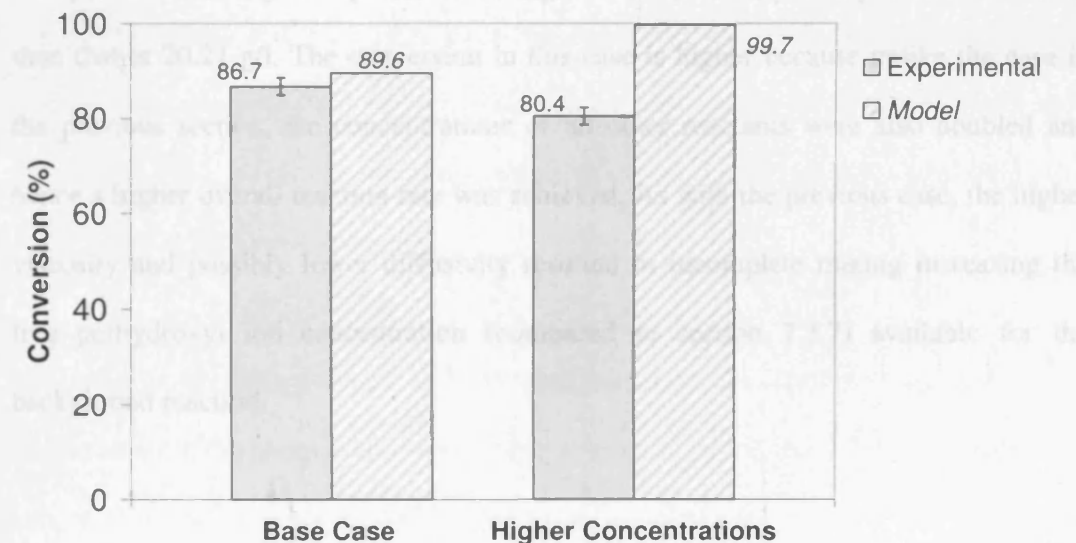
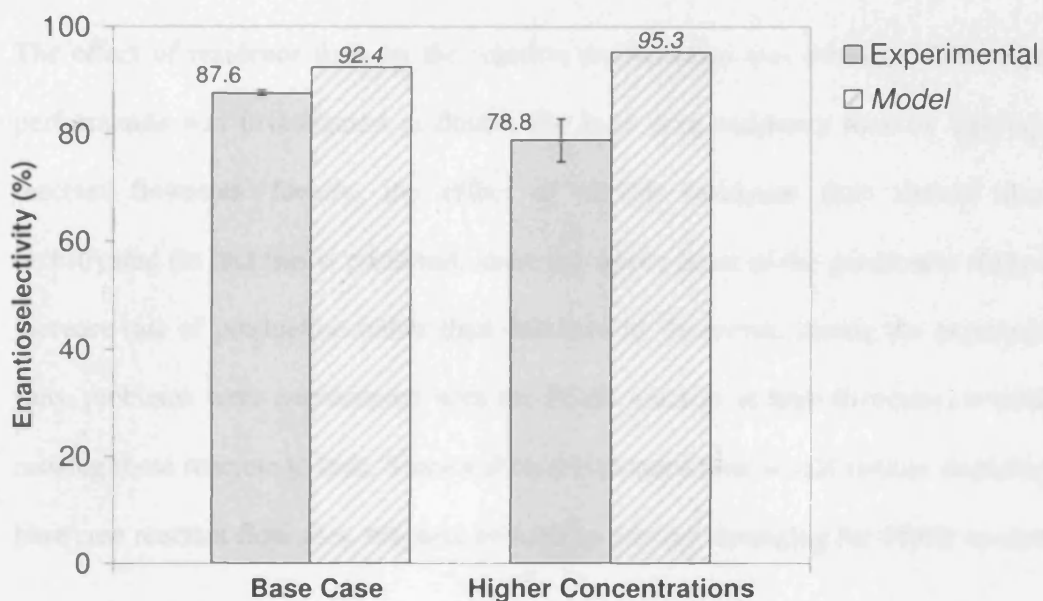


Figure 7.19: Effect of higher concentrations of all reactants on enantioselectivity

The explanation for this is simple. In both cases the solution viscosities would have increased while the solute diffusivities would have decreased, although at 25.03 g/l catalyst, the viscosity is expected to be higher and diffusivity is expected to be lower than that at 20.21 g/l. The conversion in this case is higher because unlike the case in the previous section, the concentrations of all other reactants were also doubled and hence a higher overall reaction rate was achieved. As with the previous case, the higher viscosity and possibly lower diffusivity resulted in incomplete mixing increasing the free perhydroxyl ion concentration (compared to section 7.3.7) available for the background reaction.

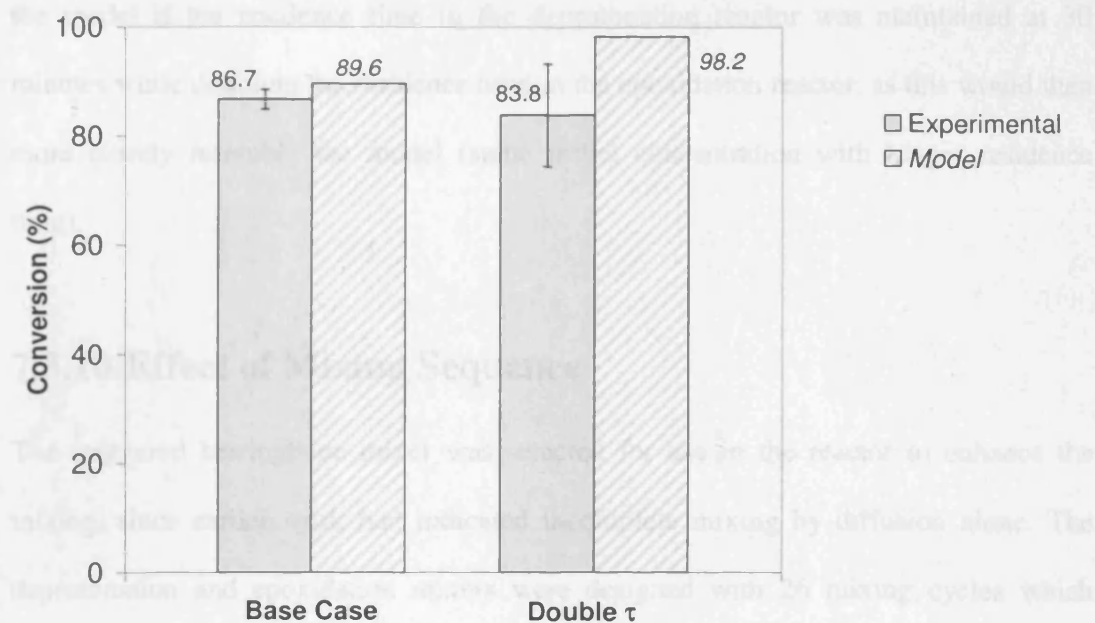
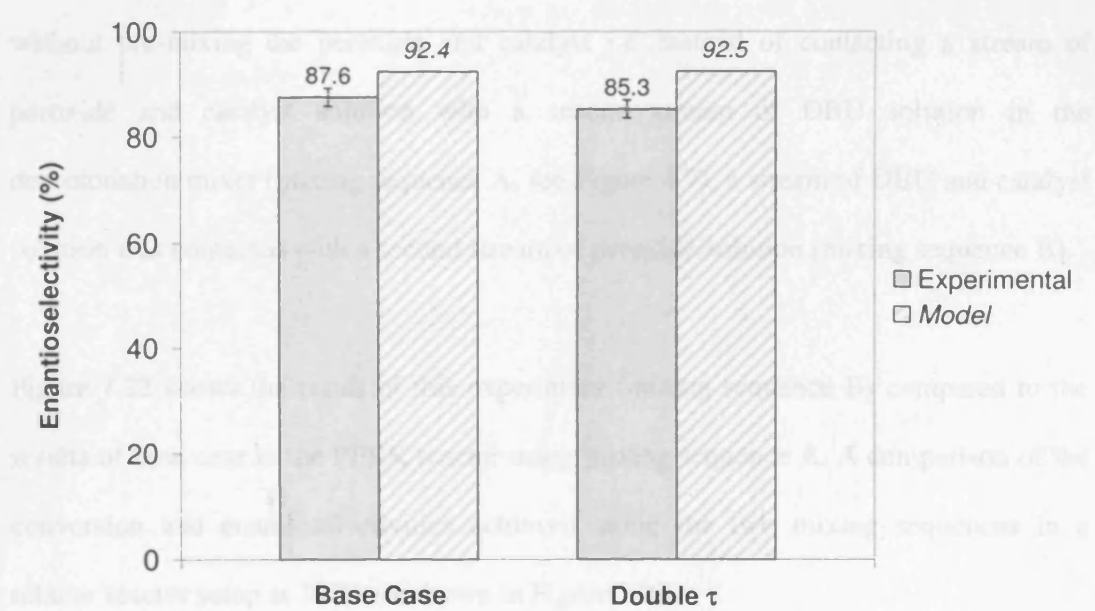
the residence time before the reacting species is not too far from the perhydroxyl ion, whose conversion is governed by the rate of dehydrogenation and the rate of decomposition of the perhydroxyl ion as well as the residence time in the dehydrogenation reactor. With the doubling of the residence time in both dehydrogenation and decomposition reactors, the lower conversion is probably due to the effect of incomplete mixing of the perhydroxyl ions.

7.3.9. Effect of Residence Time

The effect of residence time on the reaction performance was evaluated. The reaction performance was investigated at double the base case residence time by halving the reactant flowrates. Ideally, the effect of shorter residence time should also be investigated (in fact this is preferred, since the whole point of the parametric study is to increase rate of production rather than decrease it). However, during the experimental runs, problems were encountered with the PEEK reactors at high flowrates, sometimes causing these reactors to leak. Since a shorter residence time would require doubling the base case reactant flowrates, this was avoided to prevent damaging the PEEK reactors.

Doubling of the residence time resulted in a decrease in conversion from 86.7 to 83.8 % in contrast to the predicted increase to 98.2 % while the enantioselectivity decreased slightly from 87.6 to 85.3 %, as shown in Figures 7.20 and 7.21 respectively. It is interesting to note that the results were consistent with the results obtained from batch experimental study of the effect of deprotonation time, where the conversion decreased slightly (~ 4%), while the enantioselectivity remained more or less constant, as the deprotonation time was increased.

The reaction did not proceed to near completion as predicted even with the doubling of the residence time because the reactive species is not the peroxide but the perhydroxyl ion, whose concentration is determined by the rate of deprotonation and the rate of decomposition of the perhydroxyl ion as well as the residence time in the deprotonation reactor. With the doubling of the residence time in both deprotonation and epoxidation reactors, the lower conversion is probably due to the effect of decomposition of the perhydroxyl ions.

Figure 7.20: Effect of longer residence time on conversion**Figure 7.21: Effect of longer residence time on enantioselectivity**

The experimental performance is expected to more closely match values predicted by the model if the residence time in the deprotonation reactor was maintained at 30 minutes while doubling the residence time in the epoxidation reactor, as this would then more closely resemble the model (same initial concentration with longer residence time).

7.3.10. Effect of Mixing Sequence

The staggered herringbone mixer was selected for use in the reactor to enhance the mixing, since earlier work had indicated incomplete mixing by diffusion alone. The deprotonation and epoxidation mixers were designed with 26 mixing cycles which represents approximately three times the calculated required mixing length in both cases. The base case epoxidation reaction was carried out using mixing sequence B (see Figure 4.6) to determine if this new mixer design can provide sufficient mixing even without pre-mixing the peroxide and catalyst i.e. instead of contacting a stream of peroxide and catalyst solution with a second stream of DBU solution in the deprotonation mixer (mixing sequence A, see Figure 4.7), a stream of DBU and catalyst solution was contacted with a second stream of peroxide solution (mixing sequence B).

Figure 7.22 shows the result of this experiment (mixing sequence B) compared to the results of base case in the PEEK reactor using mixing sequence A. A comparison of the conversion and enantioselectivities achieved using the two mixing sequences in a tubular reactor setup at 30°C are shown in Figure 7.23.

Figure 7.22: Effect of mixing sequence on conversion and enantioselectivity in PEEK reactor at 23.1 °C

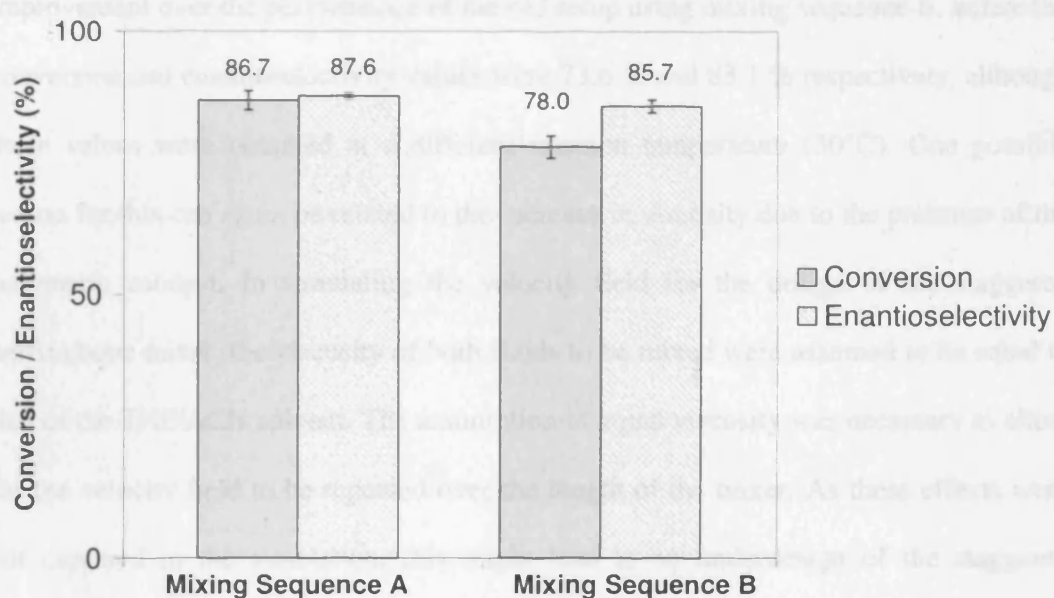
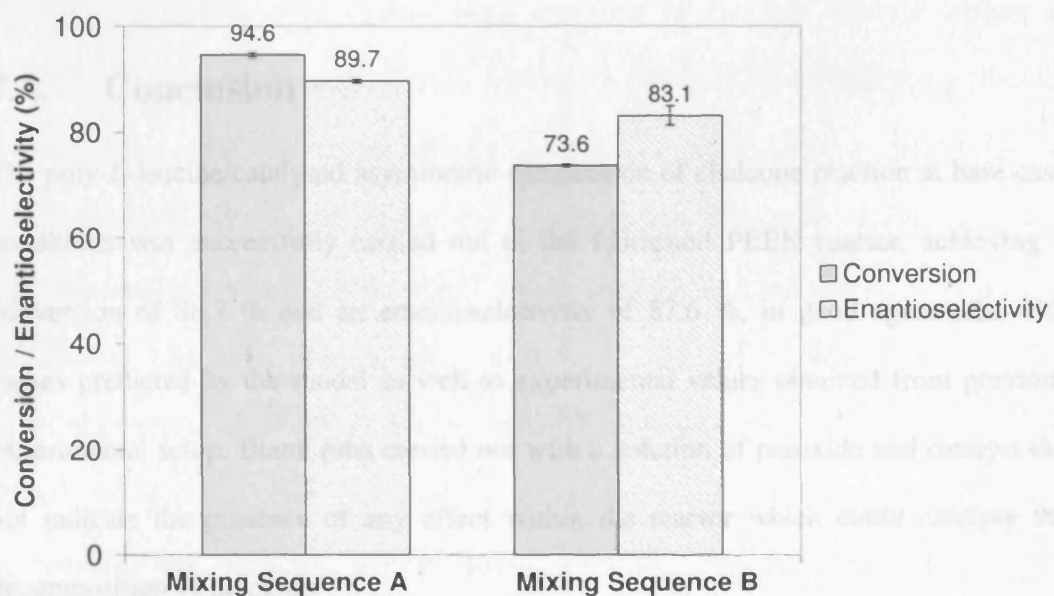


Figure 7.23: Effect of mixing sequence on conversion and enantioselectivity in a tubular reactor at 30°C



The conversion was only 78 % while the enantioselectivity was 85.7 %, lower than that using mixing sequence A in the PEEK reactor. However, there was a slight improvement over the performance of the old setup using mixing sequence B, where the conversion and enantioselectivity values were 73.6 % and 83.1 % respectively, although these values were obtained at a different reaction temperature (30°C). One possible reason for this can again be related to the increase in viscosity due to the presence of the polymeric catalyst. In simulating the velocity field for the design of the staggered herringbone mixer, the viscosity of both fluids to be mixed were assumed to be equal to that of the THF/ACN solvent. The assumption of equal viscosity was necessary to allow for the velocity field to be repeated over the length of the mixer. As these effects were not captured in the simulation, this might lead to an underdesign of the staggered herringbone mixer used in the PEEK reactor and explain the poor performance obtained using mixing sequence B. The slight improvement in performance in the PEEK reactor over the performance in the tubular reactors with mixing sequence B may be due to the large design margin incorporated for the mixer design.

7.4. Conclusion

The poly-*L*-leucine catalysed asymmetric epoxidation of chalcone reaction at base case conditions was successfully carried out in the fabricated PEEK reactor, achieving a conversion of 86.7 % and an enantioselectivity of 87.6 %, in good agreement with values predicted by the model as well as experimental values obtained from previous experimental setup. Blank runs carried out with a solution of peroxide and catalyst did not indicate the presence of any effect within the reactor which could catalyse the decomposition of peroxide.

A parametric study of the effects of reaction temperature, residence time and concentrations of the various reactants and catalyst on the reaction performance was carried out and the base case conditions appeared to produce the best results. Increasing the reaction temperature from 15 to 23.1°C resulted in a marginal improvement in both conversion and enantioselectivity although increasing the reaction temperature further to 30°C resulted in a drop in reaction performance, which was attributed to formation of gas plugs within the reactors due to increased peroxide decomposition. The effect of increasing chalcone concentration on conversion displayed a similar trend to that predicted by the model although the predicted enantioselectivity values differed from those obtained experimentally, attributed to a difference in actual background reaction rate compared to that predicted by the model. The change in peroxide, DBU and poly-*L*-leucine concentrations all indicated that the optimal performance was achieved at base case conditions.

The difference between experimental and predicted values in the cases of changing peroxide and DBU concentrations were attributed to the fact that the change in perhydroxyl ion concentration with a change in either DBU or hydrogen peroxide concentration was not accounted for in the model. Increasing poly-*L*-leucine concentration resulted in a sharp decrease in performance, in contrast with the predicted improvement in conversion, attributed to the increase in fluid viscosity as well as decrease in diffusivity, which resulted in incomplete mixing. At higher concentrations of all reactants, a similar effect was observed which was compensated somewhat by the faster reaction rate. Increasing the residence time did not improve the reaction performance as predicted by the model and this was attributed to the lower concentration of perhydroxyl ions due to decomposition in the deprotonation reactor.

The decrease in performance when the original mixing sequence (B) was used, was again attributed to the increased viscosity of the catalyst solution which affected the velocity profile and mixing behaviour which was not taken into account during the design of the mixers. The results of these studies have brought to light some unexpected phenomena, which were not taken into account during the design of the reactors. The effect of the polymeric catalyst solution on viscosity and molecular diffusivity which was not captured in the mixing simulations, resulted in a mixer which was not adequately designed, although the design margin compensated for this effect somewhat. While the assumption of equal viscosities for a two-fluid flow is commonly employed in other studies of mixing since the viscosity difference was generally assumed to be small, the increase in viscosity due to the presence of the catalyst would have a huge effect which was neglected in the studies. The results of this work also suggest that the differences between predicted and experimental results are mainly attributed to the following factors (apart from experimental error):

- slight difference in catalytic activity between the catalyst used in the kinetic studies and the catalyst batch used in this study,
- rate equations do not account for the change in perhydroxyl concentration with a change in either hydrogen peroxide or DBU concentrations,
- the rate of the background reaction in the presence of the catalyst is not reflected accurately by the rate equation, due to perhydroxyl ion sequestration by the catalyst.

Chapter 8

Numbering Up of Chalcone Epoxidation

System

8.1. Introduction

One of the often cited advantages of microchemical processing is the ease of increasing the throughput by scaling out i.e. increasing the number of microreactors operating in parallel. With numbering up, the single unit system is studied and optimised and large scale production is achieved via interconnection of large numbers of microreactors, with each unit running under the same optimum conditions as those found in the single unit. This avoids the problems associated with scaling-up, which occurs due to a change in the heat and mass transfer characteristics. It is arguable however that rather than solving the problems with scale-up, scaling out merely changes the nature of the problem to one of delivering precise reagent flow rates to each parallel operating reactor.

There are two different structures used for distributing flows. The consecutive type manifold consists of a header distributing to a number of outlets while in the bifurcation manifold structure flow is split into two streams repeatedly. Where there are no dimensional variations, uniform flow distribution is always achieved in the bifurcation structure provided the channels at each level have the same size and the length of channel after each bend is sufficient for a symmetrical velocity profile to develop. In the consecutive manifold structure however, careful design of the distributing and collecting headers is required for flow equipartition. In general, there are two main approaches to achieving even flow distribution in consecutive headers. The *first method* achieves uniform flow distribution by careful design of the shape of both distributing and collecting header geometries. Optimal header geometries were obtained via CFD investigations, taking into consideration among other things, the effects of header shape and channel geometry (Commengé et al, 2002; Tonomura et al, 2004; Delsman et al, 2004; Rebrov et al, 2007).

In the ***second method***, uniform flow distribution is achieved by making the average pressure drop across the microchannel outlets substantially larger than the pressure variation along the length of the distribution header which, unlike the first method, has a uniform cross section (Perry and Green, 1997). The relative variation in pressure drop across the various microchannel outlets will therefore be small, reducing the variation in flow. This method is based on similar methods for macro scale equipment and is more amenable to mass manufacture due to its simple principle and hence seems to be the more popular approach adopted for the various real applications reported to date (Kikutani et al, 2002; Schwalbe et al, 2005; Tonkovich et al, 2005; de Mas et al, 2005; Tonkovich et al, 2005; Wada et al, 2006).

Amador et al (2004) used a method based on electrical resistance network to study both the bifurcation manifold structure as well as consecutive structure, using both the main methods of achieving flow distribution (described in the previous paragraphs). The second method for consecutive manifolds, based on reduction of pressure drop in the distribution channel relative to that in the reaction channels, was found to be preferable since it is simpler. However when a constant depth is required, the first method which involves careful design of distributing and collecting header geometries may be preferable. At high Re , a bifurcation structure may be preferable to the consecutive manifold. Other recent work on flow distribution in microstructured devices include the work of Pfeifer et al (2004) who developed techniques for quantification of fluid flow distribution using hot wire anemometry.

Delsman et al (2005) also studied the effects of differences between microchannels such as channel flow rate, channel diameter, the amount of catalyst in the channel as well as channel temperature on microreactor performance for a first order heterogeneous reaction. Influence of flow maldistribution on the overall conversion was found to be small with factors such as channel diameter variation and amount of catalyst coating producing a more pronounced effect on conversion.

In this work, the approach based on macro scale distributors was adopted to size the distributing header appropriately to ensure equal flow distribution. The reactors were then assembled and tested with the poly-*L*-leucine catalysed asymmetric epoxidation of chalcone and the results obtained compared to those obtained in a single unit.

8.2. Experimental

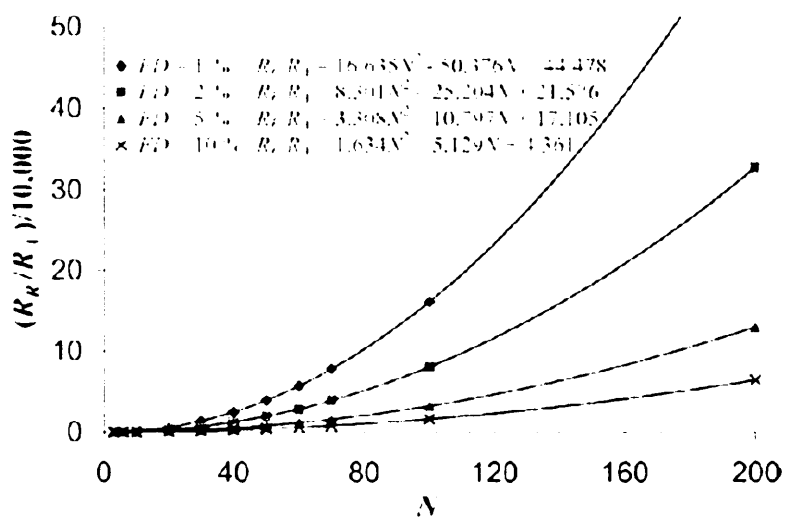
8.2.1. Flow Distribution

The approach taken here is based on similar methods used in the design of large scale flow distributors such as the perforated-pipe distributor, where uniform flow distribution is achieved by making the average pressure drop across each distributor hole significantly larger compared to the pressure drop across the distributor header (Perry and Green, 1997). The required ratio of distributor header resistance to distribution channel resistance as a function of N , the number of distribution channels has been established for several values of the divergence from flow equipartition, FD , ranging from 1 to 10 % (Amador et al, 2004). The flow divergence is defined as:

$$FD(\%) = \max_{j=1}^N \left[100 \frac{|Q_{EQUI} - Q_{R,j}|}{Q_{EQUI}} \right] \quad [8.1]$$

When manufacturing tolerances were taken into account, the design for $FD = 1\%$ resulted in only a 0.52 % improvement in the mean standard deviation of the residence time over the design for $FD = 5\%$, while the latter design allowed for a less demanding design requirement. For this reason, the inlet stream headers for the PEEK reactors were designed for $FD = 5\%$ as this value maximises flow equipartition without requiring excessively large distributor header dimensions. Figure 8.1 reproduced from Amador et al (2004) allows the ratio of header to channel cross sectional areas required for flow equipartition to be estimated. For the purpose of sizing the distribution header, each individual PEEK reactor in the stack can be assumed to be analogous to a reaction channel and the header feeding each inlet stream in the stack analogous to the distribution header. The required ratio of header to PEEK reactor resistance for 5 % flow divergence in a 10 reactor stack can then be estimated using Figure 8.1. However, due to the complicated flow structures on the reactor, the ratio taken from Figure 8.1 cannot be viewed as a simple ratio of header to channel cross sectional areas.

Figure 8.1: Ratio R_H/R_A required for flow equipartition as a function of number of channels N and divergence from flow equipartition, FD (Amador et al, 2004).



Instead, the pressure drop across one PEEK reactor was first estimated and the header dimensioned to ensure the ratio of header to reactor pressure drop was equal to the value obtained from Figure 8.1, i.e. $\Delta P_{\text{header}} = \Delta P_{\text{reactor}}/(R_R/R_A)$, where R_R is the frictional resistance across the reactor and R_A is the frictional resistance in the distributing header. The overall mechanical energy balance (Geankoplis, 1993) for an incompressible flow is shown below:

$$\frac{1}{2\alpha} \rho(u_{2,\text{av}}^2 - u_{1,\text{av}}^2) + \rho g(z_2 - z_1) + (P_2 - P_1) + \sum F + W_s = 0 \quad [8.2]$$

where $\alpha = 0.5$ for laminar flow, $W_s = 0$ and $\sum F$ is the sum of frictional and secondary losses. From [8.2], the gravitational pressure change can be removed if the stack of reactors are placed horizontally, since $\Delta z = 0$ across all sections on a horizontal PEEK reactor plate. However, the stack of PEEK reactors were placed vertically because calculation of the pressure change due to elevation change in the headers were found to be substantial. If the stack of PEEK reactors were placed horizontally, the big change in R_A would require R_R to be increased substantially since the flow distribution is improved with increased R_R/R_A . As R_R is fixed by design and relatively much bigger than R_A , placing the stack of reactors vertically allows a reasonably high R_R/R_A to be achieved by careful design of the inlet headers.

The pressure drop across each reactor plate was computed as the sum of the frictional pressure drop in the mixers, the frictional pressure drop across the delay loops and the pressure change due to change in elevation (taken as the distance between inlet and outlet headers). All other pressure losses (including losses due to expansion and contraction) were substantially smaller than the frictional losses and therefore were not taken into consideration when sizing the headers. The equations used for estimating the secondary pressure losses are shown in Appendix 8-1.

The frictional losses in the staggered herringbone mixers were estimated from the mixer simulation. Frictional losses in the mixer inlet sections and the delay loops, both of which have rectangular cross sections, were computed using the equation:

$$\Delta P = \frac{K \mu Q L}{w h^3} \quad [8.3]$$

where the value of K was taken as 25.619 in the mixer inlet sections and 13.535 in the delay loops (see Table 5.12). The different flow sections considered are shown in Table 8.1 and Figure 8.2 while the calculated pressure losses in a single PEEK reactor are shown in Table 8.2.

Table 8.1: The various flow sections considered

Section	Cross-section	Relevant ratio ^c
1 Inlet header 1 (Peroxide + PLL feed)	Circular	R_T / R_1 ^a
2 Inlet header 2 (DBU feed)	Circular	R_T / R_2 ^a
3 Inlet header 3 (Chalcone feed)	Circular	R_{ER} / R_3 ^b
4 Mixer 1 inlet section (both identical)	Rectangular	N/A
5 Mixer 1	Rectangular	N/A
6 Deprotonation delay loop	Rectangular	N/A
7 Mixer 2 inlet section	Rectangular	N/A
8 Mixer 2	Rectangular	N/A
9 Epoxidation delay loop	Rectangular	N/A
10 Outlet header	Circular	R_T / R_{10}

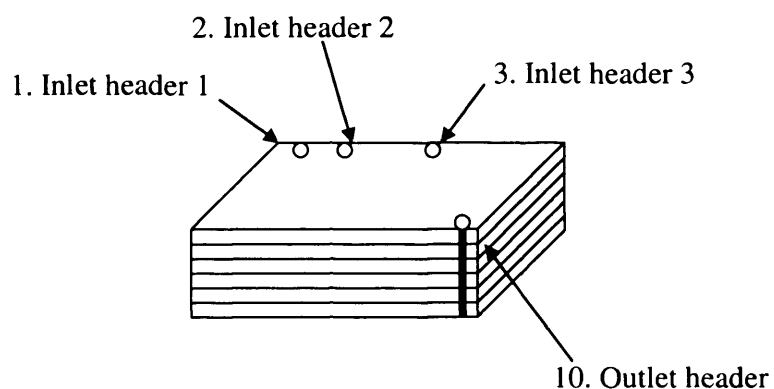
a. R_T = total pressure drop across both deprotonation and epoxidation sections.

b. R_{ER} = pressure drop in the epoxidation section only, i.e. sections 7 – 9 only.

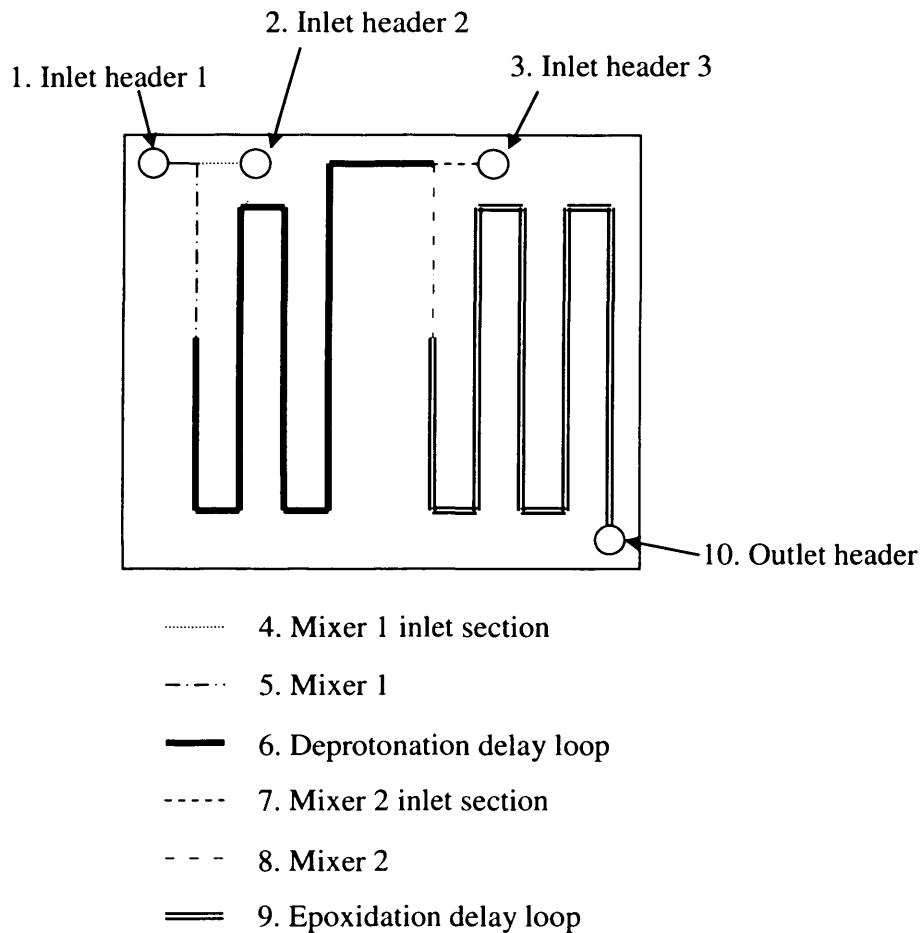
c. Relevant ratio for sizing the distribution header.

Table 8.2: Pressure change on a single PEEK reactor

Section	Pressure change (Pa)
Elevation change	698.30
Mixer 1 inlet section	-140.82
Mixer 1	26 cycles x 12.88 Pa/cycle = - 334.76
Deprotonation delay loop	-5.72
<i>Total frictional losses in Loop 1</i>	$R_D = -481.3$
Mixer 2 inlet section	-281.63
Mixer 2	26 cycles x 25.75 Pa/cycle = -669.60
Epoxidation delay loop	-12.20
<i>Total frictional losses in Loop 2</i>	$R_E = -963.43$
<i>Total Reactor</i>	$R_T = -481.3 - 963.43 + 698.3 = -746.43$
<i>Total Reactor (Epoxidation loop only)</i>	$R_{ER} = -963.43 + 698.3 = -265.13$

Figure 8.2: Schematic of the various flow sections**(a) View of the inlet/outlet headers**

(b) View from the top of the reactor plate



From Figure 8.1, for $FD = 5\% R_R/R_A$ can be computed from:

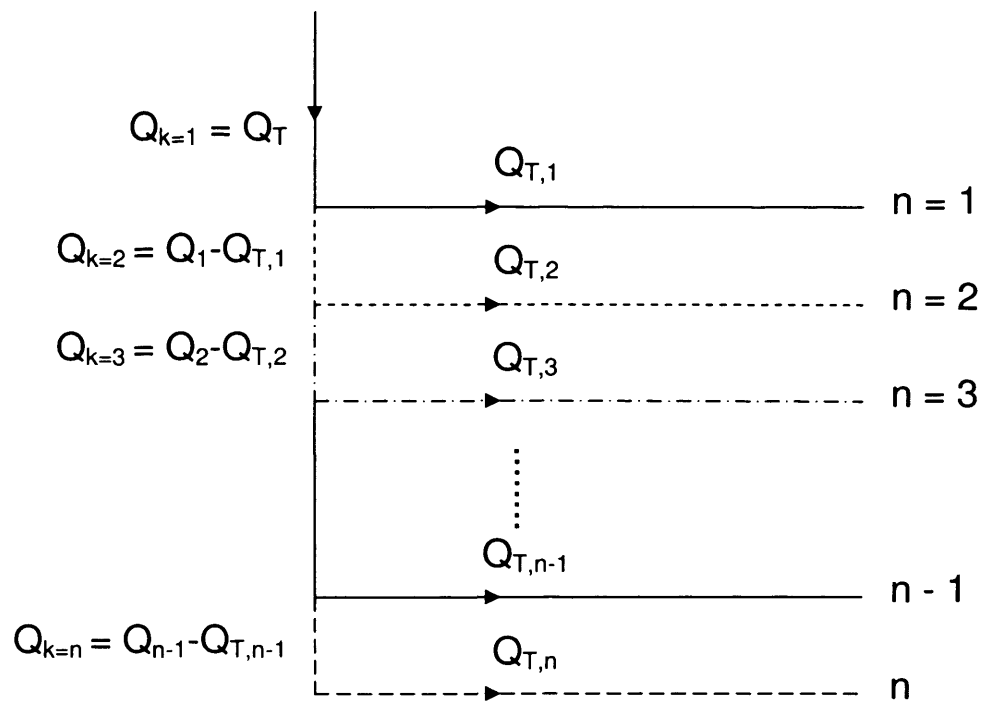
$$\frac{R_R}{R_A} = 3.308N^2 - 10.797N + 17.105 \quad [8.4]$$

The required R_R/R_A for $N = 10$ PEEK reactors was computed as ~ 240 . Since the pressure drop in a single PEEK reactor was $\sim 746.43 \text{ Pa}$ (265.13 Pa for epoxidation loop only), the pressure drop across inlet headers 1 and 2, R_1 and R_2 should be around 3.1 Pa at most and a maximum of $R_3 = 1.1 \text{ Pa}$ for inlet header 3. For a stack of N reactors as shown in Figure 8.3, the pressure drop across the header is calculated as:

$$\Delta P_{header} = \sum_{k=1}^N \Delta P_k \quad [8.5]$$

$$\Delta P_k = \frac{128\mu L_k Q_k}{\pi d^4} \quad [8.6]$$

Figure 8.3: Flowrates across different sections of the inlet header



The minimum inlet diameter for a stack of 10 PEEK reaction reactors, assuming distance between each reactor of around 10 mm ($L_k = 10$ mm), which resulted in $\Delta P \leq 3.1$ Pa for inlet sections 1 and 2 were computed as ~ 710 μm while for section 3, the inlet diameter which resulted in $\Delta P \leq 1.1$ Pa was ~ 1100 μm . For comparison, the minimum diameter for the three inlet sections were also computed based on a second set of criteria established for a perforated pipe distributor, in which the pressure drop across the distributor holes should be about 10 times the pressure drop across the length of the distributor header for 5 % maldistribution (Perry and Green, 1997):

$$\% \text{ maldistribution} = 100 \left(1 - \sqrt{\frac{\Delta p_o - |\Delta p_p|}{\Delta p_o}} \right) \quad [8.7]$$

Based on this second set of criteria, the minimum diameter for inlet sections 1 and 2 was $\sim 320 \mu\text{m}$ while the minimum diameter for section 3 was $\sim 590 \mu\text{m}$. The calculations above were repeated for a stack of 4 PEEK reactors, as the experimental work was carried out with a stack of 4 reactors rather than 10. This was because while 10 PEEK reactors were fabricated for the experimental work, many became unusable due to clogging and by the time the scale-out was attempted there were only 4 working PEEK reactors left.

For a stack of 4 reactors, the required R_R/R_A ratio was ~ 27 . Hence, the pressure drop across the inlet sections 1 and 2 should be around 27.6 Pa at most and a maximum of 9.8 Pa for inlet section 3. The corresponding minimum header diameter values computed using the first method (Amador et al), were $270 \mu\text{m}$ for inlet sections 1 and 2 and $410 \mu\text{m}$ for inlet section 3. The minimum header diameter values computed using the second method (Perry and Green, 1997) were $210 \mu\text{m}$ for inlet sections 1 and 2 and $320 \mu\text{m}$ for inlet section 3.

Clearly, the design criteria established by Amador et al was more conservative and the values for a stack of 4 PEEK reactors were well within the actual design value, with the fabricated distribution header diameter slightly $> 1000 \mu\text{m}$. The final dimensions of the inlet and outlet headers are indicated in Table 8.3, along with corresponding pressure drop across the inlet and outlet headers.

If the stack of reactors were placed horizontally rather than vertically, the current header design would not satisfy the required R_R/R_A ratio, since the gravitational pressure change across a 2 layer stack alone amount to $\sim 82 \text{ Pa}$, higher than the calculated maximum allowable pressure change (27.6 Pa for sections 1 and 2 and 9.8 Pa for section 3).

Table 8.3: Inlet and outlet header dimensions

Number of reactors	Section n^a	Diameter (mm)	Pressure drop ^b (Pa)	Reference ^c R_R	R_R/R_A^d
4	1	1	0.137	746.43	5448
4	2	1	0.137	746.43	5448
4	3	1	0.275	265.13	964
4	10	1	0.550	746.43	1357
10	1	1	0.756	746.43	987
10	2	1	0.756	746.43	987
10	3	1	1.512	265.13	175
10	10	1	3.024	746.43	247

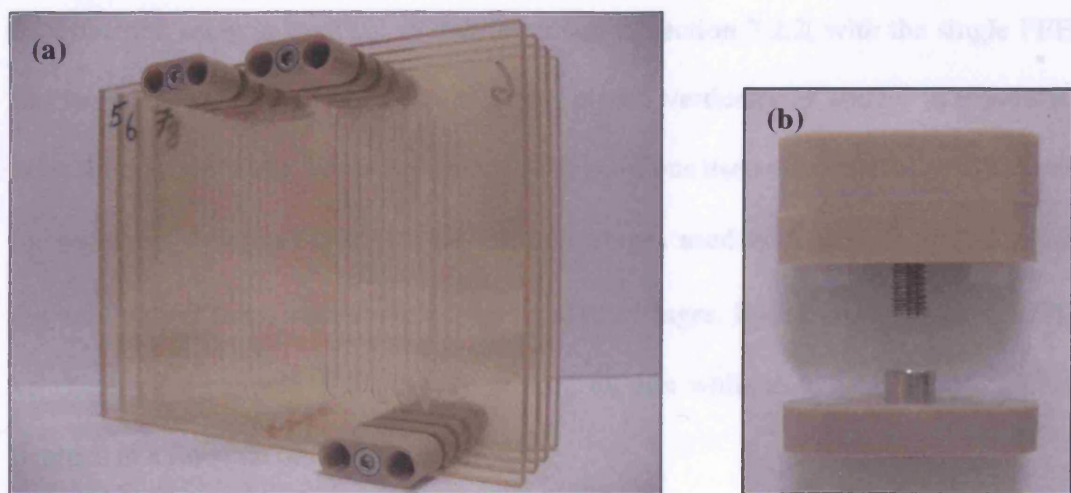
- a. Section n , refers to the various flow sections as outlined in Table 8.1 and Figure 8.2.
- b. Pressure drop across the entire section n , i.e. for stack of 4 reactors, this is pressure drop in the header across all 4 stacks.
- c. Pressure drop across PEEK reactor used to determine maximum ΔP_{header} , for sizing the distribution headers. This is either R_T or R_{ER} , see Table 8.1.
- d. The values of the actual pressure ratios obtained using actual header diameter value of 1000 μm .

8.2.2. Scaled Out Reactor Configuration

Both PEEK and acrylic reactors were fabricated by Epigem Ltd, U.K. as described in section 5.4.4. The reactors were stacked up using PEEK connector fittings, as shown in Figure 8.4 for the acrylic reactors. PTFE ferrules were used with the PEEK fittings for sealing. This arrangement allows the reactant streams to flow between reactors while ensuring all stacked reactors were maintained at water bath temperature. The stacked PEEK reactors are shown in Figure 8.5.

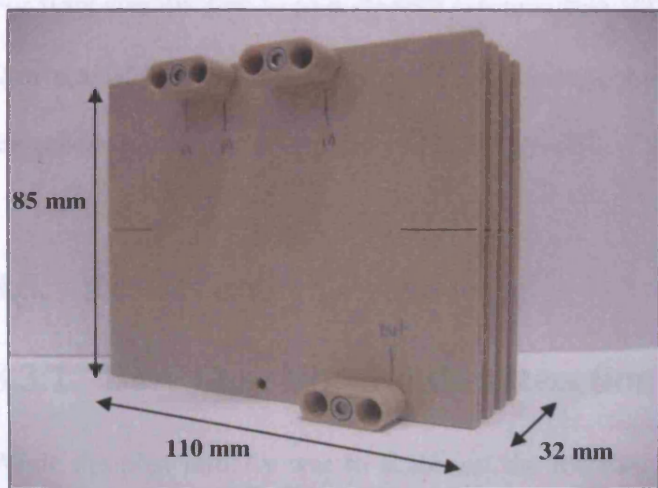
Figure 8.4: (a) Stacked acrylic reactors using PEEK connector fittings. (b) PTFE ferrules used with the PEEK fittings provide sealing between connector fitting and PEEK reactor plate.

The experimental methods were similar to those described in section 4.2. The



8.2.3. Flow Visualisation

The flow visualisation experiments were carried out using a dark red solution of Rhodamine 6G in the top inlet and plain water in the second inlet. For flow visualisation experiments in a single reactor, two 50 μ l syringes were used with the KF 3000 Modular Digital Pump (Cetech), each at a flow rate of 0.01 μ l/sec.

Figure 8.5: Stacked PEEK reactors

8.2.3. Setup

The experimental methods were similar to those described in section 4.2. The experimental setup is identical to that described in section 7.2.2, with the single PEEK reactor replaced by the scaled out reactors, placed vertically as shown in Figure 8.5, with the reactant inlets located at the top. The solutions used were similar, however due to the higher flowrates required, the 50 μ l syringes used with the XP 3000 Modular Digital Pump (Cavro) were replaced with 100 μ l syringes. Both DBU and peroxide/PLL solutions were pumped at a flowrate of 0.02 ml/min while the chalcone solution was pumped at a flowrate of 0.04 ml/min.

8.2.4. Flow Visualisation

The flow visualisation experiments were carried out using a dark red solution of Rhodamine 6G for the first inlet and plain water in the second inlet. For flow visualisation experiments in a single reactor, two 50 μ l syringes were used with the XP 3000 Modular Digital Pump (Cavro), each at a flow rate of 0.01 ml/min.

For flow visualisation in four stacked reactors, two 100 μ l syringes were used, each at a flow rate of 0.04 ml/min in the first case (equivalent to single unit experiments) and in the second case each at a flowrate of 0.02 ml/min.

8.3. Results and Discussions

8.3.1. Base Case Epoxidation Reaction

While the plan initially was to scale out the reactors by a factor of 10, the persistent problems with clogging of the PEEK reactors meant that by the time the scale out was attempted, many of the PEEK reactors fabricated were defective. As a result, a scale out factor of 4 was attempted using the remaining functional PEEK reactors. The scaled out reactors were tested with the poly-*L*-leucine catalysed asymmetric epoxidation of chalcone at base case conditions (Table 4.1). The base case epoxidation in a stack of 4 PEEK reactors at 23.1°C resulted in an average conversion of 31.4 % much lower than the values obtained in a single PEEK reactor, although the enantioselectivity value of 82.7 % was just slightly below the value obtained in a single reactor, as shown in Table 8.4.

Table 8.4: Performance of a stack of 4 PEEK reactors at base case epoxidation compared to performance of single reactor.

	Stack of 4 PEEK reactors	Single PEEK reactor
Conversion (%)	31.4 ± 2.4	86.7 ± 1.8
Enantioselectivity (%)	82.7 ± 1.8	87.6 ± 0.5

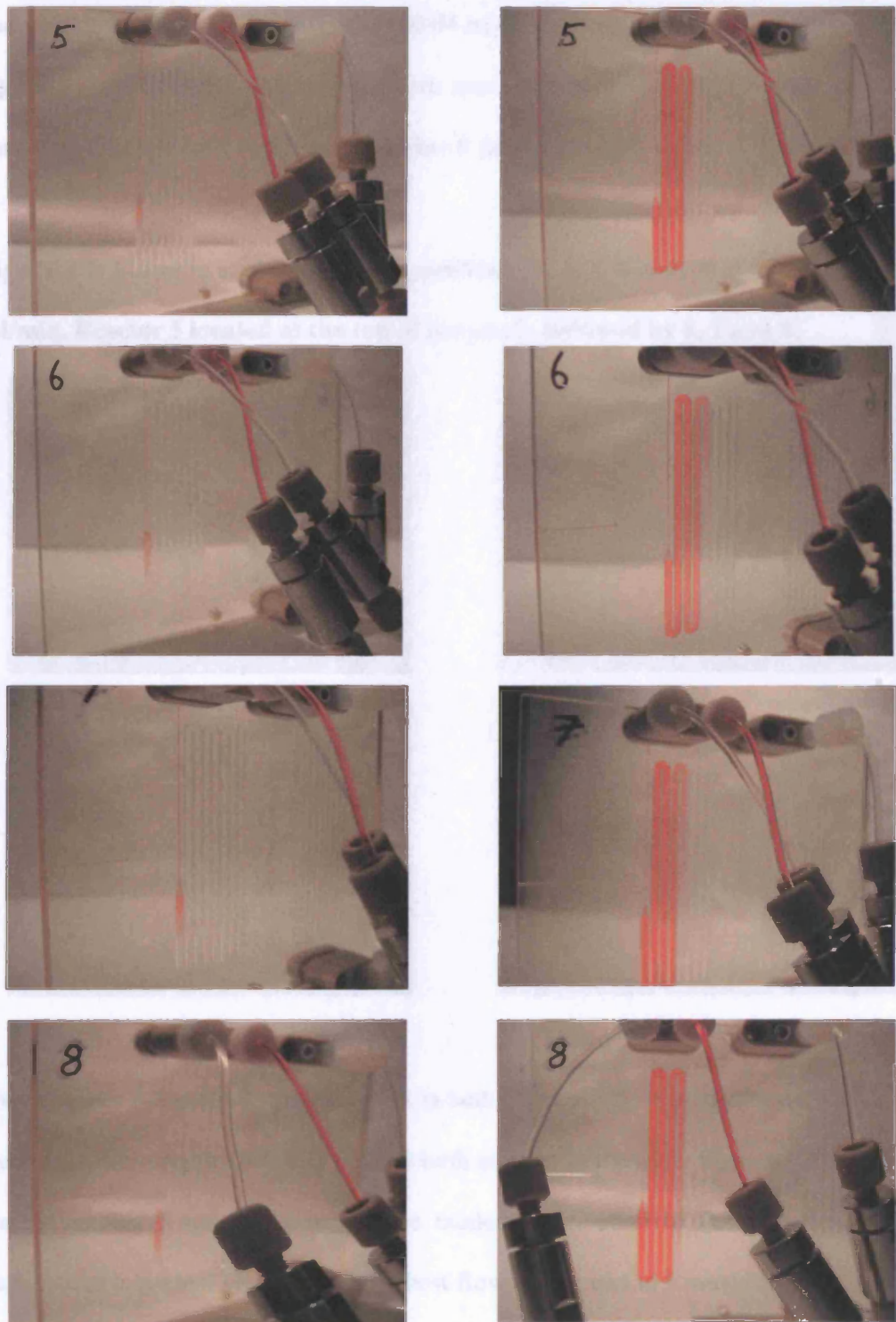
a. Conversion and enantioselectivity values given with calculated standard deviation.

The results clearly show that uniform flow distribution was not achieved in the scaled out unit. A simple flow visualisation study was carried out to establish the flow distribution in the stack of reactors. As the PEEK reactors are opaque, several acrylic reactors with identical designs were fabricated which allow the flows within these reactors to be seen. Clearly the acrylic reactors may have different properties which affect the flows within these reactors differently; however these studies are meant only for gaining a better insight into what was happening in the stack of reactors and how these could affect the reaction outcome. A detailed flow distribution study would fall outside the scope of the current work.

8.3.2. Flow Visualisation

As a first step, the flow in each acrylic reactor was checked to ensure that the fluids were flowing normally and no unforeseen effects were present. A solution of rhodamine in water was prepared to visualise the flows. The acrylic reactors were placed in an ultrasonic bath and flushed with water to remove any trapped air bubbles and to make sure that the acrylic reactors are liquid full. To prevent air bubbles from getting trapped when assembling the stacked reactors, the acrylic reactors were immersed in a water bath after flushing out the air bubbles and the stack of acrylic reactors were assembled in the water. To ensure that the inlet header for Rhodamine is filled with Rhodamine (rather than water) prior to pumping, a microsyringe was filled with Rhodamine solution and used to flush out the water from the inlet header before connecting the Rhodamine inlet tube to the connector fittings. The rhodamine solution was pumped into one inlet while water was pumped into the second inlet, both at a flowrate of 0.01 ml/min. The third inlet at the entrance to the epoxidation reactor was covered to ensure the fluids were pumped to the outlet. These are shown in Figure 8.6.

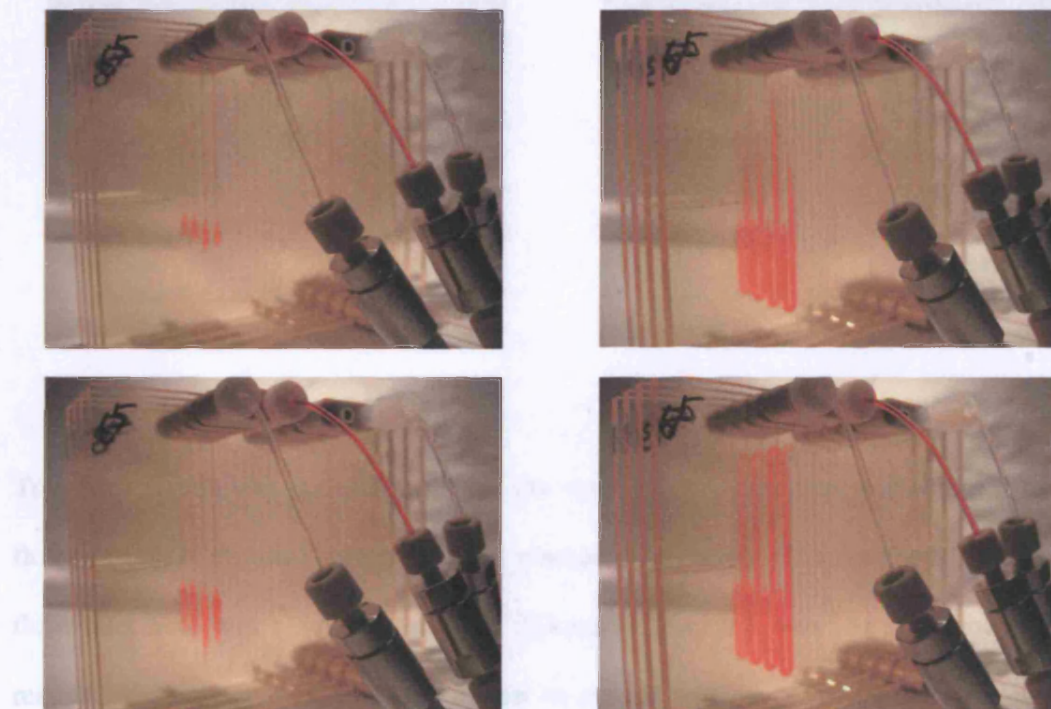
Figure 8.6: Flows in single reactors (5 – 8) at total flows of 0.02 ml/min at the start of the experiment (left) and at some time later (right).



end) of a starting chalcone and (b) flow visualization with respect to the process

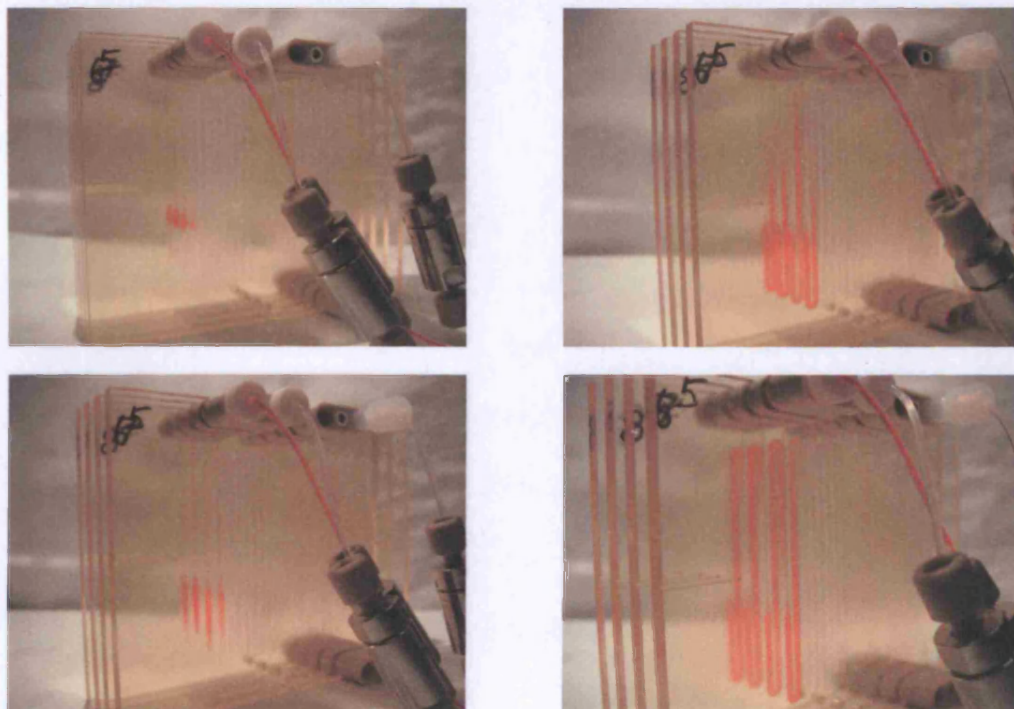
The flow visualisation in the stacked acrylic reactors were carried out at two different flowrates, one at a total flow rate of 0.08 ml/min (equivalent to single unit experiments) and a second run at half the flowrate at 0.04 ml/min. These are shown in Figure 8.7 and Figure 8.8 respectively. The reactors were numbered from 5 -8, with reactor number 5 nearest to the fluid inlet and reactor number 8 furthest away from the fluid inlet.

Figure 8.7: Flows in scaled-out configurations (5, 6, 7 and 8) at a flowrate of 0.08 ml/min. Reactor 5 located at the top of the stack, followed by 6, 7 and 8.



From Figures 8.7 and 8.8, it is clear that in both cases, the flow in reactor number 6 was the fastest, followed by reactors 7 and 8 both at roughly the same flowrate. The flow in reactor number 5 was the slowest. The random distribution of flows to the reactors (rather than a gradual change from highest flow at one end to lowest flow at the other end) is a strong indication that the flow maldistribution was related to the fabrication process.

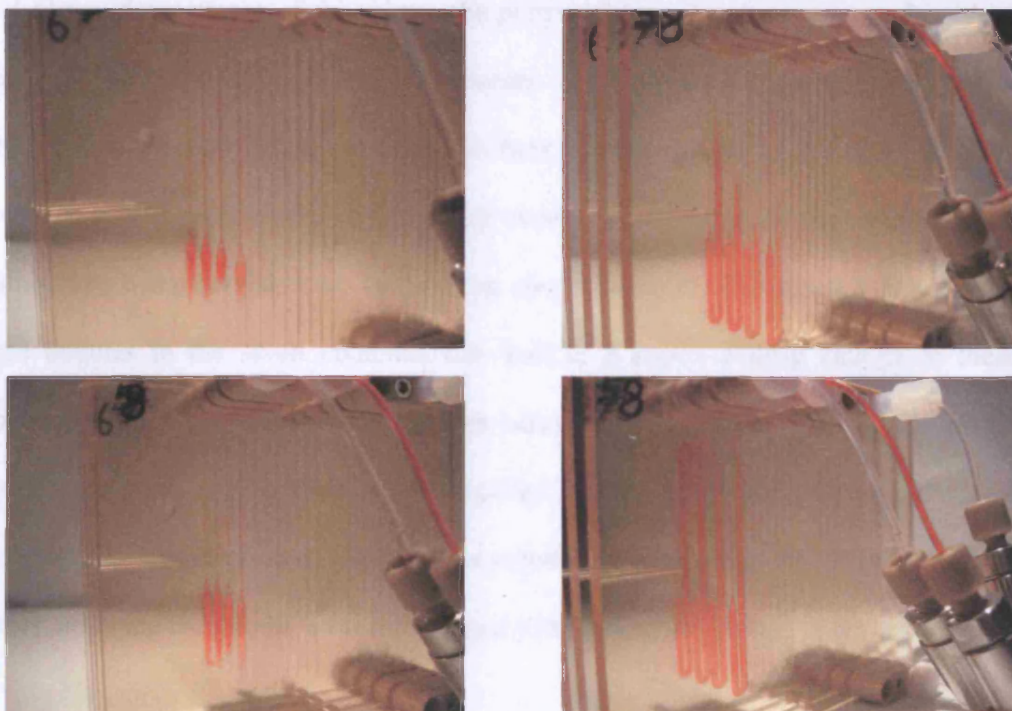
Figure 8.8: Flows in scaled-out configurations (5, 6, 7 and 8) at a flowrate of 0.04 ml/min. Reactor 5 located at the top of the stack, followed by 6, 7 and 8.



8.3.5. Liquid Distribution Results

To verify if this was indeed the case, the experiments were repeated again (at total flowrate = 0.04 ml/min) with a different reactor arrangement. The reactor nearest to the fluid inlet here was reactor number 8, followed by reactor numbers 5, 7 and 6. The results were similar, with the fastest flow in reactor number 6, followed by reactors 7 and 8 which were again roughly equal and the slowest flow was found in reactor number 5 as shown in Figure 8.9. These results provide further support that the flow maldistribution in the reactors was linked to the reactor fabrication process.

Figure 8.9: Flows in scaled-out configurations (8, 5, 7 and 6) at a flowrate of 0.04 ml/min. Reactor 8 located at the top of the stack, followed by 5, 7 and 6.



8.3.3. Liquid Distribution Problem

Flow maldistribution could affect the reaction outcome by changing the residence time for the reaction. From the flow visualisation studies, it is clear that defects in each reactor could lead to imbalances in flow distribution as this effectively resulted in variation in resistance between the reactors. This would affect the performance since the reaction mixture would have different residence time in each reactor. However, the drastic drop in conversion cannot be attributed to flow maldistribution alone. The poor performance can be explained by the fact that there were three reactant inlets, leading to a potential for imperfect mixing ratios within each PEEK reactor in the stack since the three inlet reactant flows may not be distributed in the same manner e.g. peroxide may flow into the first reactor at twice the chalcone flowrate.

A second observation was the fact that although all three reactant inlet feeds were in the liquid phase, downstream of the mixer, the peroxide starts to decompose and produce gaseous oxygen as a byproduct. The presence of small amounts of gas may cause bubble clogging at low liquid velocities, as bubbles may adhere to the walls reducing the effective flow path, especially in sharp corner bends although this effect can be minimised by using curved bends (as was the case with the PEEK reactors). Entrapment of gas bubbles in the small channels can lead to a pressure drop change in these channels and variation in resistance between reactors (Schenk et al, 2003) since excess pressure may be required to dislodge the bubbles. Fouling due to reaction may also be a factor here; the introduction of inline filters significantly improved the ‘lifetime’ of the reactors, allowing them to be used for a longer time before any plugging occurs.

Two-phase flow pressure drop is greater than that of single-phase flow. The presence of peroxide decomposition makes it difficult to predict the actual pressure drop within each reactor since the amount of gaseous oxygen produced may be different in each reactor. For an order of magnitude estimate of the increase in pressure drop due to the presence of small amounts of gas bubbles, the flow can be imagined as a bubbly type flow, where the gas phase is distributed as discrete spherical bubbles in a continuous liquid phase. The bubble size d is smaller than the channel height h . The pressure drop can then be estimated as (Cubaud and Ho, 2004):

$$\Delta P_{2\text{-phase}} = \Delta P_L \alpha_L^{-1} \quad [8.8]$$

where ΔP_L is the single liquid flow pressure drop associated with the liquid flowrate in the channel.

Taking a value of $\alpha = 0.75$ (transition point between bubbly and wedging flow, which consists of elongated bubbles where $d > h$), the maximum two-phase pressure drop can be estimated as $4/3$ times greater than that of single phase liquid flow (for a rough conservative estimate). This can significantly affect the pressure drop differences between reactors.

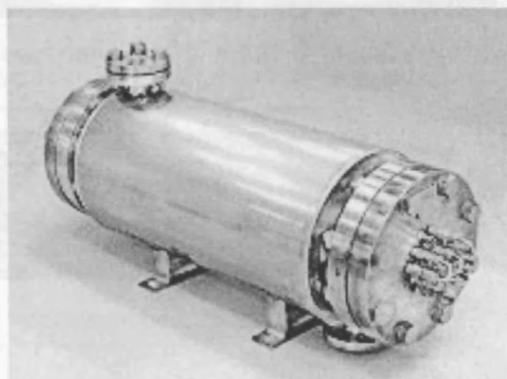
For reactors with two-phase flow, de Mas et al (2005) introduced the use of pressure drop channels before the entrance to the two-phase flow reactor, which prevent cross talk between each channel by creating a sufficiently large resistance such that any pressure differences downstream of the pressure drop channels are negligible. To achieve a similar effect in the current system would require using a much longer pressure drop channel, due to the low flowrates used and resulting low pressure drop per unit length. A smaller geometric dimension can also be used, although given the problems with clogging encountered even with the existing dimensions (of the inlet slit), this does not appear to be a sensible option.

For continuous production of a similar scale, a micromixer-tubular reactor type arrangement may be a better option since it avoids the problem of uneven reactant mixing ratios. Micromixers such as the staggered herringbone and split and recombine, which can be numbered up internally by increasing the number of cycles can be used for rapid mixing of reactants. The tubular reactors are then used to provide sufficient residence time for the reaction to take place.

For larger scale production, tubular reactors operated in parallel such as the flex reactor (BHR group) can be used (see Figure 8.10)¹. While flow maldistribution may still be an issue with such a design, the tubular reactors can then be designed with sufficient margin (i.e. longer residence time) such that even the tubular reactor with the shortest residence time will achieve sufficient conversion. This will have a slight effect on performance, since for homogeneous systems the reaction starts to react on contact. However, it is expected to have a less damaging effect than imperfect mixing ratio. Clearly, it can be seen that flow distribution is a bigger issue for homogeneous systems, since heterogeneous systems can be mixed perfectly prior to splitting them into different channels where the catalysts are incorporated for the reaction to take place.

For the current system, this would require having two mixer-tubular reactor arrangements and if parallel tubular reactors are used, all outlet streams from the deprotonation parallel tubular reactors would need to be recombined as one inlet stream into the second mixer. This would correspond to plant structure (b) in Figure 5.1.

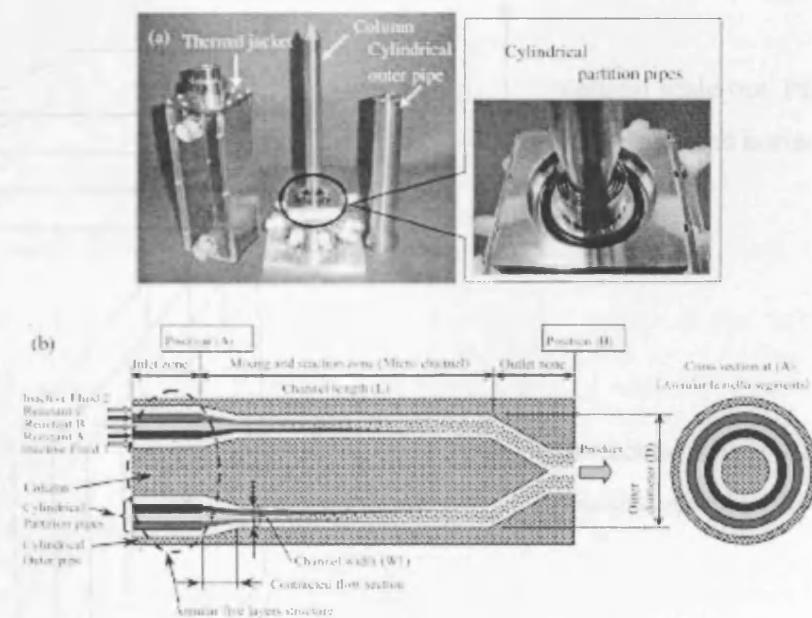
Figure 8.10: ‘Flex reactor’ from BHR group



¹ <http://www.bhrgroup.co.uk/>

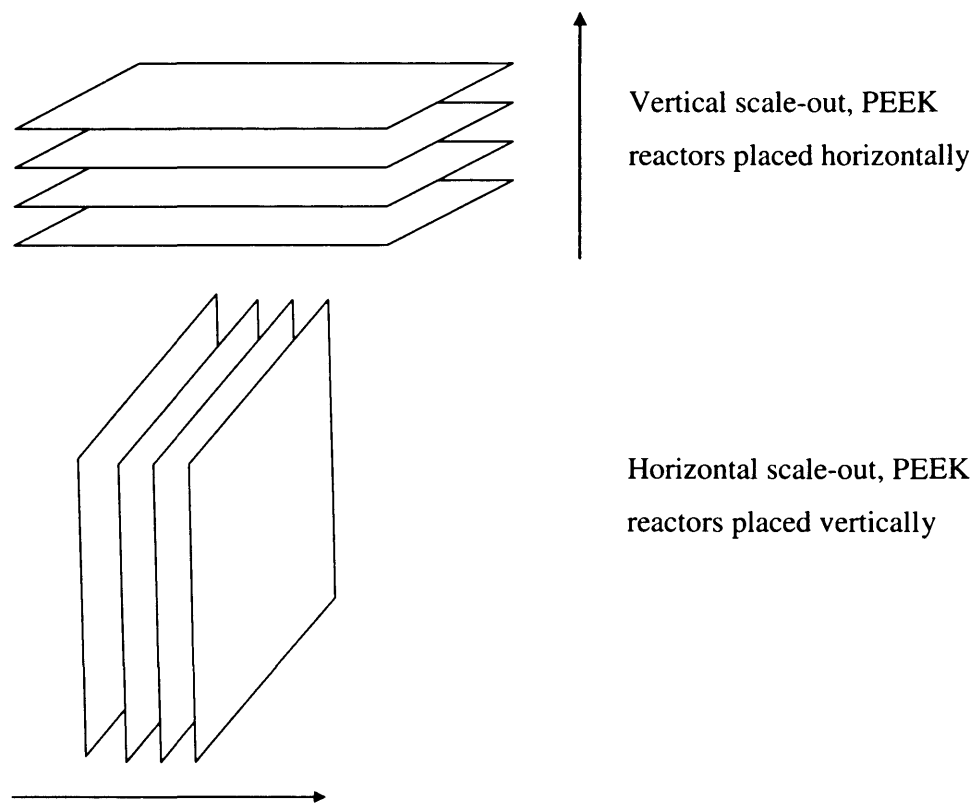
Alternatively, a microreactor based on annular multilamination may be a good idea since it allows for capacity to be increased without changing the characteristic dimension of the system (Nagasawa and Mae, 2006). The reaction section consists of some stainless steel parts, a column, a cylindrical outer pipe and four inner cylindrical pipes with different diameters forming partitions for injecting five different fluids. The inner cylindrical pipes allow multiple thin layers of reactant feed streams to be formed for rapid mixing by diffusion, as shown in Figure 8.11. For increased flowrates, the length of the annular reactor can be increased correspondingly to provide sufficient residence time without altering the characteristic dimensions. The chalcone epoxidation reaction can be run by having two of these in series, one for deprotonation and one for epoxidation.

Figure 8.11: Annular multilamination micro reactor (Nagasawa and Mae, 2006)



The stack of PEEK reactors was placed vertically in this study to minimise the effects of gravitational pressure losses in the inlet headers. The stack of PEEK reactors were placed such that the inlet headers were located at the top and the outlet header at the bottom. In retrospect, since flow distribution is improved with increased R_R/R_A , placing the stack vertically with the inlet headers at the bottom rather than the top can only improve the flow distribution since this effectively increases the R_R rather than reduce the R_R (as was the case in this study). The gravitational losses in liquid flow systems can be significant and hence the total height of any stack of reactors scaled out vertically should be minimised. This limits the scale out factor to a certain extent and a better approach to scaling out liquid phase systems may be by scaling out horizontally (see Figure 8.12).

Figure 8.12: Vertical versus horizontal scale out of PEEK reactors.



While scaling-out may seem like an obvious answer to the current issues affecting the fine chemicals and pharmaceutical industry, it is not a one size fits all solution. Careful design of distributing headers and fabrication precision are clearly important, however, scaling out may be a more promising solution for reactions that are non-fouling and for heterogeneous reactions. Flow maldistribution alone has a small effect on reaction performance, which can be compensated with a design margin; however imperfect mixing ratios can have a profoundly negative effect on reaction performance. The final decision on whether to scale out will also ultimately depend on the targeted production rate and for small production targets (with relatively small scale out factor), it may prove to be a promising option.

8.4. Conclusion

The scale-out of the PEEK reactors was investigated. Reactant feed headers were sized accordingly, using methods based on macro scale distribution header design, taking care to ensure that the pressure drop downstream of the distribution header was much higher than that along the length of the header to minimise effects of variation in reactor resistance. The stack of PEEK reactors were operated vertically rather than horizontally (horizontal scale-out) to minimise the pressure change in the inlet headers as the gravitational pressure change was found to be substantial. The scaled-out system was applied for the poly-*L*-leucine catalysed asymmetric epoxidation of chalcone. The conversion and enantioselectivity in the stack of 4 PEEK reactors were 31.4 % and 82.7 % respectively, lower than the values obtained in the single reactor. Flow visualisation studies in acrylic reactors (of a similar design) indicated that the flow was not evenly distributed and was governed by the precision of the fabrication process, in line with those observed elsewhere (Kikutani et al, 2002; Schenk et al, 2004).

However, the drastic drop in conversion can be explained as a combined effect of flow maldistribution and hence uneven residence time, as well as a biased distribution of reactants to the various reactors, resulting in imperfect mixing ratio of reactants. The presence of gas bubbles in the reaction system, due to peroxide decomposition as well as possible fouling of the reaction channels were also contributing factors, although the extent of these effects cannot be readily quantified.

Chapter 9

Conclusions and Future Work

9.1. Conclusions

In this thesis, the design of a microstructured reactor for the poly-*L*-leucine catalysed asymmetric epoxidation of chalcone has been investigated. The aim of the work was to approach the design of a microstructured reactor from a top down perspective using existing methods from literature and developing appropriate methods where necessary. The work also aims to fill some of the gap in literature on scaled-out microstructured reaction systems by providing a discussion on the design of the scaled out system and experimental verification of the design.

The six reaction protocols for the reaction were screened and the homogeneous system was selected for the case study due to the cost effectiveness of the system as well as the better availability of data. The cost contribution of the catalyst for all reaction protocols was found to be > 96 %, highlighting the need for suitable methods for recovering and recycling the catalyst to be developed.

Next, a continuous reaction protocol for the homogeneous system was established. An initial difficulty with running the reaction in continuous mode was the formation of white precipitate on adding the peroxide dissolved in pure Acetonitrile to a THF solution containing all other reactants. This was eliminated by using premixed solvents for dissolving the urea-hydrogen peroxide instead of pure Acetonitrile. A change in deprotonation reaction time was found to affect the epoxidation reaction outcome with an optimal time of 30 minutes determined for the system at base case conditions. The low molecular diffusivity value of the catalyst was found to be a major issue resulting in slow mixing of the reactants.

After the initial transfer of the reaction from batch to small scale continuous tubular reactor, a microstructured reactor design was established for the reaction system, including the provision of enhanced mixing. A suitable scale out structure was determined at the outset since this influences the design and construction of the single unit. This exercise was not straightforward due to the lack of knowledge and experience on the performance of scaled-out production systems, making it difficult to identify and select the best structure for a given reaction system quantitatively. As such, much of the work was guided by a set of desired features for a chemical production system and a qualitative description of the characteristics of the various plant structures from literature. The final layout of the structure was determined by the requirement to minimise the material transfer time and to allow for flexibility in production rates. The dimensioning of the reactor channel was based on keeping the flow as close to plug flow as possible without making the reactor excessively long, to keep the footprint small as well as minimise pressure losses.

Methods for enhancing mixing were screened and the staggered herringbone mixer was selected for contacting the reactant streams, guided by the requirement for enhanced mixing using a relatively simple construction. The design of the staggered herringbone mixer was studied in detail in Chapter 6, due to the lack of available methods for adequate design of the mixer. Several methods were used to characterize the mixing performance of the staggered herringbone mixer. A method based on using computed stretch values to determine the required mixer length for complete mixing was developed, unlike other methods reported to date which allow mixing quality to be determined at a given mixer length. This is desirable from a design point of view, since it allows for provision of sufficient mixer length to achieve complete mixing. The

effects of laminating the inlet streams prior to the grooved microchannel was briefly explored and qualitatively observed to produce better mixing, suggesting a relatively easy method to further improve the mixing performance. Using the methods developed, a mixer length for the reaction system was determined.

The fabricated microstructured reactor was then tested experimentally at base case conditions to confirm the validity of the design. A parametric study was also carried out experimentally to examine the effects of various parameters on the reaction performance, in order to identify optimum operating conditions for the system. The effects of reactant concentrations, temperature and residence time on the reaction performance were evaluated. Fouling of the reactors was found to be a major issue, which was alleviated to a certain extent by using inline filters.

The results of the parametric study demonstrate the complexity of the system and the many factors which influence the system performance. The system is essentially a two-step reaction process, with the concentration of the perhydroxyl ions for the epoxidation influenced by the outcome of the deprotonation step. There appears to be a maximum catalyst concentration beyond which performance is not further improved; this was attributed to the fact that an increase in the catalyst concentration resulted in a corresponding increase in viscosity and decrease in diffusivity values, both of which decrease the mixing performance. The effect of a lower molecular diffusivity value on the decrease in reaction performance is believed to be minimal since the staggered herringbone micromixers were over designed. The increase in viscosity is believed to affect the mixing performance since this can strongly affect the flow profile due to the increase in the viscosity ratio, which was assumed to be negligible in the simulation.

The results also suggest that the base case condition was the optimal condition without the need to use concentrated reactants to speed up the reaction, since this caused poorer performance and increased the likelihood of fouling.

In order to increase production rates in microstructured systems, the scale-out of the microstructured system was addressed next. With the plant structure decided right at the outset, the task here is to ensure that the header is adequately sized to ensure even distribution of reactant flows to each reactor arranged in parallel. This was done using a method commonly used for macro scale flow distribution system; by making sure that the pressure drop along the header was sufficiently low compared to pressure drop across each reactor, using mainly the method of Amador et al. The gravitational pressure change in the header was found to be substantial for the stack of microstructured reactors placed horizontally; the stack of reactors was therefore placed vertically. As the inlet headers were located at the top (direction of flow from top to bottom), this effectively reduced the ratio of losses in the reactor to losses in the header, R_R/R_A .

The reaction performance in the scaled out system was poor; this was attributed to uneven reactant distribution for all three reactant streams resulting in imperfect mixing ratios as well as a variation in residence times in the reactors. Additionally, due to the presence of both base and peroxide, gas bubbles were spontaneously produced as a product of peroxide decomposition, further aggravating the problem with bubble clogging. Flow visualisation studies suggested that the flow maldistribution was due mainly to fabrication errors.

This work highlights the importance of maintaining a high level of precision when fabricating microstructured devices since the relative fabrication errors for microstructured systems is larger than for macro scale equipment. The effects of fabrication errors could be alleviated somewhat by providing a pressure drop channel, with sufficiently high pressure drop. Due to the low flowrates of the system, high pressure drops could be achieved by reducing the channel dimensions. This was not recommended due to existing problems encountered with clogging. Additionally, in systems which involve more than one reactant stream, it may be better to premix the reactants prior to splitting the flow; clearly this is a problem with homogeneous systems which react on contact.

The results of this work suggest that increasing throughput of microstructured systems by numbering up is not straightforward for every type of reaction. Careful consideration of the physical factors for every system is necessary and a multi-scale approach which combines the use of microstructured elements to improve reaction performance with macro scale equipment may be a better approach. A summary of the main findings of the thesis is provided below:

- Physical factors can limit the development of continuous processes, for example the presence of solids and bubbles can disrupt process productivity which is exacerbated by small apertures and narrow microchannels. However, careful adjustment of process parameters such as solvent or flowrate allows some of these difficulties to be eliminated, as demonstrated in Chapter 4, where the use of premixed solvents avoided the formation of white precipitates in the system.

- Due to the lack of a quantitative method to evaluate the various possible plant structures or scale-out strategies, the final choice of plant structure was guided by a set of identified desired features and qualitative characteristics of the plant structures as outlined in Chapter 5. An external scale-out approach for the entire system was selected to minimise material transfer time and allow for flexibility in production rates.
- A method to determine the required mixer length for complete mixing based on stretch values computed for the system has been developed in Chapter 6. Using this method, the required mixer length for the epoxidation reaction was determined.
- Every effort should be made at the outset to anticipate and alleviate any unexpected phenomena. The results of the parametric study demonstrates the complexity of the reaction system which resulted in problems ranging from bubble clogging to insufficient mixing due to increased viscosity of the reaction mixture (and hence higher viscosity ratios of the fluid streams to be mixed) as well as reduced diffusivity.
- The results of the experimental work provide support for the sequestration of perhydroxyl ions by the catalyst, resulting in lower background reaction rates in the presence of the catalyst. The results also suggest that the rate equations provided do not capture this effect nor do they capture the effects of changing DBU/peroxide concentration and deprotonation time on the concentration of the perhydroxyl ions.
- The precision of the fabrication methods was found to strongly influence the flow distribution of the scaled out unit, as suggested by flow visualisation studies in Chapter 8. The uneven flow distribution resulted in a range of residence times for the reactors arranged in parallel which was exacerbated by imperfect mixing ratios of all three reactant streams.

- For systems with more than one reactant inlet stream, it may be better to premix the streams prior to entering the reactor to avoid imperfect mixing ratios on scale out. This is easily achieved for heterogeneous systems since the reaction only starts on contact with the catalyst in the reactor. For homogeneous systems which start to react on contact, a decision needs to be made as to whether this would offset the benefits of eliminating imperfect mixing ratios, or should a different plant structure be used instead. In the case of the epoxidation reaction, where the background reaction is relatively slow, prior mixing would still make flow distribution a challenging task since bubbles are formed spontaneously making it difficult to distribute the bubbly flow evenly.
- Fouling of the microstructured reactors was found to be a major issue. Unblocking the reactors using high liquid flowrates proved tricky since the reactor starts to leak at high flowrates. It would therefore be desirable for future designs to allow for easy and regular cleaning of the reactors. Due to the costs constraints, an inert microstructured reactor with good optical properties such as glass was not possible. Availability of such a reactor is desired since it permits visual inspection of the system.
- Methods to optimise the reaction conditions for poly-*L*-leucine catalysed asymmetric epoxidation of chalcone must take into account the effects of varying parameters on the deprotonation reaction since this affects the initial concentration of the peroxy anion. Some of the parameters which can influence the deprotonation reaction include DBU concentration, temperature and deprotonation residence time.
- It is common to run the reaction at higher concentrations and temperatures where possible, to improve productivity compared to the dilute conditions used in the laboratory. However, this is not appropriate for the current protocol as higher

concentrations result in a viscous reaction solution (due to the higher polymeric catalyst concentration) which resulted in poorer mixing and more importantly makes the reaction more prone to fouling. Higher temperatures also led to increased bubble formation.

9.2. Suggestions for Future Work

In the course of this work, many difficulties have been encountered mostly linked to the lack of suitable quantitative methods to guide decision making and the occurrence of unexpected physical phenomena, including clogging and leaking of the microstructured reactors which resulted in losses in time and costs. Suggestions for addressing some of these difficulties are given below:

- In the design of the staggered herringbone mixer, the viscosities of the two fluid streams to be mixed were assumed to be identical (a necessary condition to allow the velocity field to be reused successively). In light of the experimental results, this assumption appears to be erroneous, since increasing the viscosity ratio between two fluid streams has been shown to result in a change in the flow profile of a Y-channel micromixer. It would therefore be interesting to see the effects of increased viscosity ratio on the performance of the staggered herringbone mixer and indeed for these effects to be quantified so that a suitable design margin can be provided.
- The grooved micromixer has clearly generated a lot of interest from the research community. In recent years, the effects of various geometric parameters on mixing performance have been evaluated. However, a relatively easy method to rapidly enhance mixing is by combining lamination with chaotic mixing, a method which has recently gained considerable interest as evidenced by the hybrid split and

recombine and chaotic serpentine mixers. This was briefly examined in Chapter 6; however it would be interesting to explore this further (e.g. the effect of mixing ratios and to quantify the improvement in vertical versus horizontal lamination) and develop and test such a mixing device.

- The decision to use PEEK reactors in this work was purely an economic decision. However, given the problems encountered in this work, it would be better for future work to be carried out in glass reactors, since this would allow visual inspection of the reactors, making it easier to diagnose problems. Glass reactors also allow for flow visualisation studies to be carried out in the same reactor, rather than using a similar design in a different material. The result from the flow visualisation studies using acrylic reactors can only be assumed to be transferable to the PEEK reactors; however, there is a possibility that the PEEK reactors have a different fabrication error.
- The problems with frequent clogging and the difficulties in cleaning (high flowrates can lead to leaking from the PEEK reactors) can be alleviated if a more robust reactor (which does not leak at high flowrates) can be used as this facilitates frequent cleaning of the reactors.
- The uneven flow distribution achieved in the scaled-out PEEK reactors was attributed mainly to fabrication errors. Another potential source of uneven flow was bubble clogging formed from the decomposition of peroxide. The poor performance of the scaled-out reactor was also attributed to imperfect mixing ratios. All of these suggest that a different plant structure may be more appropriate and hence it would be desirable for a multi-scale microstructured system to be developed for this system (e.g. use of microstructured mixers with macro scale residence time loop will avoid bubble clogging).

- The PEEK reactors were scaled-out horizontally (i.e. PEEK reactors were vertical while inlet headers were horizontal) because the calculations indicated substantial gravitational pressure change in the inlet headers for vertical scale-out. Since flow distribution is improved with increasing pressure change in the reactors compared to the headers, the flow distribution is likely to improve if the PEEK reactors were scaled-out horizontally with the inlet headers located at the bottom rather than the top (as was the case in this work). It would be interesting to look into the effects of vertical versus horizontal scale-out more closely.
- The experimental results also indicate that the rate equations did not accurately reflect the effect of various parameters on the reaction performance, notably the sequestration of peroxide by the catalyst, the changing perhydroxyl ion concentration with varying peroxide/DBU concentrations and the effects of temperature. An improved rate equation to capture these effects or quantify these effects would be desirable.

Much of the decisions made in the design work were guided by qualitative factors. It is clear that while many different types of devices and contacting principles have been developed, much work needs to be done to quantify and map suitable applications for the devices. For example, it is clear that some mixing devices offer superior mixing performance; however this almost always comes at the cost of increased pressure losses or complicated construction. The choice of mixing device then depends on the specific application and hence a quantitative comparison of the performance of the various types of mixers is desirable. Similarly, a quantitative comparison of the performance and applications of the different plant structures is preferable over a qualitative approach in selecting a suitable structure for a given application. Clearly, more published examples are required before mapping of the performance can be done.

Bibliography

Global Chiral Technology Markets, 2001, Frost & Sullivan Report,

Catalysts Industry Booms as Environmental Regulations and Advanced Technologies Drive Demand, 2004a, Frost & Sullivan Report,

Chiral Chemistry, Chemical and Engineering News, 82, 47-62, 2004b

US Pharmaceutical Intermediates Markets, 2004c, Frost & Sullivan Report,

Adger, B.M., Barkley, J.V., Bergeron, S., Cappi, M.W., Flowerdew, B.E., Jackson, M.P., McCague, R., Nugent, T.C., and Roberts, S.M., Improved Procedure for Julia-Colonna Asymmetric Epoxidation of Alpha,Beta-Unsaturated Ketones: Total Synthesis of Diltiazem and Taxol (TM) Side-Chain, Journal of the Chemical Society-Perkin Transactions 1, 3501-3507, 1997

Allen, J.V., Drauz, K.H., Flood, R.W., Roberts, S.M., and Skidmore, J., Polyamino Acid-Catalysed Asymmetric Epoxidation: Sodium Percarbonate As a Source of Base and Oxidant, Tetrahedron Letters, 40, 5417-5420, 1999

Allen, J.V., Roberts, S.M., and Williamson, N.M., Polyamino Acids As Man-Made Catalysts, Advances in Biochemical Engineering / Biotechnology, 63, 125-144, 1998

Amador, C., Gavriilidis, A., and Angeli, P., Flow Distribution in Different Microreactor Scale-Out Geometries and the Effect of Manufacturing Tolerances and Channel Blockage, Chemical Engineering Journal, 101, 379-390, 2004

Anderson, N.G., Practical Use of Continuous Processing in Developing and Scaling Up Laboratory Processes, Organic Process Research & Development, 5, 613-621, 2001

Aoki, N. and Mae, K., Effects of Channel Geometry on Mixing Performance of Micromixers Using Collision of Fluid Segments, Chemical Engineering Journal, 118, 189-197, 2006

Aubin, J., Fletcher, D.F., Bertrand, J., and Xuereb, C., Characterization of the Mixing Quality in Micromixers, Chemical Engineering & Technology, 26, 1262-1270, 2003a

Aubin, J., Fletcher, D.F., and Xuereb, C., Design of Micromixers Using CFD Modelling, Chemical Engineering Science, 60, 2503-2516, 2005b

Augustyn, J.A.N., Bezuidenhoudt, B.C.B., and Ferreira, D., Enantioselective Synthesis of Flavonoids .1. Poly-Oxygenated Chalcone Epoxides, Tetrahedron, 46, 2651-2660, 1990

Baars, S., Drauz, K.H., Krimmer, H.P., Roberts, S.M., Sander, J., Skidmore, J., and Zanardi, G., Development of the Julia-Colonna Asymmetric Epoxidation Reaction: Part 1. Preparation and Activation of the Polyleucine Catalyst, *Organic Process Research & Development*, 7, 509-513, 2003

Banfi, S., Colonna, S., Molinari, H., Julia, S., and Guixer, J., Asymmetric Epoxidation of Electron-Poor Olefins. 5. Influence on Stereoselectivity of the Structure of Poly-Alpha-Aminoacids Used As Catalysts, *Tetrahedron*, 40, 5207-5211, 1984

Bayer, T., Jenck, J., and Matlosz, M., IMPULSE - A New Approach to Process Design, *Chemical Engineering & Technology*, 28, 431-438, 2005

Bennett, J.P. and Wiggins, C.H., A Computational Study of Mixing Microchannel Flows, *American Physical Society, Annual APS March Meeting 2003*, March 3-7, 2003, 2003

Bentley, P.A., Bergeron, S., Cappi, M.W., Hibbs, D.E., Hursthouse, M.B., Nugent, T.C., Pulido, R., Roberts, S.M., and Wu, L.E., Asymmetric Epoxidation of Enones Employing Polymeric Alpha- Amino Acids in Non-Aqueous Media, *Chemical Communications*, 739-740, 1997a

Bentley, P.A., Cappi, M.W., Flood, R.W., Roberts, S.M., and Smith, J.A., Towards a Mechanistic Insight into the Julia-Colonna Asymmetric Epoxidation of Alpha, Beta-Unsaturated Ketones Using Discrete Lengths of Poly-Leucine, *Tetrahedron Letters*, 39, 9297-9300, 1998

Bentley, P.A., Flood, R.W., Roberts, S.M., Skidmore, J., Smith, C.B., and Smith, J.A., The Effect of the Primary Structure of the Polypeptide Catalyst on the Enantioselectivity of the Julia-Colonna Asymmetric Epoxidation of Enones, *Chemical Communications*, 1616-1617, 2001

Bentley, P.A., Kroutil, W., Littlechild, J.A., and Roberts, S.M., Preparation of Polyamino Acid Catalysts for Use in Julia Asymmetric Epoxidation, *Chirality*, 9, 198-202, 1997b

Berkessel, A., Gasch, N., Glaubitz, K., and Koch, C., Highly Enantioselective Enone Epoxidation Catalyzed by Short Solid Phase-Bound Peptides: Dominant Role of Peptide Helicity, *Organic Letters*, 3, 3839-3842, 2001

Bertsch, A., Heimgartner, S., Cousseau, P., and Renaud, P., Static Micromixers Based on Large-Scale Industrial Mixer Geometry, *Lab on A Chip*, 1, 56-60, 2001

Bessoth, F.G., deMello, A.J., and Manz, A., Microstructure for Efficient Continuous Flow Mixing, *Analytical Communications*, 36, 213-215, 1999

Bird, R.B., Stewart, W.E., and Lightfoot, E.N., *Transport Phenomena*, 2nd, John Wiley & Sons, Inc, 2002

Boswell, C., Microreactors Gain Wider Use As Alternative to Batch Production, *Chemical Market Reporter*, 266, 2004

Bibliography

Brandrup, J., Immergut, E.H., and Grulke, E.A., *Polymer Handbook*, InterScience, New York, 1967

Branebjerg, J., Gravesen, P., Krog, J.P., and Nielsen, C.R., Fast Mixing by Lamintaion, Proceedings of the IEEE-MEMS 1996, 1996

Branebjerg, J., Larsen , U.D., and Blankenstein, G., Fast Mixing by Parallel Multilayer Lamination, Proceedings of the 2nd International Symposium on Miniaturized Total Analysis Systems, mTAS96 – Special Issue of Analytical Methods & Instrumentation AMI, 1996 Basel

Camesasca, M., Kaufman, M., and Manas-Zloczower, I., Staggered Passive Micromixers With Fractal Surface Patterning, *Journal of Micromechanics and Microengineering*, 16, 2298-2311, 2006a

Camesasca, M., Manas-Zloczower, I., and Kaufman, M., Entropic Characterization of Mixing in Microchannels, *Journal of Micromechanics and Microengineering*, 15, 2038-2044, 2005b

Cappi, M.W., Chen, W.P., Flood, R.W., Liao, Y.W., Roberts, S.M., Skidmore, J., Smith, J.A., and Williamson, N.M., New Procedures for the Julia-Colonna Asymmetric Epoxidation: Synthesis of (+)-Clausenamide, *Chemical Communications*, 1159-1160, 1998

Carde, L., Davies, H., Geller, T.P., and Roberts, S.M., PaaSicats: Powerful Catalysts for Asymmetric Epoxidation of Enones. Novel Syntheses of Alpha-Arylpropanoic Acids Including (S)-Fenoprofen, *Tetrahedron Letters*, 40, 5421-5424, 1999

Caroff, E., From Micrograms to Multikilos Report: Polyamino acid Catalysed Asymmetric Epoxidation, 2002, University of Liverpool, Liverpool, U.K.

Carrea, G., Colonna, S., Meek, A.D., Ottolina, G., and Roberts, S.M., Enantioselective Epoxidation of Chalcone Catalysed by the Artificial Enzyme Poly-L-Leucine: Kinetic Mechanism, *Tetrahedron-Asymmetry*, 15, 2945-2949, 2004a

Carrea, G., Colonna, S., Meek, A.D., Ottolina, G., and Roberts, S.M., Kinetics of Chalcone Oxidation by Peroxide Anion Catalysed by Poly-L-Leucine, *Chemical Communications*, 1412-1413, 2004b

Carrea, G., Colonna, S., Meek, A.D., Ottolina, G., and Roberts, S.M., Kinetics of Chalcone Oxidation by Peroxide Anion Catalysed by Poly-L-Leucinet, *Chemical Communications*, 1412-1413, 2004c

Cave, S.R. and Edwards, D.W., Chemical Process Route Selection Based on Assessment of Inherent Environmental Hazard, *Computers & Chemical Engineering*, 21, S965-S970, 1997

Caygill, G., Zanfir, M., and Gavriilidis, A., Scalable Reactor Design for Pharmaceuticals and Fine Chemicals Production. 1: Potential Scale-Up Obstacles, *Organic Process Research & Development*, 10, 539-552, 2006

Cha, J., Kim, J., Ryu, S.K., Park, J., Jeong, Y., Park, S., Park, S., Kim, H.C., and Chun, K., A Highly Efficient 3D Micromixer Using Soft PDMS Bonding, *Journal of Micromechanics and Microengineering*, 16, 1778-1782, 2006

Chambers, R.D., Fox, M.A., Holling, D., Nakano, T., Okazoe, T., and Sandford, G., Elemental Fluorine - Part 16. Versatile Thin-Film Gas-Liquid Multi-Channel Microreactors for Effective Scale-Out, *Lab on A Chip*, 5, 191-198, 2005

Chambers, R.D., Holling, D., Spink, R.C.H., and Sandford, G., Elemental Fluorine - Part 13. Gas-Liquid Thin Film Microreactors for Selective Direct Fluorination, *Lab on A Chip*, 1, 132-137, 2001

Chang, S. and Cho, Y.H., Static Micromixers Using Alternating Whirls and Lamination, *Journal of Micromechanics and Microengineering*, 15, 1397-1405, 2005

Chen, H. and Meiners, J.C., Topologic Mixing on a Microfluidic Chip, *Applied Physics Letters*, 84, 2193-2195, 2004

Chow, A.W., Lab-on-a-Chip: Opportunities for Chemical Engineering, *Aiche Journal*, 48, 1590-1595, 2002

Chung, Y.C., Hsu, Y.L., Jen, C.P., Lu, M.C., and Lin, Y.C., Design of Passive Mixers Utilizing Microfluidic Self- Circulation in the Mixing Chamber, *Lab on A Chip*, 4, 70-77, 2004

Colonna, S., Molinari, H., Banfi, S., Julia, S., Masana, J., and Alvarez, A., Synthetic Enzymes. 4. Highly Enantioselective Epoxidation by Means of Polyaminoacids in a Triphase System - Influence of Structural Variations Within the Catalysts, *Tetrahedron*, 39, 1635-1641, 1983

Commengé, J.M., Falk, L., Corriou, J.P., and Matlosz, M., Optimal Design for Flow Uniformity in Microchannel Reactors, *Aiche Journal*, 48, 345-358, 2002

Cubaud, T. and Ho, C.M., Transport of Bubbles in Square Microchannels, *Physics of Fluids*, 16, 4575-4585, 2004

Cussler, E.L., *Diffusion: Mass Transfer in Fluid Systems*, Second Edition, Cambridge University Press, Cambridge, 1997

Cynthia Challener, Chiral Technologies Put a New Spin on the Fine Chemicals Toolbox, *Chemical Market Reporter*, 262, 2002

de Mas, N., Gunther, A., Kraus, T., Schmidt, M.A., and Jensen, K.F., Scaled-Out Multilayer Gas-Liquid Microreactor With Integrated Velocimetry Sensors, *Industrial & Engineering Chemistry Research*, 44, 8997-9013, 2005

de Mello, A., Plastic Fantastic?, *Lab on A Chip*, 2, 31N-36N, 2002

de Mello, A. and Wootton, R., But What Is It Good for? Applications of Microreactor Technology for the Fine Chemical Industry, *Lab on A Chip*, 2, 7N-13N, 2002

Delsman, E.R., de Croon, M.H.J.M., Elzinga, G.D., Cobden, P.D., Kramer, G.J., and Schouten, J.C., The Influence of Differences Between Microchannels on Microreactor Performance, *Chemical Engineering & Technology*, 28, 367-375, 2005

Delsman, E.R., Pierik, A., de Croon, M.H.J.M., Kramer, G.J., and Schouten, J.C., Microchannel Plate Geometry Optimization for Even Flow Distribution at High Flow Rates, *Chemical Engineering Research & Design*, 82, 267-273, 2004

Dhanda, A., Drauz, K.H., Geller, T., and Roberts, S.M., PaaSiCats: Novel Polyamino Acid Catalysts, *Chirality*, 12, 313-317, 2000

Dietrich, T.R., Freitag, A., and Scholz, R., Production and Characteristics of Microreactors Made From Glass, *Chemical Engineering & Technology*, 28, 477-483, 2005

Drese, K.S., Optimization of Interdigital Micromixers Via Analytical Modeling - Exemplified With the SuperFocus Mixer, *Chemical Engineering Journal*, 101, 403-407, 2004

Ebrahim, S. and Wills, M., Synthetic Applications of Polymeric Alpha-Amino Acids, *Tetrahedron-Asymmetry*, 8, 3163-3173, 1997

Edwards, D.W. and Lawrence, D., Assessing the Inherent Safety of Chemical Process Routes - Is There a Relation Between Plant Costs and Inherent Safety, *Process Safety and Environmental Protection*, 71, 252-258, 1993

Ehlers, S., Elgeti, K., Menzel, T., and Wiessmeier, G., Mixing in the Offstream of a Microchannel System, *Chemical Engineering and Processing*, 39, 291-298, 2000

Ehrfeld, W., Hessel, V., and Lowe, H., Microreactors: New Technology for Modern Chemistry, First Edition, Wiley-VCH Verlag GmbH, Weinheim, 2000

Ehrfeld, W., Hessel, V., and Lehr, H., Microreactors for Chemical Synthesis and Biotechnology - Current Developments and Future Applications, *Microsystem Technology in Chemistry and Life Science*, 194, 233-252, 1998

Engler, M., Kockmann, N., Kiefer, T., and Woias, P., Numerical and Experimental Investigations on Liquid Mixing in Static Micromixers, *Chemical Engineering Journal*, 101, 315-322, 2004

Erickson, D. and Li, D.Q., Integrated Microfluidic Devices, *Analytica Chimica Acta*, 507, 11-26, 2004

Bibliography

Evans, D.F. and Upton, M.W., Studies on Singlet Oxygen in Aqueous-Solution .4. the Spontaneous and Catalyzed Decomposition of Hydrogen-Peroxide, *Journal of the Chemical Society-Dalton Transactions*, 2525-2529, 1985

Feng, X.Z., Haswell, S.J., and Watts, P., Organic Synthesis in Micro Reactors, *Current Topics in Medicinal Chemistry*, 4, 707-727, 2004

Ferstl, W., Loebbecke, S., Antes, J., Krause, H., Haeberl, M., Schmalz, D., Muntermann, H., Grund, M., Steckenborn, A., Lohf, A., Hassel, J., Bayer, T., Kinzl, M., and Leipprand, I., Development of an Automated Microreaction System With Integrated Sensorics for Process Screening and Production, *Chemical Engineering Journal*, 101, 431-438, 2004

Fletcher, P.D.I., Haswell, S.J., Pombo-Villar, E., Warrington, B.H., Watts, P., Wong, S.Y.F., and Zhang, X.L., Micro Reactors: Principles and Applications in Organic Synthesis, *Tetrahedron*, 58, 4735-4757, 2002

Flisak, J.R., Gombatz, K.J., Holmes, M.M., Jarmas, A.A., Lantos, I., Mendelson, W.L., Novack, V.J., Remich, J.J., and Snyder, L., A Practical, Enantioselective Synthesis of Sk-And-F 104353, *Journal of Organic Chemistry*, 58, 6247-6254, 1993

Flood, R.W., Geller, T.P., Petty, S.A., Roberts, S.M., Skidmore, J., and Volk, M., Efficient Asymmetric Epoxidation of Alpha,Beta-Unsaturated Ketones Using a Soluble Triblock Polyethylene Glycol-Polyamino Acid Catalyst, *Organic Letters*, 3, 683-686, 2001

Floyd-Smith, T.M., Golden, J.P., Howell, P.B., and Ligler, F.S., Characterization of Passive Microfluidic Mixers Fabricated Using Soft Lithography, *Microfluidics and Nanofluidics*, 2, 180-183, 2006

Fu, X., Liu, S.F., Ruan, X.D., and Yang, H.Y., Research on Staggered Oriented Ridges Static Micromixers, *Sensors and Actuators B-Chemical*, 114, 618-624, 2006

Gavriilidis, A., Angeli, P., Cao, E., Yeong, K.K., and Wan, Y.S.S., Technology and Applications of Microengineered Reactors, *Chemical Engineering Research & Design*, 80, 3-30, 2002

Geankoplis, C.J., *Transport Processes and Unit Operations*, Third Edition, Prentice Hall, New Jersey, 1993

Geller, T., Gerlach, A., Kruger, C.M., and Militzer, H.C., Novel Conditions for the Julia-Colonna Epoxidation Reaction Providing Efficient Access to Chiral, Nonracemic Epoxides, *Tetrahedron Letters*, 45, 5065-5067, 2004a

Geller, T., Gerlach, A., Kruger, C.M., and Militzer, H.C., The Julia-Colonna Epoxidation: Access to Chiral, Non-Racemic Epoxides, *Journal of Molecular Catalysis A-Chemical*, 251, 71-77, 2006

Geller, T., Kruger, C.M., and Militzer, H.C., Scoping the Triphasic/PTC Conditions for the Julia-Colonna Epoxidation Reaction, *Tetrahedron Letters*, 45, 5069-5071, 2004b

Geller, T. and Roberts, S.M., A New Procedure for the Julia-Colonna Stereoselective Epoxidation Reaction Under Non-Aqueous Conditions: the Development of a Catalyst Comprising Polyamino Acid on Silica (PaaSiCat), *Journal of the Chemical Society-Perkin Transactions 1*, 1397-1398, 1999

Gerlach, A. and Geller, T., Scale-Up Studies for the Asymmetric Julia-Colonna Epoxidation Reaction, *Advanced Synthesis & Catalysis*, 346, 1247-1249, 2004

Gobby, D., Angeli, P., and Gavriilidis, A., Mixing Characteristics of T-Type Microfluidic Mixers, *Journal of Micromechanics and Microengineering*, 11, 126-132, 2001

Gonsalves, A.M.D.R., Johnstone, R.A.W., Pereira, M.M., and Shaw, J., Dissociation of Hydrogen Peroxide Adducts in Solution - The Use of Such Adducts for Epoxidation of Alkenes, *Journal of Chemical Research-S*, 208-209, 1991

Hardt, S., Dietrich, T., Freitag, A., Hessel, V., Lowe, H., Hofmann, C., Oroskar, A., Schonfeld, F., and Van den Bussche, K., Radial and Tangential Injection of Liquid/Liquid and Gas/Liquid Streams and Focusing Thereof in a Special Cyclone Mixer, *Sixth International Conference on Microreaction Technology*, IMRET 6, New Orleans, USA, 2002

Hardt, S., Drese, K.S., Hessel, V., and Schonfeld, F., Passive Micromixers for Applications in the Microreactor and Mu TAS Fields, *Microfluidics and Nanofluidics*, 1, 108-118, 2005

Hardt, S., Pennemann, H., and Schonfeld, F., Theoretical and Experimental Characterization of a Low-Reynolds Number Split-and-Recombine Mixer, *Microfluidics and Nanofluidics*, 2, 237-248, 2006

Hardt, S. and Schonfeld, F., Laminar Mixing in Different Interdigital Micromixers: II. Numerical Simulations, *Aiche Journal*, 49, 578-584, 2003

Hasebe, S., Design and Operation of Micro-Chemical Plants - Bridging the Gap Between Nano, Micro and Macro Technologies, *Computers & Chemical Engineering*, 29, 57-64, 2004

Hassell, D.G. and Zimmerman, W.B., Investigation of the Convective Motion Through a Staggered Herringbone Micromixer at Low Reynolds Number Flow, *Chemical Engineering Science*, 61, 2977-2985, 2006

Haswell, S. and Skelton, V., Chemical and Biochemical Microreactors, *Trac-Trends in Analytical Chemistry*, 19, 389-395, 2000

Haswell, S.J. and Watts, P., Green Chemistry: Synthesis in Micro Reactors, *Green Chemistry*, 5, 240-249, 2003

Hendershot, D.C., Conflicts and Decisions in the Search for Inherently Safer Process Options, *Process Safety Progress*, 14, 52-56, 1995

Hendershot, D.C., Inherently Safer Chemical Process Design, *Journal of Loss Prevention in the Process Industries*, 10, 151-157, 1997a

Hendershot, D.C., Measuring Inherent Safety, Health and Environmental Characteristics Early in Process Development, *Process Safety Progress*, 16, 78-79, 1997b

Hessel, V., Angeli, P., Gavriilidis, A., and Lowe, H., Gas-Liquid and Gas-Liquid-Solid Microstructured Reactors: Contacting Principles and Applications, *Industrial & Engineering Chemistry Research*, 44, 9750-9769, 2005a

Hessel, V., Hardt, S., Hofmann, C., Pennemann, H., and Schonfeld, F., Micro Mixing Principles and Applications - A Review on Specific Multi-Lamination, Split-Recombine and Chaotic Approaches, *Abstracts of Papers of the American Chemical Society*, 226, 006-CATL, 2003a

Hessel, V., Hardt, S., and Lowe, H., *Chemical Micro Process Engineering: Fundamentals, Modelling and Reactions*, Wiley-VCH Verlag GmbH, Weinheim, 2004

Hessel, V., Hardt, S., Lowe, H., and Schonfeld, F., Laminar Mixing in Different Interdigital Micromixers: I. Experimental Characterization, *Aiche Journal*, 49, 566-577, 2003b

Hessel, V. and Lowe, H., Microchemical Engineering: Components, Plant Concepts User Acceptance - Part I, *Chemical Engineering & Technology*, 26, 13-24, 2003a

Hessel, V. and Lowe, H., Microchemical Engineering: Components, Plant Concepts, User Acceptance - Part II, *Chemical Engineering & Technology*, 26, 391-408, 2003b

Hessel, V. and Lowe, H., Microchemical Engineering: Components, Plant Concepts, User Acceptance - Part III, *Chemical Engineering & Technology*, 26, 531-544, 2003c

Hessel, V. and Lowe, H., Mixing Principles for Microstructured Mixers: Active and Passive Mixing, *Microreactor Technology and Process Intensification*, 914, 334-359, 2005a

Hessel, V. and Lowe, H., Organic Synthesis With Microstructured Reactors, *Chemical Engineering & Technology*, 28, 267-284, 2005b

Hessel, V., Lowe, H., Muller, A., and Kolb, G., *Chemical Micro Process Engineering: Processing and Plants*, Wiley-VCH Verlag GmbH, Weinheim, 2005b

Hessel, V., Lowe, H., and Schonfeld, F., Micromixers - a Review on Passive and Active Mixing Principles, *Chemical Engineering Science*, 60, 2479-2501, 2005c

Hobbs, D.M. and Muzzio, F.J., The Kenics Static Mixer: a Three-Dimensional Chaotic Flow, *Chemical Engineering Journal*, 67, 153-166, 1997

Hobbs, D.M. and Muzzio, F.J., Reynolds Number Effects on Laminar Mixing in the Kenics Static Mixer, *Chemical Engineering Journal*, 70, 93-104, 1998

Hobbs, D.M., Swanson, P.D., and Muzzio, F.J., Numerical Characterization of Low Reynolds Number Flow in the Kenics Static Mixer, *Chemical Engineering Science*, 53, 1565-+, 1998

Holladay, J.D., Brooks, K.P., Wegeng, R., Hu, J., Sanders, J., and Baird, S., Microreactor Development for Martian in Situ Propellant Production, *Catalysis Today*, 120, 35-44, 2007

Hong, C.C., Choi, J.W., and Ahn, C.H., A Novel in-Plane Passive Microfluidic Mixer With Modified Tesla Structures, *Lab on A Chip*, 4, 109-113, 2004

Howell, P.B., Mott, D.R., Fertig, S., Kaplan, C.R., Golden, J.P., Oran, E.S., and Ligler, F.S., A Microfluidic Mixer With Grooves Placed on the Top and Bottom of the Channel, *Lab on A Chip*, 5, 524-530, 2005

Howell, P.B., Mott, D.R., Golden, J.P., and Ligler, F.S., Design and Evaluation of a Dean Vortex-Based Micromixer, *Lab on A Chip*, 4, 663-669, 2004

Huikko, K., Kostiainen, R., and Kotiaho, T., Introduction to Micro-Analytical Systems: Bioanalytical and Pharmaceutical Applications, *European Journal of Pharmaceutical Sciences*, 20, 149-171, 2003

Hung, C.I., Wang, K.C., and Chyou, C.K., Design and Flow Simulation of a New Micromixer, *Jsme International Journal Series B-Fluids and Thermal Engineering*, 48, 17-24, 2005

Itsuno, S., Sakakura, M., and Ito, K., Polymer-Supported Poly(Amino Acids) As New Asymmetric Epoxidation Catalyst of Alpha,Beta-Unsaturated Ketones, *Journal of Organic Chemistry*, 55, 6047-6049, 1990

Iwasaki, T., Kawano, N., and Yoshida, J., Radical Polymerization Using Microflow System: Numbering-Up of Microreactors and Continuous Operation, *Organic Process Research & Development*, 10, 1126-1131, 2006

Jahnisch, K., Baerns, M., Hessel, V., Ehrfeld, W., Haverkamp, V., Lowe, H., Wille, C., and Guber, A., Direct Fluorination of Toluene Using Elemental Fluorine in Gas/Liquid Microreactors, *Journal of Fluorine Chemistry*, 105, 117-128, 2000

Jen, C.P., Wu, C.Y., Lin, Y.C., and Wu, C.Y., Design and Simulation of the Micromixer With Chaotic Advection in Twisted Microchannels, *Lab on A Chip*, 3, 77-81, 2003

Jensen, K.F., Microchemical Systems: Status, Challenges, and Opportunities, *Aiche Journal*, 45, 2051-2054, 1999

Jensen, K.F., Microreaction Engineering - Is Small Better?, *Chemical Engineering Science*, 56, 293-303, 2001

Jeon, M.K., Kim, J.H., Noh, J., Kim, S.H., Park, H.G., and Woo, S.I., Design and Characterization of a Passive Recycle Micromixer, *Journal of Micromechanics and Microengineering*, 15, 346-350, 2005

Jiang, F., Dreser, K.S., Hardt, S., Kupper, M., and Schonfeld, F., Helical Flows and Chaotic Mixing in Curved Micro Channels, *Aiche Journal*, 50, 2297-2305, 2004

Johnson, T.J., Ross, D., and Locascio, L.E., Rapid Microfluidic Mixing, *Analytical Chemistry*, 74, 45-51, 2002

Julia, S., Guixer, J., Masana, J., Rocas, J., Colonna, S., Annuziata, R., and Molinari, H., Synthetic Enzymes. 2. Catalytic Asymmetric Epoxidation by Means of Polyamino-Acids in a Triphase System, *Journal of the Chemical Society-Perkin Transactions 1*, 1317-1324, 1982

Julia, S., Masana, J., and Vega, J.C., Synthetic Enzymes - Highly Stereoselective Epoxidation of Chalcone in a Triphasic Toluene-Water-Poly[(S)-Alanine] System, *Angewandte Chemie-International Edition in English*, 19, 929-931, 1980

Kang, T.G. and Kwon, T.H., Colored Particle Tracking Method for Mixing Anlysis of Chaotic Micromixers, *Journal of Micromechanics and Microengineering*, 14, 891-899, 2004

Kelly, D.R., Bui, T.T.T., Caroff, E., Drake, A.F., and Roberts, S.M., Structure and Catalytic Activity of Some Soluble Polyethylene Glycol-Peptide Conjugates, *Tetrahedron Letters*, 45, 3885-3888, 2004

Kelly, D.R. and Roberts, S.M., The Mechanism of Polyleucine Catalysed Asymmetric Epoxidation, *Chemical Communications*, 2018-2020, 2004

Kelly, D.R. and Roberts, S.M., Oligopeptides As Catalysts for Asymmetric Epoxidation, *Biopolymers*, 84, 74-89, 2006

Keoschkerjan, R., Richter, M., Boskovic, D., Schnurer, F., and Lobbecke, S., Novel Multifunctional Microreaction Unit for Chemical Engineering, *Chemical Engineering Journal*, 101, 469-475, 2004

Khakhar, D.V., Franjione, J.G., and Ottino, J.M., A Case-Study of Chaotic Mixing in Deterministic Flows - the Partitioned-Pipe Mixer, *Chemical Engineering Science*, 42, 2909-2926, 1987

Kikutani, Y., Hibara, A., Uchiyama, K., Hisamoto, H., Tokeshi, M., and Kitamori, T., Pile-Up Glass Microreactor, *Lab on A Chip*, 2, 193-196, 2002

Kim, B.J., Liu, Y.Z., and Sung, H.J., Micro PIV Measurement of Two-Fluid Flow With Different Refractive Indices, *Measurement Science & Technology*, 15, 1097-1103, 2004a

Kim, D.S., Lee, I.H., Kwon, T.H., and Cho, D.W., A Barrier Embedded Kenics Micromixer, *Journal of Micromechanics and Microengineering*, 14, 1294-1301, 2004b

Kim, D.S., Lee, S.H., Kwon, T.H., and Ahn, C.H., A Serpentine Laminating Micromixer Combining Splitting/Recombination and Advection, *Lab on A Chip*, 5, 739-747, 2005

Kim, D.S., Lee, S.W., Kwon, T.H., and Lee, S.S., A Barrier Embedded Chaotic Micromixer, *Journal of Micromechanics and Microengineering*, 14, 798-805, 2004c

Kim, H., Saitmacher, K., Unverdorben, L., and Wille, C., Pigments With Improved Properties - Microreaction Technology As a New Approach for Synthesis of Pigments, *Macromolecular Symposia*, 187, 631-640, 2002

Kirschneck, D., Kober, M., and Marr, R., New Scopes in Process Design Using Microstructured Devices, *Chemical Engineering & Technology*, 28, 314-317, 2005

Knight, J.B., Vishwanath, A., Brody, J.P., and Austin, R.H., Hydrodynamic Focusing on a Silicon Chip: Mixing Nanoliters in Microseconds, *Physical Review Letters*, 80, 3863-3866, 1998

Kobayashi, J., Mori, Y., and Kobayashi, S., Triphase Hydrogenation Reactions Utilizing Palladium-Immobilized Capillary Column Reactors and a Demonstration of Suitability for Large Scale Synthesis, *Advanced Synthesis & Catalysis*, 347, 1889-1892, 2005

Koch, M., Schabmueller, C.G.J., Evans, A.G.R., and Brunschweiler, A., Micromachined Chemical Reaction System, *Sensors and Actuators A-Physical*, 74, 207-210, 1999

Kockmann, N., Kiefer, T., Engler, M., and Woias, P., Convective Mixing and Chemical Reactions in Microchannels With High Flow Rates, *Sensors and Actuators B-Chemical*, 117, 495-508, 2006a

Kockmann, N., Kiefer, T., Engler, M., and Woias, P., Silicon Microstructures for High Throughput Mixing Devices, *Microfluidics and Nanofluidics*, 2, 327-335, 2006b

Kozer, N., Kuttner, Y.Y., Haran, G., and Schreiber, G., Protein-Protein Association in Polymer Solutions: From Dilute to Semidilute to Concentrated, *Biophys. J.*, *biophysj*-2006

Lauret, C., Epoxy Ketones As Versatile Building Blocks in Organic Synthesis, *Tetrahedron-Asymmetry*, 12, 2359-2383, 2001

Lauret, C. and Roberts, S.M., Asymmetric Epoxidation of Alpha,Beta-Unsaturated Ketones Catalyzed by Poly(Amino Acids), *Aldrichimica Acta*, 35, 47-51, 2002

Lee, N.Y., Yamada, M., and Seki, M., Development of a Passive Micromixer Based on Repeated Fluid Twisting and Flattening, and Its Application to DNA Purification, Analytical and Bioanalytical Chemistry, 383, 776-782, 2005

Lee, S.W., Kim, D.S., Lee, S.S., and Kwon, T.H., A Split and Recombination Micromixer Fabricated in a PDMS Three-Dimensional Structure, Journal of Micromechanics and Microengineering, 16, 1067-1072, 2006

Li, C.A. and Chen, T.N., Simulation and Optimization of Chaotic Micromixer Using Lattice Boltzmann Method, Sensors and Actuators B-Chemical, 106, 871-877, 2005

Li, S.U. and Gainer, J.L., Diffusion in Polymer Solutions, Industrial & Engineering Chemistry Fundamentals, 7, 433-&, 1968

Liu, R.H., Stremler, M.A., Sharp, K.V., Olsen, M.G., Santiago, J.G., Adrian, R.J., Aref, H., and Beebe, D.J., Passive Mixing in a Three-Dimensional Serpentine Microchannel, Journal of Microelectromechanical Systems, 9, 190-197, 2000

Liu, Y.Z., Kim, B.J., and Sung, H.J., Two-Fluid Mixing in a Microchannel, International Journal of Heat and Fluid Flow, 25, 986-995, 2004

Lob, P., Dresel, K.S., Hessel, V., Hardt, S., Hofmann, C., Lowe, H., Schenk, R., Schonfeld, F., and Werner, B., Steering of Liquid Mixing Speed in Interdigital Micro Mixers - From Very Fast to Deliberately Slow Mixing, Chemical Engineering & Technology, 27, 340-345, 2004

Lobbecke, S., Ferstl, W., Panic, S., and Turcke, T., Concepts for Modularization and Automation of Microreaction Technology, Chemical Engineering & Technology, 28, 484-493, 2005

Lopez-Pedrosa, J.M., Pitts, M.R., Roberts, S.M., Saminathan, S., and Whittall, J., Asymmetric Epoxidation of Some Arylalkenyl Sulfones Using a Modified Julia-Colonna Procedure, Tetrahedron Letters, 45, 5073-5075, 2004

Losey, M.W., Jackman, R.J., Firebaugh, S.L., Schmidt, M.A., and Jensen, K.F., Design and Fabrication of Microfluidic Devices for Multiphase Mixing and Reaction, Journal of Microelectromechanical Systems, 11, 709-717, 2002

Mackay, D. and Paterson, S., Calculating Fugacity, Environmental Science & Technology, 15, 1006-1014, 1981

Madou, M., Fundamentals of Microfabrication, 2nd, CRC, 2002

Mae, K., Maki, T., Hasegawa, I., Eto, U., Mizutani, Y., and Honda, N., Development of a New Micromixer Based on Split/Recombination for Mass Production and Its Application to Soap Free Emulsifier, Chemical Engineering Journal, 101, 31-38, 2004

Markowz, G., Microreaction Engineering, Degussa Elements Science Newsletter, 4, 5-9, 2003

Markowz, G., Schirrmeister, S., Albrecht, J., Becker, F., Schutte, R., Caspary, K.J., and Klemm, E., Microstructured Reactors for Heterogeneously Catalyzed Gas-Phase Reactions on an Industrial Scale, Chemical Engineering & Technology, 28, 459-464, 2005

Mathew, S., From Micrograms to Multikilos Report: Kinetics of epoxidation of chalcone to chalcone epoxide using soluble poly-L-leucine catalyst, 2003, University of Hull, Hull, U.K.

Mathew, S.P., Gunathilagan, S., Roberts, S.M., and Blackmond, D.G., Mechanistic Insights From Reaction Progress Kinetic Analysis of the Polypeptide-Catalyzed Epoxidation of Chalcone, Organic Letters, 7, 4847-4850, 2005

Mathews, J.H. and Fink, K.K., Numerical Methods Using Matlab, 4th Edition, Prentice-Hall, New Jersey, 2004

McCreedy, T., Fabrication Techniques and Materials Commonly Used for the Production of Microreactors and Micro Total Analytical Systems, Trac-Trends in Analytical Chemistry, 19, 396-401, 2000

Mendenhall, W. and Sincich, T., Statistics for Engineering and the Sciences, Fourth Edition, Prentice-Hall, New Jersey, 1995

Mengeaud, V., Josserand, J., and Girault, H.H., Mixing Processes in a Zigzag Microchannel: Finite Element Simulations and Optical Study, Analytical Chemistry, 74, 4279-4286, 2002

Muller, A., Cominos, V., Hessel, V., Horn, B., Schurer, J., Ziogas, A., Jahnisch, K., Hillmann, V., Grosser, V., Jam, K.A., Bazzanella, A., Rinke, G., and Kraute, A., Fluidic Bus System for Chemical Process Engineering in the Laboratory and for Small-Scale Production, Chemical Engineering Journal, 107, 205-214, 2005

Munson, M.S. and Yager, P., Simple Quantitative Optical Method for Monitoring the Extent of Mixing Applied to a Novel Microfluidic Mixer, Analytica Chimica Acta, 507, 63-71, 2004

Nagasawa, H., Aoki, N., and Mae, K., Design of a New Micromixer for Instant Mixing Based on the Collision of Micro Segments, Chemical Engineering & Technology, 28, 324-330, 2005

Nagasawa, H. and Mae, K., Development of a New Microreactor Based on Annular Microsegments for Fine Particle Production, Industrial & Engineering Chemistry Research, 45, 2179-2186, 2006

Nauman, E.B., Chemical Reactor Design, Optimization, and Scaleup, McGraw-Hill, New York, 2002

Nguyen, N.T. and Wu, Z.G., Micromixers - a Review, Journal of Micromechanics and Microengineering, 15, R1-R16, 2005

Nichols, K.P., Ferullo, J.R., and Baeumner, A.J., Recirculating, Passive Micromixer With a Novel Sawtooth Structure, *Lab on A Chip*, 6, 242-246, 2006

Ottino, J.M. and Wiggins, S., Introduction: Mixing in Microfluidics, *Philosophical Transactions of the Royal Society of London Series A-Mathematical Physical and Engineering Sciences*, 362, 923-935, 2004

Park, S.J., Kim, J.K., Park, J., Chung, S., Chung, C., and Chang, J.K., Rapid Three-Dimensional Passive Rotation Micromixer Using the Breakup Process, *Journal of Micromechanics and Microengineering*, 14, 6-14, 2004

Pennemann, H., Hessel, V., and Lowe, H., Chemical Microprocess Technology - From Laboratory-Scale to Production, *Chemical Engineering Science*, 59, 4789-4794, 2004a

Pennemann, H., Watts, P., Haswell, S.J., Hessel, V., and Lowe, H., Benchmarking of Microreactor Applications, *Organic Process Research & Development*, 8, 422-439, 2004b

Perry, R.H. and Green, D.W., *Perry's Chemical Engineers' Handbook* (7th Edition), 7th, McGraw-Hill, 1997

Pfeifer, P., Wenka, A., Schubert, K., Liauw, M.A., and Emig, G., Characterization of Flow Distribution in Microchannel Reactors, *Aiche Journal*, 50, 418-425, 2004

Porter, M.J., Roberts, S.M., and Skidmore, J., Polyamino Acids As Catalysts in Asymmetric Synthesis, *Bioorganic & Medicinal Chemistry*, 7, 2145-2156, 1999

Porter, M.J. and Skidmore, J., Asymmetric Epoxidation of Electron-Deficient Olefins, *Chemical Communications*, 1215-1225, 2000

Quiram, D.J., Jensen, K.F., Schmidt, M.A., Ryley, J.F., Mills, P.L., Wetzel, M.D., Ashmead, J.W., Bryson, R.D., Delaney, T.M., Kraus, D.J., and McCracken, J.S., Development of a Turnkey Multiple Microreactor Test Station, *Proceedings of the 4th International Conference on Microreaction Technology*, 2000 Atlanta, U.S.A.

Raja, L.L., Kee, R.J., Deutschmann, O., Warnatz, J., and Schmidt, L.D., A Critical Evaluation of Navier-Stokes, Boundary-Layer, and Plug-Flow Models of the Flow and Chemistry in a Catalytic-Combustion Monolith, *Catalysis Today*, 59, 47-60, 2000

Rebrov, E.V., Ilyas, Z., I, Rahul, P.E., Mart, H.J.M., and Jaap, C.S., Header Design for Flow Equalization in Microstructured Reactors, *Aiche Journal*, 53, 28-38, 2007

Roberge, D.M., Ducry, L., Bieler, N., Cretton, P., and Zimmermann, B., Microreactor Technology: A Revolution for the Fine Chemical and Pharmaceutical Industries?, *Chemical Engineering & Technology*, 28, 318-323, 2005

Rosagutti, N.R., Fletcher, D.F., and Haynes, B.S., Laminar Flow and Heat Transfer in a Periodic Serpentine Channel, *Chemical Engineering & Technology*, 28, 353-361, 2005

Sato, H., Ito, S., Tajima, K., Orimoto, N., and Shoji, S., PDMS Microchannels With Slanted Grooves Embedded in Three Walls to Realize Efficient Spiral Flow, *Sensors and Actuators A-Physical*, 119, 365-371, 2005

Schenk, R., Hessel, V., Hofmann, C., Kiss, J., Lowe, H., and Ziogas, A., Numbering-Up of Micro Devices: a First Liquid-Flow Splitting Unit, *Chemical Engineering Journal*, 101, 421-429, 2004

Schenk, R., Hessel, V., Hofmann, C., Lowe, H., and Schonfeld, F., Novel Liquid-Flow Splitting Unit Numbering-Up of Liquid/Liquid Specifically Made for Chemical Microprocessing, *Chemical Engineering & Technology*, 26, 1271-1280, 2003

Schmitt, C., Agar, D.W., Platte, F., Buijssen, S., Pawlowski, B., and Duisberg, M., Ceramic Plate Heat Exchanger for Heterogeneous Gas-Phase Reactions, *Chemical Engineering & Technology*, 28, 337-343, 2005

Schonfeld, F. and Hardt, S., Simulation of Helical Flows in Microchannels, *Aiche Journal*, 50, 771-778, 2004

Schonfeld, F., Hessel, V., and Hofmann, C., An Optimised Split-and-Recombine Micro-Mixer With Uniform 'Chaotic' Mixing, *Lab on A Chip*, 4, 65-69, 2004

Schwalbe, T., Autze, V., Hohmann, M., and Stirner, W., Novel Innovation Systems for a Cellular Approach to Continuous Process Chemistry From Discovery to Market, *Organic Process Research & Development*, 8, 440-454, 2004

Schwalbe, T., Kursawe, A., and Sommer, J., Application Report on Operating Cellular Process Chemistry Plants in Fine Chemical and Contract Manufacturing Industries, *Chemical Engineering & Technology*, 28, 408-419, 2005

Schwesinger, N., Frank, T., and Wurmus, H., A Modulator Microfluid System With an Integrated Micromixer, *Journal of Micromechanics and Microengineering*, 6, 99-102, 1996

Sherwood, T.K., Pigford, R.L., and Wilke, C.R., *Mass Transfer*, McGraw Hill, New York, 1975

Song, Y.J., Kumar, C.S.S.R., and Hormes, J., Fabrication of an SU-8 Based Microfluidic Reactor on a PEEK Substrate Sealed by a 'Flexible Semi-Solid Transfer' (FST) Process, *Journal of Micromechanics and Microengineering*, 14, 932-940, 2004

Stitt, E.H., Alternative Multiphase Reactors for Fine Chemicals - A World Beyond Stirred Tanks?, *Chemical Engineering Journal*, 90, 47-60, 2002

Bibliography

Stone, H.A. and Kim, S., Microfluidics: Basic Issues, Applications, and Challenges, *Aiche Journal*, 47, 1250-1254, 2001

Stroock, A.D., Dertinger, S.K., Whitesides, G.M., and Ajdari, A., Patterning Flows Using Grooved Surfaces, *Analytical Chemistry*, 74, 5306-5312, 2002a

Stroock, A.D., Dertinger, S.K.W., Ajdari, A., Mezic, I., Stone, H.A., and Whitesides, G.M., Chaotic Mixer for Microchannels, *Science*, 295, 647-651, 2002b

Stroock, A.D. and McGraw, G.J., Investigation of the Staggered Herringbone Mixer With a Simple Analytical Model, *Philosophical Transactions of the Royal Society of London Series A-Mathematical Physical and Engineering Sciences*, 362, 971-986, 2004

Sudarsan, A.P. and Ugaz, V.M., Fluid Mixing in Planar Spiral Microchannels, *Lab on A Chip*, 6, 74-82, 2006

Takagi, R., Manabe, T., Shiraki, A., Yoneshige, A., Hiraga, Y., Kojima, S., and Ohkata, K., The Julia-Colonna Asymmetric Epoxidation Reaction of Chalcone Catalyzed by Length Defined Oligo-L-Leucine: Importance of the N-Terminal Functional Group and Helical Structure of the Catalyst in the Asymmetric Induction, *Bulletin of the Chemical Society of Japan*, 73, 2115-2121, 2000a

Takagi, R., Shiraki, A., Manabe, T., Kojima, S., and Ohkata, K., The Julia-Colonna Type Asymmetric Epoxidation Reaction Catalyzed by Soluble Oligo-L-Leucines Containing an Alpha- Aminoisobutyric Acid Residue: Importance of Helical Structure of the Catalyst on Asymmetric Induction, *Chemistry Letters*, 366-367, 2000b

Thomas, H., The Reality of Small Scale Continuous Processing, 2003

Thornell, G. and Johansson, S., Microprocessing at the Fingertips, *Journal of Micromechanics and Microengineering*, 8, 251-262, 1998

Tonkovich, A., Fitzgerald, S., and Arora, R., Commercial Scale Microchannel Technology Methodology and Capabilities: Demonstrating Sufficient Flow Distribution, *Proceedings of the 8th International Conference on Microreaction Engineering*, 2005a

Tonkovich, A., Kuhlmann, D., Rogers, A., McDaniel, J., Fitzgerald, S., Arora, R., and Yusichak, T., Microchannel Technology Scale-Up to Commercial Capacity, *Chemical Engineering Research & Design*, 83, 634-639, 2005b

Tonkovich, A.L.Y., Zilka, J.L., Powell, M.R., and Call, C.J., The Catalytic Partial Oxidation of Methane in a Microchannel Chemical Reactor, *Process Miniaturization: 2nd International Conference on Microreaction Technology*, New Orleans, USA, 1998

Tonkovich, A.Y., Perry, S., Wang, Y., Qiu, D., LaPlante, T., and Rogers, W.A., Microchannel Process Technology for Compact Methane Steam Reforming, *Chemical Engineering Science*, 59, 4819-4824, 2004

Tonomura, O., Tanaka, S., Noda, M., Kano, M., Hasebe, S., and Hashimoto, L., CFD-Based Optimal Design of Manifold in Plate-Fin Microdevices, *Chemical Engineering Journal*, 101, 397-402, 2004

Tsogoeva, S.B., Woltinger, J., Jost, C., Reichert, D., Kuhnle, A., Krimmer, H.P., and Drauz, K., Julia-Colonna Asymmetric Epoxidation in a Continuously Operated Chemzyme Membrane Reactor, *Synlett*, 707-710, 2002

Veenstra, T.T., Lammerink, T.S.J., Elwenspoek, M.C., and van den Berg, A., Characterization Method for a New Diffusion Mixer Applicable in Micro Flow Injection Analysis Systems, *Journal of Micromechanics and Microengineering*, 9, 199-202, 1999

Wada, Y., Schmidt, M.A., and Jensen, K.F., Flow Distribution and Ozonolysis in Gas-Liquid Multichannel Microreactors, *Industrial & Engineering Chemistry Research*, 45, 8036-8042, 2006

Wakami, H. and Yoshida, J., Grignard Exchange Reaction Using a Microflow System: From Bench to Pilot Plant, *Organic Process Research & Development*, 9, 787-791, 2005

Wang, H.Z., Iovenitti, P., Harvey, E., and Masood, S., Optimizing Layout of Obstacles for Enhanced Mixing in Microchannels, *Smart Materials & Structures*, 11, 662-667, 2002

Wang, H.Z., Iovenitti, P., Harvey, E., and Masood, S., Numerical Investigation of Mixing in Microchannels With Patterned Grooves, *Journal of Micromechanics and Microengineering*, 13, 801-808, 2003

Wang, L.L. and Yang, J.T., An Overlapping Crisscross Micromixer Using Chaotic Mixing Principles, *Journal of Micromechanics and Microengineering*, 16, 2684-2691, 2006

Wang, L., Yang, J.T., and Lyu, P.C., An Overlapping Crisscross Micromixer, *Chemical Engineering Science*, 62, 711-720, 2007

Watts, P. and Haswell, S.J., The Application of Microreactors for Small Scale Organic Synthesis, *Chemical Engineering & Technology*, 28, 290-301, 2005

Werner, B., Hessel, V., and Lob, P., Mixers With Microstructured Foils for Chemical Production Purposes, *Chemical Engineering & Technology*, 28, 401-407, 2005

Wille, C., Gabski, H.P., Haller, T., Kim, H., Unverdorben, L., and Winter, R., Synthesis of Pigments in a Three-Stage Microreactor Pilot Plant-an Experimental Technical Report, *Chemical Engineering Journal*, 101, 179-185, 2004

Bibliography

Wong, S.H., Ward, M.C.L., and Wharton, C.W., Micro T-Mixer As a Rapid Mixing Micromixer, Sensors and Actuators B-Chemical, 100, 359-379, 2004

Yamaguchi, Y., Ogino, K., Yamashita, K., and Maeda, H., Rapid Micromixing Based on Multilayer Laminar Flows, Journal of Chemical Engineering of Japan, 37, 1265-1270, 2004

Yang, J., Li, C.W., and Yang, M.S., Lab-on-a-Chip (Microfluidics) Technology, Acta Biochimica Et Biophysica Sinica, 34, 117-123, 2002

Yang, J.T., Huang, K.J., and Lin, Y.C., Geometric Effects on Fluid Mixing in Passive Grooved Micromixers, Lab on A Chip, 5, 1140-1147, 2005

Yi, C.Q., Li, C.W., Ji, S.L., and Yang, M.S., Microfluidics Technology for Manipulation and Analysis of Biological Cells, Analytica Chimica Acta, 560, 1-23, 2006

Yi, H., Zou, G., Li, Q., Chen, Q., Tang, J., and He, M.Y., Asymmetric Epoxidation of Alpha,Beta-Unsaturated Ketones Catalyzed by Silica-Grafted Poly-(L)-Leucine Catalysts, Tetrahedron Letters, 46, 5665-5668, 2005

Zalc, J.M., Szalai, E.S., Muzzio, F.J., and Jaffer, S., Characterization of Flow and Mixing in an SMX Static Mixer, Aiche Journal, 48, 427-436, 2002

Zech, T., Honicke, D., Fichtner, M., and Schubert, K., Superior Performance of Static Micromixers, Proceedings of the 4th International Conference on Microreaction Technology, IMRET 4, 2000 Atlanta, USA